

University of London  
Imperial College of Science, Technology and Medicine  
Department of Computing

**An image segmentation and registration  
approach to cardiac function analysis using  
MRI**

Wenzhe Shi

Submitted in part fulfilment of the requirements for the transfer of  
Doctor of Philosophy in Computing of the University of London and  
the Diploma of Imperial College, August 2012



## Abstract

Cardiovascular diseases (CVDs) are one of the major causes of death in the world. In recent years, significant progress has been made in the care and treatment of patients with such diseases. A crucial factor for this progress has been the development of magnetic resonance (MR) imaging which makes it possible to diagnose and assess the cardiovascular function of the patient. The ability to obtain high-resolution, cine volume images easily and safely has made it the preferred method for diagnosis of CVDs. MRI is also unique in its ability to introduce noninvasive markers directly into the tissue being imaged (MR tagging) during the image acquisition process. With the development of advanced MR imaging acquisition technologies, 3D MR imaging is more and more clinically feasible. This recent development has allowed new potentially 3D image analysis technologies to be deployed. However, quantitative analysis of cardiovascular system from the images remains a challenging topic.

The work presented in this thesis describes the development of segmentation and motion analysis techniques for the study of the cardiac anatomy and function in cardiac magnetic resonance (CMR) images. The first main contribution of the thesis is the development of a fully automatic cardiac segmentation technique that integrates and combines a series of state-of-the-art techniques. The proposed segmentation technique is capable of generating an accurate 3D segmentation from multiple image sequences. The proposed segmentation technique is robust even in the presence of pathological changes, large anatomical shape variations and locally varying contrast in the images.

Another main contribution of this thesis is the development of motion tracking techniques that can integrate motion information from different sources. For example, the radial motion of the myocardium can be tracked easily in untagged MR imaging since the epi- and endocardial surfaces are clearly visible. On the other hand, tagged MR imaging allows easy tracking of both longitudinal and circumferential motion. We propose a novel technique based on non-rigid image registration for the myocardial motion estimation using both untagged and 3D tagged MR images. The novel aspect of our technique is its simultaneous use of complementary information from both untagged and 3D tagged MR imaging. The similarity measure is spatially weighted to maximise the utility of information from both images.

The thesis also proposes a sparse representation for free-form deformations (FFDs) using

the principles of compressed sensing. The [sparse free-form deformation \(SFFD\)](#) model can capture fine local details such as motion discontinuities without sacrificing robustness. We demonstrate the capabilities of the proposed framework to accurately estimate smooth as well as discontinuous deformations in 2D and 3D [CMR](#) image sequences. Compared to the standard [FFD](#) approach, a significant increase in registration accuracy can be observed in datasets with discontinuous motion patterns.

Both the segmentation and motion tracking techniques presented in this thesis have been applied to clinical studies. We focus on two important clinical applications that can be addressed by the techniques proposed in this thesis. The first clinical application aims at measuring longitudinal changes in cardiac morphology and function during the cardiac remodelling process. The second clinical application aims at selecting patients that positively respond to [cardiac resynchronization therapy \(CRT\)](#).

The final chapter of this thesis summarises the main conclusions that can be drawn from the work presented here and also discusses possible avenues for future research.

## Acknowledgements

I would like to thank my supervisor, Prof. Daniel Rueckert, for his sage advice, patient encouragement and insightful guide throughout the course of my research.

I would also like to thank my second supervisor Dr. Philip "Eddie" Edwards, for his valuable input and important suggestions for these projects.

Sincere thanks also go to Dr. Declan O'Regan of the Robert Steiner MR imaging unit at Hammersmith Hospital, Dr. Simon Duckett and Prof. Reza Razavi at St Thomas Hospital for acquiring the many MR data sets used in this report. In addition, thanks to all dear cooperators from Kings College London and University of Oxford.

I would also like to thank my colleagues and friends in the biomedical image analysis group for their help and support. Especially to Dr. Paul Aljabar, Dr. Wenjia Bai, Dr. Kanwal Bhatia, Dr. Luis Pizarro, Dr. Robin Wolz, Kai Pin (Tom) Tung and Haiyan Wang.



## Dedication

This thesis is dedicated to my family to their emotional and financial support, especially to my father and mother for instilling the importance of hard work and higher education; to my wife for supporting me each step of the way; to my grandma, grandpa who I wish can notice this from the other side of the world.

‘Rich in Knowledge and Tenacious of Purpose; Inquiring with Earnestness and Reflecting with Self-practice.’

*ZiXia @ Analects of Confucius*

‘Learning without thought is indiscriminate; Thinking without learning is perilous.’

*Confucius @ Analects of Confucius*

# Acronyms

**AAM** active appearance models. [xxii](#), [37](#), [38](#)

**ACPS** adaptive control point status. [xxii](#), [42](#)

**ACS** acute coronary syndrome. [6](#)

**AHA** American heart association. [107](#), [108](#), [114](#), [115](#), [119](#), [138](#)

**ASM** active shape model. [36](#), [37](#)

**AV** atrioventricular. [2–4](#), [8](#)

**BEM** boundary element method. [52](#)

**bSSFP** balanced steady state free precession. [15](#), [27](#), [92](#)

**CCD** congenital cardiovascular defects. [7](#), [8](#)

**CHD** coronary heart disease. [5](#)

**CIRC** left circumflex artery. [4](#)

**CMR** cardiac magnetic resonance. [i](#), [ii](#), [xxi](#), [13–16](#), [26](#), [27](#), [33](#), [38](#), [49](#), [54](#), [57](#), [65](#), [134](#), [136–138](#), [142](#), [148](#), [149](#)

**CO** cardiac output. [19](#), [20](#), [49](#)

**CRT** cardiac resynchronization therapy. [ii](#), [xxiii](#), [11](#), [12](#), [24](#), [93](#), [108](#), [115](#), [116](#), [134–136](#), [145](#)

**CSPAMM** complementary spatial modulation of magnetisation imaging. [15](#), [16](#), [95](#), [96](#)

**CT** computed tomography. [12](#), [13](#), [29](#), [39](#), [56](#)

**CTA** computed tomography angiography. 56

**CVDs** cardiovascular diseases. i, xix, 1, 2, 5, 7, 26, 90

**DCM** dilated cardiomyopathy. 11

**DP** dynamic programming. 33

**ECG** electrocardiography. 15, 18, 135

**ED** end diastolic. 9, 29, 31, 40, 51, 65, 69, 99, 103, 128, 136–138

**EDV** end-diastolic volume. 19, 20, 67, 88, 148

**EF** ejection fraction. xix, 19, 20, 29, 49, 53, 67, 93, 117, 118, 135, 136, 148, 150

**EFFD** extended free-form deformation. 51

**EM** expectation maximisation. 33, 41, 45, 46, 68, 69, 73–75, 77, 81, 85, 144, 149

**EPI** echo planar imaging. 94, 137

**ES** end systolic. 29, 128

**ESV** end-systolic volume. 11, 19, 135

**FEM** finite element method. 52, 61

**FFD** free-form deformation. i, ii, xix, xxii–xxiv, 24, 42, 51, 54, 55, 111, 121–132, 149–151, 153

**FOV** field of view. 94, 137

**GMM** Gaussian mixture models. 33

**HARP** harmonic phase tracking. 50, 56–58, 60, 63, 65, 90

**HLA** horizontal long-axis. 15, 94, 103, 104

**ICD-9** international statistical classification of diseases and related health problems. 7, 9

**IQR** interquartile range. 131

**LA** long-axis. [xxi](#), [13](#), [14](#), [22](#), [23](#), [27–29](#), [51](#), [58](#), [60](#), [64](#), [67](#), [69](#), [70](#), [72](#), [78](#), [80](#), [84](#), [86](#), [90–92](#), [94](#), [95](#), [97](#), [98](#), [101](#), [103–105](#), [107](#), [109](#), [113](#), [119](#), [148](#), [150](#)

**LAD** left anterior descending artery. [4](#)

**LARM** locally affine registration method. [xxii](#), [23](#), [41](#), [42](#), [48](#), [68](#), [74](#), [86](#), [87](#), [149](#)

**LDA** linear discriminant analysis. [83](#)

**LGE** late gadolinium enhancement. [16](#), [140](#), [142–144](#), [146](#)

**LM** left main coronary artery. [4](#), [5](#)

**LV** left ventricle. [xxi](#), [xxii](#), [xxiv](#), [2–5](#), [11](#), [12](#), [15](#), [19](#), [20](#), [26](#), [29–35](#), [37](#), [38](#), [47](#), [48](#), [51–53](#), [60–63](#), [65](#), [69](#), [71](#), [74](#), [75](#), [90](#), [92–94](#), [98](#), [99](#), [104](#), [107](#), [116](#), [118](#), [132](#), [135–139](#), [146](#), [148–150](#)

**LVM** left ventricular mass. [19](#), [67](#), [88](#), [148](#)

**LVV** left ventricular volume. [19](#), [88](#)

**MCEM** multiple component expectation maximisation. [23](#), [69](#), [75](#), [78](#), [80](#), [84](#), [86](#), [87](#), [140](#), [144](#), [149](#)

**MI** mutual information. [64](#), [126](#)

**MR** magnetic resonance. [i](#), [iii](#), [xxi](#), [1](#), [13](#), [15](#), [16](#), [22–31](#), [35](#), [38](#), [39](#), [43](#), [48–53](#), [56–58](#), [60–65](#), [67](#), [69–71](#), [73](#), [75](#), [79](#), [84](#), [87](#), [90–101](#), [103](#), [104](#), [109–113](#), [116](#), [119](#), [136](#), [137](#), [141](#), [142](#), [145](#), [148–152](#)

**MRF** Markov random fields. [34](#), [41](#), [78](#), [79](#), [85](#)

**MRMCEM** multi-image refined multiple component expectation maximisation. [78](#), [83](#), [84](#), [86](#)

**NMI** normalized mutual information. [64](#), [73](#), [74](#), [98](#), [126](#), [128](#), [129](#)

**PCA** principle component analysis. [36](#), [37](#)

**PDA** posterior descending artery. [4](#)

**PDF** probability density function. [36](#)

**PDM** point distribution model. 36, 38

**PET** positron emission tomography. 12, 13

**PRDM** parameter distribution model. 52

**PV** partial volume. 27, 33

**RCA** right coronary artery. 4

**RF** radio frequency. 13, 15

**RMSt** regional myocardial strain. 20, 22, 49, 50, 88, 90, 93, 148

**ROI** region of interest. xxi, 28, 31, 32, 39, 83, 100

**RPM** robust point matching. 51, 59

**RV** right ventricle. 2–5, 26, 29, 31, 34, 61, 65, 74, 75

**RWM** regional wall motion. 20–22, 49, 53, 65, 67, 88, 148

**RWN** regional wall thickening. 20–22, 50, 53, 67, 88, 148

**SA** short axis. xxi, 14, 15, 22, 23, 26–30, 51–53, 57, 58, 60, 64, 67, 69–73, 78, 84, 90–92, 94, 95, 97–101, 103, 104, 106, 109, 113, 119, 136, 137, 140, 142, 144, 148, 150

**SAt** sino-atrial. 4, 10

**SD** standard deviation. 135, 139

**SDI** systolic dyssynchrony index. xix, xxiii, xxiv, 93, 107, 108, 115, 117–119, 135–137, 139–142

**SDM** statistical deformation models. 37

**SFFD** sparse free-form deformation. ii, xix, xxiv, 24, 119, 124–132, 153

**SPAMM** spatial modulation of magnetisation imaging. 15

**SPECT** single-photon emission computed tomography. 12, 13

**SSD** sum of squared differences. 126, 128, 129, 144

**SSFP** steady state free precession. 64, 65, 94, 95, 136, 140, 142, 146

**STAPLE** simultaneous truth and performance level estimation. [46](#), [47](#)

**STEMI** ST-elevation myocardial infarction. [24](#), [140](#), [142](#), [145](#), [146](#), [151](#)

**SV** stroke volume. [19](#), [20](#), [49](#)

**TDFFD** temporal diffeomorphic free form deformations. [xxii](#), [54](#), [55](#)

**TFE** turbo field echo. [17](#), [22](#), [29](#), [65](#), [67](#), [94](#), [137](#), [149](#)

**TOF** tetralogy of fallot. [8](#)

**US** echocardiogram. [12](#), [51](#), [54](#), [64](#)

**VECG** vector electrocardiography. [136](#)

**VLA** vertical long-axis. [15](#), [94](#), [103](#), [104](#)



# Contents

<b>Abstract</b>	<b>i</b>
<b>Acknowledgements</b>	<b>iii</b>
<b>Acronyms</b>	<b>vi</b>
<b>1 Introduction</b>	<b>1</b>
1.1 Background and motivation . . . . .	1
1.1.1 The anatomy and structure of the heart . . . . .	2
1.1.2 Cardiovascular diseases . . . . .	5
1.1.3 Cardiac dyssynchrony, remodelling and resynchronisation therapy . . . . .	11
1.1.4 Cardiac magnetic resonance imaging . . . . .	12
1.1.5 Indices of cardiac function . . . . .	19
1.2 Objectives and challenges . . . . .	22
1.3 Contributions . . . . .	23
1.4 Overview of thesis . . . . .	24
1.5 Statement of originality . . . . .	25

<b>2</b>	<b>Cardiac image segmentation</b>	<b>26</b>
2.1	Challenge of cardiac segmentation . . . . .	26
2.2	Methods of cardiac image segmentation . . . . .	30
2.2.1	Cardiac localisation . . . . .	30
2.2.2	Low-level segmentation algorithms . . . . .	33
2.2.3	High-level segmentation algorithms . . . . .	34
2.3	Multi-atlas and patch based segmentation . . . . .	43
2.4	Evaluation methods and benchmarks . . . . .	46
2.5	Conclusion . . . . .	47
<b>3</b>	<b>Cardiac motion analysis</b>	<b>49</b>
3.1	Introduction . . . . .	49
3.2	Motion tracking for cine MR images . . . . .	50
3.2.1	Sparse feature tracking . . . . .	51
3.2.2	Deformable models . . . . .	52
3.2.3	Dense tracking methods . . . . .	53
3.3	Motion tracking for tagged MR images . . . . .	56
3.3.1	Harmonic phase tracking . . . . .	57
3.3.2	Gabor filter banks . . . . .	58
3.3.3	Sparse feature tracking . . . . .	59
3.3.4	Deformable models . . . . .	61
3.3.5	Registration methods . . . . .	63
3.4	Evaluation methods and benchmarks . . . . .	64

---

3.5	Conclusion . . . . .	65
<b>4</b>	<b>Automatic segmentation of different pathologies from cardiac MR images</b>	<b>66</b>
4.1	Introduction . . . . .	66
4.1.1	Limitations of current cardiac image segmentation approaches . . . . .	67
4.1.2	Overview and contributions . . . . .	69
4.2	Myocardium segmentation from multiple image sequences . . . . .	70
4.2.1	Detection of the LV using a cascade classifier . . . . .	70
4.2.2	Spatio-temporal registration . . . . .	72
4.2.3	Initial atlas-based segmentation of the heart . . . . .	73
4.2.4	Multi-component EM estimation . . . . .	74
4.2.5	Multi-image graph-cuts refinement . . . . .	78
4.3	Uncertainty definition and evaluation . . . . .	81
4.3.1	Registration uncertainty . . . . .	81
4.3.2	Segmentation uncertainty . . . . .	82
4.3.3	Uncertainty quantification and user interaction . . . . .	83
4.4	Results . . . . .	84
4.5	Discussion and conclusion . . . . .	87
<b>5</b>	<b>A comprehensive cardiac motion estimation framework</b>	<b>89</b>
5.1	Introduction . . . . .	89
5.1.1	Overview and contributions . . . . .	91
5.2	Cardiac MR image acquisition . . . . .	93
5.3	Spatial and temporal alignment . . . . .	94

5.3.1	Temporal alignment . . . . .	95
5.3.2	Spatial alignment . . . . .	96
5.4	Comprehensive motion tracking . . . . .	98
5.4.1	Overview . . . . .	99
5.4.2	Automatic detection and segmentation of the heart . . . . .	100
5.4.3	Weighted similarity measure for motion tracking . . . . .	100
5.4.4	Valve plane tracking . . . . .	103
5.4.5	Adaptive incompressibility for motion tracking . . . . .	105
5.5	Motion tracking in patients undergoing cardiac resynchronisation therapy . . . . .	107
5.5.1	Parcellation of the myocardium . . . . .	107
5.5.2	Regional SDI analysis . . . . .	107
5.6	Evaluation . . . . .	108
5.6.1	Accuracy results . . . . .	110
5.6.2	SDI results . . . . .	116
5.7	Discussion and conclusion . . . . .	119
<b>6</b>	<b>Registration using sparse free-form deformations</b>	<b>121</b>
6.1	Introduction . . . . .	121
6.1.1	Overview and contributions . . . . .	123
6.2	Classic free-form deformation model . . . . .	124
6.3	Sparse free-form deformation model . . . . .	124
6.3.1	Sparse representation of transformation . . . . .	125
6.4	Results . . . . .	127

---

6.4.1	Datasets . . . . .	127
6.4.2	Implementation details . . . . .	128
6.4.3	Effects of the sparsity constraint . . . . .	129
6.4.4	Evaluation . . . . .	131
6.5	Discussion and conclusions . . . . .	132
<b>7</b>	<b>Clinical applications</b>	<b>134</b>
7.1	Introduction . . . . .	134
7.2	Application to cardiac resynchronisation therapy . . . . .	135
7.2.1	Introduction . . . . .	135
7.2.2	Image acquisition . . . . .	136
7.2.3	Methods . . . . .	137
7.2.4	Results . . . . .	139
7.3	Application to remodelling after acute myocardial infarction . . . . .	139
7.3.1	Introduction . . . . .	140
7.3.2	Image acquisition . . . . .	142
7.3.3	Methods . . . . .	143
7.3.4	Results . . . . .	145
7.4	Discussion and conclusions . . . . .	145
<b>8</b>	<b>Conclusion</b>	<b>148</b>
8.1	Summary of current achievements . . . . .	148
8.2	Limitations and future work . . . . .	152

A List of publications	154
B Derivation of energy gradient	157
C Definition of wall-curvature	162
Bibliography	163

# List of Tables

1.1	Percentage breakdown of deaths due to CVDs [Members et al., 2012]. . . . .	5
4.1	Segmentation results: The Dice overlap measure. . . . .	84
4.2	Segmentation results: The average surface-to-surface distances. . . . .	84
5.1	Inter-observer variance of the relative error for the surface tracking. . . . .	109
5.2	Average maximum displacement (based on manual tracking) for patients and volunteers. . . . .	112
5.3	Change of myocardial mass computed using the different motion tracking methods.	117
5.4	Evaluation of ejection fraction (EF) accuracy. . . . .	117
5.5	Evaluation against TomTec’s regional volume systolic dyssynchrony index (SDI) measurement. . . . .	118
5.6	Evaluation of regional strain SDI against the TomTec’s regional volume SDI. . .	118
6.1	Accuracies from the SFFD with different coarsest spacing. . . . .	131
6.2	Accuracies from the classic FFDs with different initial and final spacing and the SFFD with different normalised sparsity parameter. . . . .	131



# List of Figures

1.1	The heart consists of two pumps lying side by side. . . . .	2
1.2	The cardiac conduction system. . . . .	4
1.3	The coronary circulation. [Institute, 2010] . . . . .	5
1.4	The typical orientation of CMR imaging planes [Heller et al., 2002] . . . . .	14
1.5	The images from left to right show respectively short axis (SA), horizontal long-axis and vertical long-axis views of the heart. . . . .	14
1.6	This figure shows a simulated long-axis (LA) view of the heart which has been obtained by stacking a set of SA images. . . . .	14
1.7	Example cine SSFP and LGE images from a volunteer. . . . .	17
1.8	Example whole heart TFE and tagged MR images from a volunteer. . . . .	18
1.9	Bull-eye plot of the 17 segments of the left ventricular myocardium. . . . .	21
2.1	Variability among cardiac images. . . . .	27
2.2	A region of interest (ROI) identifying the heart and anatomy for SA cine MR images [Petitjean and Dacher, 2011] . . . . .	28
2.3	Variability of the heart in SA MR images along the LA. [Petitjean and Dacher, 2011] . . . . .	28
2.4	The feature set defining the heart left ventricle (LV). [Jolly, 2006] . . . . .	31

2.5	LV location procedure. [Lu et al., 2009] . . . . .	32
2.6	Deformable models and anatomical constraints for the segmentation of the LV. [Paragios, 2002] . . . . .	35
2.7	Segmentation results by 3D active appearance models (AAM). [Mitchell et al., 2002] . . . . .	38
2.8	Whole heart segmentation result using deformable models [Peters et al., 2007]. .	39
2.9	Anatomical atlas-based segmentation. [Lorenzo-Valdés et al., 2002] . . . . .	41
2.10	Temporal registration and resampling. [Lorenzo-Valdés et al., 2004] . . . . .	41
2.11	Comparison of manual segmentation, Affine+FFD, locally affine registration method (LARM)+FFD, and LARM+adaptive control point status (ACPS). [Zhuang et al., 2010]. . . . .	42
2.12	The general framework for multi-atlas based segmentation. . . . .	44
3.1	Example of contour tracking from [Remme et al., 2005]. . . . .	52
3.2	Overview of the temporal diffeomorphic free form deformations (TDFFD) framework. [De Craene et al., 2012] . . . . .	55
3.3	Example of HARP motion tracking. [Pan et al., 2005] . . . . .	57
3.4	Example of motion tracking using deformable models. [Haber et al., 2000] . . . .	61
4.1	Overall workflow of the segmentation framework. . . . .	70
4.2	Positive (green) and negative (red) examples from the training set for the cardiac detector. . . . .	71
4.3	Some examples of the results from the cardiac detector. . . . .	72
4.4	Example of the constructed probabilistic atlas. . . . .	75
4.5	Workflow of the multi-component EM estimation based segmentation component.	76
4.6	Randomly selected segmentation results of different patients. . . . .	78

4.7	The histogram of the Jacobian determinant and fitted Rician distribution from different subjects. . . . .	82
4.8	The example images from different pathological groups. . . . .	85
4.9	Myocardial segmentation and registration uncertainties. . . . .	86
5.1	Multiple image acquisitions for cardiac motion tracking. . . . .	91
5.2	Workflow of the proposed comprehensive cardiac motion method. . . . .	92
5.3	Spatial alignment of different images. . . . .	95
5.4	Removal of tags from 3D tagged MR. . . . .	97
5.5	The spatial weight map for the comprehensive motion tracking. . . . .	103
5.6	Automatic detection of valve points. . . . .	104
5.7	The parcellation of the endocardial surface into 16 segments. . . . .	108
5.8	This figure shows the relative landmark error in % when comparing the results of manual tag tracking with the registration-based motion tracking. . . . .	110
5.9	This figure shows the relative landmark error in % when comparing the results of manual tag tracking with registration-based motion tracking. . . . .	111
5.10	This figure shows the relative surface distance when comparing the result of an automatic segmentation with a manual segmentation. . . . .	112
5.11	This figure shows the manual landmark identification and distribution of the landmarks. . . . .	113
5.12	This figure shows the radial motion estimated from different methods. . . . .	114
5.13	This figure shows the longitudinal motion estimated from different methods. . . . .	114
5.14	This figure shows the circumferential motion estimated from different methods. . . . .	115
5.15	This figure shows the SDI curves from a normal subject and a CRT candidate. . . . .	115

5.16	A visualisation of the myocardial motion field in radial, longitudinal and circumferential directions. . . . .	116
6.1	Sparse representations of FFDs. . . . .	122
6.2	Visual comparison between the classic FFDs and the proposed SFFD using the colour scheme from [Baker et al., 2007]. . . . .	125
6.3	The accuracy of different parameters. . . . .	130
6.4	The effect of the sparsity parameter. . . . .	130
7.1	This figure shows the graphs for SDI. . . . .	140
7.2	Acute response and remodelling against volume and muscle thickening SDI. [Duckett et al., 2012] . . . . .	141
7.3	Acute response and remodelling against strain SDIs. [Duckett et al., 2012] . . . .	142
7.4	Flow chart showing the main steps for co-registering and segmenting the cardiac MR images to obtain a 3D transformation between baseline and follow-up images.	143
7.5	3D visualisation of different indices of the LV in an 51 year old male patient. [Oregan et al., 2012] . . . . .	146
7.6	A Dot density histogram for each variable derived from the image registration model at baseline and follow-up. [Oregan et al., 2012] . . . . .	147

# Chapter 1

## Introduction

This chapter gives an introduction to this thesis. [Cardiovascular diseases \(CVDs\)](#) is one of the major causes of death in the western world. In recent years, significant progress has been made in the care and treatment of patients with such diseases. A crucial factor in this progress has been the development of [magnetic resonance \(MR\)](#) imaging which makes it possible to diagnose and assess the cardiovascular function of the patient non-invasively. The ability to obtain high-resolution, cine volumetric images easily and safely has made it the preferred method for diagnosis of cardiovascular diseases. [MR](#) images is also unique in its ability to introduce noninvasive markers directly into the tissue being imaged ([MR tagging](#)) during the image acquisition process. With the development of advanced [MR](#) imaging acquisition technologies, 3D [MR](#) imaging is more and more clinically feasible. This recent development has allowed new potentially 3D image analysis technologies to be deployed. Quantitative analysis of the cardiovascular system from the images remains a challenging topic.

### 1.1 Background and motivation

In this section, we review the basic anatomy and function of the heart and give a brief introduction of [CVDs](#) and the main [MR](#) imaging techniques that have been developed for diagnosing patients with [CVDs](#). In addition, we describe some of the basic clinical parameters

which are widely used in the assessment of CVDs.

### 1.1.1 The anatomy and structure of the heart

The cardiovascular system [Bray, 1999, Katz, 2005] is comprised of the heart and blood vessels whose main function is to circulate blood around the body. They act as a transport system for delivering oxygen from the lungs and nutrients from the gastrointestinal tract to the cells of the body. The heart (Figure 1.1) consists of two pumps lying side by side which pump in phase with each other. Each pump has an atrium and a ventricle as shown in the figure. The right atrium receives venous blood from the body and passes it through into the **right ventricle (RV)** where it is pumped to the lungs (pulmonary circulation) for oxygenation. At the same time the left atrium receives oxygenated blood from the lungs and the **left ventricle (LV)** pumps it out to the rest of the body (systemic circulation).

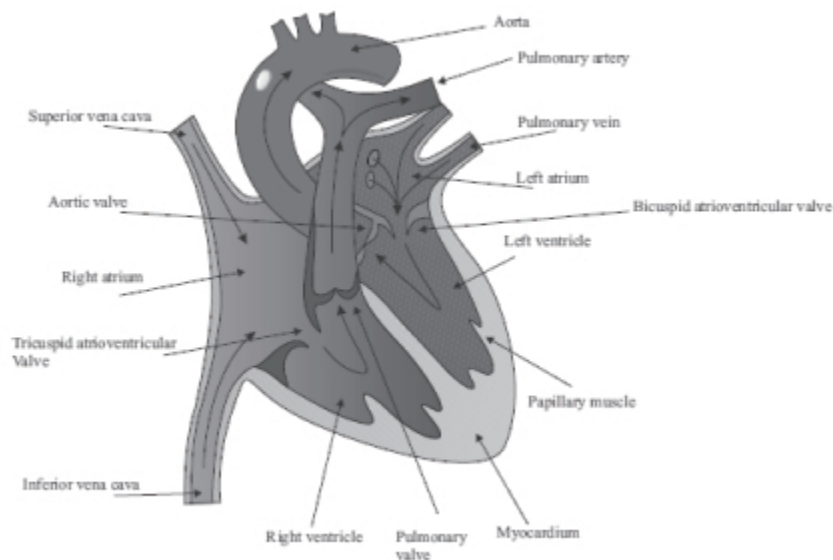


**Figure 1.1** – The heart consists of two pumps lying side by side. The arrows show the direction of blood flow in the two sides. This figure has been adapted from Figure 13.3 in [Bray, 1999].

The four chambers of the heart are separated from each other and the rest of the body by four sets of valves. The bicuspid (or mitral) and tricuspid **atrioventricular (AV)** valves separate the left and right atria and ventricles respectively, while the aortic valve separates the **LV** from the aorta, and the pulmonary valve separates the **RV** from the pulmonary artery. Thin chords called the chordae tendineae are attached to the **AV** valves and projections of the ventricular

muscles known as the papillary muscles. During ventricular contraction the papillary muscles tense and prevent the valves from inverting into the atrium.

### **The cardiac cycle**

Venous blood returning to the heart from the rest of the body flows continuously from the superior and inferior vena cava into the right atrium, while oxygenated blood from the lungs enters the left atrium through the pulmonary veins. When the pressure in the atria exceeds the pressure in the ventricles, the AV valves open and the blood enters the ventricles. When the ventricles are about 80% full, the atria contract and propel more blood into the ventricles completing the ventricular filling. This stage of the cardiac cycle, when the ventricular filling takes place, is known as diastole.

After a very short pause (approx. 0.1 s), the ventricles contract. This stage is known as systole. As the ventricles contract the pressure in the ventricles increases rapidly and exceeds the atrial pressure, causing the AV valves to close. Simultaneously, the papillary muscles contract so that the AV valves do not revert back into the atria. The continued contraction raises the ventricular pressure beyond the pressure in the aorta and the pulmonary artery. This causes the pulmonary and aortic valves to open and blood is ejected at low pressure from the RV into the pulmonary circuit and at high pressure from the LV into the systemic circuit. When the pressure in the ventricles falls below that in the pulmonary artery and the aorta, the pulmonary and aortic valves close. Similarly when the ventricular pressure falls below the atrial pressure, the AV valves open and the ventricles start to refill with blood again and the cycle repeats.

### **The electrical activation of the heart**

The myocardium (the heart muscle) is comprised of muscle cells called myocytes. These are typically  $10 - 20\mu\text{m}$  in diameter and  $50 - 100\mu\text{m}$  in length. The junction between adjacent myocytes, called the intercalated disc, allows electrical impulses to be transmitted from cell to cell making the myocardium act like an electrically continuous sheet. The contraction of the

heart is initiated by the [sino-atrial \(SA\)](#) node which acts as a pacemaker, dictating the rate of beating of the heart (Figure 1.2). The node is composed of myocytes which generate an action potential roughly once every second that excites the adjacent atrial work cells and causes a wave of depolarisation to travel across the two atria and initiates atrial systole.

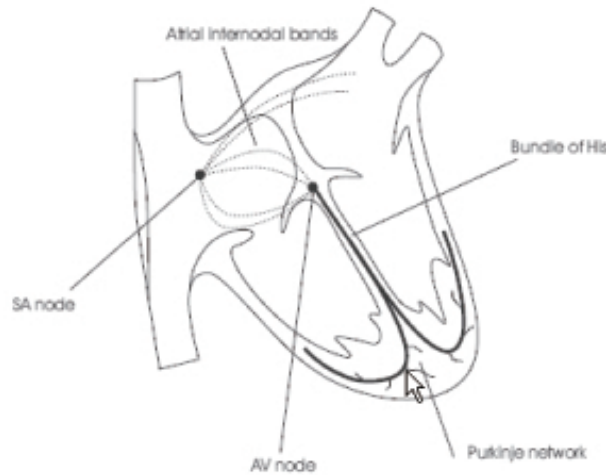


**Figure 1.2** – The cardiac conduction system adapted from figure 13.5 in [Bray, 1999].

The electrical impulse then reaches the [AV](#) node in the atrial septum (the wall separating the two atria). The impulse is delayed by the [AV](#) node allowing the atria to finish contracting before the ventricles are activated. The electrical impulse then travels down a narrow bundle of conduction fibers called the bundle of His, which separates into two parts, one activating the [LV](#) of the heart and the other in the [RV](#). The bundle of His terminates in the Purkinje network, located in the subendocardium, which distributes the electrical impulse rapidly to the work cells of the myocardium.

### The coronary circulation

The heart receives the energy it needs from the coronary circulation (Figure 1.3), which consists of five main arteries: the [left main coronary artery \(LM\)](#), the [right coronary artery \(RCA\)](#), the [left anterior descending artery \(LAD\)](#), the [left circumflex artery \(CIRC\)](#), and the [posterior descending artery \(PDA\)](#). The [RCA](#) and the [LM](#) arise from the aorta, while the [LAD](#) and [CIRC](#) arise from the [LM](#) when it splits into two. The [PDA](#) arises from the [RCA](#) in approximately 90% of the human population and from the [CIRC](#) in approximately 10% of the population.

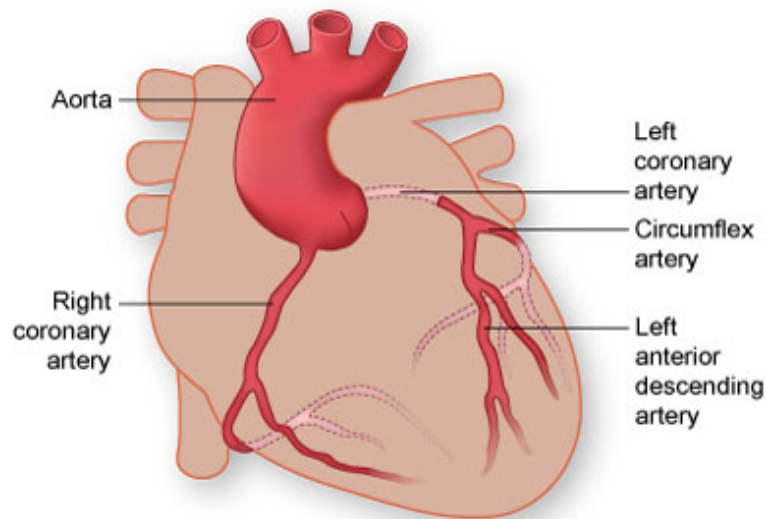


**Figure 1.3** – The coronary circulation. [Institute, 2010]

Type of CVD	Deaths (in %)
Coronary heart disease	49.9
Stroke	16.5
High blood pressure	7.5
Congestive heart failure	7.0
Diseases of the arteries	3.4
Other	15.6

**Table 1.1** – Percentage breakdown of deaths due to CVDs [Members et al., 2012].

The blood flow from the coronary arteries reaches the myocardium by vessels which penetrate the walls of the ventricles. This means that the endocardial regions of the heart are very vulnerable to cell death, or infarction, if coronary artery occlusion occurs. This is especially the case for the myocardium of the **LV** which has a much thicker wall than the **RV**. Occlusion of the **LM** is much more serious than occlusion of any one of the other arteries since this blocks off all of the blood supply to the myocardium of the **LV**.

### 1.1.2 Cardiovascular diseases

Table 1.1 shows a percentage breakdown of the deaths due to CVDs in the USA [Members et al., 2012]. In both the USA and Europe, the greatest proportion of deaths resulting from CVDs are due to coronary heart disease (CHD) [Members et al., 2012].

## Coronary heart disease, acute coronary syndrome, and angina pectoris

Coronary heart disease is the narrowing or blockage of the coronary arteries, usually caused by atherosclerosis. Atherosclerosis is the buildup of cholesterol and fatty plaques on the inner walls of the arteries. These plaques can restrict blood flow to the heart muscle by physically clogging the artery or by causing abnormal artery tone and function. Without an adequate blood supply, the heart becomes starved of oxygen and the vital nutrients it needs to work properly. This can cause chest pain known as angina. If the blood supply to a portion of the heart muscle is cut off entirely, or if the energy demands of the heart become much greater than its blood supply, a heart attack may occur.

[Acute coronary syndrome \(ACS\)](#) refers to any group of symptoms attributed to the obstruction of the coronary arteries. The most common symptom prompting diagnosis of [ACS](#) is chest pain, often radiating to the left arm or angle of the jaw, pressure-like in character, and associated with nausea and sweating. Acute coronary syndrome usually occurs as a result of one of three problems: ST elevation myocardial infarction (30%), non ST elevation myocardial infarction (25%), or unstable angina (38%) [[Torres and Moayed, 2007](#)]. Here the ST elevations refers to a finding of an electrocardiogram, wherein the trace in the ST segment is abnormally high above the isoelectric line. The ST segment corresponds to a period of ventricle systolic depolarisation, when the cardiac muscle is contracted.

Angina pectoris, commonly known as Angina, refers to chest pain due to ischemia of the heart muscle, generally caused by the obstruction or spasm of the coronary arteries. Coronary artery disease, the main cause of angina, is due to atherosclerosis of the cardiac arteries. Angina occurs when there is an imbalance between the heart's oxygen demand and supply. This imbalance can result from an increase in demand (e.g. during exercise) without a proportional increase in supply. When the symptoms of coronary occlusive disease do not change the patient is said to have stable angina pectoris. Stable angina often decreases in severity over weeks and months because of the development of collateral vessels and enlargement of partially occluded coronary arteries.

## Stroke (cerebrovascular disease)

Stroke is one of the [CVDs](#), which affects the arteries leading to and within the brain. A stroke occurs when a blood vessel carrying oxygen and nutrients to a part of the brain is blocked by a clot, or ruptures. As a result, the affected area of the brain cannot function, which might result in an inability to move one or more limbs on one side of the body, inability to understand or formulate speech, or an inability to see one part of the visual field. The part of the brain affected can be damaged because of the lack of blood flow and the consequences can be devastating. The patient may become paralysed in addition to the loss of language skills and vision. Stroke can be treated, if the warning signs are detected early enough, by drugs or surgical intervention.

## High blood pressure

High blood pressure, is often called the "silent killer" as no symptoms are shown in a person suffering from this [CVDs](#). Untreated it can lead to stroke, heart attack, heart failure, or kidney failure. Medications are available which can help to reduce and control high blood pressure but it is a lifelong disease, which cannot be cured. It may also lead to hypertensive heart disease. Systemic hypertension is one of the most prevalent and serious causes of coronary artery and myocardial disease in the United States [[Rubin and Reisner, 2009](#)]. Chronic hypertension leads to pressure overload and results first in compensatory left ventricular hypertrophy and, eventually, cardiac failure.

## Congenital cardiovascular defects

[Congenital cardiovascular defects \(CCD\)](#), also known as congenital heart defects, are structural problems that arise from abnormal formation of the heart or major blood vessels. Significant congenital cardiovascular defects occur in almost 1% of all live births. The [International statistical classification of diseases and related health problems \(ICD-9\)](#)<sup>1</sup> lists 25 congenital

---

<sup>1</sup><http://www.who.int/classifications/icd/en/>

heart defects codes, of which 21 designate specified anatomic or hemodynamic lesions [Members et al., 2012].

Defects range in severity from tiny pinholes between chambers that may resolve spontaneously, to major malformations that can require multiple surgical procedures before school age and may result in death in utero, in infancy, or in childhood. Common complex defects include the following [Members et al., 2012, Rubin and Reisner, 2009]:

- **Tetralogy of fallot (TOF)** represents 10% of all cases of **CCD** and is the most common cyanotic heart disease in older children and adults. It involves four heart malformations: e.g. infundibular pulmonary stenosis, overriding aorta, ventricular septal defect and right ventricular hypertrophy.
- **AV** septal defects are caused by an abnormal or inadequate fusion of the superior and inferior endocardial cushions with the mid portion of the atrial septum and the muscular portion of the ventricular septum.
- Coarctation of the aorta is a local constriction that almost always occurs immediately below the origin of the left subclavian artery at the site of the ductus arteriosus.
- Hypoplastic left heart syndrome is a **CCD** in which the left ventricle of the heart is severely underdeveloped. If part of the endocardial tube gets pinched shut in a region that becomes the future ventricle, hypoplastic heart syndrome will occur. If the pinched part of the endocardial tube is the bulbus-cordis region of the developing heart, hypoplastic *right* syndrome will occur. If it is in the ventricle region, it will be on the *left* side that is hypoplastic.

Congenital heart defects are serious and common conditions that have a significant impact on morbidity, mortality, and health care costs for children and adults.

## Cardiomyopathy and heart failure

Because of the heart's capacity to compensate, congestive heart failure is often tolerated for years. The heart's ability to adapt to injury is based on the same mechanisms that allow cardiac output to increase in response to stress. The fundamental compensatory mechanism is the Frank-Starling mechanism [Rubin and Reisner, 2009]: the cardiac stroke volume is a function of diastolic fiber length. Within certain limits, a normal heart will pump whatever volume is brought to it by the venous circulations. Stroke volume, a measure of ventricular function, is enhanced by increasing ventricular **end diastolic (ED)** volume secondary to an increase in atrial filling pressure.

Anything that increases cardiac workload for a prolonged period or produces structural damage may eventually lead to myocardial failure. Ischemic heart disease is by far the most common condition responsible for cardiac failure, accounting for 87% of strokes from heart disease [Members et al., 2012]. Most of the remaining cases are caused by nonischemic forms of heart muscle disease and congenital heart disease. Ventricular hypertrophy is observed in virtually all conditions associated with chronic heart failure.

## Cardiac dysrhythmias

Cardiac dysrhythmias refer to any variation from the normal rate or rhythm (which may include the origin of the impulse and/or its subsequent propagation) in the heart. The heartbeat may be too fast or too slow, and may be regular or irregular. A heart beat that is too fast is called tachycardia and a heart beat that is too slow is called bradycardia.

It can be classified into the following forms according to [ICD-9](#):

- Paroxysmal supraventricular tachycardia: An episodic form of supraventricular tachycardia, with abrupt onset and termination.
- Paroxysmal ventricular tachycardia: A tachycardia arising distal to bundle of His, with a rate greater than 100 beats per minute.

- Atrial fibrillation: An arrhythmia in which minute areas of the atrial myocardium are in various uncoordinated stages of depolarisation and repolarisation; instead of intermittently contracting, the atria quiver continuously in a chaotic pattern, causing a totally irregular, often rapid ventricular rate.
- Atrial flutter: An electrocardiographic finding of an organised rhythmic contraction of the atria, generally at a rate of 200-300 beats per minute.
- Ventricular fibrillation: An arrhythmia characterised by an irregular pattern of high or low-amplitude waves that cannot be differentiated into QRS complexes or T waves. These electrocardiographic waves occur as a result of fibrillary contractions of the ventricular muscle due to rapid repetitive excitation of myocardial fibers without coordinated contraction of the ventricle.
- Ventricular flutter: A ventricular tachyarrhythmia characterised electrocardiographically by smooth undulating waves with QRS complexes merged with T waves, a rate of approximately 250 per minute.
- Cardiac arrest: Sudden cessation of the pumping function of the heart, with disappearance of arterial blood pressure, connoting either ventricular fibrillation or ventricular standstill.
- Sinoatrial node dysfunction: A derangement in the normal functioning of the sinoatrial node. Typically, SA node dysfunction is manifest as sinoatrial exit block or sinus arrest, but may present as an absolute or relative bradycardia in the presence of a stressor. It may be associated with bradycardia-tachycardia syndrome.
- Other specified and unspecified cardiac dysrhythmias.

The most common symptom of arrhythmia is an abnormal awareness of the heartbeat, called palpitations. These may be infrequent, frequent, or continuous. Some of these arrhythmias are harmless (though distracting for patients) but many of them predispose to adverse outcomes. Some arrhythmias do not cause symptoms and are not associated with increased mortality. However, some asymptomatic arrhythmias are associated with adverse events. Examples

include a higher risk of blood clotting within the heart and a higher risk of insufficient blood being transported to the heart because of weak heartbeat. Other increased risks are of embolisation and stroke, heart failure and sudden cardiac death. Medical assessment of the abnormality using an electrocardiogram is the most common way to diagnose and assess the risk of any given arrhythmia.

### 1.1.3 Cardiac dyssynchrony, remodelling and resynchronisation therapy

Patients with [dilated cardiomyopathy \(DCM\)](#) that is further complicated by intra-ventricular conduction delay with dyssynchronous wall motion have an increased mortality risk as compared to the general [DCM](#) population. Dyssynchrony reduces cardiac systolic function while increasing oxygen consumption, and may be a source of arrhythmia [[Kass, 2002](#)]. The recent development of endocardial lead systems to activate the left ventricle prematurely has yielded the novel therapeutic option of resynchronisation therapy to correct cardiac dyssynchrony. Using either biventricular or left ventricular pre-excitation, systolic function and energetic efficiency can be substantially enhanced in heart failure patients who have underlying discoordinate contraction.

Left ventricular remodelling is the process by which ventricular size, shape, and function are regulated by mechanical, neurohormonal, and genetic factors [[Pfeffer and Braunwald, 1990](#), [Sutton and Sharpe, 2000](#)]. Remodelling may be physiological and adaptive during normal growth or pathological due to myocardial infarction, cardiomyopathy, hypertension, or valvular heart disease. Postinfarction remodelling has been arbitrarily divided into an early phase (within 72 hours) and a late phase (beyond 72 hours) [[Pfeffer and Braunwald, 1990](#)]. The early phase involves expansion of the infarct zone, which may result in early ventricular rupture or aneurysm formation. Late remodelling involves the left ventricle globally and is associated with time-dependent dilatation, the distortion of ventricular shape, and mural hypertrophy. The failure to normalise increased wall stresses results in progressive dilatation, recruitment of border zone myocardium into the scar, and deterioration in contractile function [[Sutton and](#)

Sharpe, 2000].

On the other hand, a reduction in **LV end-systolic volume (ESV)** of 10% signifies clinically relevant reverse remodelling, which is a strong predictor of lower long-term mortality and heart failure events [Yu et al., 2005]. [Yu et al., 2005] suggests that assessing volumetric changes after an intervention in patients with heart failure provides information predictive of natural history outcomes.

[Bax et al., 2004] found an interesting relationship between cardiac dyssynchrony and **cardiac resynchronization therapy (CRT)**:

- The LV dyssynchrony is larger in responders than non-responders to **CRT**;
- baseline LV dyssynchrony of 65 ms or more has a sensitivity and specificity of 80% to predict clinical response and 92% to predict reverse LV remodelling;
- patients with extensive dyssynchrony who undergo CRT have an excellent prognosis (6% event rate), whereas patients who do not have dyssynchrony and undergo CRT have a poor prognosis (event rate 50

This leads to the conclusion that patients with extensive **LV** dyssynchrony respond well to **CRT**. Using a cutoff level of 65 ms, a sensitivity and specificity of 80% were obtained for predicting clinical response of reverse remodelling and 92% for predicting reverse LV remodelling. Moreover, patients with LV dyssynchrony of approximate 65 ms had an excellent prognosis after **CRT**, in contrast to patients with < 65 ms who had a high event rate (50%) during one-year follow-up.

#### 1.1.4 Cardiac magnetic resonance imaging

Common cardiac imaging techniques include **echocardiogram (US)**, **positron emission tomography (PET)**, **computed tomography (CT)** and **single-photon emission computed tomography (SPECT)**. An echocardiogram uses ultrasonic waves for real-time visualisation of the heart

chamber and blood flow. Recently, it has become one of the most commonly used tools in the diagnosis of heart problems, as it allows non-invasive, low-cost visualisation of the heart. In addition the blood flow in the heart can be visualised using a technique known as Doppler US. CT is an imaging methodology which uses X-rays to produce tomographic images of the body. This is achieved by reconstructing a tomographic image from a large series of two-dimensional X-ray images taken around a single axis of rotation. While CT offers high spatial and temporal resolution, it requires a significant amount of radiation to produce good quality images. PET is an imaging methodology based on positron emitting radioisotopes. It enables visual analysis of multiple different metabolic processes (e.g. glucose uptake) and is thus one of the most flexible functional imaging technologies. However, it only offers low spatial and temporal resolution and can only be carried out in specialised centres. SPECT is similar to PET in its use of radioactive tracer material and detection of gamma rays. Cardiac gated acquisitions are possible with SPECT, however, the image quality is often inferior to that of PET imaging.

The work in this thesis focuses on MR imaging [Lauterbur, 1973] which is primarily a medical imaging technique most commonly used in radiology to visualise the anatomy and function of the body. MR imaging provides a much greater contrast between the different soft tissues of the body compared to CT, making it especially useful in neurological (brain), musculoskeletal, cardiovascular, and oncological (cancer) imaging. Unlike CT, it does not use ionising radiation, but a powerful magnetic field to align the magnetisation of (usually) hydrogen atoms in water or fat in the body. Radio frequency (RF) fields are used to systematically alter the alignment of this magnetisation, causing the hydrogen nuclei to produce a rotating magnetic field detectable by the scanner. This signal can be manipulated by additional magnetic fields to build up enough information to construct a tomographic image of the body.

## Imaging planes

As the heart is continuously in motion, it is difficult to acquire a volume. Instead, we have to acquire slices. In this case, it is necessary to acquire images in multiple orientations so that an

accurate diagnosis can be made. It is common to define, orient, and display the heart using the **long-axis (LA)** of the left ventricle and selected planes at 90 degree angles relative to the **LA**. The commonly used imaging planes are shown in Figure 1.4 and some example images are shown in Figure 1.5. Other factors which also make **cardiac magnetic resonance (CMR)** imaging challenging are patient motion, respiration, and the anisotropic resolution of the images acquired. Typically, the in-plane resolution (1-2.5mm) is much higher than the through-plane resolution (8-10mm) as shown in Figure 1.6.

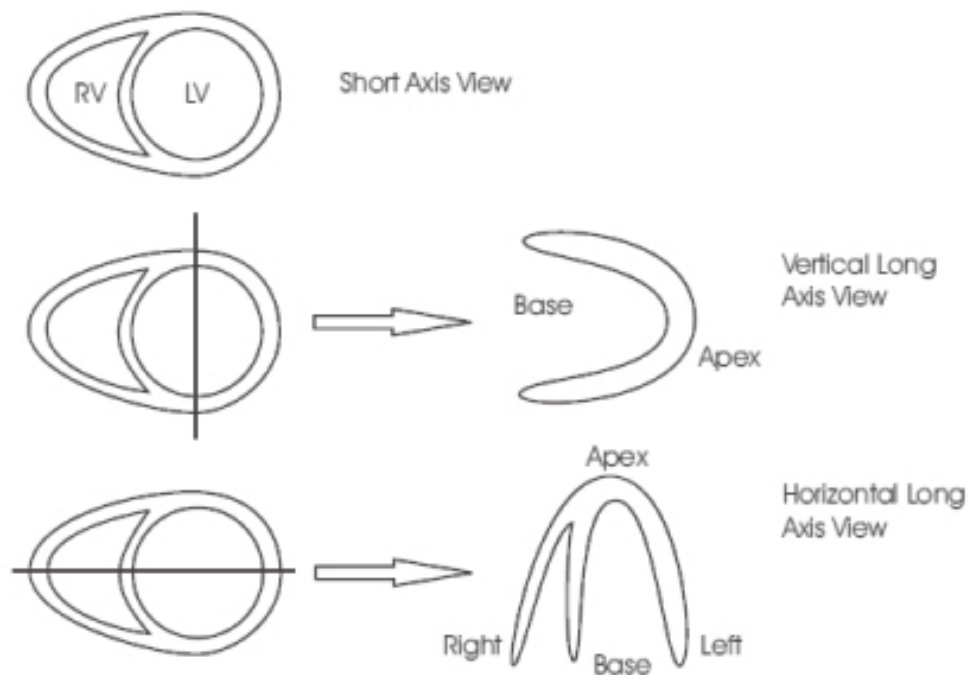


**Figure 1.4** – The typical orientation of **CMR** imaging planes [Heller et al., 2002]



**Figure 1.5** – The images from left to right show respectively **SA**, horizontal long-axis and vertical long-axis views of the heart.

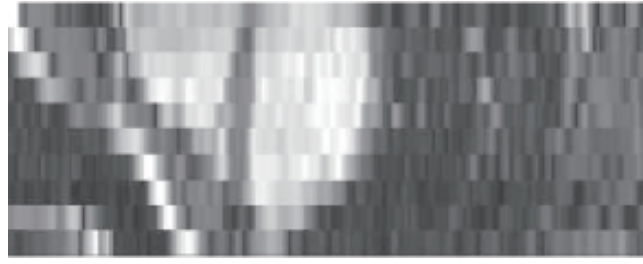


**Figure 1.6** – This figure shows a simulated LA view of the heart which has been obtained by stacking a set of SA images. As can be seen the through-plane resolution is much lower than the in-plane resolution.

### Cine steady state free precession (cine MR imaging)

Images of the heart may be acquired in real-time with CMR, but the image quality is limited. Instead, most sequences use electrocardiography (ECG) gating to acquire images at each phase of the cardiac cycle by accumulating information over several heart beats with breath holding. However, the breath holding introduces respiratory motion between slices acquired during different breath holds. Nevertheless, this technique forms the basis of functional assessment by CMR. Blood typically appears bright in these sequences due to its contrast properties and rapid flow. The technique can discriminate very well between blood and myocardium. The most frequently used MR acquisition sequence for this is called balanced steady state free precession (bSSFP) [Carr, 1958]. SA, four (4CH or horizontal long-axis (HLA)), three (3CH) and two chamber (2CH or vertical long-axis (VLA)) views are often acquired during a routine clinical setting. An example of this image modality is given in Figure 1.7.

### Spatial modulation of magnetisation imaging (tagged MR imaging)

Myocardial tissue in the body can be labelled by altering its magnetisation properties which are persistent even in the presence of motion. By measuring the motion of the labelled tissue, deformation fields in the myocardium can be reconstructed. Magnetic resonance tagging was first proposed in [Zerhouni et al., 1988]. [Axel and Dougherty, 1989b, Axel and Dougherty, 1989a] used a spatial modulation of magnetisation imaging (SPAMM) technique as a means of non-invasively introducing markers within the myocardium of the LV. The technique relies on the perturbation of the magnetisation in the myocardium by using a sequence of RF

saturation pulses before the acquisition of images using conventional MR imaging. Because the myocardium retains knowledge of the perturbation in the magnetisation the motion of the myocardium can be tracked during systole. To capture complex 3D cardiac motion patterns, multiple 2D tagged slices are usually acquired in different orientations. SPAMM has been later extended to complementary spatial modulation of magnetisation imaging (CSPAMM) [Fischer et al., 1993] which separates the component of the magnetisation with the tagging information from the relaxed component by the subtraction of two measurements with first a positive and then a negative tagging grid. This technique improves the grid contrast and greatly facilitates the automatic evaluation of the myocardial motion. Thus the motion assessment of the heart throughout the entire cardiac cycle becomes possible. Recent reviews of MR tagging are given in [Axel et al., 2005].

Despite the advantage of the tagged imaging, a common difficulty to estimate cardiac motion from tagged images arises from the inevitable fading of the tag during the cardiac cycle. Tags which will survive the fading are usually manually segmented or identified in the last phase of the sequence of tagged images. Another difficulty is low temporal resolution: a sufficiently large motion will lead to misalignment between material points due to a lack of information between the tags.

### 3D tagged MR imaging

3D tagging has recently been implemented using three sequentially acquired 3D data sets with line tag preparation in each of the three spatial dimensions [Rutz et al., 2008]. Conventional 2D CSPAMM approaches are prone to slice misregistration and associated with long acquisition times. In the 3D tagging approach, a fast method for acquiring 3D CSPAMM data has been proposed. This 3D tagging method allows measuring the deformation of the whole heart in three breath-holds with a duration of 18 heartbeats each. Three acquisitions are sequentially performed with line tag preparations in each orthogonal direction. An example of this image modality is given in Figure 1.8.

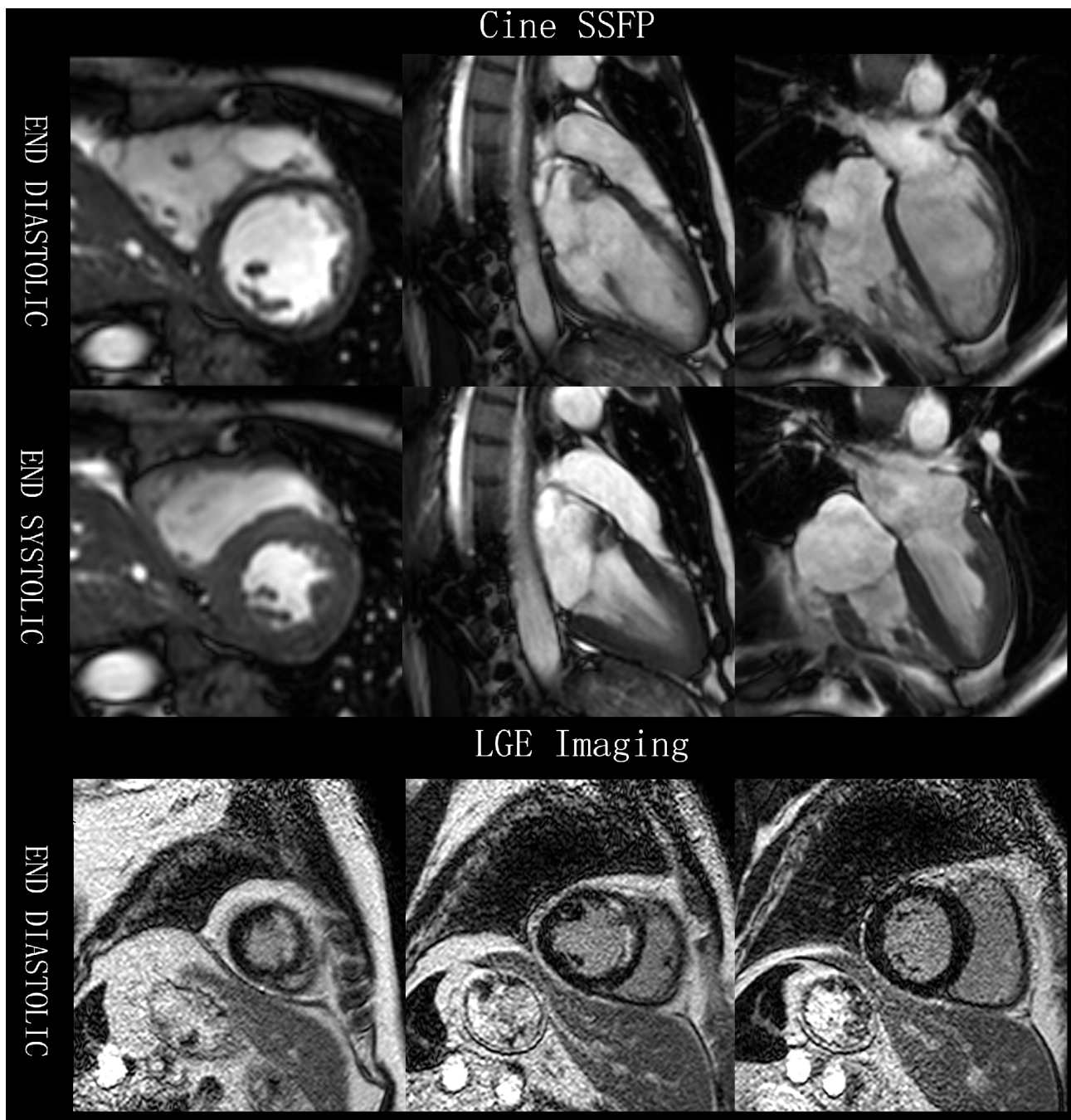


**Figure 1.7** – Example cine SSFP and LGE images from a volunteer. SSFP = Steady State Free Precession; LGE = Late Gadolinium Enhancement.

### Late gadolinium enhancement MR imaging

Late gadolinium enhancement (LGE) MR imaging was introduced by [Saeed et al., 1989, Kim et al., 1996, McCrohon et al., 2003], to identify infarcted myocardial tissue using CMR. This technique incorporates the administration of relatively inert extracellular gadolinium contrast during gradient-echo inversion recovery imaging. In this image acquisition, areas of noninfarcted

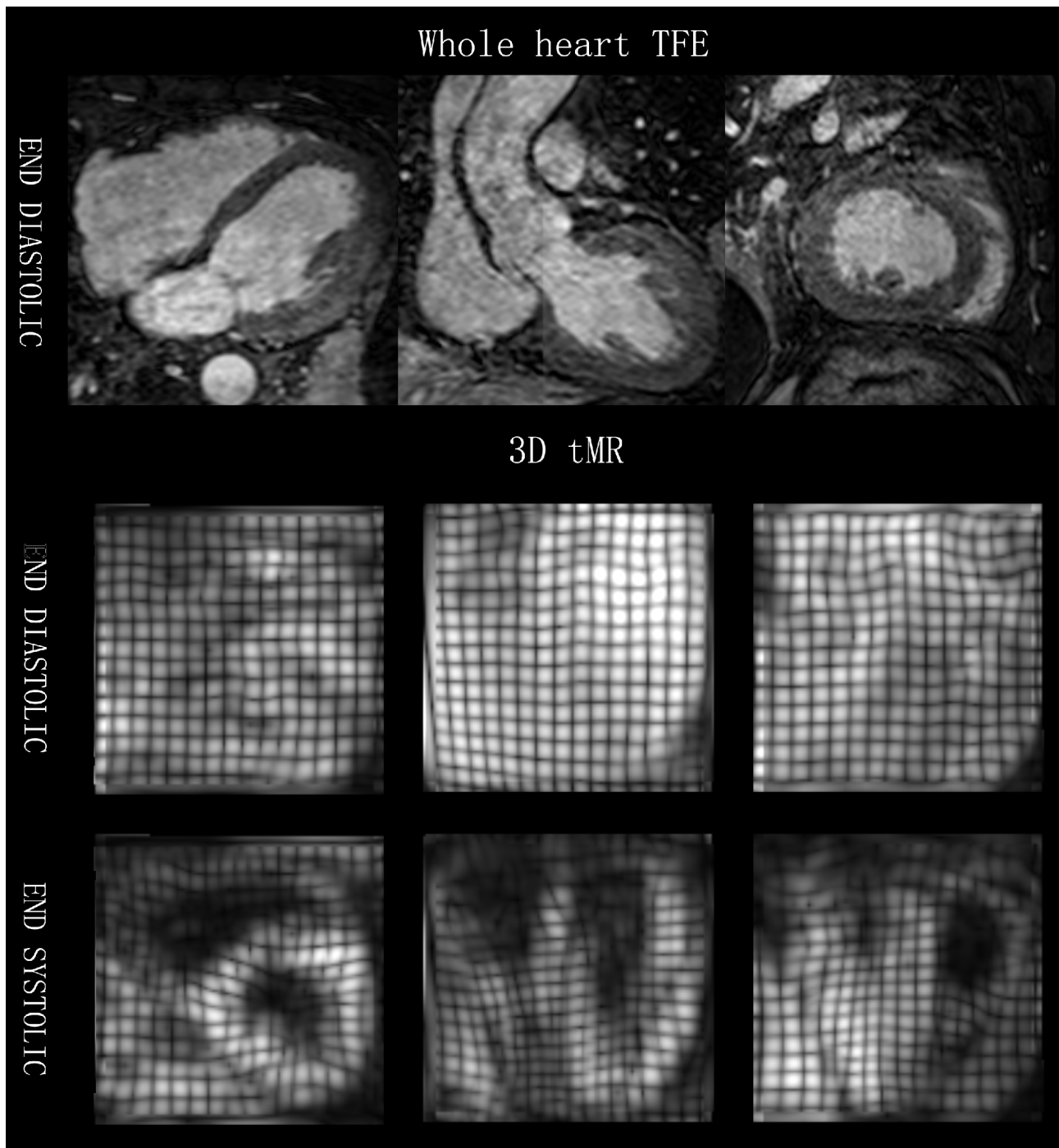


**Figure 1.8** – Example whole heart TFE and tagged MR images from a volunteer. TFE = Turbo Field Echo; 3D tMR = 3D Tagged Magnetic Resonance Imaging.

tissue appear dark, and infarcted or fibrotic tissue appears bright, because of reduced clearance and increased volume of distribution of the gadolinium [Saeed et al., 1989]. This fundamental aspect of delayed enhancement MR has led to the expression: "bright is dead." [Mandapaka et al., 2006]. An example of this image modality is given in Figure 1.7.

## Whole heart Turbo Field Echo

The whole heart turbo field echo (TFE) sequence acquires an isotropic non-angulated volume [Uribe et al., 2007]. Images were acquired during free breathing with respiratory gating and at end-diastole with ECG gating. Different from previous acquisitions that were limited to 2D imaging, the isotropic 3D resolution enables the assessment of cardiac anatomy and function with minimum planning or patient cooperation. The respiratory self-gating technique is shown to improve image quality in free-breathing scanning. The resulting image gives a consistent single-phase high resolution image of the whole-heart anatomy. It can be treated as a baseline to align other image modalities into a common space [Zhuang et al., 2011], or to segment the whole-heart anatomy [Zhuang et al., 2008]. An example of this image modality is given in Figure 1.8.

### 1.1.5 Indices of cardiac function

Functional indices are used clinically to assess and characterise cardiac function. Indices can be classed into two different categories: global and local indices. Global measures of cardiac function describe the overall ability of the heart to deliver blood to the rest of the body, while local functional indices are used to assess regional dysfunction in the heart, which is determined by the state of the myocardial tissue.

#### Global indices

Global indices assess the overall performance of the ventricles in their ability to eject blood. The left ventricular volume (LVV), left ventricular mass (LVM), stroke volume (SV), ejection fraction (EF) and cardiac output (CO) have all been used to assess the performance of the LV [Frangi et al., 2001].

LVV is defined as the volume enclosed by the LV. Volume-time curves of the left-ventricular cavity can provide information about the global contractility of the myocardium.

**LVM** is the mass of the **LV** and is equal to the volume of the myocardium,  $V_m$ , multiplied by the density of the myocardium,  $\rho_m = 1.05g/cm^3$  [Foppa et al., 2005]:

$$LVM = V_m \rho_m \quad (1.1)$$

**SV** is defined as the volume ejected during systole and is equal to the difference between the **end-diastolic volume (EDV)** and the **ESV**:

$$SV = EDV - ESV \quad (1.2)$$

**EF** is defined as the ratio of the **SV** to the **EDV**:

$$EF = \frac{SV}{EDV} \times 100\% \quad (1.3)$$

**CO** is the amount of blood ejected from the **LV** per minute and is equal to the **SV** multiplied by the heart rate (HR):

$$CO = SV \times HR \quad (1.4)$$

Although global indices can be used to identify the abnormal functioning of the heart they do not indicate which regions of the heart have reduced contractile function. Moreover, for some patients, global indices fall within normal limits even though the wall motion may be abnormal. For example, patients suffering from hypertensive left ventricular hypertrophy may have normal **EF** while circumferential and longitudinal shortening are depressed [Kramer et al., 1994]. Measuring local indices can help to detect areas of the myocardium which have been damaged because of reduced blood flow.

## Local indices

A widely recognised regional analysis technique for left ventricle myocardium is to use the 17-segment division model suggested by [Heller et al., 2002]. The motion of the heart can

be characterised in terms of its contraction in the radial, circumferential and longitudinal directions. The **regional wall motion (RWM)**, **regional wall thickening (RWN)** and **regional myocardial strain (RMSt)** in different directions are the local indices. These indices are often used to identify the abnormality.

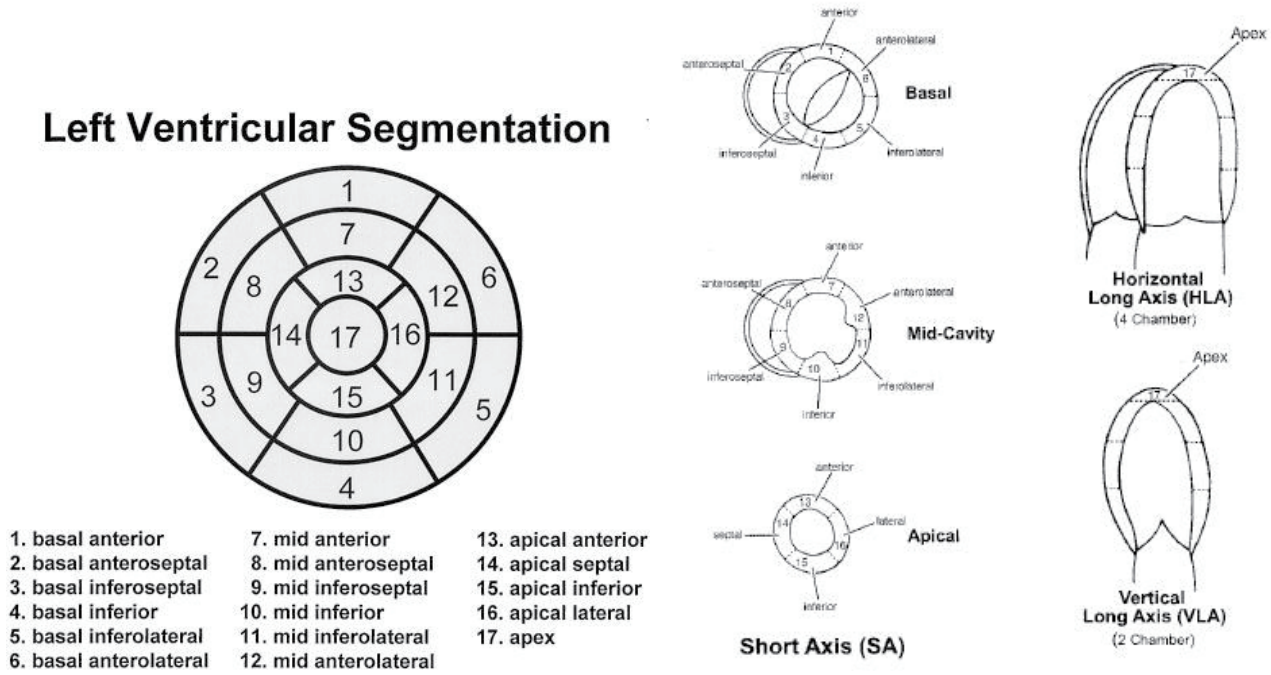


**Figure 1.9** – Bull-eye plot of the 17 segments of the left ventricular myocardium suggested by [Heller et al., 2002], Left the bull-eye plot, Right the anatomy landmarks for the bull-eye plot segments

**RWM** is defined as the myocardial movement of each segment. The functional abnormality of myocardium affects its contraction movement. It may, as a result, affect the total movement of a segment. Regional wall motion provides an indication of how healthy a specific segment is. In clinical practice, visual assessment by an experienced cardiologist is normally used to score the index as a semi-quantitative evaluation [Cigarroa et al., 1993]. For automatic assessment, the average radial distance from the myocardial region to the central axis is defined as the **RWM**:

$$RWM = (\delta_{ES} - \delta_{ED}) / \delta_{ED} \times 100\% \quad (1.5)$$

Here,  $\delta$  is the radial distance from a myocardial point in one segment to the central axis of the blood cavity; ES is end-systolic; ED denotes end-diastolic.

**RWN** is a measure related to the thickness of myocardium at different phases. It provides an alternative to **RWM** and can be more sensitive in discriminating between passive motion and active motion. The index can be manually scored [Cigarroa et al., 1993] or automatically quantified by the following equation:

$$RWN = (\eta_{ES} - \eta_{ED})/\eta_{ED} \times 100\% \quad (1.6)$$

Here  $\eta$  is the thickness of the myocardium in a local region, defined as the distance between the endocardial and epicardial surfaces.

**RMSt** is the fractional change of the length from a reference state to a subsequent state in the radial, circumferential and longitudinal directions. **RMSt** is now considered the superior index to **RWM** and **RWN** in discriminating infarcted myocardium from ischemic one [Götte et al., 2001]. **RMSt** in the different directions can be defined in terms of the off-diagonal terms of the Lagrangian strain tensor [Amini and Prince, 2001].

## 1.2 Objectives and challenges

It is now clear that **MR** imaging is becoming the modality of choice for cardiovascular image analysis as it has a number of advantages over other imaging techniques. It is safe, noninvasive and flexible. 2D, 3D and 4D images with high spatial and temporal resolution of the anatomy and physiology of the heart can be acquired in arbitrary orientations. Additionally, **MR** tagging can be used to measure detailed information about the myocardial deformation. However, there are a few technical challenges which need to be addressed.

Firstly, the ability to segment the images with pathological changes is necessary to gain a better understanding of the remodelling process of the heart following infarction. For example, determining the evolution of left ventricular remodelling and the relative contribution made by infarcted and remote myocardium to chamber dilatation has importance for evaluating interventions aimed at preventing heart failure. However, most existing cardiac image

segmentation algorithms do not explicitly address subjects with pathological changes in the MR images caused by myocardial infarction, e.g. large shape variation and local varying levels of signal contrast. The contrast of the myocardial can be different in MR images due to infarction due to different tissue property between normal and infarcted myocardium. The consequence is that measuring remodelling following infarction is difficult or inaccurate using automated image segmentation techniques.

Secondly, different MR acquisitions, including SA and LA cine MR images, 3D TFE MR images and 3D tagged MR images, are often treated independently during the subsequent analysis of cardiac function. The global and local cardiac functional parameters may not be available from one acquisition and may differ across different acquisitions. For example, regional volume change over the cardiac cycle can be captured from SA and LA cine MR images. However, this does not take into account the difference between active and passive motion. Potential ways of taking into account active myocardial motion are to use muscle thickening or strain. The strain index can only be fully extracted from a combination of different modalities.

Finally, most existing cardiac registration algorithms do not explicitly address the fact that the motion of different organs maybe different. This can lead to motion discontinuities in the image domain. For example, in the case of the heart, a sliding motion occurs at the pericardium. It is challenging to develop a motion tracking algorithm that can adaptively adjust to these motion discontinuities.

## 1.3 Contributions

The focus of the research presented in this thesis is the integrated use of multiple MR image acquisitions for cardiac function analysis. The work presented in this thesis makes three main technical contributions to the analysis of cardiac function in the context of segmentation and motion tracking. We also show two clinical applications that highlight the potential use of the developed techniques. The main contributions of the thesis are contained in chapters 4-7:

- A fully automatic cardiac segmentation technique is developed. The proposed segmentation technique is capable of generating an accurate 3D segmentation from multiple MR image acquisitions. To identify the cardiac anatomy from multiple image sequences, a spatial correction step is performed before segmentation. A 3D atlas is propagated to the SA and LA images using a single transformation across multiple acquisitions. A locally affine registration method (LARM) is used to cope with the large anatomical shape variations. A multiple component expectation maximisation (MCEM) is employed to compensate for locally varying intensity contrast. Finally, 4D graph-cuts segmentation is used to extract the cardiac anatomy within each image acquisition consistently.
- A novel technique for myocardial motion estimation using both untagged and 3D tagged MR images is proposed. The novel aspect of our technique is in its simultaneous use of complementary information from both untagged and 3D tagged MR images. To estimate the motion within the myocardium, we register a sequence of tagged and untagged MR images during the cardiac cycle to a set of reference tagged and untagged MR images at end-diastole. The similarity measure is spatially weighted to maximise the utility of information from both images. In addition, the proposed approach integrates a valve plane tracker and adaptive incompressibility into the motion tracking framework.
- A sparse representation for cardiac motion tracking using free-form deformations (FFDs) based on the principles of compressed sensing is proposed. The sparse free-form deformation (SFFD) model can capture fine local details such as motion discontinuities without sacrificing robustness. We demonstrate the capabilities of the proposed framework to accurately estimate smooth as well as discontinuous deformations in 2D and 3D image sequences. Compared to the classic FFD motion tracking approach, a significant increase in registration accuracy can be observed, in particular for images which exhibit discontinuous motion.
- Finally, two clinical applications for the above techniques are presented. We developed a framework which uses measures of myocardial motion to predict the response of individual patients to CRT. We also demonstrate the feasibility of using 3D probabilistic cardiac

atlases together with image registration to map the anatomical changes that occur over time in response to acute [ST-elevation myocardial infarction \(STEMI\)](#).

A list of publication arising from the work in this thesis can be found in [Appendix A](#).

## 1.4 Overview of thesis

In this thesis, following this chapter, we review the current state-of-the-art for segmentation ([Chapter 2](#)) and motion tracking ([Chapter 3](#)) methods for cardiac [MR](#) images. The methods and algorithms that have been developed during our research are presented in the subsequent chapters. In [Chapter 4](#) we develop a method for cardiac anatomy segmentation using atlas-based methods. In [Chapter 5](#) a comprehensive cardiac motion tracking framework using tagged and untagged [MR](#) images is developed. In [Chapter 6](#) we extend the classic non-rigid image registration with free-form deformations to a sparse representation. In [Chapter 7](#) two clinical research applications that can be addressed by the techniques proposed in the thesis are presented.

Finally, in [Chapter 8](#), we summarise the work presented in this thesis and discuss future work.

## 1.5 Statement of originality

The material in this thesis has not previously been submitted for a degree at any university, and to the best of my knowledge contains no material previously published or written by another person except where due acknowledgement is made in the thesis itself.

# Chapter 2

## Cardiac image segmentation

In this chapter, we review several automatic and semi-automatic segmentation methods for **CMR** images. The remainder of the chapter is organised as follows: The challenge of the cardiac segmentation is presented in Section 2.1. In Section 2.2, a selection of current cardiac segmentation methods are categorised. In Section 2.3, recent popular methods in medical image segmentation, especially multi-atlas and patch-based segmentation, are discussed. In Section 2.4, we discuss the development of evaluation techniques and benchmarks. Finally, the conclusions regarding the state-of-the-art are summarised in Section 2.5.

### 2.1 Challenge of cardiac segmentation

Most research effort in cardiac image segmentation has focused on the **LV**. This is largely due to the fact that the function of the **RV** is often less studied than that of the **LV** in **CVDs**. In addition, the **LV** is often easier to be identified and delineated than the **RV**: It has a well-defined ellipsoidal shape and is surrounded by the myocardium with a typical thickness of 6mm to 16mm [Petitjean and Dacher, 2011]. In contrast, the **RV** has a more complex crescent-like shape. The wall is also three to six times thinner than that of the **LV**, reaching the limit of the spatial resolution of **MR** imaging [Petitjean and Dacher, 2011].

The most common image obtained during a typical **CMR** acquisition is the **SA** cine **MR** images

(shown in Figure 1.7). The most frequently used MR acquisition technique for this is called **bSSFP** (as discussed in the introduction). A typical **SA** cine MR acquisition covers the whole heart with about 8-10 slices of an in-plane resolution of 1-2mm and through plane resolution of 8-10mm. Each slice is acquired in a separate breath-hold of the patient. About thirty cardiac phases can be obtained during one cardiac cycle depending on the heart rate.

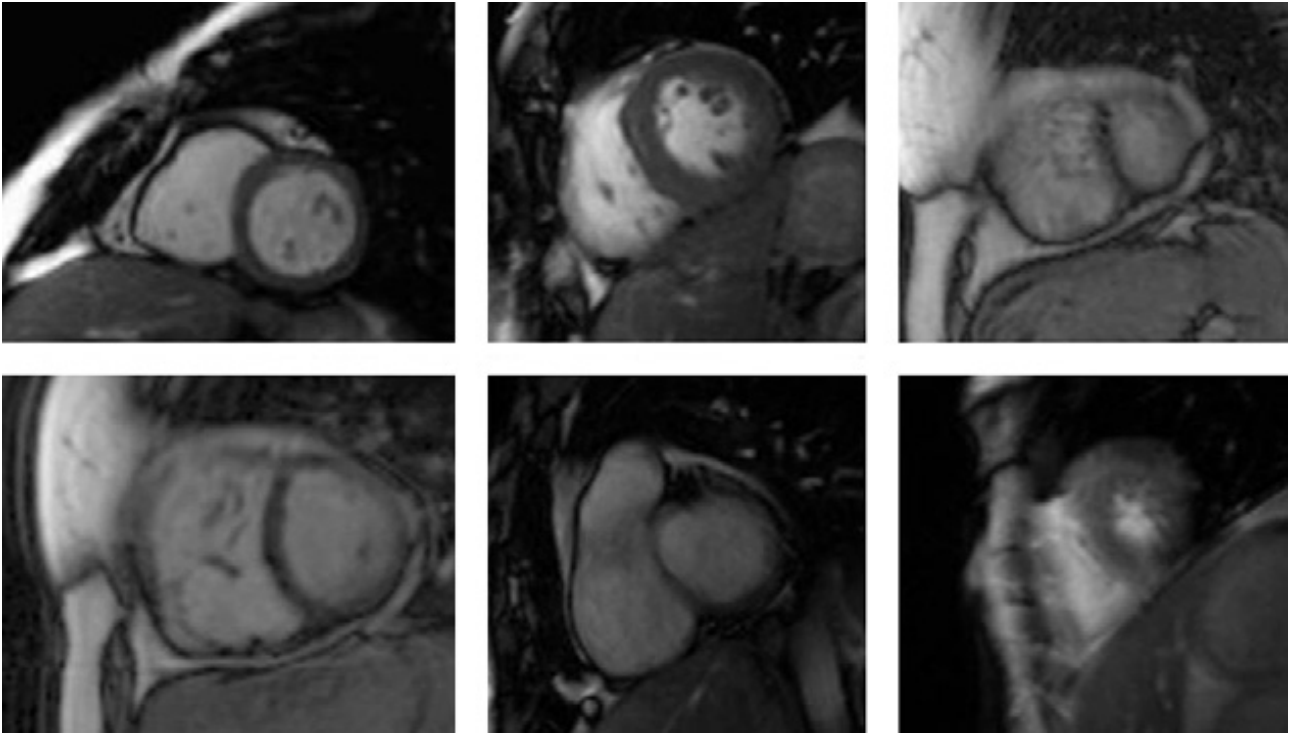


**Figure 2.1** – Variability among cardiac images. The image of the heart varies in terms of both intensity and shape. [Petitjean and Dacher, 2011]

One of the challenges for cardiac segmentation algorithms is that, as shown in Figure 2.1, **CMR** images exhibit a great variability, both in terms of appearance and shape. The appearance may differ due to the use of the different MR scanners or differences in the acquisition protocols. It can also be caused by **partial volume (PV)** effects due to the non-zero thickness of MR images slices: In some areas, a voxel can contain a mixture of several tissue types. Finally, pathological changes like infarction may cause local varying intensity contrast [Shi et al., 2011]. In terms of the shape, the ventricle can vary significantly across subjects, across different pathologies (dilation or hypotrophy), across time (before and after remodelling) and along the **LA**. This variability must be accounted for during the segmentation.

Examples of the challenges for cardiac image segmentation are shown in Figure 2.2: The

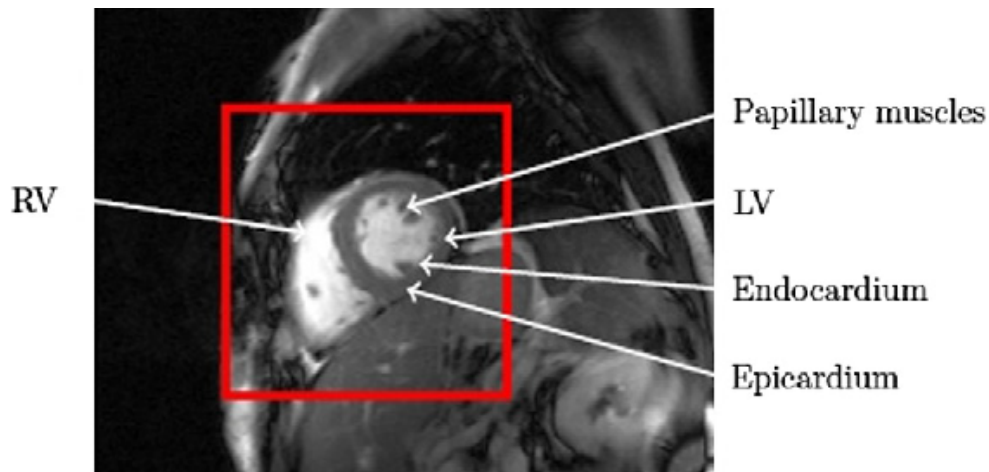


**Figure 2.2** – A ROI identifying the heart and anatomy for SA cine MR images [Petitjean and Dacher, 2011]

epicardial wall consists of the boundary between the myocardium and the surrounding tissues. Some of the surrounding tissues show poor contrast compared to the myocardium. The segmentation is thus difficult. In contrast to this, MR images usually provide quite good contrast between the myocardium and the blood pool. This means that the endocardial wall is easier to be identified. However, intensity inhomogeneity caused by blood flow artifacts can make the segmentation challenging. In addition, the papillary muscles and trabecular inside the heart chambers have the same intensity as the myocardium. Thus it is often difficult to distinguish them from the myocardium. In most clinical segmentation protocols, the papillary muscles and trabecular should not be taken into account for the delineation of the endocardial wall.

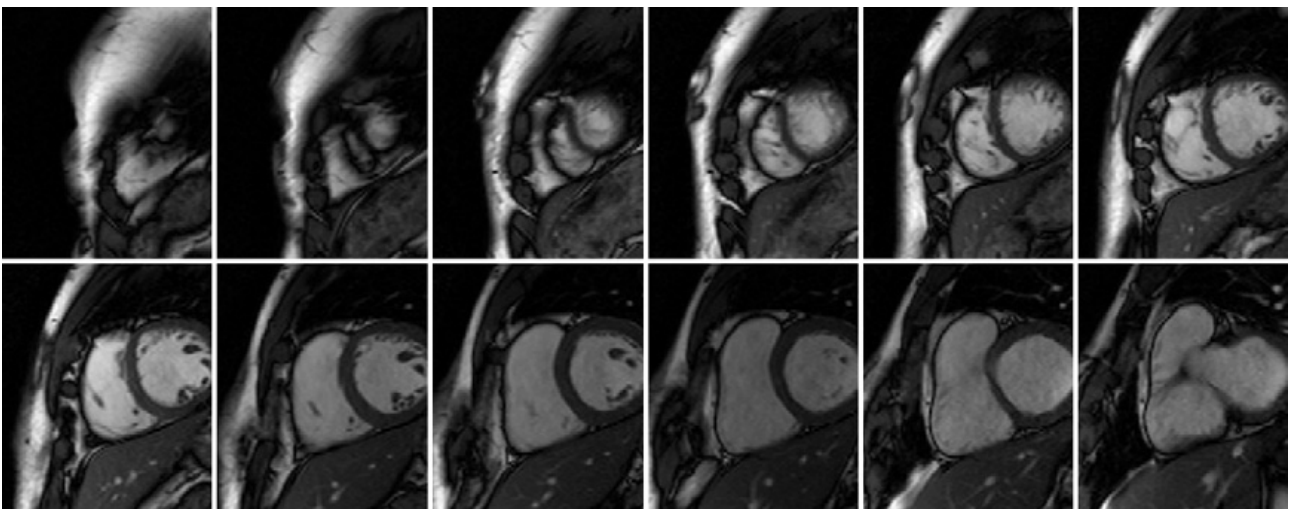


**Figure 2.3** – Variability of the heart in SA MR images along the LA. [Petitjean and Dacher, 2011]

Another major challenge in the segmentation of SA cine MR images is the large variability along the LA as shown in Figure 2.3. The apical and basal slices are more difficult to be segmented than mid-ventricular ones. Small structures at the apex are usually degraded due to the large through plane resolution. On the other hand, the shape of the LV varies often drastically in slices close to the base of the heart, because of the vicinity of the atria. In general, the RV shape varies even more along the LA.

Spatial misalignment is another challenge in the segmentation of SA cine MR images. Due to potential differences in the position of the heart during different breath-holds (e.g. due to respiration) there is usually some spatial misalignment between the images (inter-sequence misalignment) as well as between individual slices of the SA and LA images (intra-sequence misalignment). The image segmentation can be correct in 2D slices but distorted in 3D anatomical space and the distorted 3D segmentation can cause inconsistencies and inaccuracies in the final derived indices of cardiac function.

Several attempts have been made to segment the myocardium from 3D whole-heart images, include CT [Zheng et al., 2007] and 3D TFE MR images [Peters et al., 2007, Zhuang et al., 2010]. Compared to SA cine MR images, 3D whole-heart images are limited in terms of clinical availability as well as in terms of temporal resolution. This limits the ability to compute clinical parameters like EF which require segmentation at the end systolic (ES) and ED phases of the cardiac cycle. On the other hand, 3D whole-heart images provide nearly isotropic image resolution, which can increase segmentation accuracy on apical and basal segments and avoid the spatial misalignment problem.

The segmentation of the ventricles during the full cardiac cycle allows temporal volume and the mass changes to be assessed and is of great interest as an indicator of cardiac performance [Caudron et al., 2011]. However, because of the lack of landmarks inside the myocardium, the circumferential (twisting) and the longitudinal (through plane) myocardial motion cannot be analysed from SA cine MR images but requires dedicated modalities such as 2D or 3D tagged MR images [Chandrashekhara et al., 2004, Rougon et al., 2005, Rutz et al., 2008].

## 2.2 Methods of cardiac image segmentation

A common categorisation for medical image segmentation algorithms is low-level segmentation algorithms like thresholding as well as edge-based and region-based approaches [Pham et al., 2000]. Voxel-based classification methods without strong a-priori information can also be included into this category [Petitjean and Dacher, 2011]. Numerous segmentation problems require the use of a-priori knowledge to increase the robustness and accuracy compared to low-level segmentation algorithms. On one hand, user interaction can be regarded as a-priori knowledge [Pham et al., 2000]. On the other hand, a-priori information usually consists of a model, e.g. in form of the spatial relationships between objects or in form of assumptions about the shape and appearance of anatomical structures.

Deformable models, including snakes and their variants, offer a popular framework for incorporating a-priori knowledge. They can include anatomical information, as well as high-level information through active shape and appearance models. Finally, atlas-based segmentation approaches make use a-priori information in form of a set of manually labelled images.

In this section, we will first introduce the idea of cardiac localisation followed by the low-level segmentation algorithms commonly used in cardiac image analysis. Then, we will discuss high-level segmentation algorithms methods such as deformable models, active shape and appearance models and atlas-based approaches.

### 2.2.1 Cardiac localisation

The first step of cardiac segmentation especially myocardium segmentation requires an approximate delineation of the object of interest to be provided. Cardiac localisation techniques often rely on the following assumptions:

1. The intensity of blood is higher than that of myocardium.
2. MR images are SA multi-stack images in which the LV appears as approximately circular in shape.

3. Localisation is based on 2D images and heart is approximately at the centre of the images.

Ray casting from the hypothetical centre of LV is often used to detect the ROI [Kedenburg et al., 2006, Jolly, 2006]. These methods rely on the unique geometry, intensity distribution and gradient of the boundary between LV, myocardium and other tissues in MR images as shown in figure 2.4.

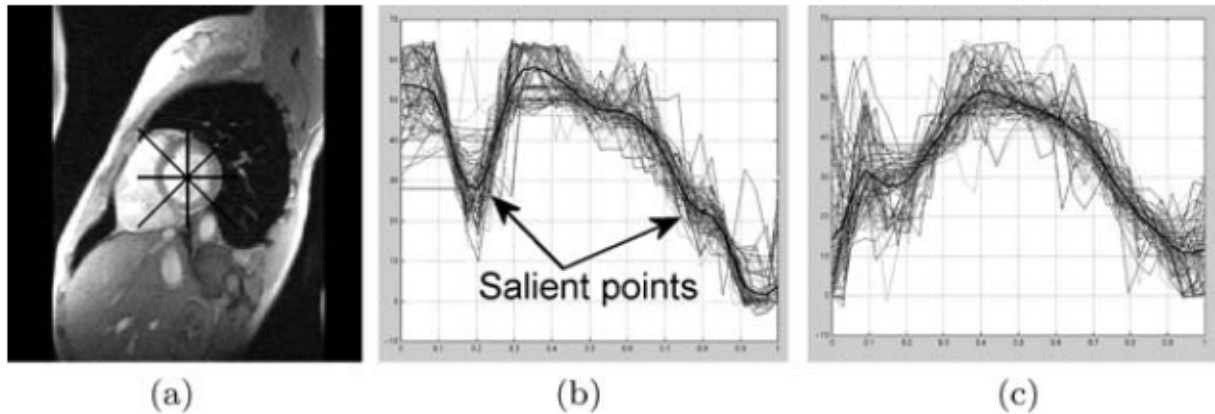


**Figure 2.4** – The feature set defining the heart LV. (a) The four cross sections through the ventricle used to extract the features; Aligned training profiles along with their average for the (b) horizontal cross section and (c) vertical cross section. [Jolly, 2006]

[Su Huang, 2009] used multilevel Otsu thresholding [Otsu, 1975] to find the intensity distribution of blood. They then applied a region growing method using the image centre as the seed point. A convex hull based on the grown region is then used as the initial location of the LV to approximate a circular ROI. Based on the assumption that the LV blood pool is more circular than the RV blood pool, [Lu et al., 2009] selected the LV from the result of the Otsu thresholding by computing a roundness metric  $R = \frac{4\pi A}{p^2}$  of each surviving convex object. Here  $A$  denotes area and  $p$  is perimeter length. The resulting measure  $R$  is equal to 1 for a perfect circle.

[Uzumcu et al., 2006, Wijnhout et al., 2009] used a circle-based Hough transformation using the results of Canny edge detection [Canny, 1986] step . For each of the images in the ED phase, the Hough Transform generates an accumulator image with identical dimensions as the input image, with high values near centre points of objects having a radius within the specified range (2 – 60mm).

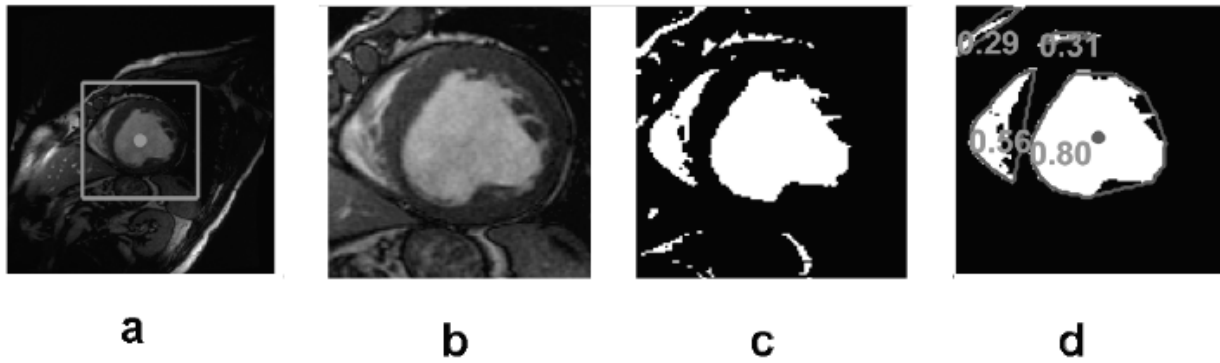


**Figure 2.5** – LV location procedure. (a) Target image with rectangular ROI (green box) and image centre (green point), (b) ROI image, (c) Binary image, (d) Surviving objects' convex hulls (red) and the corresponding roundness metric (green). The detected LV blood pool centroid is labelled as a red point. [Lu et al., 2009]

[Lin et al., 2006] proposed to use a novel combination of temporal Fourier analysis of image slices with simple contour detection to achieve a fast localisation of the heart. First a Fourier transform over time at each pixel location is performed. The first harmonic image is used to detect the ROI. In order to reduce the effect of noise and signal from non-cardiac structures, the H1 images were filtered with a smoothing filter and all pixels with magnitude less than 5% of the maximum magnitude within the 3D volume were set to zero. Then, the ROI for each slice was iteratively refined.

In contrast to previous approaches the cardiac localisation problem can be viewed as a general object detection problem. Haar-like features are image features that are widely used in general object recognition and may be applied to localise the LV in cardiac images. A simple rectangular Haar-like feature can be defined as the difference of areas inside a rectangle, which can be at any position and scale within the original image. This feature set is called two-rectangle feature. The values indicate certain characteristics of a particular area of the image. Each feature type can indicate the existence (or absence) of certain characteristics in the image, such as edges or changes in texture. [Viola and Jones, 2002] proposed an automatic object detection framework based on a Haar feature cascade classifier. Two-, three- and four-rectangle features are used together with a cascade classifier to identify human faces. This framework can be generalised and applied to different object detection tasks with task-specific training set.

### 2.2.2 Low-level segmentation algorithms

Thresholding can be an effective segmentation strategy when the focus is to find the endocardial contour [Goshtasby and Turner, 1995, Nachtomny et al., 1998]. In addition, [dynamic programming \(DP\)](#) can improve the result of the thresholding by taking advantage of the approximate circular geometry of the [LV](#) when using polar coordinates. After the initial thresholding, a one-dimension optimal path is located under polar coordinates which best describes the endocardial contour. The design of the cost matrix for the optimal path search can be based on thresholding [Liu et al., 2006], wavelet-based enhancement [Fu et al., 2000] radial lines [Yan et al., 2007], or the gradient values [Cousty et al., 2010] to weight a spatio-temporal graph. In [Jolly et al., 2009], a shortest path algorithm was applied to an average image to locate the [LV](#). The average image was created from all phases over one cardiac cycle. Contours in each individual image were then recovered using minimum surface segmentation.

Voxel-based classification method is another popular segmentation strategy when little or no prior knowledge is available. In cardiac segmentation, the features for classification usually are the intensities and the segmentation is often performed using two standard unsupervised techniques: [Gaussian mixture models \(GMM\)](#) and clustering [Petitjean and Dacher, 2011].

[GMM](#) is usually used to model the histogram of image intensities with a mixture of Gaussians. The Gaussian parameters (mean, variance) are then typically found using the [expectation maximisation \(EM\)](#) algorithm [Dempster et al., 1977]. The number of Gaussians used is often assumed to be known and fixed a-priori. In [CMR](#) images four Gaussians are frequently chosen to represent the intensities of the different tissue classes. These Gaussians then model the background, myocardium, blood pool and fat. [PV](#) effects occur due to the fact that a voxel can contain a mixture of different tissues. This is especially problematic for images with low spatial resolution or large slice thickness. [PV](#) effects can be accounted for in [GMM](#)-based methods by adding multiple Gaussians representing [PV](#) between myocardium and blood or myocardium and air [Pednekar et al., 2006]. The papillary muscles can be taken into account by assigning a mixture of two Gaussians (blood pool and papillary muscle) to a single label (blood pool) [Senegas et al., 2004]. The [EM](#) algorithm can be initialised by using a heart

detector [Pednekar et al., 2006] or using priors like an atlas (cardiac atlases will be discussed later in the chapter). The result of the EM segmentation can be improved to increase spatial consistency of the segmentation. This can be achieved using dynamic programming [Pednekar et al., 2006] or Markov random fields (MRF) [Gering, 2003].

A different approach to the low-level segmentation of cardiac images consists of clustering voxels within a feature space. [Lynch et al., 2006a] used a K-means based clustering to obtain separate clusters. After the initial clustering step the LV cavity is identified by computing the similarity between the blood pool and a circle. The closest blood pool to LV cavity is the RV cavity. The wall between these two cavities is measured to assess the myocardium thickness, which acts as a guide for segmenting the epicardial wall from the endocardial wall using image gradients. Finally, the epicardial wall is approximated using a smooth spline.

Several methods have been proposed to exclude papillary muscles during the endocardial wall segmentation: the computation of the convex hull of the contour [Lin et al., 2006], applications of mathematical morphology such as opening and closing on the contour [Cousty et al., 2010], or fitting a parametric curve to the contour to enforce smoothness.

Low-level segmentation algorithms with little prior knowledge can detect the epicardium once the endocardial contours have been detected. This often relies on a spatial model that incorporates assumptions about myocardial thickness or mathematical morphology operators applied on the endocardial contour [Petitjean and Dacher, 2011]. However, the epicardial contour is much more variable from image to image in terms of intensity distribution, geometry and surrounding tissues as shown in Figure 2.3. Thus a robust segmentation requires stronger prior knowledge but image-based and classification-based approaches can only offer limited flexibility for incorporating strong prior knowledge. In the next section, we review some of the high-level segmentation algorithms that can incorporate stronger a-priori knowledge for heart segmentation.

### 2.2.3 High-level segmentation algorithms

The low-level segmentation algorithms described above are mainly intensity driven. This makes the segmentation flexible but can also result in random and unrealistic segmentations due to noise, artifacts, and low-contrast boundaries present in the image. High-level segmentation algorithms avoid these problems by incorporating additional a-priori information, e.g. about the shape and appearance of the object of interest. Typical high-level segmentation algorithms include deformable models, active shape and appearance models and atlas-based segmentation.

#### Deformable models

Active contours or snakes [Kass et al., 1988] is a framework which minimises an energy function that is associated with a contour embedded in the image. The energy is a linear combination of internal and external energy terms. The external energy is driven by edge information in the image. The internal energy is minimised when the shape of the active contour achieves some desirable properties, such as smoothness. Active contours are one of the most popular approaches in model-based segmentation due to their ability to deal with objects with complex shapes. Prior information about the expected geometry of the heart can be incorporated in the predefined model as internal energy terms.

[Paragios, 2002] proposed a variational technique to segment MR cardiac images. Firstly the authors computed the mean signed distance map to a reference shape model. Then, the alignment to this reference shape is incorporated into the energy function to be minimised. The approach includes the coupled propagation of both contours so that it maintains the relative positions of the endocardial and epicardial contours according to a pre-defined distance model. Image intensity information is integrated through a gradient vector flow-based [Xu and Prince, 1997] boundary term and a regional term that aims at best separating the cardiac contours/regions according to their global intensity properties. The resulting equations of motions for the contours are implemented using a level set approach [Osher and Sethian, 1988, Sethian, 1996] and a fast and stable numerical approximation scheme, the additive operator

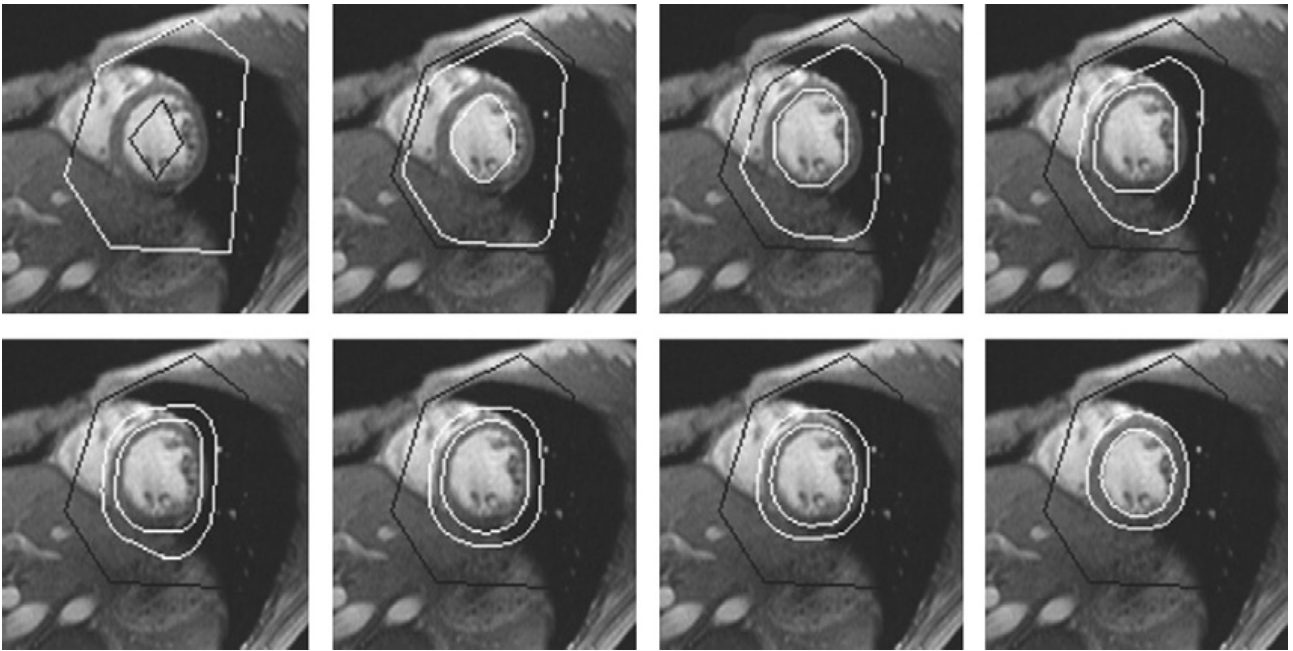


**Figure 2.6** – Deformable models and anatomical constraints for the segmentation of the LV. Black contours: initial conditions. White contours: active contours. [Paragios, 2002]

splitting [Weickert et al., 1998, Goldenberg et al., 2001] is used. An example of the propagation is shown in Figure 2.6.

An alternative approach based on [probability density functions \(PDFs\)](#) was proposed in [Lynch et al., 2006b]. Here PDFs are computed from the data by adding the binary segmentation images of both contours from a training dataset. The prior information is applied in a global sense after scaling and alignment to avoid leaking and the selection of spurious local minima. The PDF is embedded as a multiplicative term in the equations of motions in a region-based fashion. The region-based information improves flexibility in the segmentation of a wide variety of cardiac morphologies.

### Statistical models

A number of different representations for shape models with prior information have been proposed, including [point distribution model \(PDM\)](#) and deformable models. In the following paragraphs these works are briefly reviewed.

[Active shape model \(ASM\)](#) consist of a statistical shape model, called [PDM](#), obtained by

principle component analysis (PCA) on the set of aligned shapes, and a method for searching the model in an image [Cootes et al., 1995]. The PDM is a model for representing the mean geometry of a shape and as well as the statistical modes of geometric variation as inferred from a training set of shapes. PDMs rely on landmark points. A set of training images is manually landmarked with enough corresponding landmarks to sufficiently approximate the geometry of the original shapes. Let  $\mathbf{X} = \{X[m, n]\}$  represent the data matrix of the landmarks, where each column contain  $m$  landmarks in a training image from  $n$  training images. PCA is used to compute normalised eigenvectors and eigenvalues of the covariance matrix across all training shapes. The matrix of the top  $y$  eigenvectors is given as  $\mathbf{P}$ , and each eigenvector describes a principal mode of variation along the data set. A linear combination of the eigenvectors is used to define a new shape  $\mathbf{X}'$ , mathematically defined as:

$$\mathbf{X}' = \bar{\mathbf{X}} + \mathbf{P}\mathbf{c} \quad (2.1)$$

where  $\bar{\mathbf{X}}$  is defined as the mean shape across all training images, and  $\mathbf{c}$  is a vector of the shape parameters for each principal component. Therefore, by modifying the variable an infinite number of new shapes can be defined. The magnitude of  $\mathbf{c}$  is often constrained to ensure that the new shapes are all within the variation seen in the training set and thus plausible.

In addition, ASMs provide a search strategy in which the similarity between the model and the image is maximized in an iterative fashion. The ASM can be extended to model the appearance in terms of intensities. This extension is called active appearance models (AAM) [Edwards et al., 1998] and represents both the shape and texture variability seen in a training set.

AAM have been first applied to LV segmentation in [Mitchell et al., 2000]. The authors later introduced a multistage hybrid model, combining ASMs and AAMs [Mitchell et al., 2001]. They have argued that the AAM is optimised on global appearance while the ASM provides more precise border locations. They proposed to concatenate several matching phases, starting with an AAM that positions the model onto the heart, followed by a hybrid ASM/AAM stage. After the position refinement, a final stage of AAM search helps to locate local structures

precisely. Eventually, this segmentation approach was extended to 3D in [Mitchell et al., 2002]. An example of a 3D AAM-based segmentation of the LV is shown in Figure 2.7

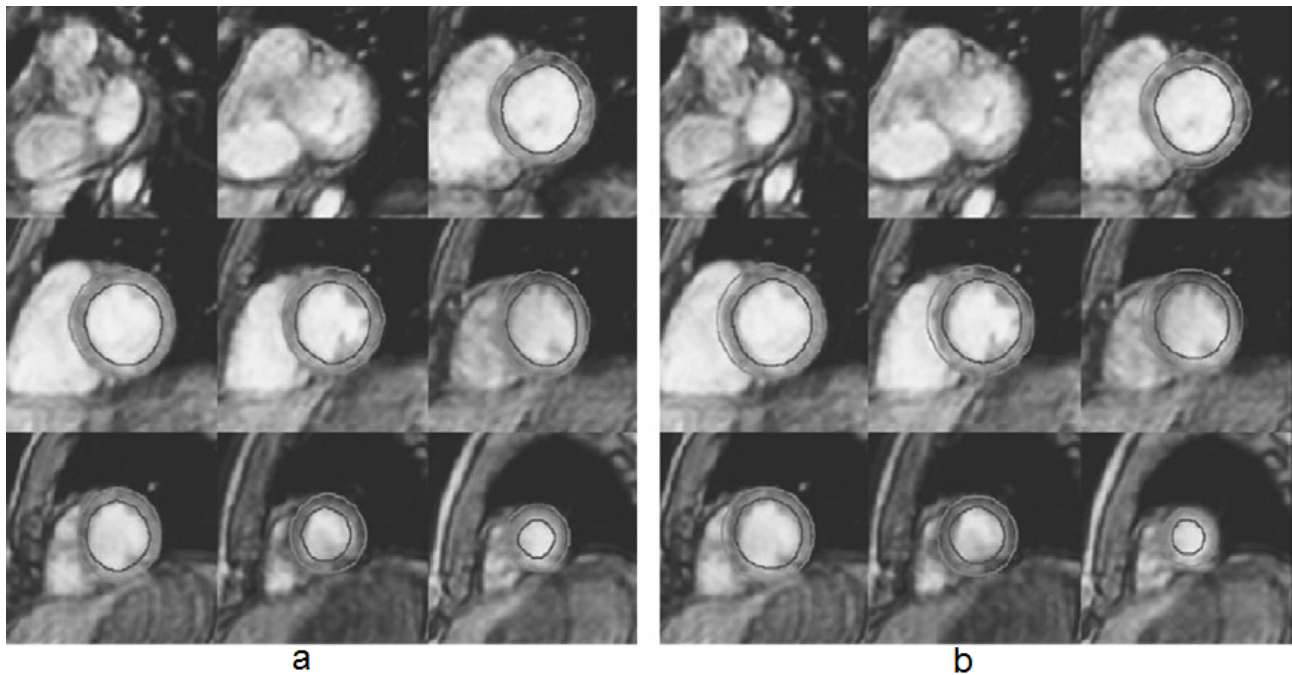


**Figure 2.7** – Segmentation results by 3D AAM. (a) Manually identified contours. (b) 3D AAM-based segmentation of the LV [Mitchell et al., 2002].

[Lapp et al., 2004] used a combination of AAM and statistical deformation models (SDM) [Rueckert et al., 2003] for cardiac segmentation. The authors applied the idea of statistical deformation models to AAM and used a deformable registration step for establishing point-to-point correspondences. PCA is performed on both texture vector and deformation vector to extract appearance and shape information. To incorporate both shape and appearance information into one model a further PCA is applied on the concatenated texture and deformation parameters. The result statistical atlas of the heart allows the creation of arbitrary plausible images of the heart in both terms of shape and appearance within the variations of the training datasets.

[Kaus et al., 2004] presented a fully automated deformable model technique for the segmentation of the myocardium in 3D MR images. This approach integrates various sources of a-priori knowledge learned from annotated image data into a deformable model. The inter-individual shape variation is represented by a statistical PDM. For a new contour or surface to be estimated, the shape as well as pose parameters are iteratively updated by a gradient

descent minimisation of the region-based energy terms. The spatial relationship of the epi- and endocardium was modelled by adapting two coupled triangular surface meshes. Compared to other approach, the proposed approach includes two types of prior information: (a) spatially varying appearance features and (b) surface connectivity in order to improve the segmentation robustness.

[Rouchdy et al., 2007] generated a deformable elastic template with nonlinear material properties and applied it to rodent CMR image segmentation. A mesh model is first localised in the images using affine registration. The edge information from the image is used as the driving force to locally deform the mesh to refine the segmentation of local details. The deformation is regularised by the nonlinear elastic property of the physical model. This results in a more realistic deformation field during the adaptation.

[Ecabert et al., 2008, Peters et al., 2007] extended the work of [Kaus et al., 2004] and applied it to whole heart segmentation of CT and MR images. They used a generalised Hough transform to locate the ROI, e.g. the chambers of the heart. In order to deal with variable cardiac morphology in the whole heart segmentation, a piecewise-affine adaptation was introduced. This adaptation significantly increased the ability of the model to achieve a better initialisation of the whole-heart model segmentation. Finally, the segmentation is refined by optimising both the transformation parameters and the vertex locations of the mesh model through the competition of the external and internal energy. An example of the resulting whole-heart segmentation is shown in Figure 2.8.

By imposing constraints on the segmentation through the use of statistical models, the above methods overcome the previously mentioned segmentation problems of low-level segmentation algorithms without the need for user interaction. However, these methods require training data, usually in the form of manual segmentations and annotations. Moreover, these statistical models cannot approximate segmentations that are not included in the training set. Although it is possible to extend the training set to include enough shape variability to achieve high accuracy, the training sets in [Mitchell et al., 2002, Kaus et al., 2004, Ecabert et al., 2008] are often restricted to small datasets. One of the problems is that it is always costly to

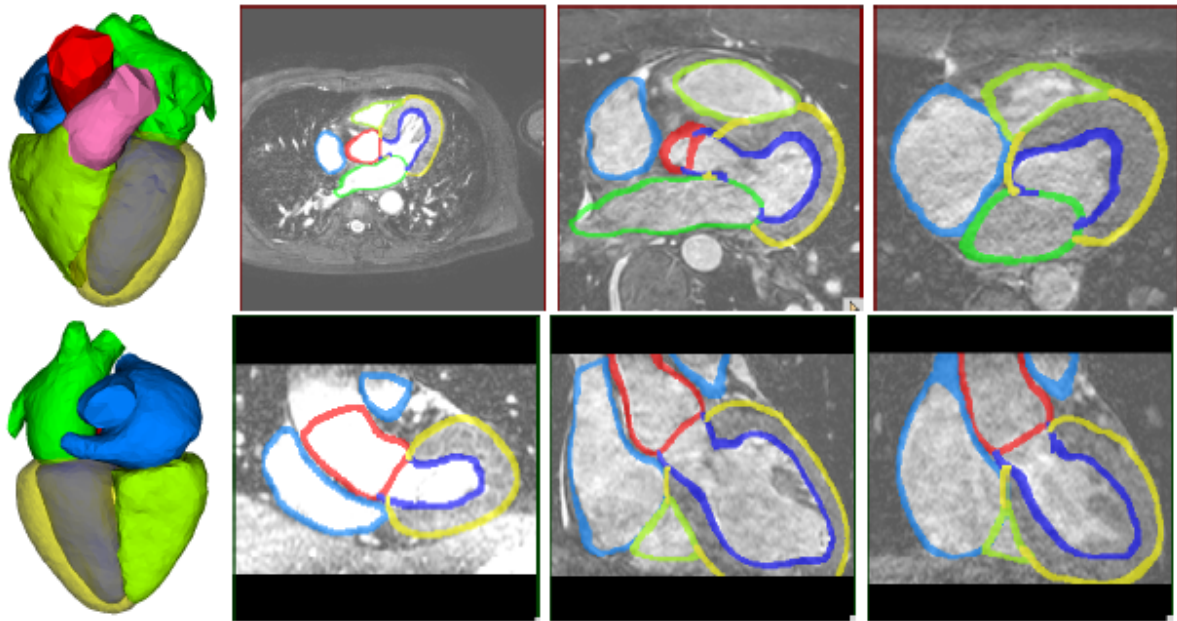


**Figure 2.8** – Whole heart segmentation result using deformable models [Peters et al., 2007].

acquire enough atlases in both terms of image acquisition and manual labelling. The atlas-based segmentation techniques described in the next section are more flexible, allowing for the recovery of shapes that are not present in the training set.

Furthermore, external features widely used in the statistical model based segmentation are mainly based on the information from a small local area of the unseen image such as the intensity or gradient value. These features are sensitive to intensity inconsistency due to different image acquisition protocols or artefacts.

### Atlas-based segmentation

Traditional medical atlases contain information about anatomy and function from single individuals. Such an atlas can be made subject-specific by transforming its coordinate system to match that of another individual. This transformation removes any subject-specific shape variations and allows subsequent comparison of structure and function between individuals or propagation of information in the atlas to the subject. Atlases can be generated from the manual segmentation of an individual subject or multiple subjects. In atlas-based segmentation the atlas is registered to unseen images. The result is not restricted to the variation of the training

set but rather by the flexibility of the registration process. If the boundary is well defined in the atlas image, using appearance information from the atlas and smoothness constraints, the segmentation propagation can retrieve boundaries with low contrast or those that are not clearly visible in the unseen image. Atlas-based segmentation techniques have been widely applied to brain segmentation [Collins et al., 1995, Dawant et al., 1999].

The construction of an atlas of the heart can be based either on the segmentation of single individual [Lorenzo-Valdés et al., 2002, Zhuang et al., 2010] or on probabilistic model, usually representing the average segmentation obtained in a population of subjects [Lorenzo-Valdes et al., 2003, Lorenzo-Valdés et al., 2004]. [Lorenzo-Valdés et al., 2002] proposed to construct a subject-specific atlas for each subject from the ED phase and propagate this atlas to all other cardiac phases of the same subject. A non-rigid registration [Rueckert et al., 1999] was used to accomplish the purpose. The process is illustrated in Figure 2.9 The limitation of this work is that the subject-specific atlas can only be applied to images from the same subject. Hence, the work is not fully automated.

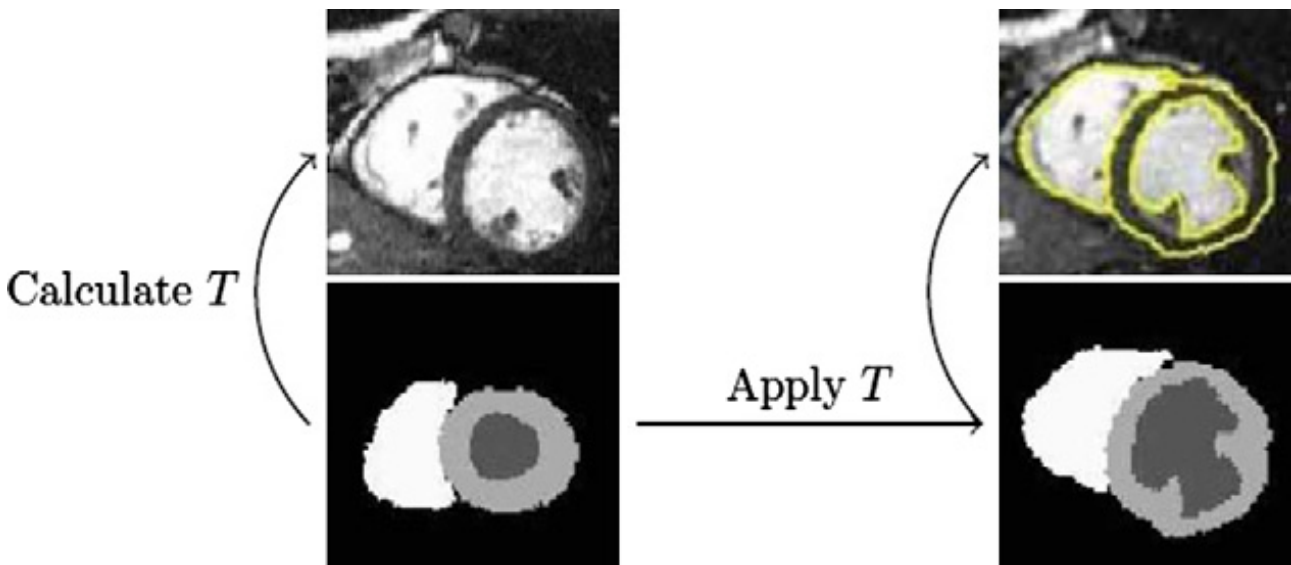


**Figure 2.9** – Anatomical atlas-based segmentation: (i) computation of the transformation  $T$  between the atlas and the image and (ii) deformation of the atlas by  $T$  [Lorenzo-Valdés et al., 2002].

[Lorenzo-Valdes et al., 2003, Lorenzo-Valdés et al., 2004] proposed to use a probabilistic atlas to initialise as tissue classification based on the EM algorithm. It is notable that the probabilistic atlas used is 4D spatio-temporal atlas. Temporal alignment was used to normalise the number of

phases of the each individual during the atlas construction and propagation Figure 2.10. The segmentation obtained after convergence of the EM algorithm is refined to integrate spatial information through a MRF.

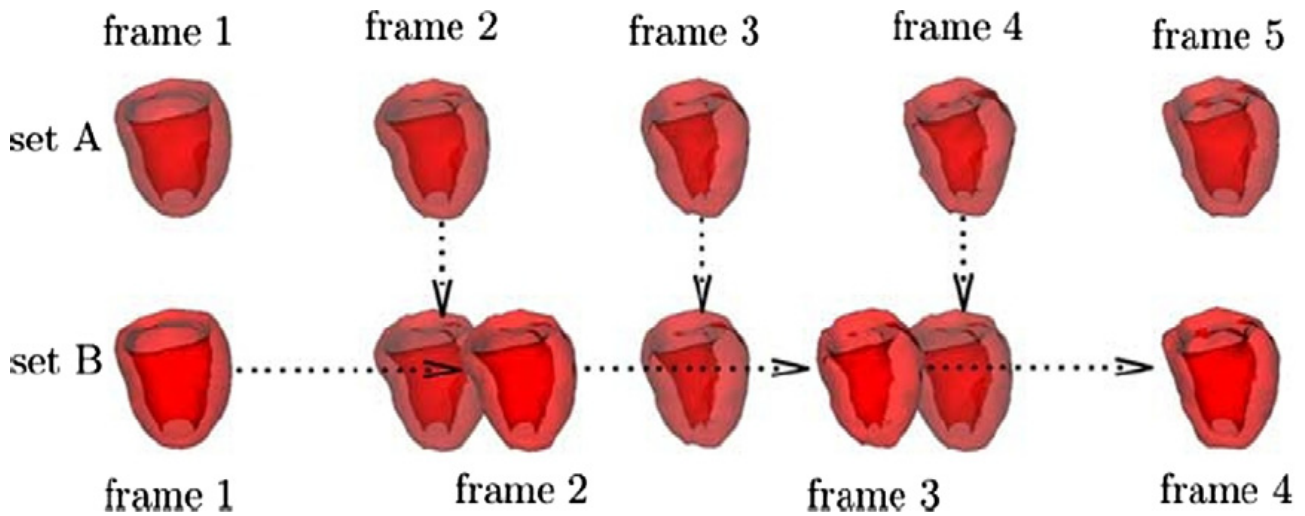


**Figure 2.10** – Temporal registration and resampling: linear interpolation is used to generate time frames from image sequence B which corresponds to those of sequence A [Lorenzo-Valdés et al., 2004].

[Zhuang et al., 2010] proposed the use of a LARM to capture the anatomical substructures during the whole-heart segmentation. LARM assigns a local affine transformation to each substructure, while globally it is a deformable registration. LARM was applied during the single atlas propagation phase after affine registration and before non-rigid registration. A robust initialisation of the different substructures of the heart was achieved. The resulting transformation between the atlas and the unseen image maintains the local shape of the predefined substructures and allows only global deformations. After this a free-form deformation with adaptive control point status (ACPS) was introduced to avoid the influence of the non-cardiac tissues adjacent to the heart with indistinct boundaries by allowing a non-uniform free-form deformation. The improvements of the different steps are shown in Figure 2.11.

The atlas-based segmentation approaches presented above are more flexible comparing to deformable models. Once an atlas has been constructed, only a single registration from the atlas to the target image is required to obtain a segmentation. On the other hand, the registration may fail if the anatomy in the unseen image is too different from the anatomy in the atlas in

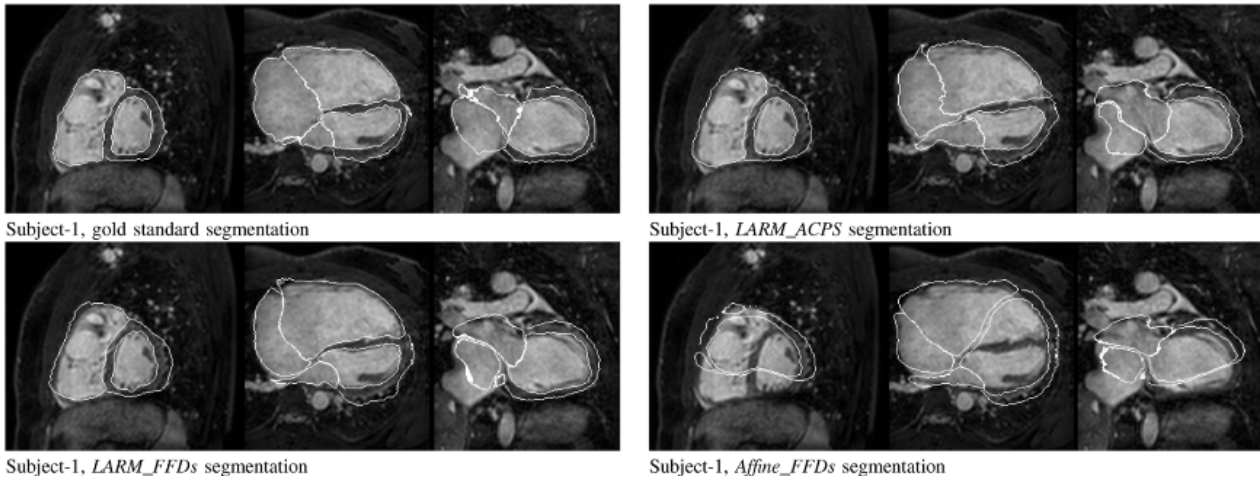


**Figure 2.11** – Comparison of manual segmentation, Affine+FFD, LARM+FFD, and LARM+ACPS. [Zhuang et al., 2010].

terms of morphology. For example, it can be difficult to register an atlas of the normal heart to the heart of a subject with dilated myocardium [Shi et al., 2011]. The registration may also fail if the anatomy in the unseen image contains some pathological changes that lead to locally varying contrast. For example, the intensities in the myocardium can exhibit this problem due to infarction. Both of these difficulties may cause the resulting transformation to be not a good registration between the atlas and unseen image.

## 2.3 Multi-atlas and patch based segmentation

To overcome the problems of the atlas-based segmentation discussed above and to make the segmentation more robust, [Rohlfing et al., 2004, Heckemann et al., 2006, Aljabar et al., 2009] proposed to use a number of different atlases. Each atlas is registered to the target image and the resulting segmentations are then fused into a consensus segmentation. It has been recently shown that using multiple atlases can yield better results for the segmentation of brain MR images [Artaechevarria et al., 2009], neck images [Han et al., 2008] and aortic images [Isgum et al., 2009]. In the fusion step it is possible to use a subset of the most successful registrations or use all registrations. Typically, fusion strategies such as majority voting, weighted voting or locally weighted voting are used. Thus, a generalised multi-atlas segmentation framework will include three steps as shown in Figure 2.12: Firstly, the atlas selection step will select

the a subset of atlases that are most similar to the subject in order to reduce complexity and increase robustness. Secondly, the atlas propagation step will propagate the selected atlases to the unseen image using affine and/or non-rigid registration. Finally, the decision fusion step is used to combine the segmentations from multiple atlases into a final segmentation of the unseen image. If the number of atlases equals to one or the atlases are fused into an average image, the framework can be reduced to the single atlas-based segmentation method. Most of the work on the multi-atlas segmentation techniques focuses on the first and the final step of the framework. In the following part we review the most commonly used approaches to multi-atlas segmentation.

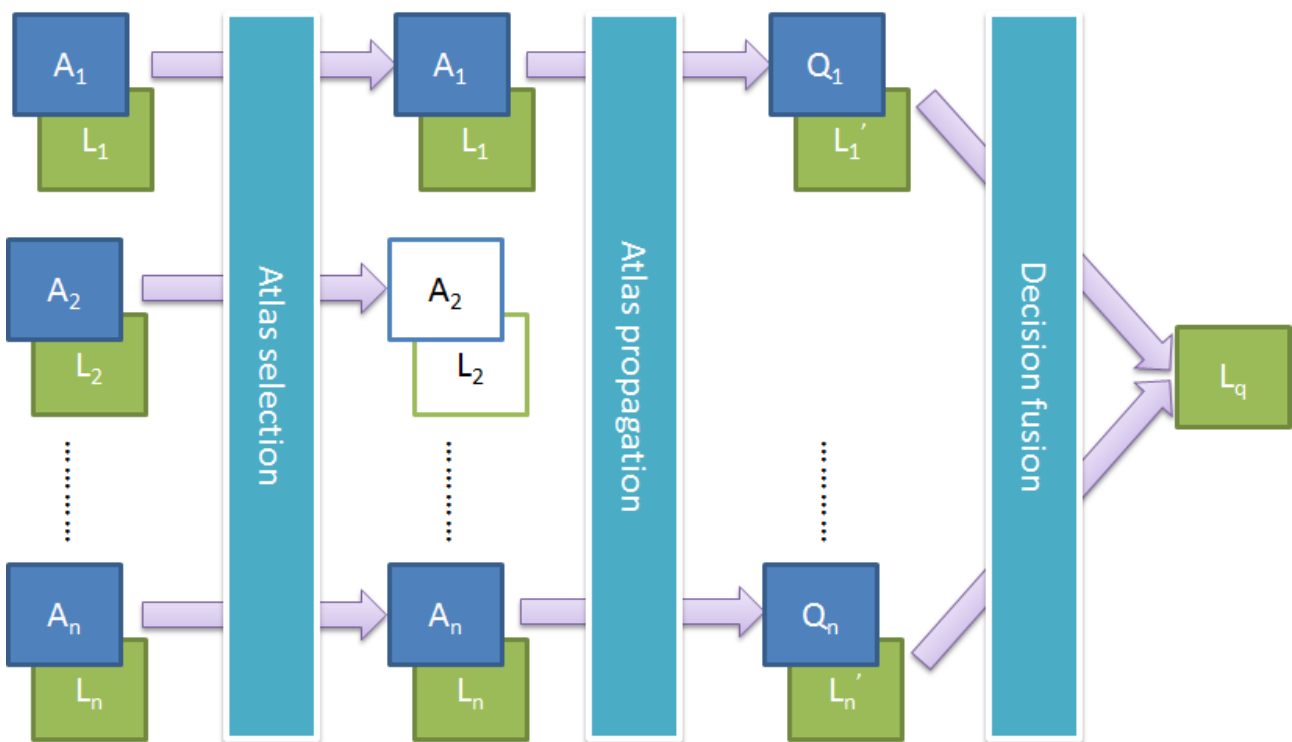


**Figure 2.12** – The general framework for multi-atlas based segmentation. Here  $A_i$  denotes the  $i$ th atlas,  $L_i$  denotes the  $i$ th label,  $Q_i$  denotes the transformed atlas and  $L'_i$  denotes the transformed label.

[Rohlfing et al., 2004] proposed to use registration to unseen images from a database of individual atlas images with subsequent multi-classifier decision fusion. The multi-classifier decision fusion strategy used in the paper is a simple majority voting with a partial volume interpolation. The method is applied to confocal microscopy images acquired from the brains of 20 bees. The multi-atlas segmentation strategy is compared against registration to an individual atlas image, an average shape atlas image and the most similar image from a database of

individual atlas images. The result suggests that the multi-atlas segmentation performs better than the alternative approaches. [Heckemann et al., 2006] applied the above methods to the human brain in MR images. The paper showed that multi-atlas segmentation performs at levels of accuracy approaching those of expert human raters in terms of the Dice overlap values obtained.

[Aljabar et al., 2009] proposed to use a subset of the most similar atlases during the atlas selection step. The authors showed that selecting the most similar subset of atlases for each unseen subject provides more accurate subcortical segmentations than those using a non-selective combination of random atlas subsets or all atlases. The selection is based on an image similarity measure between the atlas and the unseen image. In the result, the authors demonstrated that the fusion of approximately 20 out of a total of 275 atlases produced segmentations with near maximal accuracy.

The decision fusion step for the multi-atlas segmentation has been investigated in much detail. Majority voting is the most used approaches in papers including [Rohlfing et al., 2004, Heckemann et al., 2006, Aljabar et al., 2009]. Global weighted voting is proposed by [Artaechevarria et al., 2008], where the weighting is generated by the similarity between the transformed atlas and the unseen image. Although the image similarity does not necessarily correlate to the registration accuracy, experimental results on images of mouse brains showed higher accuracy of weighted voting compared to majority voting.

In global fusion strategies, the weights for the different atlases are fixed for the whole image. However, the registration between the image and atlas might be very successful in some regions of the image and might fail in other regions. Using global weighting, it is difficult to accommodate partly successful registrations.

[Artaechevarria et al., 2009] proposed to use a local weighted voting strategy instead of the global weighted voting. Instead of assigning a single weight to all voxels in the atlas, each voxel can have a different weight. Each voxel between the atlas and the unseen image is weighted by a similarity between the local patches. In their results, the authors showed that in general the local weighted fusion works better than the global weighted fusion, while different similarity

measure should be used for different sub-structures.

[Lotjonen et al., 2010] proposed to construct the final segmentation using an EM or graph cuts based optimisation after local weighted voting. The weight is used as a-priori probability for a subsequent EM-based image segmentation. In addition, they proposed to use the intensity differences after intensity normalisation to speed up the registration process which is one of the most time consuming processes during the multi-atlas propagation. The results showed a three-fold improvement in terms of computational speed as well as improved accuracy.

In the atlas propagation step, the registration is usually constrained to ensure one-to-one correspondences between the target image and the atlas. This restriction ensures a realistic deformation and preserves the topology of the atlas structures in the target image. However, this also restricts the ability of the registration ability to capture large, local variations in terms of shape. When the registration fails for small structures, it is likely that the correct correspondence can be found within the local neighbourhood. Unfortunately, most decision fusion strategies mentioned above cannot deal with these residual misregistrations between the images and the atlas.

[Coupé et al., 2011] proposed a nonlocal patch-based approach during the decision fusion step. The proposed method achieved the labelling of each voxel individually by comparing the patch centred at this voxel with other patches in atlases within a certain spatial neighbourhood. Using this method, several patches from each atlas can be used during the decision fusion. This enables a large increase in the number of sample patches and reduces the influence of registration errors. The authors used the local weighted fusion with intensity similarity based on intensity normalisation. The proposed path-based approach outperforms the above multi-atlas based methods for the segmentation of small structures like the hippocampus in terms of segmentation accuracy.

## 2.4 Evaluation methods and benchmarks

Characterising the performance of image segmentation approaches has been an important task to the development of the image segmentation approaches. Interactive drawing of the desired segmentation by human observers has been the only acceptable approach and yet suffers from intra-rater and inter-rater variability [Warfield et al., 2004]. The performance of raters (human or algorithmic) generating segmentations of medical images has been difficult to quantify because of the difficulty of obtaining or estimating a known true segmentation for clinical data. Although physical and digital phantoms can be constructed for which ground truth is known or readily estimated, such phantoms can not reproduce the full range of imaging characteristics, especially the normal and pathological anatomical variability observed in clinical data. Comparison to a collection of segmentations by raters is an attractive alternative since it can be carried out directly on the relevant clinical imaging data [Warfield et al., 2004].

[Warfield et al., 2004] proposed an EM algorithm for simultaneous truth and performance level estimation (STAPLE). The algorithm considers a collection of segmentations and computes a probabilistic estimate of the true segmentation and a measure of the performance level represented by each segmentation. The source of each segmentation in the collection may be an appropriately trained human rater or raters, or may be an automated segmentation algorithm. The probabilistic estimate of the true segmentation is formed by estimating an optimal combination of the segmentations, weighting each segmentation depending upon the estimated performance level, and incorporating a prior model for the spatial distribution of structures being segmented as well as spatial homogeneity constraints. The probabilistic framework can be easily adapted and used in the label fusion step of the multi-atlas segmentation approaches [Weisenfeld and Warfield, 2011, Asman and Landman, 2012].

[Backhaus et al., 2010] developed a new open-source database and web interface for research purposes including the evaluation of cardiac segmentation methods. This project is named "cardiac atlas project". [Suinesiaputra et al., 2012] estimated a ground truth consensus segmentation using the STAPLE algorithm where patients are selected from the cardiac atlas project. Two independent sets of expert (manual) segmentation from different sources that are

available from the cardiac atlas project were included in this study. In addition, automated segmentations from five groups were contributed. The total number of cases with segmentations from all seven raters was 18. The generated ground truth segmentation could be used for future evaluation of cardiac segmentation algorithms.

## 2.5 Conclusion

The focus of research in cardiac segmentation has gradually changed during the past 20 years, from the low-level segmentation algorithms to the high-level segmentation algorithms. By incorporating shape and appearance priors into the segmentation, high-level segmentation algorithms achieve reasonable results for the segmentation of the LV, especially in the mid-ventricular slices from normal volunteers. The precision of the segmentation is of the order of the variability of manual tracing [Petitjean and Dacher, 2011]. However, each of the high-level algorithms still has their own drawbacks.

Deformable models tend to be sensitive to local variability including noise and artifacts. Statistical models have difficulty to adapt to images that were not included in the training set. This is a significant problem given the large anatomical variability of the heart, especially in the context of different cardiac diseases. Atlas-based approaches based on image registration are one of the most flexible cardiac segmentation algorithms. However, a reliable, realistic and accurate registration, which is the key to the successful atlas propagation, is not always available. Its variant, multi-atlas segmentation with patch-based label fusion, is now widely used in brain image segmentation and might be a good candidate for further research to improve the accuracy of cardiac segmentation algorithms.

Nearly all of the existing segmentation methods have been applied and tested on normal volunteers or a subset of cardiac pathologies. In a wide group of cardiac pathologies where the heart shape could vary significantly, it will be more difficult to construct an appropriate training set for statistical model based algorithms as well as to register the atlas to unseen image for atlas-based algorithms. Furthermore, most of the automatic segmentation methods, including

model-based and atlas-based methods, assume homogenous tissue intensities. This leads to problems when segmenting subjects with myocardial infarction, as the infarcted myocardium often has a heterogeneous intensity distribution in contrast to normal myocardium, which is characterised by a more homogeneous intensity distribution. These problems are further compounded by the fact that these heterogeneous intensity distributions are difficult to model using prior knowledge since the position and intensity of the infarcted myocardium can vary in an unpredictable fashion across different subjects.

In this thesis, we will focus on the challenges of extending the existing segmentation methods to work on a wider range of pathologies using a three-step approach: Firstly, we use an automatic object detection based on a Haar feature cascade detector to identify the LV in each MR image [Viola and Jones, 2002]. In the second step a cardiac atlas from normal patients is registered to each subject's MR image using affine registration, LARM and non-rigid registration [Zhuang et al., 2008]. LARM is selected as intermediate registration due to its ability to deal with large shape variability. Finally, we automatically segment the LV and myocardium using a modified atlas-based graph cut segmentation technique [Lorenzo-Valdés et al., 2004, Boykov and Kolmogorov, 2003] to deal with the local intensity variability.

# Chapter 3

## Cardiac motion analysis

**MR** imaging is a highly advanced and sophisticated imaging modality for cardiac motion tracking and analysis, capable of providing detailed 3D analysis of global and regional cardiac function with great accuracy and reproducibility. In the past few years, numerous efforts have been developed for cardiac motion tracking and analysis from **MR** image sequences. In this chapter, we will review some of the state-of-the-art methods for cardiac motion tracking. We will primarily focus on motion tracking methods developed for **CMR** image sequences, e.g. cine and tagged **MR** imaging. The remainder of the chapter is organised as follows: Section 3.1 introduces some basic concepts of cardiac motion analysis. In Section 3.2 methods for cardiac motion analysis from cine **MR** imaging are discussed. In Section 3.3 the main algorithms for the recovery of cardiac motion from tagged **MR** imaging are presented. In Section 3.4 the evaluation strategy and public data base are discussed. Finally, conclusions are drawn in Section 3.5.

### 3.1 Introduction

There are two categories of cardiac function indices as discussed in Section 1.1.5: Global and local indices. Global indices, such as **EF**, **SV** and **CO**, can be used to assess the overall cardiac performance. Local measures, such as **RWM** and **RMSt** in different regions, can provide objective quantification of cardiac function and relate it to the location of ischemic injury. In

order to extract both global and local indices, cardiac motion analysis is used.

Cine MR imaging is the standard imaging technique for measuring global function indices [Castillo et al., 2003]. It is also well suited for measuring some important regional indices, such as RWN due to the good visibility of the myocardial boundaries. MR tagging [Axel et al., 2005, Rutz et al., 2008] is an alternative imaging technique to track deformations within myocardium. Local indices such as RMSt can be derived from tagged MR images.

The main motion analysis algorithms for cine MR images are classified into three different categories: sparse feature tracking, deformable models and dense tracking methods. Tagged MR images, due to its unique nature of image acquisition, enables specific motion analysis algorithms like harmonic phase tracking (HARP) [Osman et al., 2000, Ryf et al., 2002, Pan et al., 2005, Liu and Prince, 2010] and Gabor filter banks based methods [Montillo et al., 1996, Qian et al., 2006, Qian et al., 2008, Wang et al., 2008, Chen et al., 2010]. We will review the state-of-the-art for motion tracking for cine MR images and tagged MR images in different sections because there is a large difference in the nature of the imaging acquisition of these two sequences [Wang and Amini, 2011].

## 3.2 Motion tracking for cine MR images

The most commonly used features for motion tracking in cine MR images are the endocardial and epicardial contours. One strategy for motion tracking is to first track a set of sparse features throughout the cardiac cycle and subsequently to perform dense motion field reconstruction. For motion analysis from cine MR images, a useful constraint that can be utilised is myocardial incompressibility [Bogen et al., 1980]. The constraint of incompressibility arises from the knowledge that myocardial volume change is usually no more than 4% during the cardiac cycle [Bistoquet et al., 2008]. To reconstruct a dense motion field from cine MR images, image registration and deformable models with incompressibility constraints are often used.

### 3.2.1 Sparse feature tracking

Motion tracking techniques in this category usually involve firstly segmenting the ventricular wall followed by tracking the movement of feature points. Alternatively the feature points can be manually identified. Tracking the motion of feature points on the ventricular wall is often treated as an optimisation process. The correct correspondence between features at two time points results in the lowest energy configuration of the system. After energy minimisation the deformation vector for every feature point is calculated according to the obtained correspondences. Most tracking methods then fit a mesh model to reproduce the motion of the feature points in order to evaluate the cardiac function.

[Kuhl et al., 2004] proposed a semi-automatic border detection and volume computation algorithm for both cardiac 3D **US** and cine **MR** images. In each image plane, the mitral valve annulus or endocardial contours is outlined manually on each **ED LA** or **SA** frame. Then, based on the manually defined points, a spatio-temporal spline model based on thin-plate splines is initialised. The model ensures both smooth contours in the spatial domain and continuous, smooth motion in the temporal domain. Corresponding points for the endocardium are located in the direction perpendicular to the model's contours. The similarity between feature points is defined by a finite impulse response filter that highlights possible contours and allows morphological filtering of the intensity profile perpendicular to the current contour estimate. After that, all detected points are approximated by the spline model. Finally, the model is cut by the mitral annulus points along the **LA**. The advantage of this algorithm is its temporal smoothness and simultaneous optimisation over the temporal domain. However, it requires manual delineation of the endocardial contours on **ED** frames.

[Lin and Duncan, 2004] proposed a generalised **robust point matching (RPM)** [Rangarajan et al., 1997] framework to track the motion of the **LV** using **extended free-form deformation (EFFD)**. The **EFFD** model uses arbitrarily-shaped lattices instead of parallel-epipedical lattice shapes employed by **FFDs**. The authors argued that the **EFFD** models provide more accurate estimation of **LV** deformation compared to **FFDs**. The algorithm requires a rough segmentation of the myocardial boundary in the **ED** frame and the points are tracked over the cardiac

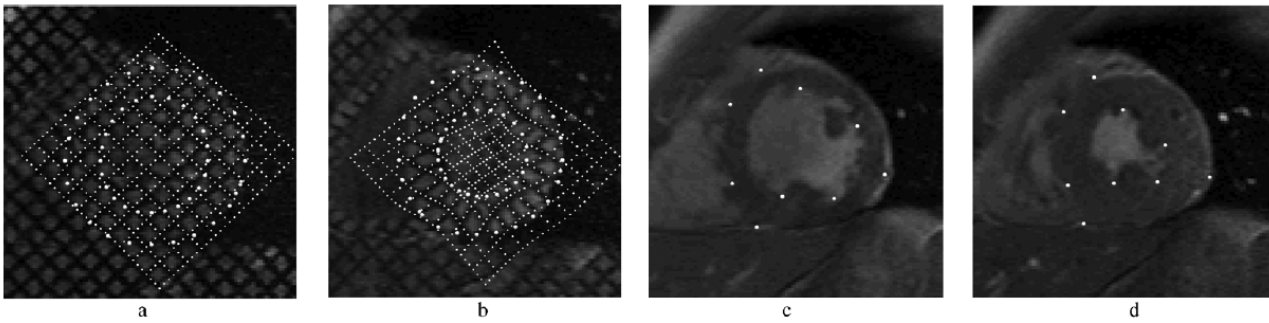


**Figure 3.1** – Example of contour tracking from [Remme et al., 2005]. Short-axis tagged MR images are shown at ED in (a) and ES in (b) with the tracked image stripe points. The larger circles outline the epicardial and endocardial surfaces. In (c) and (d), the untagged SA images at ED and ES are shown, respectively, with manually placed and tracked fiducial markers.

cycle. [Yan et al., 2007] proposed a new optimisation method called the **boundary element method (BEM)**. The most attractive feature of **BEM** compared to **finite element method (FEM)** is that it only requires discretization of the surface rather than the volume.

[Remme et al., 2005] proposed to analyse **LV** motion using manually tracked, distinct anatomical landmarks (fiducial markers) fitting with a parameter distribution model. The method focused on fitting a **FEM** to the manually marked sparse features. A **parameter distribution model (PRDM)** of **LV** deformations was obtained from a database of **MR** tagging studies. The **PRDM** was used to filter the calculated deformations and incorporate prior information on likely motions. The authors argued that by using the prior information from a database of tagged **MR** images, the motion from untagged **MR** images can be accurately reconstructed including the twisting **LV** deformation. A tracking example is presented in Figure 3.1.

### 3.2.2 Deformable models

In the deformable modelling approach, a model is deformed to fit the imaging data using energy minimisation or based on classical, physics-based equations of motion [McInerney and Terzopoulos, 1996]. The particularities of how to deform models and apply constraints to the deformable model vary with the particular application. The force to drive the deformation of the model in cine **MR** images usually originates from the endo- and epicardial contours.

Because of the sparsity of the feature information, vector field interpolation is often required to obtain a dense motion field for every point within the myocardial region. The advantages of this type of method are the easy construction of statistical models of cardiac physiology and the determination of classical measures, like [EF](#), [RWN](#) and [RWM](#), without additional steps. It is important to note that these methods assume a delineated myocardial contour as input by either manual interaction or automatic segmentation.

[\[Veress et al., 2005\]](#) proposed a deformable registration technique, called hyperelastic warping, to determine [LV](#) strains from mid-diastole to end-diastole using multiple [SA](#) cine [MR](#) images. A FE model is deformed by the difference in image intensities as a body force and a hyperelastic strain energy along the fiber angles based on continuum mechanics as the regularisation force. The boundaries of the [LV](#) were manually segmented for both epicardium and endocardium. The myocardium was represented as diffeomorphic<sup>1</sup>, hyperelastic material with fiber angles varying from  $-90^\circ$  at the epicardial surface to  $90^\circ$  at the endocardial surface.

One widely used constraint for cardiac motion analysis for cine [MR](#) images is myocardial incompressibility. [\[Bistoquet et al., 2008\]](#) proposed an incompressible deformable model to recover the motion of the biventricular from cine [MR](#) images data. The deformation is modelled by a transformation between the reference frame and the current frame. The driving force is calculated in a divergence-free space. Incompressibility is enforced by a divergence-free matrix-valued radial basis function. The function is used to project the parameter space into the space of incompressible deformations. The displacement is calculated at the middle surface nodes between the endo- and epicardial contours. The approach requires the myocardium to be segmented in the initial frame and the motion of the myocardial contour and the middle points are tracked throughout the cardiac cycle.

---

<sup>1</sup> A diffeomorphic transformation is one to one, differentiable and invertible transformation [\[Christensen et al., 1996\]](#)

### 3.2.3 Dense tracking methods

Dense or registration-based motion methods are popular solutions to cardiac motion tracking. Cardiac motion tracking can be viewed as a 4D registration problem [Makela et al., 2002]. In general, image registration is a process that aims to find the optimal transformation that transforms a source image to a reference or target image by maximising a similarity measure between the images. The advantages of casting the motion tracking problem as a registration problem are: Firstly, no preprocessing of the image sequence or segmentation is required. Secondly, registration-based methods are usually fully automatic without the need for user intervention. The potential disadvantage is that image registration techniques can get trapped in local minima and thus are prone to potential misalignment due to image noise and artifacts. However, these are common problems also for other techniques such deformable models and sparse feature tracking. Finally, the computational time for dense motion tracking is usually relatively long.

[Perperidis et al., 2005] proposed the use of a registration technique employing B-spline based FFDs for the spatio-temporal alignment of CMR image sequences. It extends the FFD-based registration approach [Rueckert et al., 1999] to 4D B-spline which is separated into spatial and temporal components. Two different optimisation strategies have been adopted. One strategy is to perform a combined optimisation with spatial and temporal components. The other strategy is to optimise each transformation component separately. The similarity is measured between the image intensities in different phases of the cardiac cycle. The results demonstrated that a significant improvement in the alignment of the image sequences is achieved by using the deformable spatio-temporal transformation model.

[Sundar et al., 2009] used a 4D image registration method to estimate cardiac motion. This framework considers the registration of the first frame to all other frames simultaneously. This facilitates the spatio-temporally consistent motion estimation as opposed to other registration-based algorithms which estimate the motion by sequentially registering one frame to another. An attribute vector for every point in the image is used to convey information about intensity, boundary, and geometric moment invariants. Hierarchical registration of image sequences is

then performed by using the most distinctive points for initial registration of the sequences and gradually adding less-distinctive points to refine the registration. The attribute vectors reduce the complexity of the registration while retaining a relatively high degree of accuracy.

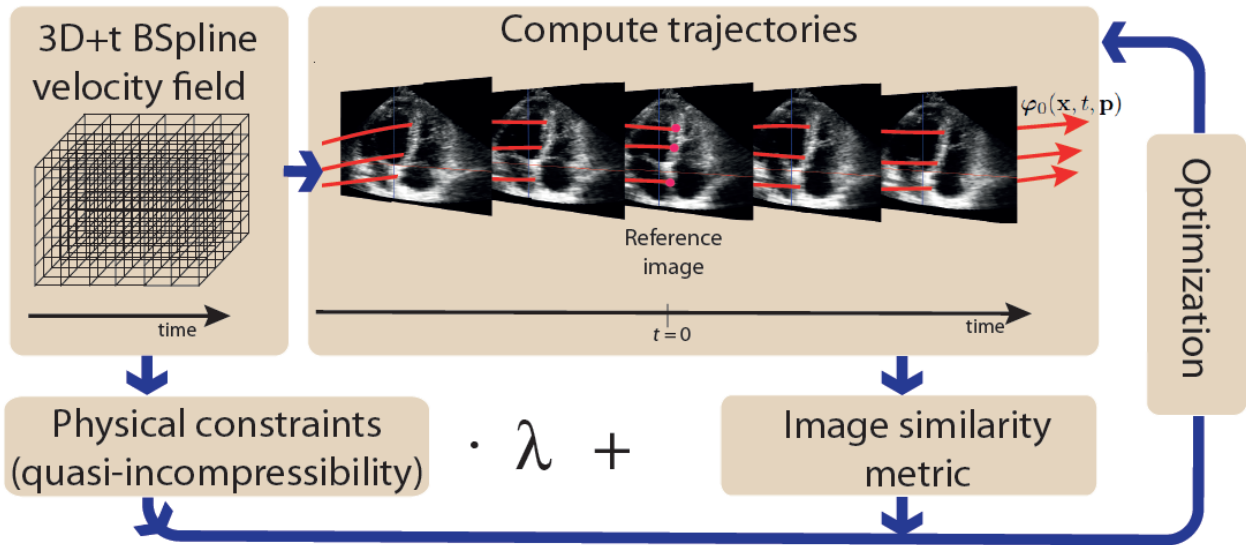


**Figure 3.2** – Overview of the TDFFD framework: Continuous spatiotemporal trajectories are computed from the 3D+t velocity field, parameterised by a 3D+t grid of control points with B-spline basis function. The image similarity is computed from image intensities for the current set of trajectories. Quasi-incompressibility is added as a biophysical constraint for regularising the velocity field. [De Craene et al., 2012]

Myocardial incompressibility can be used in registration methods as well as in the deformable methods. [De Craene et al., 2012] proposed a TDFFD to extract motion and strain from a sequence of 3D US images. An overview of the framework is presented in Figure 3.2 The energy functional consists of two terms: the image similarity and a regularisation term. The image similarity metric is defined as the sum of squared differences between the intensities of each frame and a reference frame. Any frame in the sequence can be chosen as reference frame. The regularisation term is based on the incompressibility of myocardial tissue. The originality of the approach resides in enforcing time consistency by representing the 4D velocity field as the sum of continuous spatiotemporal B-spline basis function. The spatio-temporal displacement field is recovered through forward integration of the non-stationary velocity field. The TDFFD approach proved to be more robust to a reduced temporal resolution compared to conventional registration approaches.

[Metz et al., 2011] proposed a generalised framework of temporal FFDs to extract motion

from dynamic images. The method is based on a 3D (2D + time) or 4D (3D + time) **FFDs** model. Registration is performed directly on the dynamic images. This avoids a bias towards a specifically chosen reference time point. The novelty of this approach is that, optionally, cyclic motion constraints can be imposed. When the cyclic motion constraint is enforced, the motion will be periodic in time. The similarity metric used is the variance of intensity over time and a constrained optimisation using a stochastic gradient descent method with adaptive step size estimation is also applied. The method has been quantitatively compared with existing registration techniques on synthetic data, 3D + t **CT** of the lungs and 3D + t **computed tomography angiography (CTA)** of the heart.

### 3.3 Motion tracking for tagged MR images

Conventional cine **MR** images show clearly the motion of the endo- and epicardial surfaces. However, the motion between the endo- and epicardial surfaces is more difficult to discern, largely due to the lack of discernible features inside the myocardium. Tagged **MR** images provides the means to track the myocardial motion between the endo- and epicardial boundaries. In recent times, **MR** tagging has seen increased applications in the clinic and is becoming the gold standard for quantifying regional strain function. Although **MR** tagging provides a compelling visualisation of myocardial motion, fast and accurate image analysis methods are still required before tagged **MR** images can be used for quantitative analysis [Wang and Amini, 2011]. Since the introduction of tagged **MR** images, many methods have been developed to detect and track the tags. In the rest of this section, different image analysis methods using tagged **MR** images are reviewed and discussed.

Cardiac motion analysis methods using tagged **MR** images can be divided into two different categories: The first category is feature-based motion tracking method including sparse feature tracking and deformable models. The features are often sparse tag lines, geometrically salient landmarks and tag line intersections. The accuracy of feature-based image analysis methods using tagged **MR** images highly depends on the quality of the image, the consistency of the

tagged MR images and the spacing of the tag lines. In addition, an extra step is needed to interpolate the sparse tracking result into a dense deformation field. The second category aims to obtain the deformation field directly from tagged MR images, without extracting features from the tagged MR images [Wang and Amini, 2011]. Two different types of methods fall in this category: frequency-based methods, e.g. HARP and Gabor filter methods and registration-based methods.

### 3.3.1 Harmonic phase tracking

HARP [Osman et al., 2000] is a phase-based technique for rapid analysis of tagged CMR images. Rather than working on tagged images directly, HARP uses phase information from the frequency domain. The principle of HARP tracking is that the harmonic phase of a material point remains constant as it moves during the cardiac cycle. HARP analysis operates directly in the k-space representation of the tagged MR images. Figure 3.3 shows a horizontally tagged MR image [Figure 3.3(a)] and its Fourier transform [Figure 3.3(b)]. One DC peak at the centre of Fourier space and another two harmonic spectral peaks can be seen. A bandpass filter, shown here as a circle, is applied to isolate a spectral peak. The inverse Fourier transform of this isolated region produces a complex harmonic image. The HARP magnitude image reflects the geometrical change of the heart and the image intensity change caused by fading, while the HARP angular image reflects the motion of the myocardium in the direction orthogonal to the tags. The main advantage of HARP is that it is fast and automatic with no need for extracting tag lines in a pre-processing step.

One problem with HARP motion tracking is that it can fail in the presence of a large amount of motion. Another limitation of HARP is that it can only estimate the in-plane motion, typically using 2D SA tagged MR images [Wang and Amini, 2011]. To address this problem, several solutions to extend the HARP motion tracking to 3D have been proposed. [Ryf et al., 2002] extended HARP from 2D to 3D by using a true 3D tagging technique followed by a conventional fast 3D gradient echo imaging sequence. The phase invariant property of material points in three directions is utilised after extracting spectral peaks in 3D Fourier space. The true 3D

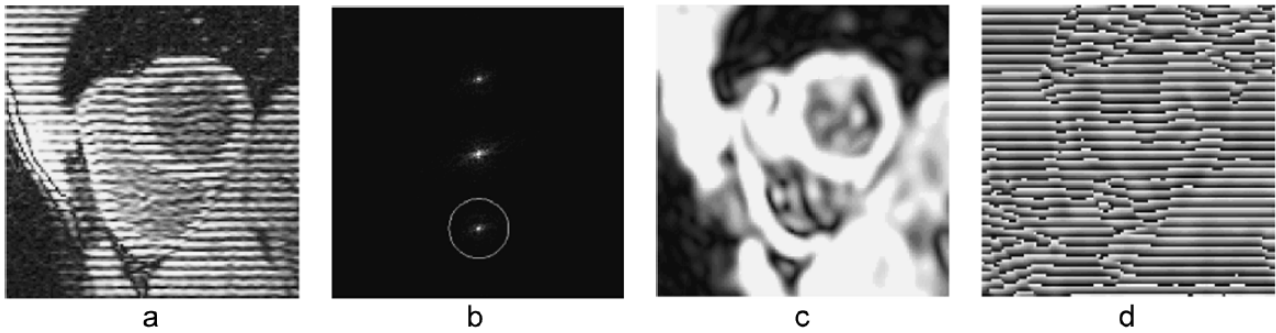


**Figure 3.3** – Example of HARP motion tracking: (a) An MR images with horizontal tags. (b) The magnitude of the Fourier transform of the tagged MR image. The circle indicates a bandpass filter which is applied to extract the spectral peak. (c) HARP magnitude image. (d) HARP angular image. [Pan et al., 2005]

motion can be captured but the scan time is quite long and demands a sophisticated breath-hold technique. Thus, this method is not very practical in typical clinical environment. [Pan et al., 2005] extended the traditional HARP method for 3D cardiac motion tracking by combining information from two orthogonal image planes of tagged MR images: A stack of SA images with a tagging grid as well as LA images with one horizontal set of tags is used. Similar to 2D HARP, the condition of phase invariance of material points is used to track the motion. A material mesh model is used for interpolation from sparse phase information from the two image planes.

To accurately estimate large motion using HARP, [Liu and Prince, 2010] proposed a refinement method based on the computation of the shortest path. The method uses a graph representation of the image and seeks an optimal tracking from a specified seed to each point in the image by solving a single source shortest path problem. In addition to this shortest path refinement, tracking in the presence of through-plane motion is improved by introducing synthetic tags at the reference time. Experimental results show that the proposed method can track the cardiac motion more robustly compared to the original HARP method.

[Arts et al., 2010] proposed to estimate the motion using a sine wave-modelling in the frequency domain directly. The method is based on simultaneous detection of the local spatial phase shift and spatial frequency in bandpass-filtered images. Although tags deteriorate with time while anatomical features reappear in the images, the proposed method appears relatively robust for these changes than the HARP method. This method and the HARP method both work in

2-D, use bandpass filtering, and need local phase and frequency information to extract local displacement. The difference is that for the sine method, the local gradient of the phase is determined directly via frequency analysis. Moreover, this method uses a measure for the quality of model fit, which is used to suppress the influence of unreliable parts in the signal.

### 3.3.2 Gabor filter banks

Gabor filters are a family of band-pass filters which consist of a Gaussian multiplied by a complex sinusoid in the spatial domain, or equivalently, a shifted Gaussian in the frequency domain [Wang and Amini, 2011]. By choosing the appropriate parameters the magnitude response of the Gabor filter can be used to remove tags in the myocardium and the phase response can be used to track tags. A Gabor filter bank is a set of 2D Gabor filters with tunable parameters that represent the variable spacing and orientation of tag lines. Utilising a phase-based optical flow, the phase response of the Gabor filter bank for a material point can be assumed to be constant during the deformation [Chen et al., 2010].

[Montillo et al., 1996] extracted deformation information in a 2D simulated model by finding the optimal parameters that maximise the Gabor filter response. The method accurately extracts the tag line spacing, orientation, displacement and effective contrast. The authors also proposed a frequency parameter interpolation method to recover all tag information at a finer resolution than those of the filter bank parameters. [Qian et al., 2006] extended the 2D Gabor filter bank method to 3D in order to extract and track deformed tag surfaces instead of tag lines. Here, a 3D Gabor filter bank based on the geometric characteristics of the tagging sheets is designed. The whole 3D image dataset is convolved with each Gabor filter in the filter bank in the Fourier domain. A set of deformable meshes is then fitted to the extracted tagging sheets and tracked over time.

Based on Gabor filter banks and deformable models, [Chen et al., 2010] proposed a three step process for 3D cardiac motion tracking: First, the method extracts the tag intersections based on local phase analysis using Gabor filter bank. Then, RPM is used to track the intersection movement. The RPM is performed by finding a transformation and a one-to-one correspondence

between grid tag intersections in different image frames. By using RPM, the influence of through-plane motion and relatively large deformation and/or relatively small tag spacing can be minimised. Finally, a meshless deformable modelling technique [Wang et al., 2008] is used to generate a dense displacement field from the sparse feature tracking result.

### 3.3.3 Sparse feature tracking

The intersection points of orthogonal tagging planes encode a unique 3D position in the myocardium. The intersection points can be used as sparse features that move along with the deforming tissue during the cardiac cycle. Due to the 3D motion of the myocardial tissue, the intersections in the reference frame may move in and out of the imaging plane.

[Kerwin and Prince, 1998] presented a method for generating accurate motion estimates over a sparse set of material points using standard tagged MR images. Each tracked point is located at the intersection of three tag surfaces. Each of tag surfaces is estimated using a thin-plate spline. Tag surfaces are used to help to estimate the out of imaging plane deformation. The intersections in each frame are determined by an iterative alternating projection algorithm. The alternating projection algorithm is used to reduce the complexity since each thin-spline equation may involve hundreds of logarithmic terms which are expensive to compute. Only the intersections within the LV boundaries are considered.

[Amini et al., 2001] proposed an efficient technique for the measurement of 3D motion of material points of the human heart from tagged MR images. The technique reconstructs 3-D B-spline surface representation of the tag planes. The parametric representation of the tag surfaces leads to an easy and robust way to compute the position of 3D intersections of each frame. The developed methods allow the extraction of non-rigid deformation of the intersections as a function of time by minimising the sum of distances between any two reconstructed tag surfaces.

Instead of extracting MR beads (the intersection of tag planes) by reconstructing tag planes, [SamPATH and Prince, 2007] proposed an automatic 3D intersection tracking method. The

3D motion of the tag intersections is obtained by combining two 2D motion estimates that are computed on both SA and LA image planes using 2D HARP tracking techniques. This technique is also referred to as slice-following. It is noticeable that in extreme cases the out of plane motion between two consequent frames can invalidate the 2D HARP tracking. The slice-following technique may fail in this case. A validation of 2D in-plane motion tracking using this acquisition sequence on a moving phantom is also presented.

### 3.3.4 Deformable models

In tagged MR images, the force to drive the deformable model can originate from tag intersections, tag lines, or tag surfaces. However, in all cases an interpolation is required to obtain a dense motion field for the model.

[Park et al., 1996, Young and Axel, 1992, Young, 1999] proposed a volumetric deformable model with parameter functions for deformation analysis. These methods used 3D FEMs and converted the FEM nodal deformations into parameter functions. The method uses tag intersection points in the image plane (three orthogonal sets) and boundary points to estimate the volumetric deformation of the LV. [Haber et al., 2000] modified this framework to estimate the motion and deformation of both LV and RV free wall and septum. The process is illustrated in Figure 3.4. [Hu et al., 2003] present a statistical model to estimate in-vivo material properties as well as strain and stress distributions in both ventricles using the displacements calculated from tagged MR images data based on the result of [Haber et al., 2000].

[Amini et al., 1998] proposed an efficient thin-plate spline warping method. By deforming an area in the plane, two embedded snake grids from two tagged frames are brought into registration and finally interpolated into a dense displacement vector field. Here the assumption is made that the motion of the LV is 2D which is roughly the case towards the apical end of the heart. However, this assumption strongly limits the method's ability to model the 3D motion towards the base of the heart. [Wang et al., 2001] proposed to use a subspace approximation technique to accomplish the same task. The authors formulate the displacement estimation as a variational problem and then project the solution into the spline subspace. A B-spline

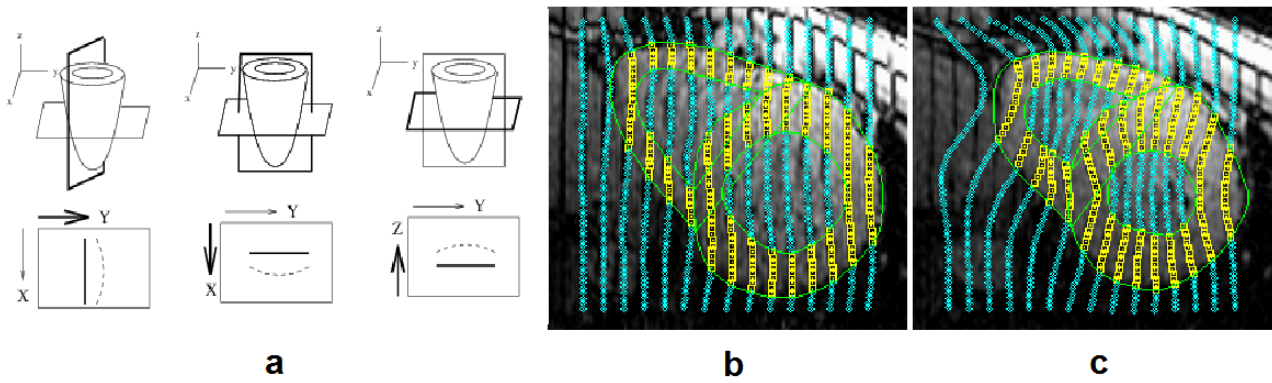


**Figure 3.4** – Example of motion tracking using deformable models: (a) 1st row: LV with image (light) and tag (dark) planes. 2nd row: 2D images with example of tag motion from initial (dark lines) to final (dashed lines) phases. (b) Initial mesh at end-diastole overlaid on the tagged MR images. Lighter coloured squares between the myocardial contours are marked active. The rest of the contours are in passive mode. (c) Final mesh at end-systole overlaid on the tagged MR images. [Haber et al., 2000]

subspace is chosen due to the fact that efficient numerical methods can be derived. The results suggest that the method significantly improves the computational time compared to the original approach [Amini et al., 1998].

A 4D B-spline cubic deformable models was introduced for analysis of cardiac motion in [Huang et al., 1999]. Here, model fitting is posed as an energy minimisation problem. The external energy encodes the distance between isoparametric planes of the model and MR images tag planes. No internal energy is enforced. The model is based on a 4D grid of control points. Smoothness of the final motion is supported by the fact that each control point contributes to a few frames in time and a few tag planes in space. The energy minimisation problem is numerically solved by an adaptive conjugate gradient descent algorithm. First, all the tag lines for all the slices and all the frames are extracted and grouped by each tag plane. Second, 4D Chamfer distance potentials is computed. The Chamfer distance is an approximation of the Euclidean distance from each model point to the nearest target point. Finally, the 4D model is deformed using the potential field. The output of the fitting process is a time-varying B-spline model whose knot planes reconstruct the tag surfaces in the three orthogonal directions in 4D. After model fitting, a 3D displacement field can be obtained by subtracting the 3D B-spline model at the initial time frame from any other time frame.

[Tustison et al., 2003] improved the 4D B-spline model framework in by proposing the following

changes: First, an internal energy function is used which is defined by the model's first and second-order partial derivatives summed over 4D space. Second, additional control points can be inserted and used for more localised interpolation.

[Deng and Denney Jr, 2005] proposed a 3D B-spline model based on a cylindrical coordinate system. This cylindrical B-spline model takes the LV myocardial shape into account and ensures smoothness in the circumferential, radial, and longitudinal directions. It has been shown that a cylindrical and prolate-spheroidal B-spline parametrisation improves the accuracy of the computed circumferential strains.

More recently, [Wang et al., 2008] proposed a meshless deformable model for 3D motion estimation and analysis of the LV based on tagged MR images. The meshless model considers the object as a set of discrete points. The external forces are computed at tag intersections which are extracted from tagged MR images using Gabor filters. Internal forces are computed from the local strain energy between neighbouring points using a moving least square method. In particular, the model performs well even when the control points (tag intersections) are relatively sparse. The meshless model has been validated on a numerical phantom, as well as in in-vivo data of healthy subjects and patients. The experimental results show that the meshless deformable model can fully recover the myocardial motion and strain in 3D.

### 3.3.5 Registration methods

Optical flow [Horn and Schunck, 1981] and free-form deformations [Rueckert et al., 1999] are widely used image registration methods to extract motion from tagged MR images [Wang and Amini, 2011]. The fundamental assumption of optical flow is that image intensity remains constant for a material point projected to image space. The assumption is not satisfied in tagged MR images due to the fading of tags. Tag fading describes the effect that due to the relaxation of the magnetisation of the spins throughout the cardiac cycle, the intensity of a material point fades from frame to frame and thus changes. Different ways are proposed to deal with the variable intensity in tagged MR images.

[Prince and McVeigh, 1992] proposed a variable brightness optical flow method to overcome the intensity variation in tagged MR images by introducing a term which accounts for the variable brightness of the tags using knowledge about the MR acquisition parameters and initial magnetisation. [Dougherty et al., 1999] utilised a Laplacian filter to compensate for the intensity and contrast loss in myocardial tags. [Florack et al., 2007] applied a multi-scale optical flow framework using HARP images to avoid the variable intensity problem. The harmonic phase of a material point remains constant as it moves during the cardiac cycle. As a result the intensity or phase should not change. A spatio-temporal Gaussian filter is applied as a pre-processing step. The pre-processing step helps to produce a stable and smoothly varying motion field of the LV myocardial wall.

Non-rigid registration using FFD was proposed by [Rueckert et al., 1999]. In this approach, the global motion is modelled by an affine transformation, while local motion is described by a FFD based on multilevel B-splines. A hierarchical registration is achieved by optimising a cost function measuring the similarity between two images as well as the smoothness of the deformation required to align the images. The cost function can be information theory based mutual information (MI) [Collignon et al., 1995, Viola and Wells III, 1997] or normalized mutual information (NMI) [Studholme et al., 1999].

[Chandrashekhara et al., 2004] made use of the non-rigid registration algorithm and applied it to the analysis of myocardial deformations. In this approach, the first frame is regarded as the reference frame and all other frame in the cardiac cycle are registered to the reference frame. In order to obtain complete a 3D motion of the myocardium, the cost function is modified to represent the normalised sum of the NMI between the registered SA and LA images. NMI is chosen in order to reduce the influence of variable intensity over time. The main advantage of this method is that tag localisation and deformation field reconstruction are performed simultaneously within the optimisation. Another advantage is that no assumptions about the nature of the tag pattern are made so that the proposed method is potentially applicable to other image modalities. In other words, the information of other image modalities can be easily incorporated.

## 3.4 Evaluation methods and benchmarks

Evaluating the performance of cardiac motion tracking algorithms is a more difficult task than characterising the performance of image segmentation approaches. The ground truth is more difficult to obtain and extremely time consuming. One solution is the interactive drawing of the desired segmentation at different time points by human observers. Apart from the problems mentioned in Section 2.4, this solution suffers from the fact that the motion within each segment can not be assessed. The development of evaluation methods and publicly available benchmarks are urgently needed.

[Tobon-Gomez et al., 2012] presented the first attempt to build a public available benchmark for cardiac motion tracking. The database includes MR and 3D US datasets from a dynamic phantom and 15 datasets from healthy volunteers. The MR acquisition included cine steady state free precession (SSFP), whole-heart TFE, and 3D tagged MR sequences. From the SSFP images, the ED anatomy was extracted using a deformable model of the LV. From the LV model, 12 landmarks were generated (4 walls at 3 ventricular levels). These landmarks were manually tracked in the 3D tagged MR data over the whole cardiac cycle by two observers. The landmarks can provide extra information for the assessment of cardiac motion tracking algorithms in addition to the segmentations from different time points.

## 3.5 Conclusion

Cardiac function analysis has focused primarily on the myocardium of the LV. This is due to the fact that LV controls systemic perfusion and is responsible for the majority of the cardiac function. The analysis of the RV is more difficult due to the fact that its wall is thinner. Moreover it has a more complex geometry and motion pattern.

In this chapter, we have reviewed cardiac motion analysis techniques for CMR images including MR images tagging and cine MR images. Several cardiac motion analysis techniques are restricted to tagged MR images such as HARP and Gabor filter banks. Sparse feature extraction

and tracking, deformable models and registration methods can be applied to both cine MR images and tagged MR images. Cine MR images provides very clear information about the anatomy of the heart which is useful for calculating global indices, but has limited ability to model the motion within the myocardium. Tagged MR images, on the other hand, contain more detailed information about the RWM.

An interesting avenue for future work is the combination of information from cine MR images and tagged MR images. It is not only desirable to obtain the cardiac motion pattern in the radial, longitudinal and circumferential directions simultaneously, but also highly feasible if deformable model or registration frameworks are used since these do not impose any assumption about the imaging modality itself. The research focus of this thesis will focus on the extraction of cardiac motion from both modalities simultaneously.

# Chapter 4

## Automatic segmentation of different pathologies from cardiac MR images

### 4.1 Introduction

The work in this chapter is based on the following published papers:

- Wenzhe Shi, Xiahai Zhuang, Robin Wolz, Duckett Simon, KaiPin Tung, Haiyan Wang, Sebastien Ourselin, Philip Edwards, Reza Razavi, and Daniel Rueckert. (2011). A multi-image graph cut approach for cardiac image segmentation and uncertainty estimation. *Statistical Atlases and Computational Models of the Heart: Imaging and Modelling Challenges (STACOM)*, pages 178-187.
- Wenzhe Shi, Xiahai Zhuang, Haiyan Wang, Duckett Simon, Declan Oregan, Sebastien Ourselin, Eddie Edwards, Daniel Rueckert. (2011). Automatic segmentation from cardiac cine MRI with different pathologies using registration and multiple component EM estimation. *Functional Imaging and Modeling of the Heart (FIMH)*, pages 163-170.
- Xiahai Zhuang, Wenzhe Shi, S Duckett, Haiyan Wang, Reza Razavi, Daniel Rueckert, Sebastien Ourselin. (2011). A Framework Combining Multi-Sequence MRI for Fully

Automated Quantitative Analysis of Cardiac Global And Regional Functions. Functional Imaging and Modeling of the Heart (FIMH), pages 367-374.

Accurate estimation of indices of cardiac function, such as [LVM](#), [EDV](#), [EF](#), [RWM](#) and [RWN](#), is important in routine clinical applications as well as in cardiovascular research aiming at better understanding the function of the heart. In order to compute these measurements of cardiac function, one of the essential steps is to identify the ventricles and the myocardium and to delineate their boundaries. Manual segmentation tends to lead to significant inter- and intra-observer variations and is extremely time-consuming. It is hence highly desirable to develop an automated method to obtain a reproducible and unbiased result.

As mentioned in the introduction, [MR](#) imaging [[Lauterbur, 1973](#)] is a medical imaging technique most commonly to visualise detailed internal anatomy and function of the body. In standard clinical practice, the most commonly available [MR](#) images of the heart are multiple stacks of [SA](#) and [LA MR](#) images. These images are typically acquired as cine sequences showing the heart throughout the entire cardiac cycle. Due to the anisotropic resolution of the images (high in-plane resolution but low out-of-plane resolution) and the fact that different slices of the stack are acquired during different breath-holds, the automated segmentation of these images is difficult. On the other hand, 3D [TFE MR](#) (3D [MR](#) for short) imaging is now becoming clinically feasible [[Uribe et al., 2007](#)]. These images have high spatial resolution and are free from inter-slice respiratory motion. However, the images have a lower signal-to-noise-ratio and lack of contrast compared to [SA](#) and [LA MR](#) images. Therefore, combining 3D and cine [MR](#) imaging data has the potential to provide better accuracy and robustness for automated segmentation.

#### 4.1.1 Limitations of current cardiac image segmentation approaches

Deformable model-based segmentation [[Huang et al., 2010](#),[Pluempitiwiriyawej et al., 2005](#),[Kaus et al., 2004](#),[Rouchdy et al., 2007](#)] achieves automatic delineation of the object of interest by deforming the surface of a pre-constructed model towards the detected boundaries, while at

the same time constraining the model to maintain a *reasonable* shape. What constitutes a *reasonable* shape is typically encoded as *a-priori* knowledge of the model. The detection of candidate boundaries in these methods is usually confined to a local region around the model surface. Therefore, constructing an appropriate a-priori model, whose shape variability can adequately capture the geometry of the heart in unseen images, is crucial for segmentation techniques in this category.

An alternative technique for segmentation is to propagate a pre-constructed atlas to the unseen images using image registration [Lorenzo-Valdés et al., 2004, Zhuang et al., 2008, Zhuang et al., 2010]. By using advanced image registration techniques such as LARM [Zhuang et al., 2010], this segmentation approach is able to deal with large shape variations of the heart. However, the segmentation accuracy reported using LARM is still limited, in particular for the segmentation of the epicardium [Zhuang et al., 2010]. This problem becomes particularly evident when the intensities in the myocardium exhibit locally varying contrast, e.g. due to infarction.

Voxel-based segmentation identifies differences between the intensity distribution of different tissues [Zhang et al., 2001, Kedenburg et al., 2006, Boykov and Kolmogorov, 2003, Jolly, 2006]. In these approaches, each voxel is assigned a classification label by modelling the intensity distribution of each tissue. One common model using the EM framework assumes that the intensity of a tissue class has a Gaussian distribution defined by the intensity mean and standard deviation. In this context the EM framework is used to maximise the likelihood of labelling parameters given the current estimation. The method is able to achieve sub-voxel accuracy but requires a good initialisation. However, the lack of geometric information makes it difficult to achieve such a good initialisation due to the large shape variation of the heart within a given population of subjects.

Most of the automatic segmentation methods, including model-based and atlas-based methods, assume homogenous tissue intensities. This leads to problems when segmenting images from patients with myocardial infarction: Infarcted myocardium often has a heterogeneous intensity distribution in contrast to normal myocardium which is characterised by a more homogeneous intensity distribution. These problems are further compounded by the fact that

these heterogeneous intensity distributions are difficult to model using prior knowledge since the position and intensity of infarcted myocardium varies across different subjects.

Atlas propagation is widely used either for the initialisation for cardiac segmentation [Lorenzo-Valdés et al., 2004] or as the primary segmentation method [Zhuang et al., 2010]. An important but not yet fully explored aspect of such image segmentation is: How can we quantify and visualise the segmentation uncertainty? This uncertainty can be further divided into uncertainty arising from the registration [Risholm et al., 2010, Kybic, 2009] and uncertainty about the final segmentation. No matter how robust a segmentation technique is, it is important to have the ability to alert the user if the uncertainty of the segmentation is high. High uncertainty can either be a sign of an unreliable segmentation result or of pathologies in the cardiac anatomy.

### 4.1.2 Overview and contributions

In this chapter we propose an integrated framework (Figure 4.1) to deal with the challenges described above. We automatically segment the LV and myocardium simultaneously from a static high-resolution 3D MR images at ED phase as well as multiple stacks of SA and LA cine MR images. The proposed framework includes a Haar feature-based cascade classifier for the detection of the heart, image registration for propagating prior information in from of a probabilistic atlas built a group of healthy subjects, and a MCEM estimation and multi-image graph-cuts based method for segmentation refinement. Before image segmentation we transform all images into a common spatial and temporal coordinate system and correct the inter- and intra-sequence misalignments [Chandler et al., 2006]. We develop a registration scheme that propagates a probabilistic atlas to the subject’s coordinate system. Using Gaussian mixture modelling in the EM estimation has been proposed by [Ashburner and Friston, 2005] to cope with partial volume voxels which exist at the interface between different tissue classes. We extend this approach by using a spatial weighting to emphasise where the components cluster and choose the number of Gaussian models explicitly from the number of potential components (for example myocardium consist of normal and infarcted myocardium and background consist

of blood tissue and air). The segmentation is then refined using a multi-image graph-cuts algorithm.

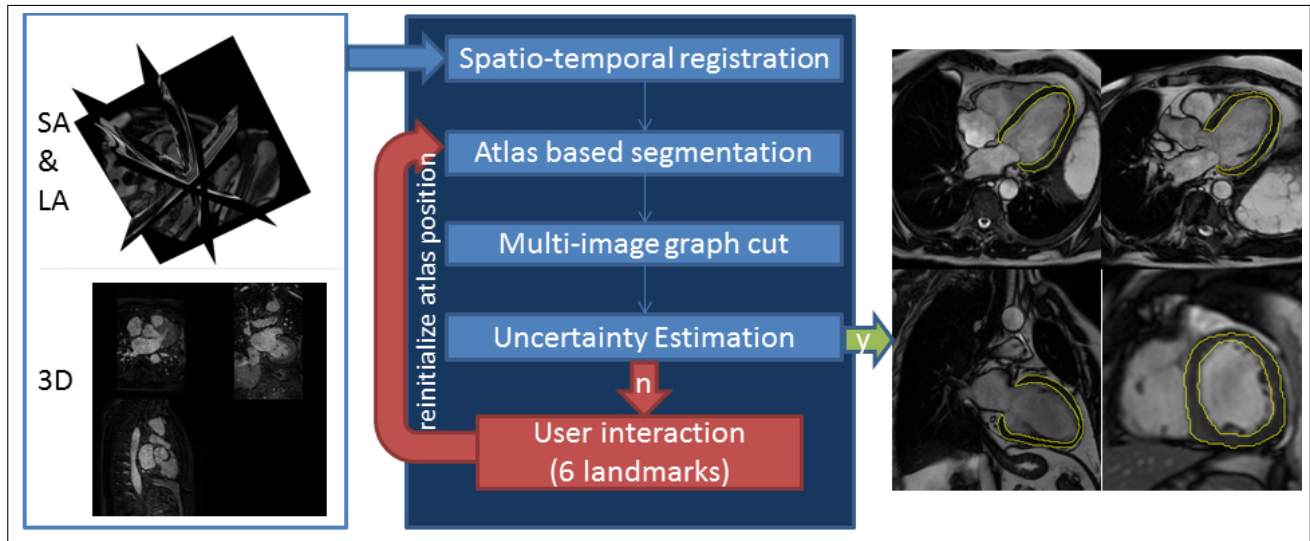


**Figure 4.1** – Overall workflow of the segmentation framework.

We also explore the potential of registration and segmentation uncertainty in improving the robustness: If and only if the uncertainty of the segmentation is high, the system will ask the user to input additional landmarks to help better initialise the atlas-to-subject registration. The landmarks include the apex, the centre of mitral valve, the centre of left ventricle and the two right ventricle insertion points. The next sections describe the segmentation framework in more detail; Section 4.3 introduces the idea of using uncertainty in the analysis. Finally, Section 4.4 illustrates the segmentation results from 32 patients while Section 4.5 summarises and concludes this chapter.

## 4.2 Myocardium segmentation from multiple image sequences

**SA** and **LA** images have high temporal resolution revealing dynamic information about the heart. By contrast, **3D MR** images acquired within a single breath-hold provide a static image of the heart with high spatial resolution in all three directions. Therefore, we propose to use all three types of **MR** images within a unified segmentation framework that employs a two-step

segmentation technique using registration- and intensity-based segmentation.

### 4.2.1 Detection of the LV using a cascade classifier

The location of the heart in MR images is highly variable as a result of the operator-defined imaging planes and the variable anatomy across different subjects. To automatically identify the position and orientation of the cardiac anatomy, we have adopted and refined the object detection approach proposed by Viola and Jones [Viola and Jones, 2002]. The basic idea of this approach is to train a Haar-feature based cascade classifier that is capable of detecting anatomical structures in medical images [Pavani et al., 2009, Zheng et al., 2007].

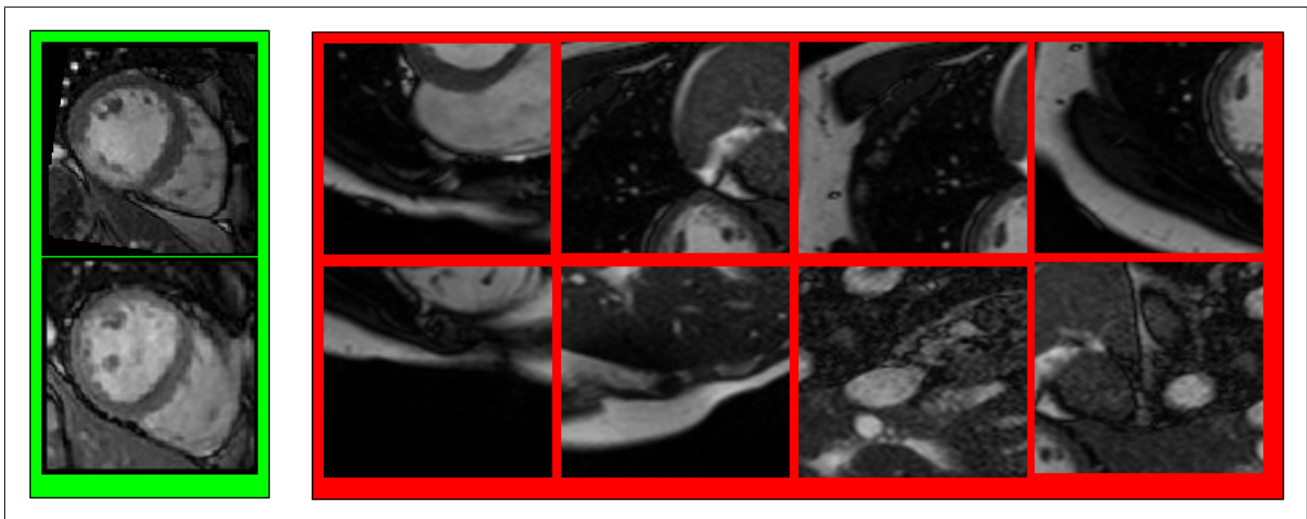


**Figure 4.2** – Positive (green) and negative (red) examples from the training set for the cardiac detector.

We adapted this algorithm to detect cardiac chambers and used a training set consisting of 25 healthy cases. These 25 cases are not used in the evaluation of the segmentation in section 4.4. To train the classifier, we manually identified a bounding box around the location of the heart in the SA MR images. From these images, positive examples for classifier are generated from every slice, excluding the basal and apical slices. Negative examples were generated by randomly sampling the images in such a way that each example either contains no cardiac anatomy or only parts of the cardiac anatomy. An illustration of the positive and negative examples are shown in Figure 4.2.

To improve the robustness of object detection we have modified the approach for the detection of the LV in cardiac MR images in three ways: (1) In a pre-processing step, image intensities are classified into air, soft tissue or blood using a Gaussian mixture model. The classifier is then only applied to those voxels labelled as blood. (2) We test the classifier in 2D for every slice; however, we exclude the apical and basal slices from hypothesis testing. (3) If multiple positive matches are returned across slices, they are fused into an average hypothesis using classifier fusion.

We have tested the proposed detector on 100 subjects including 40 healthy volunteers and 60 patients using cross validation. The detection rate and false alarm rate of our proposed approach are 96% and 4% while for the original approach [Viola and Jones, 2002] the rates are 83% and 25%. Some examples from the output of the cardiac detector are shown in Figure 4.3.

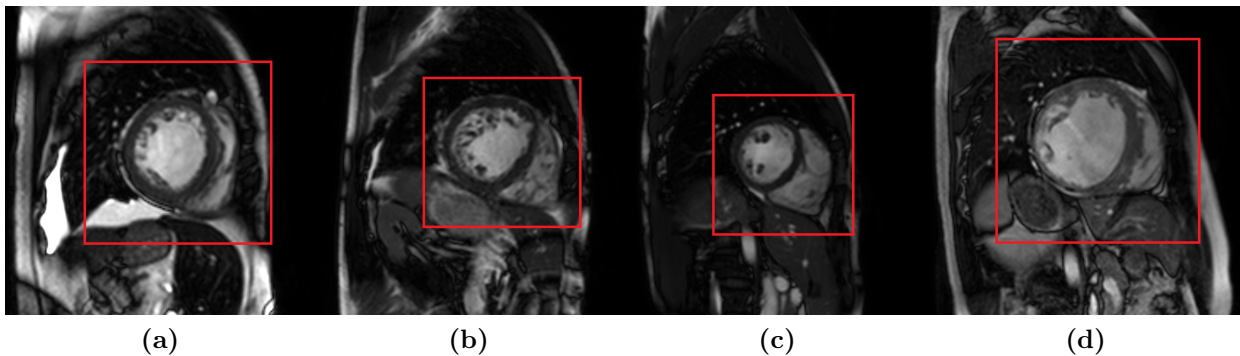


**Figure 4.3** – Some examples of the results from the cardiac detector.

## 4.2.2 Spatio-temporal registration

The images acquired for each patient consist of stacks of SA and LA images (acquired as cine images) as well as a high-resolution, 3D anatomical volume acquired at end-systole. The LA image stacks consist of four (4CH), three (3CH) and two chambers (2CH) views. It is noticeable that the SA and LA images were acquired during a separate breath-hold for each slice while the 3D anatomical image was acquired within a single breath-hold. Due to potential differences in the position of the heart (e.g. due to respiration) there is usually some spatial misalignment between the images (inter-sequence misalignment) as well as between individual

slices of the SA and LA images (intra-sequence misalignment). In addition, there is often temporal misalignment between the 3D anatomical image and the SA and LA cine images.

In order to use multiple images simultaneously, these misalignments must be corrected. The 3D anatomical volume provides good spatial resolution and can thus serve as the target for accurate slice-to-volume registration [Chandler et al., 2006]. In our approach we first register all available LA and SA image slices to the 3D image using a rigid temporal registration using NMI as a similarity measure to identify matching frames, followed by a spatial 3D rigid registration using the same similarity measure. The resulting spatio-temporal (4D) transformation corrects the inter-sequence misalignment. The intra-sequence shifts between SA slices are corrected by registering SA slices to the 3D image using multiple in-plane 2D translations. The similarity measure is a combination of the similarity between the SA slice and the 3D image and the similarity between the neighbouring SA slices. After intra-sequence slice shifts are corrected, all images are transformed to the same spatio-temporal coordinate system, in this case, the coordinate system of the 3D anatomical MR image.

### 4.2.3 Initial atlas-based segmentation of the heart

We constructed the probabilistic atlas as described in [Lorenzo-Valdés et al., 2004]. The probabilistic atlas has been constructed from 25 healthy subjects and is used as *a-priori* information for the EM algorithm. A reference image is selected from the 25 healthy subjects and all other subjects are mapped into this reference space using affine registration followed by a coarse non-rigid registration. The intensities are then averaged over all subjects in the reference space. In addition the labels are fused into a probabilistic map to produce a spatial a-priori map for each label. An example of the constructed probabilistic atlas is illustrated in Figure 4.4.

The segmentation using atlas propagation heavily relies on the result of the atlas-to-image registration. The main difficulty for the registration of an atlas to cardiac image is to localise the different parts of the heart. A global affine registration is usually not sufficient for accurate

registration. Instead, a local, non-rigid registration is often used. However, the local registration is relatively sensitive to the initialisation, i.e. the result of the global affine registration.

Once a region of interest containing the cardiac anatomy has been located via the object detection approach proposed in Section 4.2.1, we use image registration to propagate an atlas to the unseen images. The registration of an atlas to an unseen image yields an estimate of the transformation required to propagate the labels from the atlas to the unseen images.

In [Zhuang et al., 2008, Zhuang et al., 2010] the authors proposed **LARM** to address the large local shape variability of cardiac anatomy commonly seen across large populations with pathologies. **LARM** is integrated into the registration process in our proposed framework as an intermediate registration step between a global affine registration and a local non-rigid registration. Compared to traditional registration schemes, **LARM** is capable of providing a good initial alignment between the images of patients with pathologies and the atlas constructed from normal subjects.

In **LARM**, the transformation between images is defined by the following equation 4.1:

$$\mathbf{T}(\mathbf{x}) = \begin{cases} \mathbf{T}_i(\mathbf{x}) & \text{if } \mathbf{x} \in V_i \\ \sum_{i=1}^{i=n} W_i(\mathbf{x}) \mathbf{T}_i(\mathbf{x}) & \text{otherwise} \end{cases} \quad (4.1)$$

Here  $\mathbf{x}$  denotes the voxel,  $\mathbf{T}_i(\mathbf{x})$  is region  $V_i$ 's estimated affine transformation in region  $V_i$  and  $W_i$  is the distance between  $\mathbf{x}$  and  $V_i$ . In our case,  $V_i$  are respectively **LV** cavity, **LV** myocardium and **RV**. In order to avoid overlap between two local affine regions, the Jacobian (see Appendix, eq. (B.1)) of the transformation at a voxel is enforced to be larger than 0.5 during the registration. We extend the above method to multi-image atlas propagation using a combined **NMI** similarity measure which is defined by the following equation 4.2:

$$S = \frac{\sum_{i=1}^n |I_i| NMI(I_i, I_{atlas}, \mathbf{T})}{\sum_{i=1}^n |I_i|} \quad (4.2)$$

Here  $I_{atlas}$  denotes the atlas image,  $I_i$  denotes the  $i$ th image and  $|I_i|$  denotes the number of

voxels in the image.

#### 4.2.4 Multi-component EM estimation

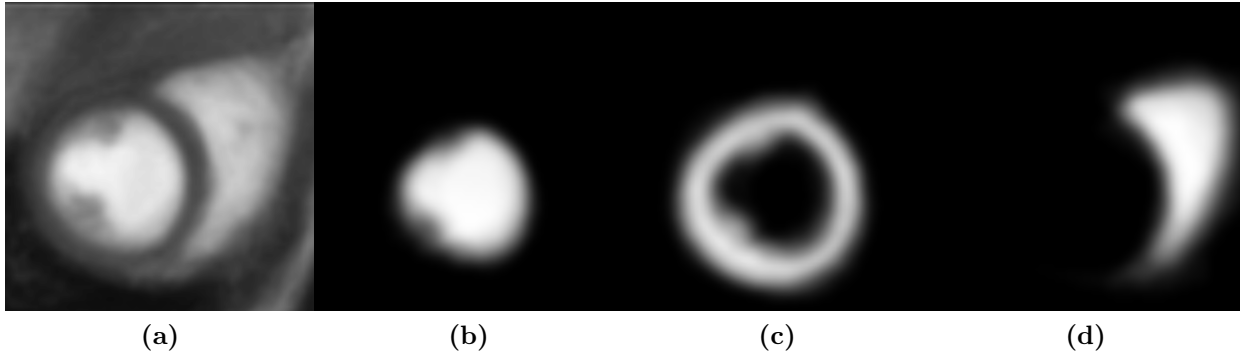


**Figure 4.4** – Example of the constructed probabilistic atlas: (a) the average intensity atlas (b) spatial probability atlas for LV (c) spatial probability atlas for myocardium and (d) spatial probability atlas for RV.

To enable voxel-based classification, we propagate a probabilistic atlas to the unseen images using the result of the previous registration process as a spatial constraint. We then use the EM algorithm to classify each voxel into one out of three labels  $\Lambda = \{L_k, L_b, L_m\}$  for background, blood pool, and myocardium respectively [Lorenzo-Valdés et al., 2004].

In our work the probabilistic atlas has been constructed from healthy subjects. In normal anatomical MR images, the intensity of myocardium is relatively homogeneous and the EM-based segmentation is able to segment normal myocardium of healthy subjects with high degree of accuracy (mean distance and standard deviation reported in [Lorenzo-Valdés et al., 2004] is  $2.05 \pm 2.19mm$ ). For patients with myocardial infarction, the intensity of the infarcted region can be significantly different from that of healthy myocardium. This leads to an inaccurate delineation of the myocardium in the infarcted region when using the traditional EM-based algorithm [Lorenzo-Valdés et al., 2004] as the example in Figure 4.5 shows.

We propose to use a MCEM algorithm to cope with this abnormal intensity distribution. The MCEM algorithm models the myocardial tissue using multiple Gaussian distributions and can thus better adapt to the heterogeneous intensity distribution in patients with infarcted tissue.

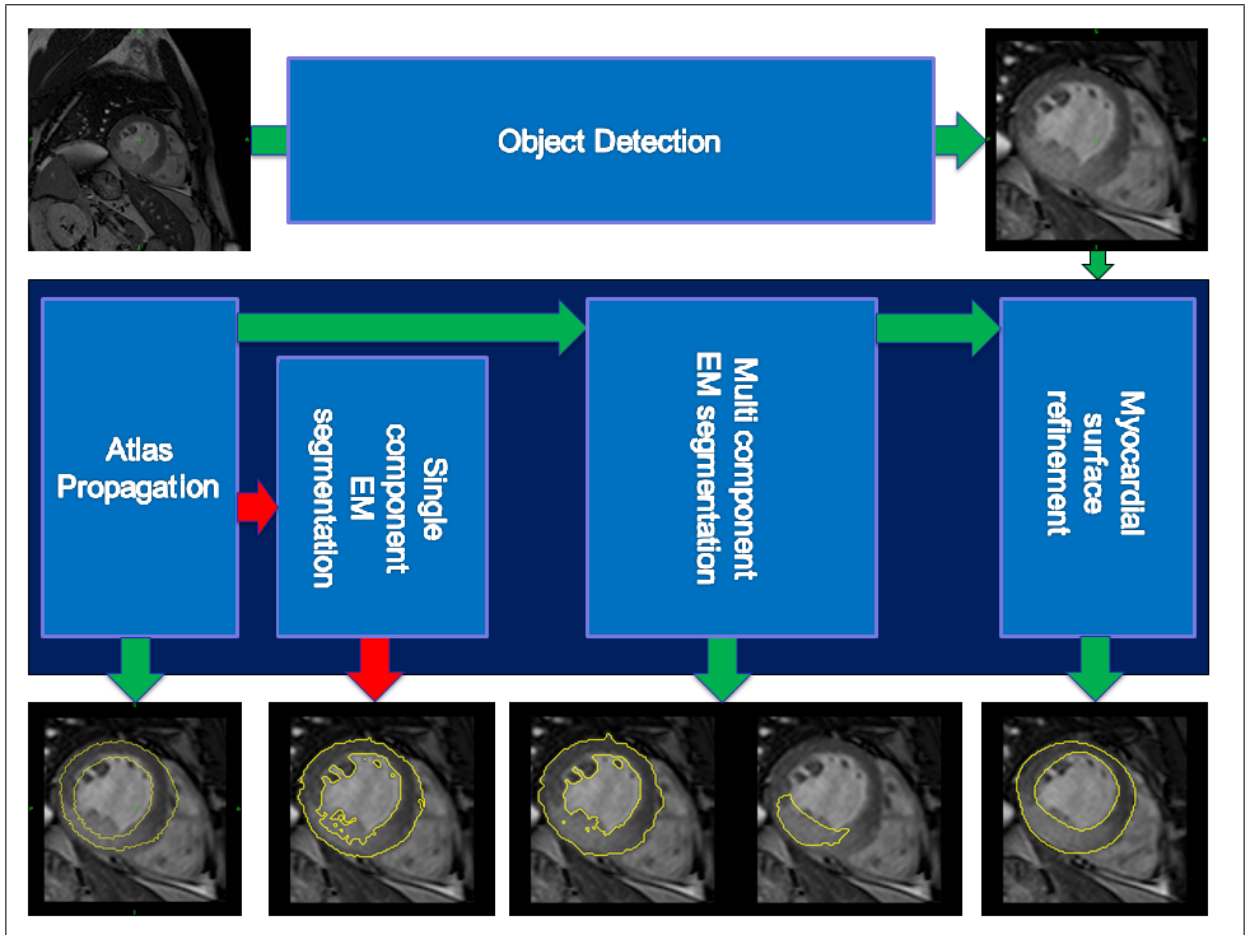


**Figure 4.5** – Workflow of the multi-component EM estimation based segmentation component. The green arrows indicate the workflow we use and the red arrows indicate the workflow in [Lorenzo-Valdés et al., 2004].

Let  $K$  be the number of labels and  $n$  be the number of voxels in the image. Let  $G(y_i, \mu, \sigma)$  represent a Gaussian distribution where  $y_i$  is the intensity, and  $\mu$  and  $\sigma$  are the mean and standard deviation respectively. Furthermore, let  $p_L^m(i)$  be the probabilistic estimate of the segmentation of a voxel  $\mathbf{x}_i$  for label  $L$  at the  $m$ -th iteration;  $p_L^{atlas}(i)$  denotes the prior probability propagated from the probabilistic atlas after the registration step. The MCEM algorithm is then initialised as follows:

$$p_L^0(i) = p_L^{atlas}(i) \quad (4.3)$$

$$\mu_L^0 = \frac{\sum_{i=1}^n y_i p_L^0(i)}{\sum_{i=1}^n p_L^0(i)}, \quad (\sigma_L^0)^2 = \frac{\sum_{i=1}^n (y_i - \mu_L^0)^2 p_L^0(i)}{\sum_{i=1}^n p_L^0(i)} \quad (4.4)$$

Given that label  $L$  is modelled using  $|l|$  components, the initial probabilistic segmentation of each component,  $p_{L_j}^0(i)$ , is given by:

$$p_{L_j}^0(i) = \frac{G(y_i, \mu_{L_j}^0, \sigma_{L_j}^0) p_L^{atlas}(i)}{\sum_{k=1}^K \sum_{o=1}^{|l|} G(y_i, \mu_{k_o}^0, \sigma_{k_o}^0) p_k^{atlas}(i)} \quad (4.5)$$

where  $\mu_{L_j}^0 = \mu_L^0 - \sigma_L^0 + \frac{2\sigma_L^0(j-1)}{|l|-1}$ ,  $(\sigma_{L_j}^0)^2 = (\sigma_L^0)^2/|l|$ , and  $\delta_{L_j}^0 = \frac{\sum_i^n p_{L_j}^0(i)}{\sum_{i,o=1}^{|l|} p_{L_o}^0(i)}$  is the proportion of component  $j$ .

To estimate the probabilistic segmentation, a spatial coefficient  $\omega_{L_j}$  which measures how close each voxel  $\mathbf{x}_i$  is to the centre of gravity  $\mathbf{c}_{L_j}$  of label  $L$ 's component  $j$  is also computed. This is important for avoiding misclassifying voxels with intensities that are similar to those of infarcted tissue but which are remote from the location of the infarct. The algorithm then proceeds by interleaving the following E- and M-steps:

E-step:

$$\mathbf{c}_{L_j} = \frac{\sum_{i=1}^n G(y_i, \mu_{L_j}^m, \sigma_{L_j}^m) p_L^{atlas}(i) \mathbf{x}_i}{\sum_{i=1}^n G(y_i, \mu_{L_j}^m, \sigma_{L_j}^m) p_L^{atlas}(i)} \quad (4.6)$$

$$\omega_{L_j}^{m+1}(i) = \frac{1}{\|\mathbf{x}_i - \mathbf{c}_{L_j}\| + 1} \quad (4.7)$$

$$p_{L_j}^{m+1}(i) = \frac{G(y_i, \mu_{L_j}^m, \sigma_{L_j}^m) p_L^{atlas}(i) \delta_{L_j}^m \omega_{L_j}^m(i)}{\sum_{k=1}^K \sum_{o=1}^{|l|} G(y_i, \mu_{k_o}^m, \sigma_{k_o}^m) p_k^{atlas}(i) \delta_{k_o}^m \omega_{k_o}^m(i)} \quad (4.8)$$

$$p_L^{m+1}(i) = \sum_{o=1}^{|l|} p_{L_o}^{m+1}(i) \quad (4.9)$$

M-step:

$$\mu_{L_j}^{m+1} = \frac{\sum_i^n y_i p_{L_j}^{m+1}(i)}{\sum_i^n p_{L_j}^{m+1}(i)}, \quad (\sigma_{L_j}^{m+1})^2 = \frac{\sum_i^n (y_i - \mu_{L_j}^{m+1})^2 p_{L_j}^{m+1}(i)}{\sum_i^n p_{L_j}^{m+1}(i)} \quad (4.10)$$

$$\delta_{L_j}^{m+1} = \frac{\sum_i^n p_{L_j}^{m+1}(i)}{\sum_{i=1}^n \sum_{o=1}^{|l|} p_{L_o}^{m+1}(i)} \quad (4.11)$$

The EM algorithm continues until the the log-likelihood changes by less than a given constant  $\epsilon$ . The result is an algorithm which allows areas of myocardial infarction to be segmented.

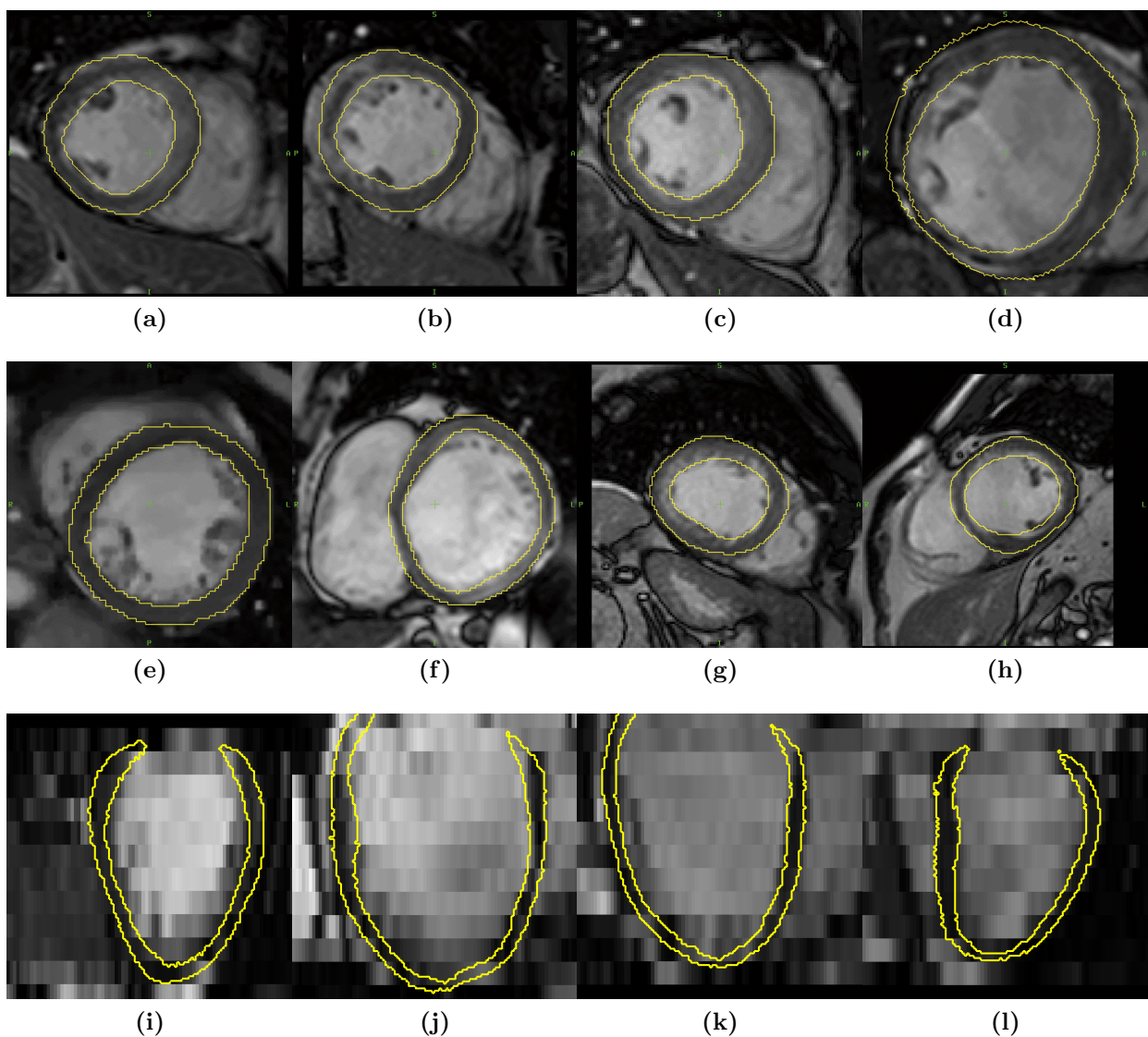


**Figure 4.6** – Randomly selected segmentation results of different patients: (a-h) SA view of SA images overlay with SA segmentation and (i-l) LA view overlay with 3D segmentation.

### 4.2.5 Multi-image graph-cuts refinement

Although the atlas is propagated to all images simultaneously, the MCEM algorithm segments the 3D, SA and LA images separately. We propose to use an energy function based on MRF in combination with graph-cuts [Boykov et al., 2001] to refine the segmentation. A MRF is used to ensure a spatially smooth segmentation across all images at the same time. In the following sections we will refer to this as the multi-image refined multiple component expectation maximisation (MRMCEM) segmentation. 4D graph-cuts have recently been used to segment image sequences [Linguraru et al., 2010, Wolz et al., 2010]. Here, we have adopted the 4D graph-cuts approach to utilise information from multiple MR images with different spatial resolutions. To differentiate our approach from a 4D graph-cuts segmentation of image sequences, we refer to it as multi-image graph-cuts segmentation. It should be pointed out that the original graph-cuts approach is a binary segmentation method. However, a segmentation using multiple labels can be achieved using the expansion and swap algorithm for the graph-cuts [Boykov et al., 2001].

Let  $I_k$  be the  $k$ -th image of the multiple image set. Segmenting  $I_k$  can be defined as a process of assigning a label  $f_i \in L$  to each voxel  $\mathbf{x}_i \in I_k$ . An MRF-based energy function can be formulated as:

$$E(f) = \lambda \sum_{\mathbf{x} \in I_k} D(f_i) + \sum_{\{\mathbf{x}_i, \mathbf{x}_j\} \in N} S^{intra}(f_i, f_j) + \sum_{\{\mathbf{x}_i, \mathbf{x}_j\} \in M} S^{inter}(f_i, f_j) \quad (4.12)$$

Here  $N$  and  $M$  denote a neighbourhood of voxels within an image and across different images respectively and  $f$  is the labelling of  $I_k$  [Boykov et al., 2001]. The data term  $D(f_i)$  measures the disagreement between the *a-priori* probabilistic model and the observed data (the image intensities) at  $\mathbf{x}_i$ .  $S^{intra}(f_i, f_j)$  and  $S^{inter}(f_i, f_j)$  are two smoothness term that penalises discontinuities in the segmentation in  $N$  or  $M$ . The parameter  $\lambda$  governs the influence of the data and smoothness terms. We found empirically that setting  $\lambda = 2$  leads to robust results for the segmentation of the myocardium. Two different smoothness terms are selected respectively for inter-image smoothness and intra-image smoothness since they are intuitively

distinguishable. For intra-image smoothness, continuity in intensity space is enforced. In contrast to this the inter-image smoothness comes from the overlap between voxels from different images. For the inter-image smoothness the continuity in intensity space is not necessarily meaningful due to the fact that the images come from different imaging sequences.

To optimise eq. (4.12), a graph  $G = \langle V, E \rangle$  with a node  $v \in V$  for each voxel  $\mathbf{x}$  is defined on the images. Each edge  $e \in E$  consists of connections between node  $v$  and two terminal nodes  $F$  and  $B$  (also called source and sink node) as well as connections between neighbouring voxels (within images and across images). The terminal nodes  $F$  and  $B$  represent the two labels describing foreground and background, respectively. By determining a minimum cut on graph  $G$ , the desired segmentation can be obtained [Boykov et al., 2001]. The data term  $D(f_i)$  is estimated using the MCEM segmentation [Shi et al., 2011] which generates a probability for each label of each voxel.

The smoothness term between neighbouring voxels within an image is defined by the following equation:

$$S^{intra} = w_{intra} \frac{1}{\ln(1 + (I(\mathbf{x}_i) - I(\mathbf{x}_j))^2) + \epsilon} \quad (4.13)$$

Here  $I$  denotes the intensity and  $\epsilon$  is a small constant value which compensates for noise when  $I(\mathbf{x}_i)$  is similar to  $I(\mathbf{x}_j)$ . For neighbouring voxels we define  $w_{intra} = 1/d$  where  $d$  is the distance between two voxels.

For voxels across different images, a different smoothness term is chosen. We define a smoothness term that depends on the degree of overlap between the voxels across different images. This addresses the fact that the intensity contrast across different images can vary and is thus not meaningful. We use the Dice metric to compute the amount of spatial overlap between voxels across different images

$$S^{inter} = w_{inter} (2\|A_{\mathbf{x}_i} \cap A_{\mathbf{x}_j}\|) / (\|A_{\mathbf{x}_i}\| \cup \|A_{\mathbf{x}_j}\|) \quad (4.14)$$

where  $A_{\mathbf{x}_i}$  and  $A_{\mathbf{x}_j}$  are the volumes of voxel  $\mathbf{x}_i$  and  $\mathbf{x}_j$  from different images and  $w_{inter}$  is a constant weight. In our experiments we have heuristically chosen as  $w_{inter} = 2$ . The result of

this equation is a value between 0 and 1 due to different voxel size and position of the images. The smoothness term is defined in a neighbourhood  $M$  where  $S^{inter} > 0$ .

By using this multi-image graph-cuts approach, we connect intra-image voxels according to their intensity similarity and neighborhood and inter-image voxels according to their spatial overlap. This enables us to segment multiple images simultaneously and consistently. To identify the endocardial contours and to remove the papillary muscle completely we computed the convex hull of the blood pool segmentation. This is done in 2D since the endocardial contour in the LA view is not always convex. Then, a Fourier representation of the epi- and endocardial contour is computed. The first few harmonic phases correspond to the low frequencies of the contour and the last harmonic phases correspond to the high frequencies. We retain the first six harmonic phases to obtain a final, smoothed segmentation [Lu et al., 2009, Su Huang, 2009, Jolly, 2006]. A 3D surface model of the myocardium can be constructed using shape based interpolation [Grevera and Udupa, 2002] and marching cubes triangulation [Lorensen and Cline, 1987]. Some examples of the resulting segmentation are shown in Figure 4.6.

## 4.3 Uncertainty definition and evaluation

An important but not yet fully explored aspect of atlas-based image segmentation is the quantification of the segmentation uncertainty. It is important to have the ability to alert the user if the uncertainty of the segmentation quality is high which can either be a sign of an unreliable segmentation result or of pathologies in the cardiac anatomy.

### 4.3.1 Registration uncertainty

Given two images,  $I_{atlas}$  and  $I_k$  (the  $k$ -th image of the subject), we can estimate a transformation  $\mathbf{T}$  which maps each voxel  $\mathbf{x}$  in image  $I_k$  to a corresponding voxel  $\mathbf{T}(\mathbf{x})$  so that their intensity values  $I_k(\mathbf{x})$  and  $I_{atlas}(\mathbf{T}(\mathbf{x}))$  should be similar. Using a probabilistic formulation for the image registration problem [Risholm et al., 2010], the uncertainty of the transformation  $\mathbf{T}$  at point  $\mathbf{x}$

can be modelled by the following equation:

$$uc(\mathbf{T}(\mathbf{x})|I_k(\mathbf{x}), I_{atlas}) = 1 - \frac{p(I_k(\mathbf{x}), I_{atlas}|\mathbf{T}(\mathbf{x}))p(\mathbf{T}(\mathbf{x}))}{p(I_k(\mathbf{x}), I_{atlas})} \quad (4.15)$$

We assume that the difference between the appearance of the subject and atlas after transformation can be represented by a normal distribution with zero mean. The degree of deformation can be modelled by a distribution around a rigid transformation that gives a single Jacobian determinant over the whole image space. Thus, we model the likelihood term,  $p(I_k(\mathbf{x}), I_{atlas}|\mathbf{T}(\mathbf{x}))$ , as a normal distribution of the intensity difference between transformed  $I_{atlas}$  and  $I_k$  estimated using an EM algorithm after histogram equalisation. Similarly, the prior of the transformation,  $p(\mathbf{T}(\mathbf{x}))$ , is modelled as a Rician distribution of the Jacobian determinant of the transformation [Rohlfing et al., 2003]. The distribution is estimated based on the inversion technique proposed in [Koay and Basser, 2006]. The Rician distribution is a non-negative and asymmetric distribution, which approximates the distribution of the Jacobian determinant well for a given transformation. The distribution is controlled by two variables:  $v$  and  $\sigma$ . The probability density function is  $f(x|v, \sigma) = \frac{x}{\sigma^2} \exp\left(-\frac{x^2+v^2}{2\sigma^2}\right) B_0\left(\frac{xv}{\sigma^2}\right)$  where  $B_0$  is the modified Bessel function of the first kind with order zero. If  $v/\sigma > 3$ , the Rician distribution becomes approximately Gaussian. If  $v = 0$  the Rician distribution reduces to a Rayleigh distribution. Some examples of the histogram of the Jacobian determinant of transformations and the fitted Rician distribution are presented in Figure 4.7. This shows that the Rician distribution approximates the true distribution of the Jacobian determinants well. Finally, the last term in eq. (4.15),  $p(I_k(\mathbf{x}), I_{atlas})$ , can be modelled as a constant term.

### 4.3.2 Segmentation uncertainty

The uncertainty of a given label from our 4D graph-cuts segmentation can be modelled by the following equation:

$$uc(L_j|I_k(\mathbf{x})) = 1 - \frac{p(I_k(\mathbf{x})|L_j)p(L_j)}{p(I_k(\mathbf{x}))} \quad (4.16)$$

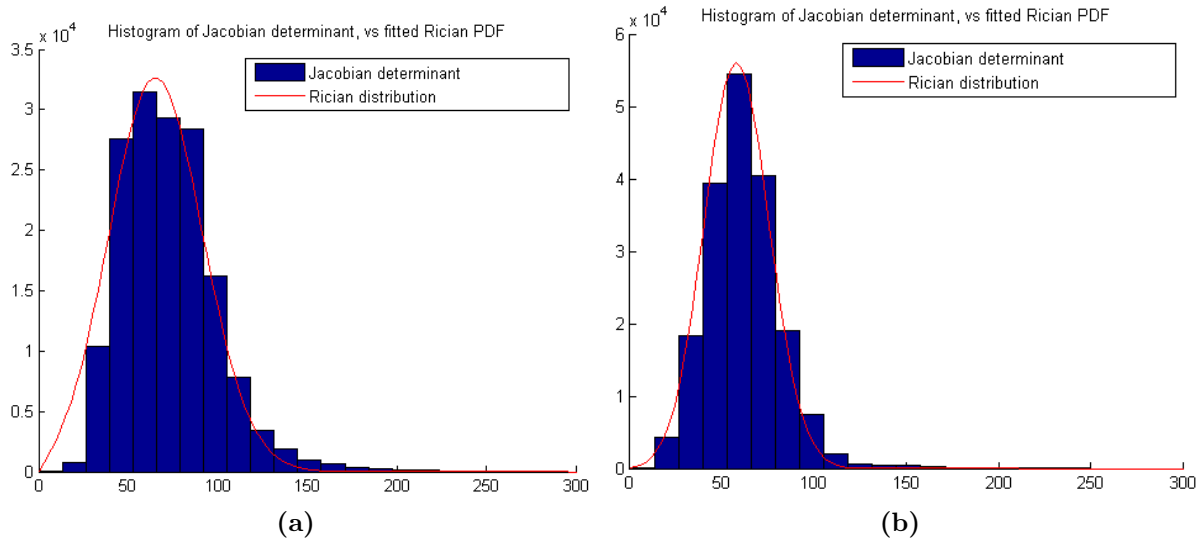


**Figure 4.7** – The histogram of the Jacobian determinant and fitted Rician distribution from different subjects.

The equation is means given the intensity at  $\mathbf{x}$  how unlikely  $L_j$  should be assigned to  $\mathbf{x}$ . The term  $p(I_k(\mathbf{x})|L_j)$  is the likelihood that the intensity of  $I_k(\mathbf{x})$  belongs to  $L_j$  as estimated by the segmentation algorithm.  $p(I_k(\mathbf{x}))$  is modelled as a constant term and the prior term is modelled as

$$p(L_j) = \frac{1}{\log(\delta_j + 1 + \epsilon)} \quad (4.17)$$

In this equation  $\epsilon$  is a small constant value and  $\delta$  is the interquartile range of the multiple component distribution that represents  $L_j$ 's intensity distribution from our segmentation method. The interquartile range is chosen because it is a robust statistic that conveys the dispersion of a distribution [Risholm et al., 2010] and corresponds well to the intra-region homogeneity of a segmentation. It is robust in the sense that it provides meaningful information even for non-Gaussian distributions such as the ones obtained from the MRMCEM segmentation.

### 4.3.3 Uncertainty quantification and user interaction

For each voxel  $\mathbf{x}_i$  in all images, its registration and segmentation uncertainty can be evaluated and visualised using eqs. (4.15) and (4.16) respectively. We can further define the registration

and segmentation uncertainty of a given region  $L_j$  by averaging over a ROI. The quantification of uncertainty can be used to inform the user about how reliable the segmentation and registration results within a ROI are.

Based on the results from uncertainty analysis, we can design a system that detects deviations from the normal level of expected uncertainty. In our analysis we have four failure cases in which the global affine registration fails during the atlas registration. The subsequent segmentations also fail. Myocardial registration uncertainty is a good indicator for failed global affine registration (failed cases  $0.86 \pm 0.14$ , successful cases  $0.39 \pm 0.08$ ,  $p < 0.0001$ ). A combination of registration and segmentation uncertainties is better in terms of classification using linear discriminant analysis (LDA) [Fisher, 1936] (failed cases  $1.73 \pm 0.12$ , successful cases  $1.2 \pm 0.08$ ,  $p \ll 0.0001$ ). A good threshold for detecting segmentation failures using the combined registration and segmentation uncertainty is 1.59 as derived from LDA with accuracy of 100%.

In the cases where we detect a segmentation failure, the user is asked to define six anatomical landmarks (apex, centre of left ventricle, anterior and inferior insertion points of right ventricle, centre of right ventricle and centre of basal plane). These landmarks are also annotated in the atlas. By introducing knowledge about these six additional landmarks, the atlas-to-image registration can be initialised more accurately and all segmentations are performed correctly.

## 4.4 Results

We acquired datasets from 32 subjects. Each dataset consists of SA, LA four, three and two chamber cine MR image sequence ( $2.2 \times 2.2 \times 10$ , mm, 30 phases) and anatomical 3D MR images ( $1.1 \times 1.1 \times 1.1$ , mm, one phase). The patients were scanned using 1.5T MR-scanner (Achieva, Philips Healthcare, Best, Netherlands) with a 32-element cardiac coil or a 5-element cardiac coil (large or claustrophobia patients). Images were divided into three different groups according to pathologies, including patients with myocardial infarction (11 cases), ventricular hypertrophy (10 cases), and healthy subjects (11 cases). Example SA images are shown in

**Table 4.1** – Segmentation results: The Dice overlap measure for the endocardial segmentation ( $L_b$ ) and epicardial segmentation ( $L_b + L_m$ ) results between automatic and manual segmentation’s label results. Lorenzo refers to [Lorenzo-Valdés et al., 2004] and Zhuang refers to [Zhuang et al., 2008].

Group	Segmentation	Lorenzo	Zhuang	MCEM	MRMCEM
normal	endocardial	$0.921 \pm 0.013$	$0.919 \pm 0.016$	$0.927 \pm 0.013$	$0.930 \pm 0.013$
	epicardial	$0.935 \pm 0.016$	$0.936 \pm 0.013$	$0.946 \pm 0.018$	$0.947 \pm 0.017$
infarction	endocardial	$0.841 \pm 0.045$	$0.853 \pm 0.036$	$0.899 \pm 0.029$	$0.910 \pm 0.019$
	epicardial	$0.932 \pm 0.015$	$0.933 \pm 0.012$	$0.950 \pm 0.011$	$0.950 \pm 0.010$
hypertrophy	endocardial	$0.748 \pm 0.228$	$0.917 \pm 0.031$	$0.917 \pm 0.028$	$0.925 \pm 0.018$
	epicardial	$0.761 \pm 0.210$	$0.929 \pm 0.028$	$0.940 \pm 0.023$	$0.948 \pm 0.019$

**Table 4.2** – Segmentation results: The average surface-to-surface distances in mm for the endocardial surfaces and epicardial surfaces between manual and automatic segmentation surface’s results. Lorenzo refers to [Lorenzo-Valdés et al., 2004] and Zhuang refers to [Zhuang et al., 2008].

Group	Surface	Lorenzo	Zhuang	MCEM	MRMCEM
normal	endocardial	$2.274 \pm 0.115$	$2.119 \pm 0.101$	$1.990 \pm 0.150$	$1.890 \pm 0.100$
	epicardial	$2.154 \pm 0.167$	$2.122 \pm 0.191$	$1.830 \pm 0.185$	$1.800 \pm 0.151$
infarction	endocardial	$2.931 \pm 0.545$	$2.637 \pm 0.590$	$1.926 \pm 0.342$	$1.867 \pm 0.243$
	epicardial	$2.192 \pm 0.325$	$2.326 \pm 0.598$	$1.775 \pm 0.195$	$1.800 \pm 0.208$
hypertrophy	endocardial	$6.738 \pm 8.198$	$2.446 \pm 0.459$	$2.349 \pm 0.418$	$2.014 \pm 0.225$
	epicardial	$7.581 \pm 8.073$	$2.862 \pm 0.528$	$2.162 \pm 0.337$	$1.932 \pm 0.318$

Figure 4.8.

Manual segmentations were performed by a cardiologist who delineated the myocardium and left ventricle. We then compared the manual segmentation to the segmentation results obtained via four different techniques: (a) the technique of [Lorenzo-Valdés et al., 2004] which uses affine and non-rigid registration of a probabilistic atlas followed by EM and MRF segmentation, (b) the technique of [Zhuang et al., 2008] which employs registration for atlas propagation, (c) the MCEM proposed in this thesis and (d) the MRMCEM proposed in this thesis. For comparisons between these methods we used the Dice metric which is defined as  $D = (2||S_a \cap S_b||)/(||S_a|| + ||S_b||)$  where  $S_a$  and  $S_b$  are the manual label segmentation and automatic label segmentation. We also used the surface-to-surface distance [Zhuang et al., 2010, Schaerer et al., 2010, Huang et al., 2010] for comparisons. The surface-to-surface distance measures the average distance between the closest vertexes from two surfaces.

The results are summarised in Table 4.1 and 4.2. The results indicate that our proposed segmentation scheme performed consistently better than the other two methods. In our

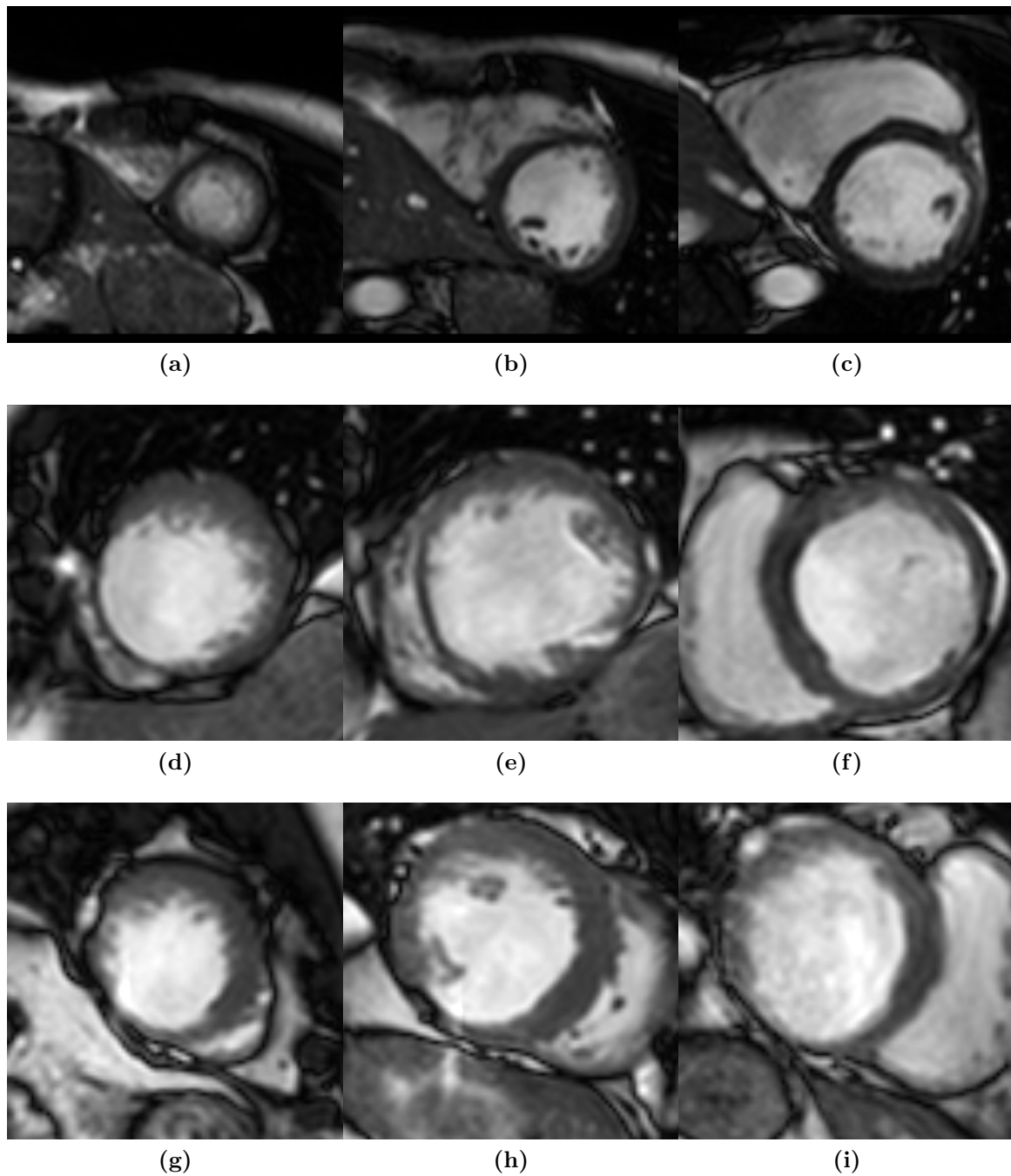


**Figure 4.8** – The example images from different pathological groups: (a-c) shows different slices from a healthy subject, (d-f) shows different slices from a ventricular hypertrophy subject and (g-i) shows different slices from a myocardial infarction subject.

experiments, the global affine registration failed for 8 out of 30 patients with ventricular hypertrophy, leading to failures using the segmentation technique proposed by [Lorenzo-Valdés et al., 2004]. On the other side the registration-based approach by [Zhuang et al., 2008] uses the LARM registration technique and thus the segmentation results are significantly better

on subjects with ventricular hypertrophy due to its ability to address the large local shape variability. Furthermore, the MCEM method outperformed both other techniques due to its ability to model infarcted myocardium using multiple tissue class components. Finally, the MRMCEM segmentation achieved high accuracy with extra information from 3D and LA images across all three groups, which compares favourably to other recent techniques [Zhuang et al., 2010, Schaerer et al., 2010, Huang et al., 2010].

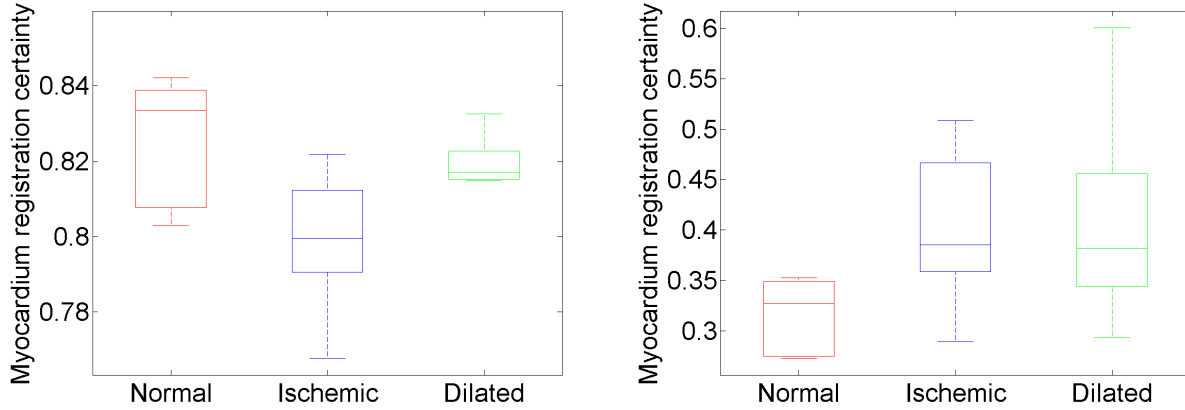


**Figure 4.9** – The left figure shows myocardial segmentation uncertainty. A t-test is performed between different groups. The p-value between normal and ischemic is 0.05, between normal and dilated is 0.47 and between ischemic and dilated is 0.03. The right figure shows myocardial registration uncertainty. The p-value between normal and ischemic is 0.02, between normal and dilated is 0.03 and between ischemic and dilated is 0.97

The proposed measure of uncertainty are a good indicator for failure of the global affine registration. If the segmentation is considered successful, the uncertainty correlates well to abnormality of the patient’s cardiac anatomy as suggested in Figure 4.9. This is possibly due to the fact that our segmentation algorithm is designed to segment pathological images well using LARM [Zhuang et al., 2010] and MCEM [Shi et al., 2011]. To examine if the uncertainty measure correlates with the degree of pathology in individual patients, we plot the uncertainty across different pathological groups. Figure 4.9 shows that myocardial segmentation uncertainty is a very good predictor for separating ischemic cardiomyopathy from the rest of subjects (ischemic subjects  $0.82 \pm 0.012$ , other subjects (normal and dealated)  $0.80 \pm 0.016$   $p < 0.001$ ). Meanwhile myocardial registration uncertainty is a good predictor for separating patients with dilated cardiomyopathy from normal subjects (patients  $0.38 \pm 0.08$ , normals  $0.33 \pm 0.04$   $p < 0.05$ ) but not from ischemic subjects. From these results, we conclude that

the segmentation uncertainty that arises from the intensity distribution correlates to abnormal intensities caused by ischemic cardiomyopathy. We believe that registration uncertainty that comes from geometry distribution corresponds well to abnormal cardiac geometry such as dilated cardiomyopathy.

## 4.5 Discussion and conclusion

In this chapter we have developed a framework for the automatic segmentation of cardiac MR images with different pathologies from multiple sequences. We evaluated our proposed method using a data set with a wide range of anatomical diversity including healthy controls, patients with myocardial infarction and patients with cardiac myopathy. The proposed segmentation algorithm has been compared to two other, state-of-art, segmentation schemes. The results showed a consistent improvement, particularly in the segmentation of subjects with myocardial infarction for which registration-based segmentation tends to perform poorly.

Also, voxel-based techniques [Lorenzo-Valdés et al., 2004] alone did not demonstrate a robust performance without a good initialisation from LARM propagation in the group with ventricular hypertrophy. The proposed integration of registration- and voxel-based segmentation has shown the ability to achieve both robustness and accuracy. The segmentation is performed simultaneously for all images using a multi-image graph-cuts approach. The accuracy of the segmentation is significantly improved compared to previous segmentation methods by utilising both intra- and inter-image information. Finally we proposed a system that detects segmentation failures using registration and segmentation uncertainties.

Cardiac pathology is not always easily detectable in images, e.g. with the transposition of vessels, but is likely to be detected by registration and segmentation uncertainty. Since we can define uncertainty for every part of the cardiac anatomy, it is desirable to investigate if the relationship between the uncertainty and the abnormality could help to detect these pathologies automatically. Static cardiac indices, like LVM, LVV and EDV, can be extracted from cardiac segmentation results. In order to measure dynamic indices, like RWN, RWM and RMSt, cardiac

---

motion tracking techniques are needed. In next chapter, we develop a comprehensive cardiac motion tracking framework to extract motion from multiple modalities simultaneously.

# Chapter 5

## A comprehensive cardiac motion estimation framework

### 5.1 Introduction

The work in this chapter is based on the following published papers:

- Wenzhe Shi, Xiahai Zhuang, Haiyan Wang, Simon Duckett, Duy V.N. Luong, Catalina Tobon-Gomez, KaiPin Tung, Philip Edwards, Kawal Rhode, Reza Razavi, Sebastien Ourselin, Daniel Rueckert. (2012). A comprehensive cardiac motion estimation framework using both untagged and 3D tagged MR images based on non-rigid registration. *IEEE Transactions on Medical Imaging*, 31(6):1263-1275.
- Haiyan Wang, Wenzhe Shi, Xiahai Zhuang, Simon Duckett, Kai Pin Tung, Philip Edwards, Reza Razavi, Sebastien Ourselin, and Daniel Rueckert. (2011). Automatic cardiac motion tracking using both untagged and 3D tagged MR images. *Statistical Atlases and Computational Models of the Heart: Imaging and Modelling Challenges (STACOM)*, pages 45-56.
- Wenzhe Shi, Maria Murgasova, Eddie Edwards, and Daniel Rueckert. (2010). Simultaneous Reconstruction of 4-D Myocardial Motion from Both Tagged and Untagged MR

Images Using Nonrigid Image Registration. *Medical Imaging and Augmented Reality (MIAR)*, pages 98-107.

The ultimate objective of cardiac image analysis is to provide useful and efficient tools for the diagnosis and treatment of patients with CVDs. Increasing attention has been focused on the estimation of regional deformation parameters, such as regional volume output and RMSt. The analysis of such parameters has been shown to help better understand diseases such as cardiomyopathy and ischemia [Edvardsen et al., 2001, Kukulski et al., 2003] and can lead to improved methods for the treatment of patients with CVDs [Bax et al., 2004, Kuhl et al., 2004].

Myocardial tissue can be labelled by altering its magnetisation properties that remain persistent even in the presence of motion. MR tagging was first proposed by [Zerhouni et al., 1988, Axel and Dougherty, 1989b, Axel and Dougherty, 1989a] and developed as a means for non-invasive motion tracking within the myocardium of the LV. Using this imaging technology, non-invasive markers can be introduced directly into the tissue during the image acquisition process. By tracking the motion and deformation of the tag patterns, the motion of the myocardium can be reconstructed using cardiac motion tracking algorithms [Osman et al., 1999, Young, 1999, Pan et al., 2005] including non-rigid image registration [Chandrashekhara et al., 2004, Mansi et al., 2009, Bistoquet et al., 2008, Ledesma-Carbayo et al., 2005].

A common difficulty in cardiac motion tracking arises from the inevitable tag fading during the cardiac cycle. Tags which survive the fading are usually manually segmented or identified in the last frame of the sequence of tagged MR images. Another difficulty is low temporal resolution: A sufficiently large motion (e.g. larger than the tag spacing) will lead to misalignment between material points due to the lack of information between the tags. An alternative approach to track the cardiac motion using MR imaging is based on HARP [Osman et al., 1999]. However, this approach is intrinsically 2D although extensions to 3D motion tracking have been proposed [Pan et al., 2005]. The lack of sufficient longitudinal information and respiratory motion are other difficulties in the reconstruction of true 3D motion from multiple SA and a small number of LA images. With the development of 3D tagged MR imaging [Rutz et al., 2008], it is now possible to estimate radial, circumferential and longitudinal motion from a consistent 3D MR

imaging dataset.

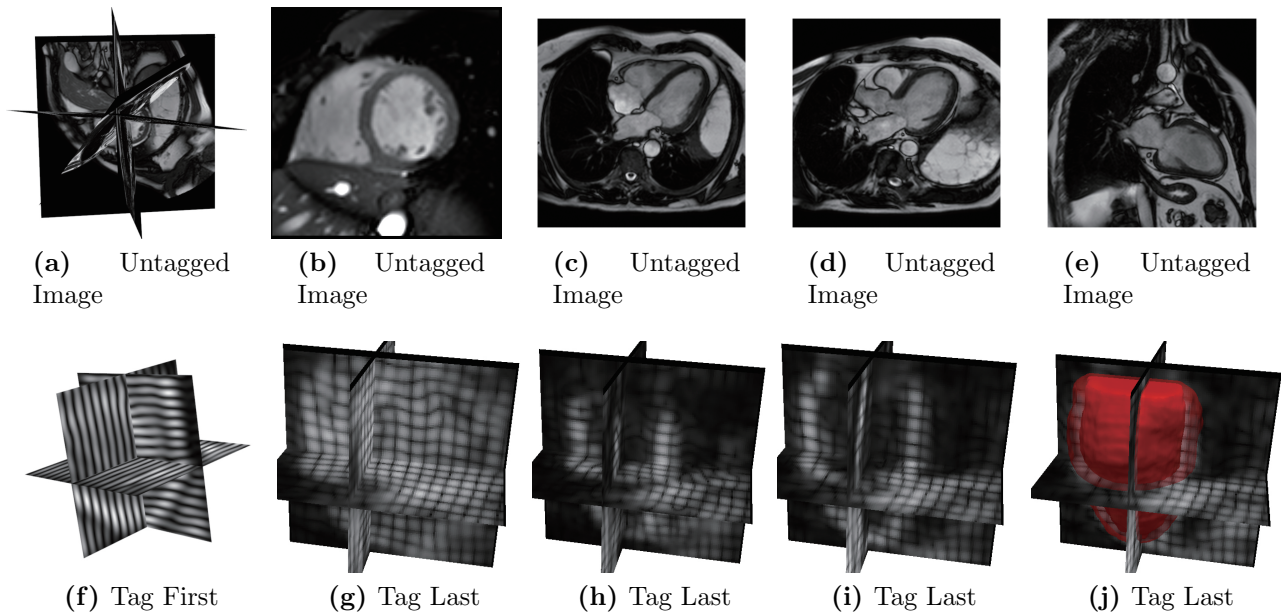


**Figure 5.1** – The figure shows (a-e) the untagged SA and LA MR images, (f) the original 3D tagged images at the  $ED_{begin}$  phase, (g-i) the average 3D tagged images extracted at respectively the  $ED_{begin}$ ,  $ES$  and  $ED_{end}$  phases and (j) the  $ED_{end}$  phase with the segmented epi- and endocardial surface.

### 5.1.1 Overview and contributions

In this chapter we propose a framework for motion tracking using both untagged and tagged MR images simultaneously. This framework is illustrated in Figure 5.1. An advantage of untagged MR images is that the cardiac anatomy, in particular the myocardium, is clearly visible and can be identified using state-of-art image segmentation algorithms [Petitjean and Dacher, 2011] including the work we developed in Chapter 4. In addition, the radial motion of the myocardium can be tracked easily in untagged MR images since the epi- and endocardial contours are clearly visible. A disadvantage of untagged MR images is that circumferential and longitudinal motion cannot be accurately quantified as there are few features inside the myocardium that can be reliably tracked and often not enough LA images available. On the other hand, 3D tagged MR images allow the easy tracking of both longitudinal and circumferential motion inside the myocardium. However, in 3D tagged MR images it is difficult to identify and quantify the cardiac anatomy as the tags obscure the anatomy. Furthermore, the tags degrade progressively

throughout the cardiac cycle. Although tag removal algorithms have been developed [Qian et al., 2007], the quality of the resulting images is not as good as conventional untagged MR images such as those obtained using bSSFP imaging sequences [Carr, 1958]. The lack of visible anatomy in the 3D tagged MR images can cause problems during the motion tracking as it is difficult to distinguish between tissue and blood in the first frame. Therefore, both types of MR images provide complementary information that can be jointly exploited.

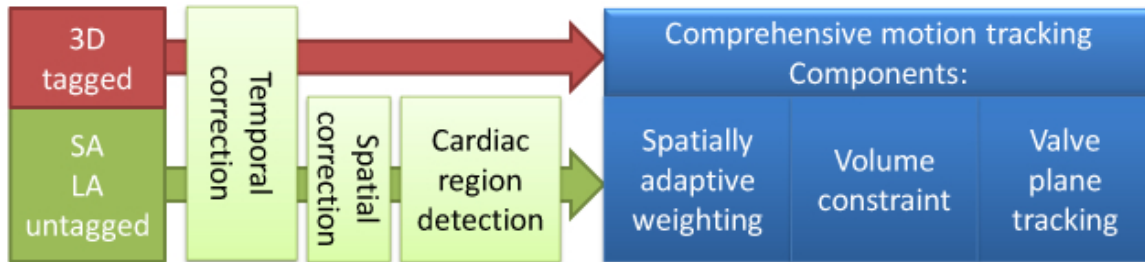


**Figure 5.2** – Workflow of the proposed comprehensive cardiac motion method.

We extend a registration algorithm that has been previously used successfully for motion tracking [Chandrashekhara et al., 2004]. In this registration-based approach the motion is reconstructed by registering a sequence of images during the cardiac cycle to a reference image at end-diastole. The proposed approach shown in Figure 5.2 uses stacks of SA and LA untagged MR cine images as well as a sequence of 3D tagged MR images. Cardiac MR images acquired within a single scanning session may have different spatial positions, due to patient movement or different respiratory positions during breath-holds, as well as different temporal resolutions. This misalignment between the different image sequences will cause inconsistencies in the simultaneous motion tracking. Thus, we have developed a spatial and temporal registration approach that maps all images to a common spatio-temporal reference space. To allow fully automated motion tracking we use a Haar-feature based object detection algorithm [Viola and Jones, 2002, Pavani et al., 2009, Zheng et al., 2007] to detect a region of interest containing the LV before motion tracking. A spatially-varying, weighted similarity measure is used for the motion tracking using image registration. This similarity measure combines information from untagged and 3D tagged images. The weighting between the different images is spatially varying and depends on the intensity gradient and segmentation of the untagged MR images: At the epicardial and endocardial boundaries (indicated by high intensity gradients in the

untagged images), the weighting favours information from the untagged MR images. Inside the myocardium (indicated by the homogenous regions of the segmentation of the untagged MR images) the weighting favours information from the 3D tagged MR images. However, even with the simultaneous use of the tagged and untagged MR images, it is hard to reconstruct the correct motion of the valve plane. We explicitly track the valve plane using a regional tracker and constrain the estimated motion to be consistent with the valve plane tracker. This leads to more accurate estimation of parameters of cardiac function such as ejection fraction.

The clinical application we focus on in this chapter are patients who undergo CRT: A significant number of these patients do not derive symptomatic benefit from the treatment or present with remodelling. Assessing global myocardial volume change such as EF and RMSt has the potential to improve patient selection. In particular, systolic dyssynchrony index (SDI) has been previously reported to be a good indicator for selecting patients who respond to CRT [Bax et al., 2004]. SDI is commonly defined as the standard deviation of the time taken to reach the minimum systolic volume or maximum function. To assess the clinical potential of the motion tracking we compare the proposed algorithm against the current clinical practice, e.g. using the TomTec 4D LV analysis tool V2.0 [Kuhl et al., 2004], for assessing EF and regional (blood) volume SDI of patients undergoing possible CRT.

The remainder of the chapter is organised as follows: Section 5.2 describes the image acquisition techniques and the data set used in this chapter. Section 5.3 explains the spatial and temporal registration between different sequences. Section 5.4 introduces details of the comprehensive motion tracking algorithm while Section 5.5 shows how the results of the motion tracking can be used to compute features relevant to cardiac function analysis. Section 5.6 evaluates the accuracy and robustness of the proposed technique. Finally, Section 5.7 presents a discussion of the results and future work.

## 5.2 Cardiac MR image acquisition

The data used in this chapter includes 12 subjects, six of which are healthy volunteers and six are CRT candidates. All subjects were scanned using a 1.5T MR scanner (Achieva, Philips Healthcare, Best, Netherlands) with a 32-element cardiac coil or a 5-element cardiac coil (for large or claustrophobic patients). Cardiac synchronisation was performed with vector electrocardiography (VECG). After localisation and a coil sensitivity reference scan, an interactive real-time scan was performed to determine the geometry of the SA, HLA and VLA views. A multiple slice SSFP scan (untagged) was performed in the SA orientation (flip angle =  $60^\circ$ , TR/TE = 2.9/1.5ms, resolution 1.45 x 1.45 x 10mm, 30 heart phases). Single slice scans were performed in LA orientations with the same spatial and temporal resolution of SA slices for HLA and VLA views. Typical SA and LA images are shown in Figure 5.1.

3D tagging was implemented using three sequentially acquired 3D data sets with line tag preparation in each of the three spatial dimensions [Rutz et al., 2008]. A respiratory navigator was used to ensure that the images are spatially aligned. 3D tagged images were acquired of the whole LV using the following parameters: tag separation = 7mm, field of view (FOV) = 108 x 108 x 108mm, echo planar imaging (EPI) factor = 7, TFE factor = 4. The voxel size for each of the three datasets is 1.00 x 1.00 x 7.71mm, where the direction of low resolution is different for each of the three acquisitions. Depending on the heart rate, cardiac phases were recorded with a temporal resolution of about 30ms with 24 to 30 phases. The temporal resolution is consistent for all three tagged image acquisitions. Several example slices from the 3D tagged images are shown in Figure 5.1. From these three different 3D tagged images a high-resolution tagged image has been created by interpolation and then averaging. This image serves as reference coordinate space and has an isotropic resolution of 1mm. This average 3D tagged image is used for temporal alignment between tagged and untagged images as well as for manual landmark tracking. An example of this average, isotropic, 3D tagged image is shown in Figure 5.4a.

### 5.3 Spatial and temporal alignment

The analysis of cardiac motion information from different images requires a common spatial and temporal reference space. However, this is a challenging task due to differences in the image acquisition for the different images. There are three major difficulties: (i) the presence of tags in 3D tagged MR images obscuring the anatomy, (ii) differences in position caused by respiratory and patient motion within sequences and across sequences and (iii) variable temporal resolution of the different image sequences. [Camara et al., 2009] presented a registration algorithm for tagged and untagged MR image sequences. This algorithm is based on phase information in order to correct the spatial misalignment between SSFP image sequences and CSPAMM image sequences, but does not include temporal misalignment. In this section, we extend this framework for the combination of information derived from untagged and 3D tagged MR image sequences which accounts for spatial misalignment as well as differences in temporal resolution.

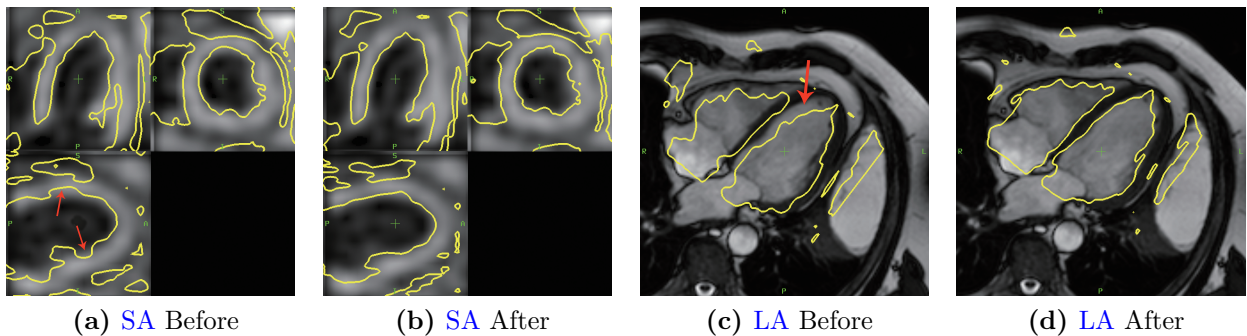


**Figure 5.3** – This figure shows the 3D tagged pseudo-anatomical image overlaid with isolines from the SA image: (a) before alignment (b) after alignment. Similarly, it shows the LA image overlap with isolines from the SA image: (c) before alignment (d) after alignment. The misalignments are highlighted by the red arrows.

#### 5.3.1 Temporal alignment

Each frame of a MR image sequence contains a DICOM meta-tag describing the trigger time. The trigger time defines how many milliseconds after the previous end-diastolic phase the acquisition of the current frame is triggered. We define  $T^s$  as the trigger time of the first phase,  $T^e$  as the trigger time of the last phase and  $N$  as the number of frames. The temporal resolution of the SA untagged MR images  $I_{SA}$  is defined as  $\Delta t = (T_{SA}^e - T_{SA}^s) / N_{SA}$ . Similarly,

the temporal resolution for each of the LA untagged MR images  $I_{4C}, I_{3C}, I_{2C}$  can be computed. Note that the temporal resolution may vary across SA and LA images. In contrast, the 3D tagged MR images  $I_{tagged}$  share the same temporal resolution. We define a common temporal resolution  $T_{ref}^s, T_{ref}^e, N_{ref}$  as follows:

$$T_{ref}^s = \max(T_{SA}^s, T_{4C}^s, T_{3C}^s, T_{2C}^s, T_{3T}^s) \quad (5.1)$$

$$T_{ref}^e = \min(T_{SA}^e, T_{4C}^e, T_{3C}^e, T_{2C}^e, T_{3T}^e) \quad (5.2)$$

$$N_{ref} = \min(N_{SA}, N_{4C}, N_{3C}, N_{2C}, N_{3T}) \quad (5.3)$$

All image sequences are resampled to this common temporal resolution using nearest neighbour interpolation. We have not used a more sophisticated interpolation scheme such as linear or spline-based interpolation since such interpolation may not yield realistic intensity values for a given voxel between two time points. For example one may introduce artificial intensity values if a voxel contains fluid in one time point and tissue in the next time point.

### 5.3.2 Spatial alignment

The 3D tagged MR images are free from respiratory motion artifacts since respiratory navigators are used during the acquisition. They contain complete 3D motion information. Thus, it is an ideal common spatial coordinate system for motion tracking. The only difficulty is the presence of tags in the images obscuring the anatomical information, which is needed to align the untagged MR images to these images. However, techniques for the removal of tags have recently been developed for CSPAMM images [Manglik et al., 2004, Qian et al., 2007]: For example, [Manglik et al., 2004] used a Gabor filter which acts as a band-pass filter with the central spatial frequency of the filter set equal to the frequency of the tags in the image. [Qian

et al., 2007] applied a 2D band-stop filter using mean shift-based clustering and principal component analysis for the same purpose.

## Removal of tags from 3D tagged MR

We have tested various techniques for tag removal [Manglik et al., 2004, Qian et al., 2007, Camara et al., 2009] on the first frame of 3D tagged images shown in Figure 5.1f. However, none of them provided satisfactory results. Compared to the CSPAMM images for which these techniques have been developed, the 3D tagged MR images used here are dominated by tag patterns and show little detail of the underlying anatomy. On the other hand, with increasing tag fading the tags in the 3D tagged images correspond to the presence of myocardium and other tissues, especially in the end-diastolic phase. One can easily extract the low frequency band by applying a Fourier transform followed by band-pass filtering and an inverse Fourier transform. We have chosen a band-pass filter that preserves the lowest 10% of the frequencies. We have performed this simple but effective approach for tag removal on all three 3D tagged images individually for all phases. After tag removal, the three *detagged* image sequences are averaged into an isotropic reference image to generate a 4D pseudo-anatomical image sequence. An example phase from this sequence is shown in Figure 5.4. The 4D pseudo-anatomical images have good contrast for the myocardium.

## Spatial registration

Images from multiple cardiac MR image sequences may be misaligned due to patient motion and different breath-hold positions during acquisition. For SA untagged MR images this misalignment can also occur between slices [Camara et al., 2009, Chandler et al., 2006] as Figure 5.3 demonstrates. We can correct these artifacts by registering the untagged MR images to the 4D pseudo-anatomical image. The 4D tagged pseudo-anatomical image after tag removal provides good spatial resolution ( $1 \times 1 \times 1mm$ ) for accurate slice-to-volume registration with the SA and LA untagged MR images.

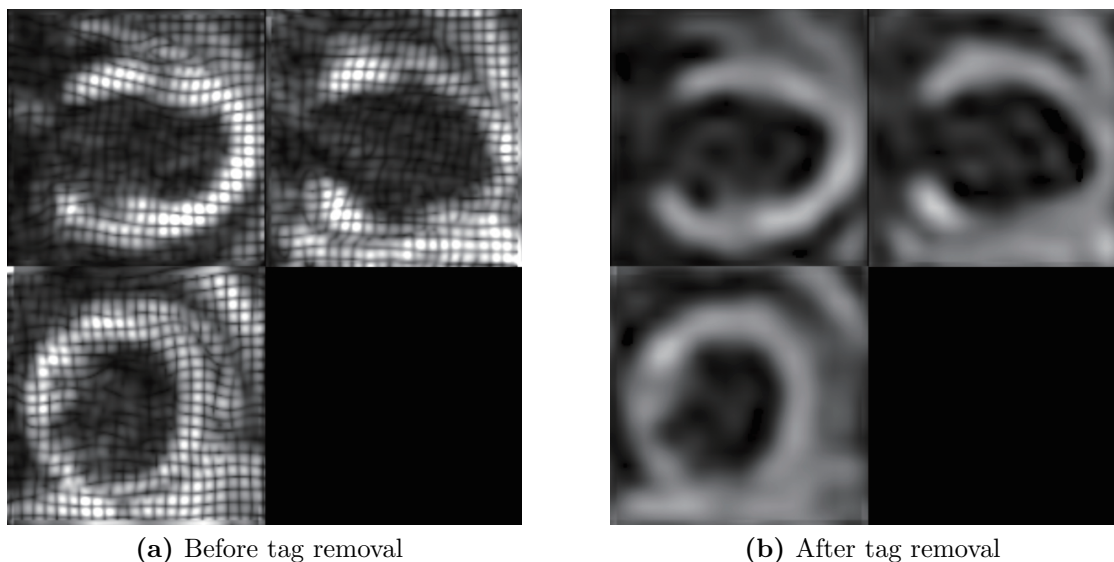


**Figure 5.4** – This figure shows (a) an average image of three 3D tagged images and (b) an average image of three 3D images after tag removal (this is referred to as 3D pseudo-anatomical image in the text).

We register all available SA and LA untagged cine MR image to the 4D pseudo-anatomical MR image using rigid registration with an extension of the work in [Chandler et al., 2006]: The registration transformation is modelled as a 3D rigid transformation between the untagged cine image sequence and the pseudo-anatomical image sequence. Additionally, a 2D in-plane rigid transformation is used for every cine slice to allow for misregistration between slices as the result of different breath-hold positions. The registration is optimised between 4D images to fully utilise the temporal information. The similarity metric function is defined as a weighted combination of the similarity between the untagged cine and the 4D pseudo-anatomical MR image and the similarity between LA and SA slices over time. We choose NMI as the similarity measure to deal with the difference between modalities. The weighting is defined by the number of voxels in the similarity metric. As a result, both inter- and intra-sequence misalignments are corrected and all images are transformed into the same common spatial temporal coordinate system. Non-rigid deformation of the heart due to breathing motion [Shechter et al., 2004] is not modelled in this spatial registration step as the limited anatomical information from the 4D pseudo-anatomical MR images makes it not feasible to introduce more flexibility into the transformation model. Figure 5.3 shows some example images before and after correction.

## 5.4 Comprehensive motion tracking

During the cardiac cycle, the LV undergoes a number of different deformations including circumferential, radial and longitudinal motion. While the 3D tagged MR images provide good information about all aspects of the motion, the SA images may provide more information of radial motion and the LA images may provide some extra information about the radial and longitudinal motion. Thus, to fully reconstruct the deformation field within the myocardium, we propose to acquire multi-slice SA, LA images as well as 3D tagged images of the LV.

Consider a material point in the myocardium at a position  $\mathbf{p}_{myo} = (x, y, z)^T$  at time  $t_0 = 0$  that moves to another position  $\mathbf{p}'_{myo} = (x', y', z')^T$  at time  $t_i = i\Delta t$  where  $\Delta t$  is the time interval between two consecutive phases and  $i$  corresponds to the time frame. The goal of the motion tracking is to find the transformation  $\mathbf{T}$  for all time phases  $i$  such that:

$$\mathbf{T}(\mathbf{p}_{myo}, t_i) = \mathbf{p}'_{myo} \quad (5.4)$$

We represent  $\mathbf{T}$  using a series of free-form deformations [Rueckert et al., 1999] as described in [Chandrashekhara et al., 2004]. An overview of the tracking algorithm is given in the following section.

### 5.4.1 Overview

The estimation of the deformation field  $\mathbf{T}$  proceeds in a sequence of steps: We first detect the region of interest containing the heart in the SA image using an object detector similar to the one proposed in [Viola and Jones, 2002] as described in the previous chapter (see Section 4.2.1). Within the bounding box, we automatically segment the myocardium of the LV at the ED phase of the untagged MR images. Various automatic segmentation tools exist [Huang et al., 2010, Rouchdy et al., 2007, Zhuang et al., 2010, Boykov and Kolmogorov, 2003] but here we have used a probabilistic atlas-based segmentation technique developed in the previous chapter (see Section. 4.2.4) to segment the untagged images. After this a gradient detector

is used to highlight the epicardial and endocardial contours. The information from both the segmentation and the gradient detector is combined into a spatially varying weighting function which moderates the influence of the tagged and untagged images during the motion tracking.

During the motion tracking we register the images taken at time  $t_1$  to the reference image at time  $t_0$  and obtain a transformation representing the motion of the myocardium at time  $t_1$  using a hierarchical B-spline transformation model and gradient descent optimisation method [Rueckert et al., 1999]. We use the resulting transformation as an input for the next time frame and continue this process until all the time frames in the sequence are registered to the first phase [Chandrashekhara et al., 2004]. The algorithm allows us to relate any point in the myocardium at time  $t_0$  to its corresponding position throughout the sequence. The cost function which is minimised during the registration can be defined as a weighted combination of four different terms including an image similarity term  $C_i$ , a smoothness term  $C_s$  based on bending energy [Rueckert et al., 1999], a valve plane tracking term  $C_v$  and a volume preservation term  $C_r$ :

$$C = C_i + \lambda C_s + \lambda_v C_v + \lambda_r C_r \quad (5.5)$$

In the following each of the steps and components mentioned above are described in detail.

### 5.4.2 Automatic detection and segmentation of the heart

The basic idea of this approach is to train a cascade of classifiers based on Haar features that is capable of detecting anatomical structures in medical images [Viola and Jones, 2002, Pavani et al., 2009, Zheng et al., 2007]. The classifier is then used to test the hypothesis whether a given region of interest contains the chambers of the heart. This approach has already been used in the previous chapter (Chapter 4) to identify the ROI containing the heart.

To train the classifier, we manually identified a bounding box around the location of the heart in SA MR images. From these images, positive examples are generated for every slice, excluding the basal and apical slices. Negative examples are generated by randomly sampling the images in such a way that each example either contains no cardiac anatomy or only parts of the

cardiac anatomy. To improve the robustness of the object detection [Viola and Jones, 2002] we have modified the approach for the detection of the heart in cardiac MR images. The details are presented in Section 4.2.1. After the heart is located we use the probabilistic atlas-based segmentation technique developed in the previous chapter (Chapter 4) to segment the untagged images. This segmentation technique uses a local affine registration and multiple component EM estimation to deal with possible pathology. The entire process takes roughly 15 minutes to segment one dataset on a standard dual-core laptop.

### 5.4.3 Weighted similarity measure for motion tracking

To exploit the complementary nature of the tagged and untagged MR images we have developed a spatially adaptive weighting function that accounts for the different types of information available: The 3D tagged MR images characterise well the motion inside the myocardium while the untagged SA and LA images characterise the motion well at the epi- and endocardial borders of the myocardium. Outside the myocardium are the blood pool or the lungs, neither of which contains any useful information for cardiac motion tracking apart from the papillary muscles. Thus, we would like to generate a weighting function that (a) is zero outside the myocardial region, (b) maximises the weighting of the tagged images within the myocardium and (c) increases the influence of the untagged images at the myocardial border. The spatial weights for the tagged and untagged images are only generated for the reference image used for the registration. In our case this is the end-diastolic phase.

The weighting for the untagged images,  $W^u(\mathbf{p})$ , is generated by multiplying the gradient of the probabilistic myocardium segmentation with the gradient of the image intensity. This will give high weight to those locations where both gradients are high which indicates a possible presence of the myocardium boundaries. In contrast it will give low weight to regions in which either gradient is low. Let  $S$  denote the segmentation of the untagged MR image  $I$ . This segmentation assigns a label  $\Lambda = \{L_{bg}, L_{myo}, L_{blood}\}$  to every voxel. A probability for the myocardium  $P(\mathbf{p}, L_{myo})$  can be derived from the multiple component EM segmentation [Shi et al., 2011]. The weights for the untagged MR image are defined as

$$W^u(\mathbf{p}) = \frac{\|\nabla I_\sigma(\mathbf{p})\| \cdot \|\nabla P_\sigma(\mathbf{p}, L_{myo})\|}{\max_{\mathbf{p} \in I} (\|\nabla I_\sigma(\mathbf{p})\| \cdot \|\nabla P_\sigma(\mathbf{p}, L_{myo})\|)} \quad (5.6)$$

where  $\|\nabla I_\sigma(\mathbf{p})\|$  and  $\|\nabla P_\sigma(\mathbf{p}, L_{myo})\|$  are the gradient of intensity and the gradient of myocardium probability at location  $\mathbf{p}$  after convolution with a Gaussian kernel  $G$  with standard deviation  $\sigma = 10mm$  respectively.

The weights for the 3D tagged image are defined as

$$W^t(\mathbf{p}) = \begin{cases} 1 - W^u(\mathbf{p}) & \text{if } L(\mathbf{p}) = L_{myo} \\ 0 & \text{otherwise} \end{cases} \quad (5.7)$$

An example of the resulting, spatially varying weight maps is shown in Figure 5.5. Given a weight map, we define the similarity between two images  $I_A, I_B$  as the weighted normalised cross-correlation between the image intensities:

$$S(I_A, I_B, W, \mathbf{T}) = \frac{\sum_{\mathbf{p} \in I_A} W(\mathbf{p})(I_A(\mathbf{p}) - \mu_A)(I_B(\mathbf{T}(\mathbf{p})) - \mu_B)}{\sqrt{\sum_{\mathbf{p} \in I_A} W^2(\mathbf{p})(I_A(\mathbf{p}) - \mu_A)^2(I_B(\mathbf{T}(\mathbf{p})) - \mu_B)^2}} \quad (5.8)$$

Here  $\mu_A$  and  $\mu_B$  denote the weighted average intensities in image  $I_A$  and  $I_B$  respectively. This means that those voxels that have a low weighting contribute little to the similarity metric and thus do not influence the registration. For simultaneous registration of the untagged and 3D tagged images, the correlation is computed separately across the tagged images and untagged images and combined into a single similarity measure:

$$\begin{aligned}
C_i = & \left\{ \sum_{s \in T} |\Omega_s| [S(I_{t_0}^{t,s}, I_{t_i}^{t,s}, W^{t,s}, \mathbf{T})] \right. \\
& + \sum_{s \in U} |\Omega_s| [S(I_{t_0}^{u,s}, I_{t_i}^{u,s}, W^{u,s}, \mathbf{T})] \left. \right\} \\
& / \sum_{s \in U, T} |\Omega_s|
\end{aligned} \tag{5.9}$$

Here  $|\Omega_s|$  denote the sum of weights in the image  $I^s$  and  $s$  is the index of the image. Note that the similarity measure takes into account that different images have usually a different number of voxels and therefore the similarity measures must be weighted accordingly.

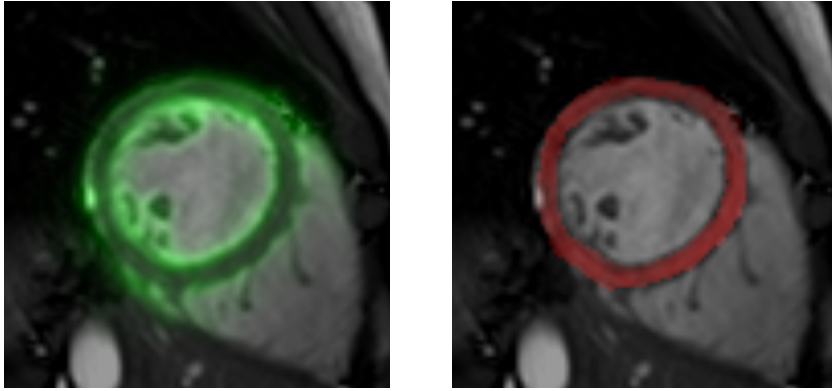


**Figure 5.5** – This figure shows a SA MR image. The colour overlay shows the weight map. Red and green colours indicate the weight for tagged images and untagged images respectively. The transparency of the colour indicates the magnitude of weight.

#### 5.4.4 Valve plane tracking

The mitral valve plane is an important landmark for accurate cardiac motion estimation but difficult to extract from tagged or untagged SA images based on intensity information alone. By tracking the valve end points in the long-axis views we are able to reconstruct the valve plane motion and can incorporate information about the tracking of the valve plane as a boundary condition into the motion tracking. We constrain the registration with tracked valve plane using the following term:

$$C_v = - \frac{\sum_{\mathbf{p} \in V_{t_0}} D(\mathbf{T}(\mathbf{p}), V_{t_i})}{|V_{t_0}|} \tag{5.10}$$

Here  $V_{t_i}$  denotes the reconstructed valve plane surface at time  $t_i$  and  $D$  is the surface distance operator. The surface distance operator  $D(\mathbf{p}, S)$  computes the distance between point  $\mathbf{p}$  and the closest point on the surface  $S$  in millimetres.

An overview of the tracking of the valve annulus is described below: For each untagged LA image, we first detect the two end-points of the valve at the ED phase using a Haar feature based cascade classifier [Pavani et al., 2009, Zheng et al., 2007] as well as a-priori knowledge about the position of the valve points. As illustrated in Figure 5.6b, the line of the intersection between the middle slice of the SA and HLA views as well as the line of the intersection between the HLA and VLA views meet at point  $O$ . This point is used as anchor point for the valve plane detection and can be seen as the origin of the heart- or patient-centric coordinate system. A bounding box can be generated relative to the point  $O$  indicating the likely location of the valve plane. A Gaussian mixture model is applied to classify the voxels in the LA images into air, soft tissue or blood. Only those voxels labelled as soft tissue are considered as candidate valve points.

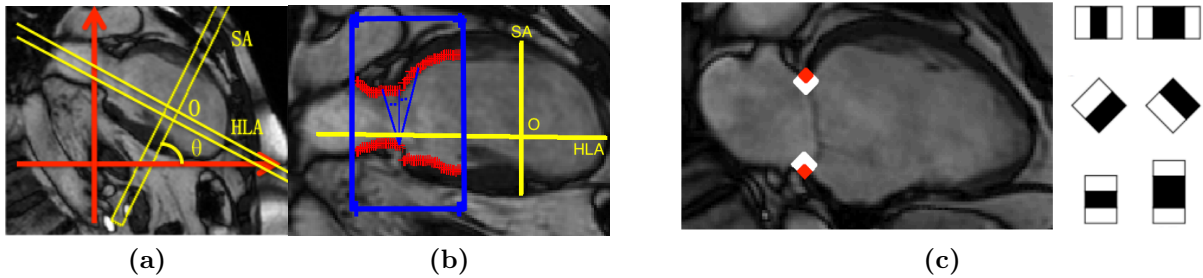


**Figure 5.6** – Automatic detection of valve points: (a) A LA view of the heart showing the orientation of the SA view and other LA views. (b) An example of the bounding box that contains possible candidate pairs for the valve plane. (c) Some of the Haar-like features used for detection of the valve plane points.

For each candidate valve point  $\mathbf{p}_i$  its normalised distance to the border of the bounding box can be used to model the likelihood for a valve point at this location. In addition, the SA view is usually planned at  $90^\circ$  relative to the LA view of the LV that intersects the apex and the centre of the mitral valve plane. Therefore, SA plane and LA plane intersect in a straight line that is perpendicular to the LA of the LV. The angle  $\theta$  between this intersection line and x-axis, as demonstrated in Figure 5.6a, determines the orientation of the LA. Ideally, if a

point  $\mathbf{p}_i$  is a valve plane point, then a second valve point  $\mathbf{q}_i$  should be present in the direction perpendicular to the LA direction. Thus, the valve plane can be found by detecting a pair of points  $\{\mathbf{p}_i, \mathbf{q}_i\}$ . No dedicated feature extraction is needed for the orientation estimation, thus reducing the computational complexity significantly. However, in practice, due the fact that the valve annulus deforms and that the scan planes may not be planned in the ideal orientation, the correct orientation of the valve plane may sometimes differ by a small angle  $\theta$ . We therefore test every point  $\mathbf{p}_i$  with every point in the neighbourhood of  $\mathbf{q}_j$  so that the set of candidate valve-planes points is  $\{\mathbf{p}_i, \mathbf{q}_j | \forall i, j = i + k\}$  where  $k$  is a predefined distance. Then these pairs of points are ranked by the likelihood tested from the Adaboost [Freund and Schapire, 1995] classification.

Most clinical cardiac MR acquisitions include multiple LA views such as HLA, VLA and 3CH views. All three views can provide useful complementary information. We therefore construct three different detectors for the three LA views to detect a pair of valve points at each view. Two layers of Adaboost [Freund and Schapire, 1995] are cascaded for each detector to avoid the training to be biased by negative samples, of which there are about 10 times more than positive samples. As different feature sets are used for the two layers, the hypotheses from the first layer are maintained to be combined with the result from the second layer. The classifier is trained on 30 patients and 10 healthy cases, for which the valve points were manually marked by clinician.

The motion of the valve annulus can then be estimated by tracking template patches around the detected end-points of the valve. To maintain robustness we track the valve points simultaneously in three LA views. When the accuracy of the tracking is reduced by noise or sudden motion in one view, the tracking in other views may be less affected and hence produces good overall performance. Initially, the positions of the valve end points are aligned along the LA across three LA planes at the ED phase and this alignment is maintained throughout the tracking. We define two regions encompassing the valve end points in each LA view and evaluate the similarity between images by cross-correlation. We reconstruct the mitral valve plane from the tracked valve end-points via triangulation.

### 5.4.5 Adaptive incompressibility for motion tracking

Several authors have proposed incompressibility constraints for the motion tracking of the myocardium [Rohlfing and Maurer, 2001, De Craene et al., 2010] to reflect the fact that the myocardium is largely incompressible while deforming. Such a constraint can be easily integrated into the registration framework by adding a penalty term based on the determinant of the Jacobian of the deformation [Rohlfing et al., 2003]. However, the question is whether this constraint should be evenly applied in space. Partial volume voxels exist at the interface between different tissue classes. We can determine the likelihood of myocardium of a given point  $P(\mathbf{p}, L_{myo})$  from the multiple component EM segmentation developed in the previous chapter. We formulate the incompressibility constraint using the following equation based on [Rohlfing et al., 2003]:

$$C_r = \sum_{\Omega_{SA}} \omega_{\mathbf{p}} E_{Jacobian}(\mathbf{p}, \mathbf{T}) \quad (5.11)$$

In this equation,  $\Omega_{SA}$  denotes the domain of untagged SA image and the Jacobian penalty term is defined as

$$E_{Jacobian}(\mathbf{p}, \mathbf{T}) = |\log(\mathbf{J}_{\mathbf{T}}(\mathbf{p}))| \quad (5.12)$$

This penalises any volume change of the transformation  $\mathbf{T}$ . The penalty term is weighted according to the likelihood of a voxel containing myocardium:

$$\omega_{\mathbf{p}} = \frac{\lambda^j}{|\log(P(\mathbf{p}, L_{myo}))| + \epsilon} \quad (5.13)$$

Here  $\epsilon$  is a small constant term,  $\lambda$  is set to 0.5 in our experiment and  $j$  denotes the iteration during the optimisation.  $j$  is introduced in the equation to allow more flexible deformation at the beginning and avoid the local minimum.

During the motion tracking the cost function is optimised using a gradient-descent optimisation as proposed in [Rueckert et al., 1999]. In the context of this optimisation this means that the volume preservation term depends on the current iteration in the optimisation. Such

an adaptive volume preservation constraint has several advantages: Firstly, it assigns higher weights to the constraint of voxels likely to be myocardium and lower weights on voxels outside the myocardium. Secondly, it overcomes one of the disadvantages of the incompressibility constraint, namely its tendency to not deform away from the initial configuration as this violates the incompressibility constraint. This means that the initial configuration often corresponds to a degenerate local minimum of the cost function. Progressively increasing the weight for the incompressibility constraint during the optimisation to avoid local minima was originally proposed and tested in [Rohlfing et al., 2003]. This allows the initial deformation to be driven by the similarity measure only and enforces the incompressibility constraint later during the optimisation. This approach can deal better with large deformations as they occur in the myocardium.

## 5.5 Motion tracking in patients undergoing cardiac resynchronisation therapy

In order to analyse cardiac motion in patients undergoing cardiac resynchronisation therapy, **SDI** is calculated from those cardiac phases in which the maximum of regional function (volume output, strain) is reached. For each of the 16 segments of the left ventricular myocardium model according to **American heart association (AHA)** model [Cerqueira et al., 2002] the phase to reach maximum regional function is recorded. From the 16 phases, the **SDI** is then defined as the standard deviation of these phases, with a high **SDI** indicating more dyssynchrony [Jaochim Nesser et al., 2007]. To allow comparison between patients with different heart rates, **SDI** is usually expressed as a percentage of the cardiac cycle, which can be determined from the temporal resolution of the image sequences. For **SDI** from regional volume and motion analysis, those segments whose output/strain magnitudes are less than 5% of the maximum function of other segments are excluded.

### 5.5.1 Parcellation of the myocardium

For each subject, we define the 16 standard segments of the left ventricular myocardium according to the AHA model [Cerqueira et al., 2002]. This is done by fitting a pre-constructed myocardium model with 16 segments to the automatically segmented myocardium [Shi et al., 2011] using non-rigid image registration [Rueckert et al., 1999]. This provides a 16 segment parcellation of the myocardium at the end-systolic phase for each subject. From this patient-specific model we can generate a 16 segment endocardial surface for regional SDI analysis of LV volume. An example of this is shown in Figure 5.7.

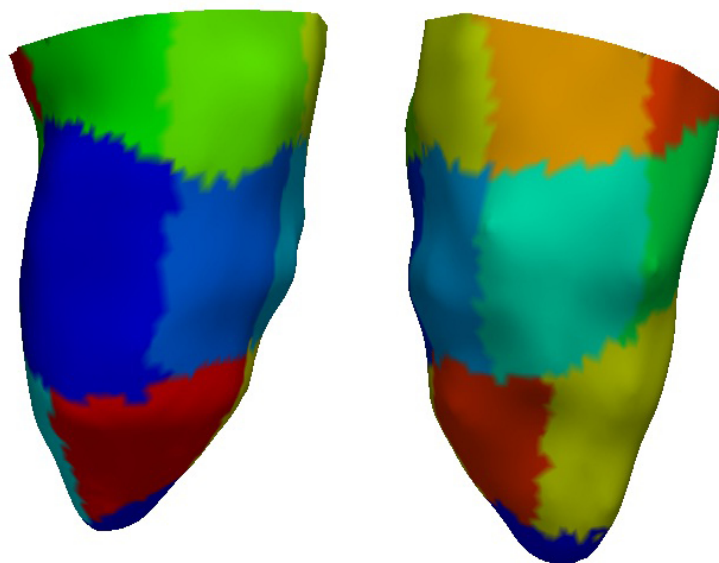


Figure 5.7 – The parcellation of the endocardial surface into 16 segments.

### 5.5.2 Regional SDI analysis

From the 16 segment endocardial surface model, we define the LA of the LV as the line between the centre of the apical segments to the centre of the basal segments. We propagate the surface using the obtained motion fields and evaluate the regional LV (blood) volume for each time frame. The regional volume SDI is calculated from the time frame in which the minimum volume is reached for each of the 16 segments.

In addition, the regional strain SDI is calculated in a similar fashion: From the 16 segment

myocardial parcellation, the strain of each voxel is averaged over every segment. We here use the Lagrangian strain tensor [Ogden, 1997] which is defined as  $\mathbf{E} = \mathbf{J}^t \mathbf{J} - \mathbf{I}$  where  $\mathbf{J}$  denotes the Jacobian matrix of the transformation and  $\mathbf{I}$  the identity tensor. The strain tensor describes the strain along any direction. Strain can then be calculated in the longitudinal, radial and circumferential directions defined in the cardiac coordinate system [Elen et al., 2008]: Longitudinal strain  $\mathbf{E}_l = \mathbf{L}^t \cdot \mathbf{E} \cdot \mathbf{L}$ , radial strain  $\mathbf{E}_r = \mathbf{R}^t \cdot \mathbf{E} \cdot \mathbf{R}$  and circumferential strain  $\mathbf{E}_c = \mathbf{C}^t \cdot \mathbf{E} \cdot \mathbf{C}$ .

## 5.6 Evaluation

In our experiments we have used images from 12 subjects, of which six are CRT candidates and six are normal volunteers. Details describing the data used can be found in Section 5.2.

To evaluate the tracking accuracy within the myocardium we have manually tracked 16 landmarks in 3D in each dataset. These landmarks correspond to intersections of the tag lines in the tagged images. We select one landmark close to the centre of each AHA segment excluding the apex. The landmarks are tracked backwards from the last frame to the first frame of the sequence. This avoids situations in which unpredictable tag fading and degrading makes tag tracking impossible. We manually identify the landmarks on the 3D tagged images (see Figure 5.4a for an example) and we then refine the position of the landmarks by applying a centre-of-gravity operator using a window size of 4. The centre of gravity of a region of voxels is defined as the average of their positions, weighted by their intensity. This allows not only for sub-voxel accuracy but also reduces inter- and intra-subject variability. Examples of how the landmarks are selected and the landmark positions are illustrated in Figure 5.11.

Since we are not able to track landmarks near endo- and epicardial borders reliably due to tag fading the accuracy of the tracking near the endo- and epicardial surfaces is assessed by computing the distance between the propagated surfaces and their manually segmented counterparts in each frame. For this we have manually segmented both the end-diastolic myocardium and the end-systolic myocardium for both SA and LA MR images. We extract

**Table 5.1** – Inter-observer variance of the relative error for the surface tracking of the endo- (ED) and epicardial (EP) contours for the different SA and LA views. The error is given as mean and standard deviation

	SA	2CH	4CH
EP	4.3% $\pm$ 1.2%	3.4% $\pm$ 0.6%	3.5% $\pm$ 1.8%
ED	7.1% $\pm$ 2.1%	4.3% $\pm$ 1.4%	3.9% $\pm$ 0.8%

smooth endo- and epicardial surfaces and contours from segmentations using shape based interpolation [Grevera and Udupa, 2002] and marching cubes [Lorensen and Cline, 1987].

In addition, we have analysed the relative inter-observer variability of the landmark tracking on a subset of three datasets (one patient and two normal subjects). Since the intrinsic motion patterns of patients and normal volunteers may be different we use the relative tracking error  $\rho$  which is defined as:

$$\rho = \frac{\|\mathbf{P}_{manual} - \mathbf{P}_{tracked}\|}{|d_{maximum}^{\mathbf{P}}|} \quad (5.14)$$

where  $\mathbf{p}$  is a point in 3D, and  $d^{\mathbf{p}}$  denotes the true displacement of  $\mathbf{p}$ . For surfaces the relative error is defined in terms of the distance between closest vertices on the surfaces.

The relative inter-observer landmark tracking error is  $7.8\% \pm 4.4\%$ . The results of relative inter-observer surface tracking error are shown in Table 5.1. In general, it is more difficult to identify the endocardial surface than the epicardial surface. This is reflected by the relative inter-observer variance and the relative errors in Figures 5.8 to 5.10 as the error for the endocardial surface tracking is always higher than the error for the epicardial surface tracking.

### 5.6.1 Accuracy results

To assess the quality of the motion tracking inside myocardium we compare the position of the manually tracked landmarks with the landmark position predicted by the proposed motion tracking algorithm. We have evaluated six different strategies for the myocardial

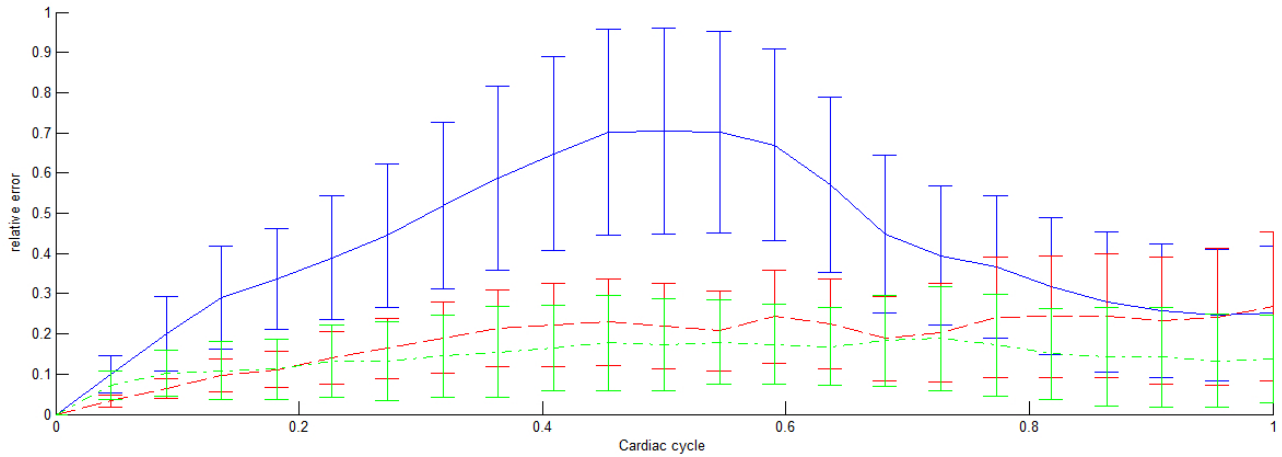


**Figure 5.8** – This figure shows the relative landmark error in % when comparing the results of manual tag tracking with the registration-based motion tracking. The lines correspond to the mean while the bars indicate the variance. The blue solid line indicates the results using untagged images only, the red dash line shows the results using 3D tagged images only and the green dash-dot line shows the results using the combined motion tracking using both the tagged and untagged MR images.

motion estimation: (a) using untagged images only, (b) using tagged images only, (c) combined tagged and untagged images without constraints, (d) combined tagged and untagged images with valve plane constraint, (e) combined tagged and untagged images with incompressibility constraint and (f) combined tagged and untagged images with all constraints. All methods use a bending energy constraint described in [Rueckert et al., 1999] to enforce smoothness of the transformation with a  $\lambda = 0.000001$ . In our experiment  $\lambda_v$  and  $\lambda_r$  are set to 0.02 and 0.8 respectively. The control point grid spacing of the FFDs has three levels starting from 40mm to 10mm and a corresponding image resolution from 4mm to 1mm. The maximum number of iterations of each step is 40. The relative error between the manually and automatically tracked landmarks (eq. 5.14) using all different approaches is shown in Figure 5.8 and Figure 5.9. The average maximum displacement for patients and volunteers is shown in Table 5.2.

The results indicate that the combined registration using tagged and untagged images performs better than the registration using either tagged or untagged images alone. The error of the motion tracking using tagged images only increases over the cardiac cycle and reliable tag tracking was achieved only in the first phases of the image sequences. This poor performance primarily comes from tag fading and degrading which introduces noise into the registration and makes tracking of large deformations difficult. Since the temporal resolution of the 3D tagged

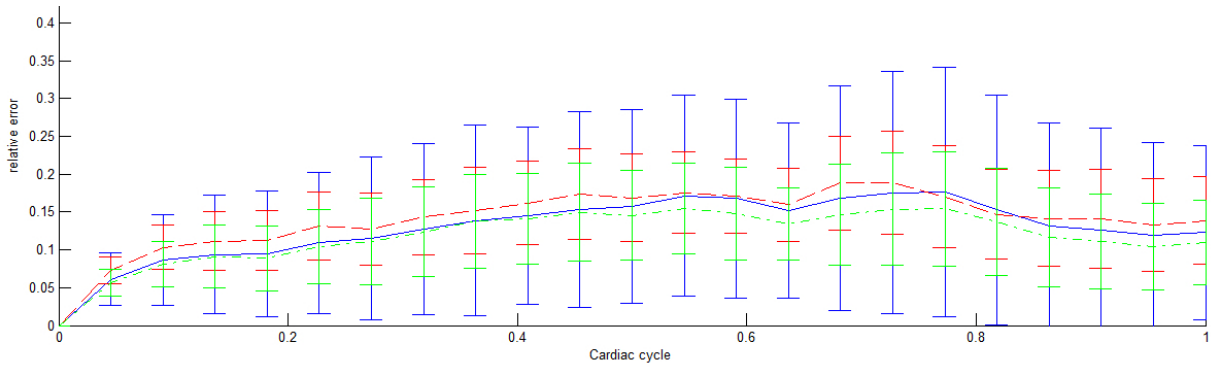


**Figure 5.9** – This figure shows the relative landmark error in % when comparing the results of manual tag tracking with registration-based motion tracking. All methods are based on the combined motion tracking. The blue solid line indicates the results using valve plane constraint, the red dash line shows the results using incompressibility constraint and the green dash-dot line shows the results using the comprehensive motion tracking with both constraints.

MR images is usually lower than that of the untagged MR images, the myocardial motion may include areas in which there is large motion between two consecutive time frames. If there is a sufficiently large motion between two time points, the motion tracking algorithm may confuse one tag line with another tag line unless anatomical information is used. This type of error is often cumulative. The motion tracking using untagged images is not expected to perform well in this evaluation due to lack of motion information within the myocardium. Nevertheless, the results show that the motion tracking using untagged images is able to limit the magnitude of the errors. This is probably due to accurate and consistent estimation of radial motion over the cardiac cycle. The primary source of error in this case comes from the underestimation of the longitudinal and circumferential motion which does not accumulate over time. Combining tagged and untagged images clearly improves the performance. The incompressibility constraint helps to constrain the distribution of the error by providing a volume preservation force but tends to underestimate the motion. Moreover, the valve plane tracking helps the longitudinal motion estimation so the error is reduced. Overall, the comprehensive motion tracking method performs best.

A realistic estimation of cardiac motion should include radial, circumferential and longitudinal motion. An accurate tracking of the endocardial and epicardial boundaries on untagged MR images indicates good radial and longitudinal motion estimation. Thus we compare the difference between the propagated surfaces and the manual surfaces using the relative surface

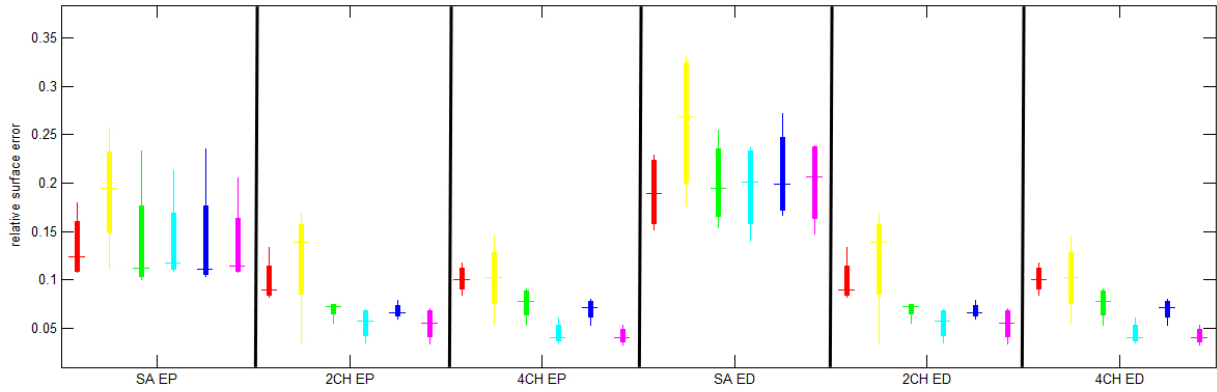


**Figure 5.10** – This figure shows the relative surface distance when comparing the result of an end-systolic segmentation (propagated from the end-diastolic time point) with a manual end-systolic segmentation. Red indicates the results using untagged images, yellow indicates the results using tagged images, green shows the results of the combined motion tracking, cyan shows the results using the valve plane constraint based on the combined motion tracking, blue indicates the results using the incompressibility constraint based on the combined motion tracking and magenta shows the results of the proposed comprehensive method. Results are shown for the endocardial surface (ED) and the epicardial surface (EP).

**Table 5.2** – Average maximum displacement (based on manual tracking) for patients and volunteers.

	Landmarks	Endocardial surface	Epicardial surface
Patients	5.3 mm	4.1 mm	2.4 mm
Volunteers	10.2 mm	8.6 mm	5.7 mm

error defined in eq. (5.14). From Figure 5.10 it can be seen that the combined motion tracking using tagged and untagged images outperforms the motion tracking using tagged images alone on every occasion. The motion tracking using tagged images alone performed poorly since tag fading makes it extremely difficult to track the myocardial boundaries accurately. Moreover, the combined motion tracking performs much better than using motion tracking in untagged images only on epicardial LA contours. This is due to the limited number of slices in the SA MR images and the low number of LA MR images in typical clinical acquisitions. The longitudinal motion information within the myocardium derived from the tagged images helps to estimate longitudinal motion more accurately. In addition, the valve plane constraint improves tracking of the contours in the LA views. The incompressibility constraint does not yield a significant improvement alone compared to the combined method. The median error of healthy controls over all frames is 1.44mm for landmark tracking, 1.04mm for endocardial surface tracking and

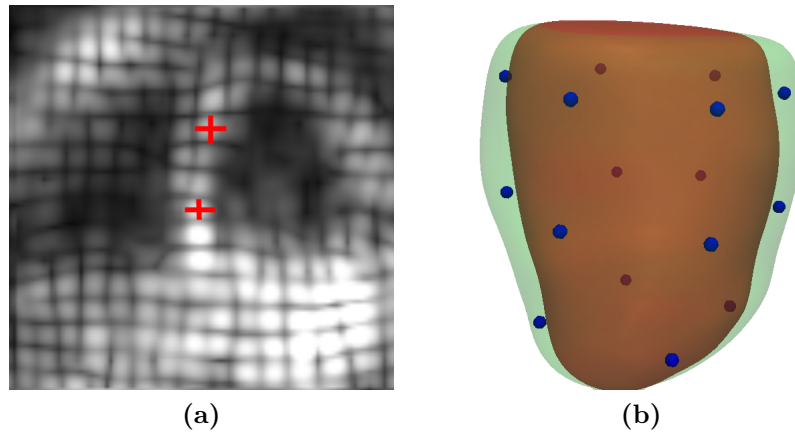


**Figure 5.11** – This figure shows the manual landmark identification and distribution of the landmarks.

0.76mm for epicardial surface tracking using the comprehensive method, compared to the voxel size 1.45mm for the untagged images and 1mm for the 3D tagged images.

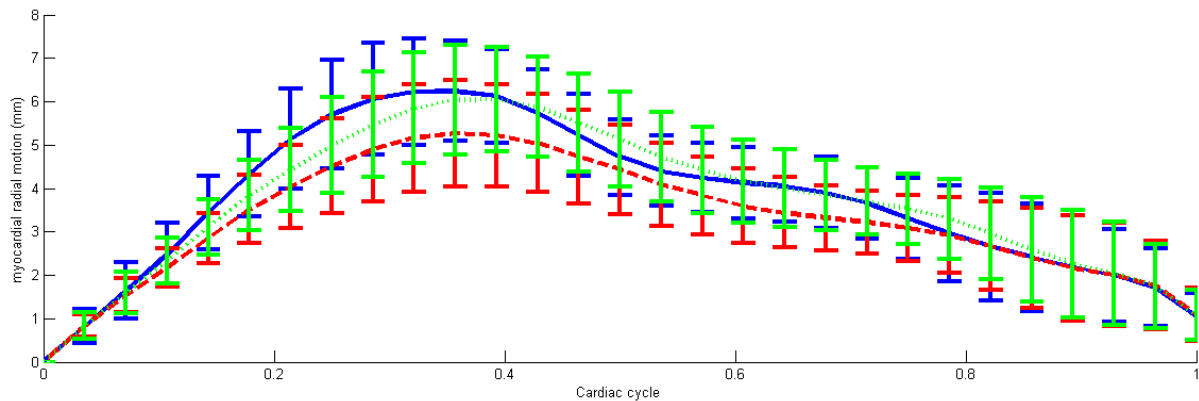


**Figure 5.12** – This figure shows the mean and standard deviation of the radial motion of all [AHA](#) segments estimated from different methods. The blue solid line indicates the results using untagged images only, the red dash line shows the results using 3D tagged images only and the green dash-dot line shows the results using the combined motion tracking using the proposed comprehensive method.

It should be pointed out that both evaluation metrics used here are biased due to different reasons: One reason for this bias is that the ground truth is obtained from either the tagged image or the untagged image. Another reason is that potential small misalignment between untagged and tagged images exists even after spatial alignment. Thus the relative landmark error is biased toward tagged only method and the relative surface error is biased towards untagged only method. However, the comprehensive method performed best in both evaluations and neither of the evaluations is biased towards the comprehensive motion tracking method.

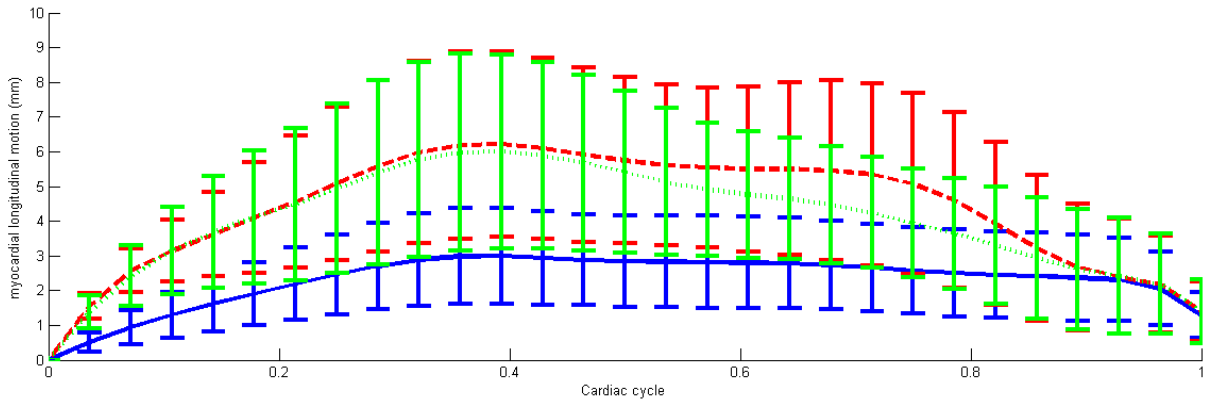


**Figure 5.13** – This figure shows the mean and standard deviation of the longitudinal motion of all **AHA** segments estimated from different methods. The blue solid line indicates the results using untagged images only, the red dash line shows the results using 3D tagged images only and the green dash-dot line shows the results using the combined motion tracking using the proposed comprehensive method.

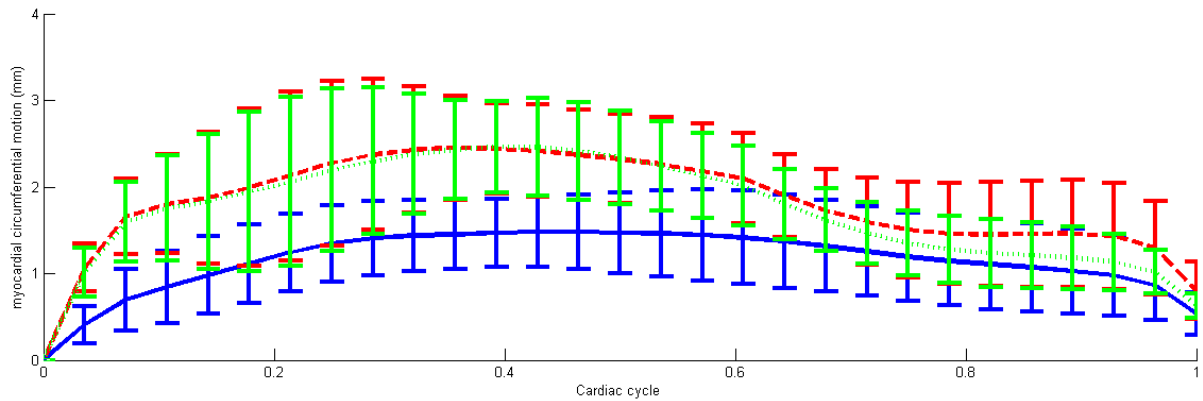


**Figure 5.14** – This figure shows the mean and standard deviation of the circumferential motion of all **AHA** segments estimated from different methods. The blue solid line indicates the results using untagged images only, the red dash line shows the results using 3D tagged images only and the green dash-dot line shows the results using the combined motion tracking using the proposed comprehensive method.

Furthermore we can observe from Figure 5.16 that the proposed motion tracking estimates radial, circumferential and longitudinal motion well.

Radial, longitudinal and circumferential motion are calculated from six normal volunteers. The mean and standard deviation of these motions from all **AHA** segmented are plotted throughout the cardiac cycle to assess the performance of different algorithms. Figure 5.12 shows the results of the radial motion where the underestimation can be observed from the tagged only method. Figure 5.13 shows the results of the longitudinal motion where the underestimation can be observed from the untagged only method. It is also noticeable that the variance between

**Table 5.3** – Change of myocardial mass computed using the different motion tracking methods. The algorithms are untagged only, tagged only, combined without constraints, combined with incompressibility constraint, with valve plane constraint and with all constraints.

Untagged	Tagged	Combined	Incompressible	Valve	All
+16%	-28%	-14%	-8%	-17%	-10%

**Table 5.4** – Evaluation of EF accuracy defined in eq. (5.14). The gold standard is used here manual is the manual segmentation. The algorithms are TomTec, untagged only, combined without constraints, combined with incompressibility constraint, with valve plane constraint and with all constraints.

TomTec [Kuhl et al., 2004]	Untagged	Combined	Incompressible	valve	All
3.3%	10.4%	5.2%	7.6%	3.5%	3.8%

different segments are large. This is probably due to the fact that the longitudinal motion predominately happens in basal segments other than in apical segments. Finally, Figure 5.14 shows the results of the circumferential motion where the underestimation can be observed from the untagged only method. These figures further confirm that the proposed motion tracking estimates radial, circumferential and longitudinal motion better than tagged only or untagged only methods.

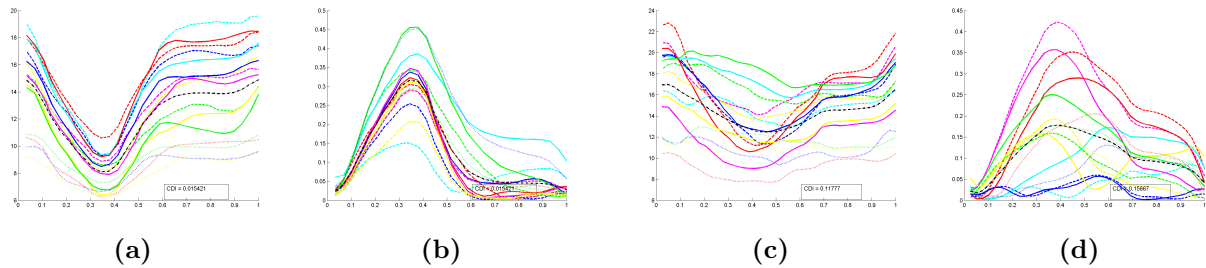


**Figure 5.15** – This figure shows the SDI curves from a normal subject and a CRT candidate. (a) regional volume SDI for a normal subject, (b) strain SDI for a normal subject, (c) regional volume SDI for a CRT candidate and (d) strain SDI for a CRT candidate.

### 5.6.2 SDI results

In this section we use the TomTec 4D LV analysis tool V2.0 based on [Kuhl et al., 2004] during our study for six CRT candidates and two normal volunteers. One of the common problems for

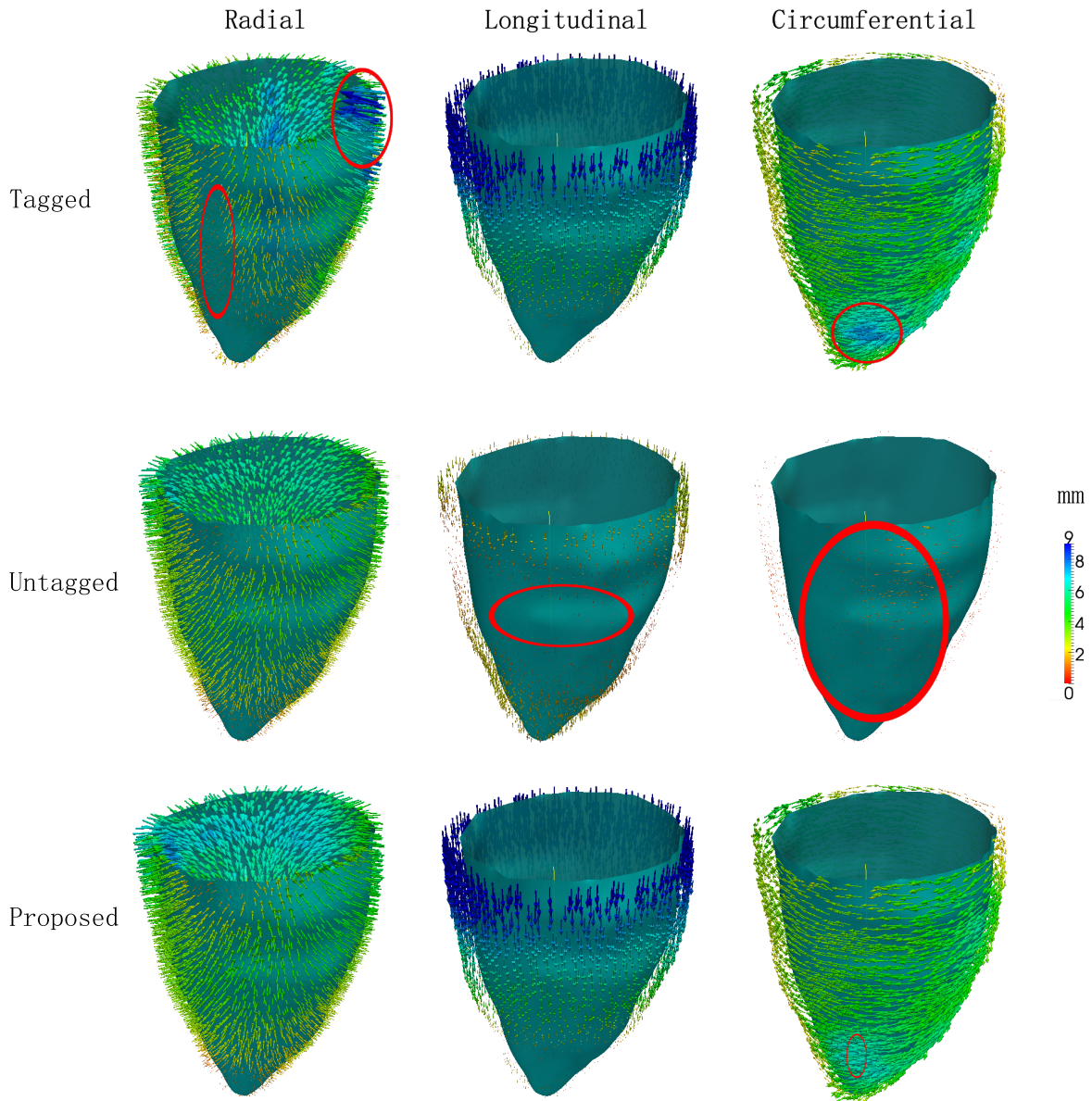


**Figure 5.16** – This figure shows a visualisation of the myocardial motion field in radial, longitudinal and circumferential directions. The first row shows the motion field derived from tagged images only. The second row shows the motion field derived from untagged images only and the third row shows the motion field derived from the comprehensive motion tracking . The red circle indicates under or over estimation of the motion.

motion estimated from tagged MR is that the mass of the myocardium is not preserved. We have assessed the myocardial mass change resulting from the extracted motion patterns. The results are presented in Table 5.3. The volume is calculated from the propagated end-systolic manual segmentation. The mass of the myocardium is overestimated by motion tracking from untagged images and is also underestimated by motion tracking from the tagged images. The mass of the myocardium is underestimated using the valve plane constraint alone. Finally,

the mass is significantly better preserved with the proposed combined registration with the incompressibility constraint.

EF, regional volume and strain SDI can also be derived from the motion tracking result from untagged images as well as from the comprehensive motion tracking. From the results in Figure 5.10 it is clear that the method based on tagged images performs poorly for the tracking of the endo- and epicardial surfaces. However, this tracking is essential for the assessment of global functional parameters such as EF and local functional parameters such as regional volume output, radial motion and radial strain. The result from the motion tracking using tagged images only is quite poor for the SDI analysis and thus has been excluded from further analysis. The accuracy is defined as:

$$\gamma = \left\| \frac{GS_{measurement} - AL_{measurement}}{GS_{measurement}} \right\| \quad (5.15)$$

where  $GS$  denotes the gold standard and  $AL$  denotes the automatic measurement. This accuracy measurement is chosen due to its robustness to variation between healthy volunteers and patients. Table 5.4 shows the accuracy for ejection fraction, Table 5.5 shows region volume SDI and Table 5.6 shows the regional strain SDI and includes a comparison against clinical measurements obtained using the TomTec system [Kuhl et al., 2004]. The gold standard for the EF are the manually segmented endocardial surfaces at both end-diastolic and end-systolic phases. TomTec as well as the methods using the valve plane constraint performed quite well. However, the untagged motion tracking performed poorly mainly due to underestimation of the EF. It suffers from the lack of longitudinal motion. Similarly, the methods without valve plane constraint underestimate the longitudinal motion within the LV blood pool. The same result can be observed for the regional volume SDI measure.

For regional strain SDI we used linear regression and the  $R^2$  coefficient to measure the correlation with regional volume SDI obtained from clinical measures. We use correlation since no ground truth is available. The regional strain SDI derived from the untagged images does not agree well with the clinical regional volume SDI measurements due to the lack of

**Table 5.5** – Evaluation against TomTec’s regional volume **SDI** measurement. The algorithms are untagged only, combined without constraints, combined with incompressibility constraint, with valve plane constraint and with all constraints.

Untagged	Combined	Incompressible	Valve	All
9.8%	6.1%	7.0%	5.4%	5.6%

**Table 5.6** – Evaluation of regional strain **SDI** against the TomTec’s regional volume **SDI**. Linear regression and R-Square distance are used instead of accuracy. Negative value indicates negative correlation. The algorithms are untagged only, combined without constraints, combined with incompressibility constraint, with valve plane constraint and with all constraints.

	Untagged	Combined	Incompressible	Valve	All
$R^2$	-0.77	0.64	0.70	0.71	0.78

circumferential and longitudinal strain. However, the regional strain **SDI** derived from the combined motion tracking method correlates better. Due to the different nature of strain and volume **SDI**, both methods do not agree with each other strongly. Finally, the incompressibility constraint and valve plane constraint both contribute to better correlation of regional strain **SDI** and volume **SDI**.

## 5.7 Discussion and conclusion

We have presented a novel method for cardiac motion tracking using 3D tagged as well as untagged image sequences from **SA** and **LA** views simultaneously. The key advantage of the proposed method is the simultaneous use of complementary motion information contained in the tagged and untagged images. Since untagged images are routinely acquired as part of clinical **MR** image acquisition, no extra scans are necessary. Our evaluation shows that there is a significant improvement of registration accuracy both in terms of tag tracking and segmentation propagation. We have proposed a spatially adaptive weighting to help extract complementary information from both tagged and untagged **MR** images. The rich anatomical information in untagged **MR** images, especially on the epi- and endocardial boundary, is used to compensate for problems such as tag fading in the tagged images. On the other hand, complete motion

information in 3D from the tagged images is helpful to estimate circumferential and longitudinal motion which is difficult to extract from untagged MR images. In addition to the spatially adaptive weighting, we have added a valve plane tracker to additionally constrain and guide the motion estimation in particular in the longitudinal direction.

The analysis of global and regional cardiac function has been performed by mapping a standard AHA model [Cerqueira et al., 2002] onto our segmentation. A comparison of our cardiac analysis and a state-of-the-art commercial software tool has been performed. The proposed motion tracking method shows very good correlation with the ejection fraction and the regional volume SDI.

By combining complementary information using a spatially dependent weighting, incompressibility and valve plane constraint, we have successfully built an accurate and realistic cardiac motion analysis framework. The accuracy in terms of landmark and surface distances is improved significantly. Moreover, 4D motion with complete radial, longitudinal and circumferential components is estimated consistently during a single process. In this work, the registration framework uses a numerical solution to approximate the partial differential equations and calculate the gradient of the energy function. The optimisation strategy is computationally expensive. In addition, it is difficult to distinguish the motion between the myocardium and its surrounding tissues. In the next chapter, we will propose a novel SFFD based registration framework with analytical optimisation to address these challenges.

# Chapter 6

## Registration using sparse free-form deformations

The work in this chapter is based on the following published paper:

- Wenzhe Shi, Xiahai Zhuang, Luis Pizarro, Wenjia Bai, Haiyan Wang, Kai-Pin Tung, Philip Edwards, Daniel Rueckert. (2012). Registration using sparse free-form deformations. Medical Image Computing and Computer Assisted Intervention (MICCAI), in Press.

### 6.1 Introduction

Image registration is one of the fundamental tasks in medical image analysis. It is a key component of both cardiac motion tracking and segmentation. The classic [FFD](#) registration approach [[Rueckert et al., 1999](#)] is widely used for medical image registration. Several improvements of the method have been proposed in the past, including a diffeomorphic variant of [FFDs](#) to generate more realistic deformation [[Rueckert et al., 2006](#), [De Craene et al., 2012](#)] which ensures a one to one mapping; a temporal [FFD](#) to allow 4D deformation [[Metz et al.,](#)

2011]; an analytical expression for the mutual information based similarity metric to accelerate the optimisation [Modat et al., 2010] as well as different optimisation strategies [Glocker et al., 2008, Klein et al., 2010]. Despite its popularity, little effort has been devoted to improve the accuracy of the formulation compared to other registration methods such as optical flow [Horn and Schunck, 1981, Mémin and Pérez, 2002, Roth and Black, 2005, Sun et al., 2010] and the Demons approach [Thirion, 1998, Vercauteren et al., 2008].

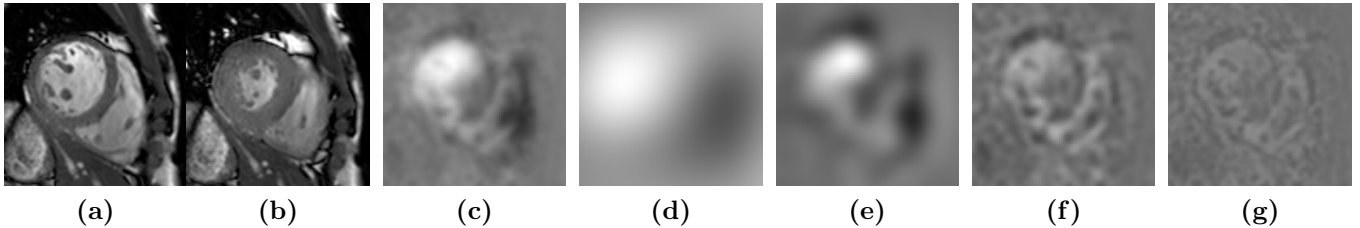


**Figure 6.1** – Sparse representations of FFDs: (a) Target image; (b) source image; (c) deformation field induced by the FFDs  $\phi$  in  $x$ -direction; (d-g) FFDs at four different levels.

In this chapter, we address one main difficulty of the classic FFD approach, namely the conflict between the robustness of the registration and the ability to model highly-localised and potentially discontinuous deformations. This conflict stems from the fact that the FFD approach uses a smooth B-spline basis to model the contribution of each control point to the deformation. To model global and smooth deformations a coarse control point spacing is typically used. To allow very localised deformations a finer control point spacing is required. However, this can make the FFD-based registration less robust as the model has far more variables which must be optimised. A conventional approach to address this issue uses a coarse-to-fine approach in which the initial coarse control point mesh is successively subdivided to produce finer control point meshes [Rueckert et al., 1999].

The standard smoothness constraints for non-rigid registration methods [Rueckert et al., 1999, Horn and Schunck, 1981, Thirion, 1998] assume that the deformation within a neighbourhood changes only gradually since the underlying deformation itself is smooth. Combining the implicit smoothness of the B-spline basis and the explicit smoothness constraint in the regularisation, the FFDs-based registration will produce smooth deformations.

As mentioned above, the control point grid spacing has a significant impact on the ability

to capture motion discontinuities robustly. Previous research focussed on the adaptive parametrisation of the B-spline control point grid [Schnabel et al., 2001, Rohlfing and Maurer, 2001, Hansen et al., 2008] has been driven by the intensity information in the images. An improved model should enable more control points to be placed in the area in which more flexibility for the modelling of deformations is required.

Many other approaches to image registration have been proposed that aim to overcome the conflict between robustness and accuracy in the motion estimation, in particular in the field of optical flow [Mémin and Pérez, 2002, Roth and Black, 2005, Sun et al., 2010]. More recently, sparse coding methods have been proposed to evaluate the patch similarity between two images [Roозgard et al., 2011] and to constrain the transformation [Shen and Wu, 2010]. However, to the best of our knowledge, no work has addressed the conflict between robustness and accuracy in the context of FFD-based registration.

### 6.1.1 Overview and contributions

In this chapter, we introduce a sparse representation for FFDs to estimate the registration transformation. Our approach is inspired by the work in [Roозgard et al., 2011, Shen and Wu, 2010]. This simple model uses standard smoothness constraints and only imposes one assumption on the deformation, namely that the deformation is sparse in the parametric space of the deformation. The assumption is generally true because the deformation between images is usually simpler than the actual images themselves. In this work, we use a multi-level FFD to represent the deformations in a parametric form. In this multi-level FFD each level consists of a B-spline control point mesh with increasingly finer resolution. As can be seen from Figure 6.4, the sparsity assumption holds in general for multi-level FFDs. Based on this assumption, we formulate the registration of two images using a sparse multi-level FFDs representation of the control points. We introduce a regularisation term to impose smoothness at each level and a sparsity term to enforce coupled multi-level sparsity.

The novelty and contributions of this chapter are the introduction of a sparsity model that avoids the *a priori* selection of an appropriate control point grid spacing. Furthermore, the

approach reduces the conflict between global smoothness (robustness) and the local level of detail of the transformation (accuracy) by optimising the different levels of the FFDs simultaneously with a sparsity constraint. These advantages allow for the robust estimation of deformation fields in the presence of highly localised or discontinuous deformations. We refer to this new approach as SFFD. In the evaluation, we demonstrate that the proposed method can consistently capture localised motion with high accuracy.

## 6.2 Classic free-form deformation model

In the classic FFD registration [Rueckert et al., 1999], a non-rigid deformation  $\phi = [X \ Y \ Z]^T$  is represented using a B-spline model in which the deformation is parameterised using a set of control points  $\psi = [U \ V \ W]^T$  such that

$$\phi = \begin{bmatrix} B & 0 & 0 \\ 0 & B & 0 \\ 0 & 0 & B \end{bmatrix} \psi, \quad (6.1)$$

where  $B$  denotes the matrix of the B-spline basis functions. To find the optimal deformation between two images, the registration minimises an energy functional  $E$  written as a function of  $\psi$ , which is typically a combination of two terms  $E(\psi) := E_D(I_t, I_s \circ \phi) + E_R(\psi)$ . The term  $E_D$  is a data constraint measuring the similarity between the target image  $I_t$  and the transformed source image  $I_s \circ \phi$ . The term  $E_R$  is a regularisation constraint that enforces a smooth transformation. The energy function is typically minimised using gradient descent approaches [Modat et al., 2010, Klein et al., 2010] or discrete optimisation approaches [Glocker et al., 2008].

### 6.3 Sparse free-form deformation model

To be able to deal with large, global deformations and to improve the robustness, the classic **FFD** registration uses a multi-level approach: First, the optimal registration parameters are determined for a control point grid with large spacing. The grid is then successively subdivided to capture local deformations [Rueckert et al., 1999]. This requires an a-priori choice of the initial and final control point spacing. Furthermore, each level is optimised separately and once a level has been optimised it is no longer updated, leading to suboptimal registration results as can be seen in Figure 6.2. It was suggested in [Shen and Wu, 2010] that a realistic transformation can be easily embedded into a sparse representation. We postulate that an automatic selection of control points across different levels can be achieved by optimising all **FFD** levels simultaneously while using a sparsity constraint.

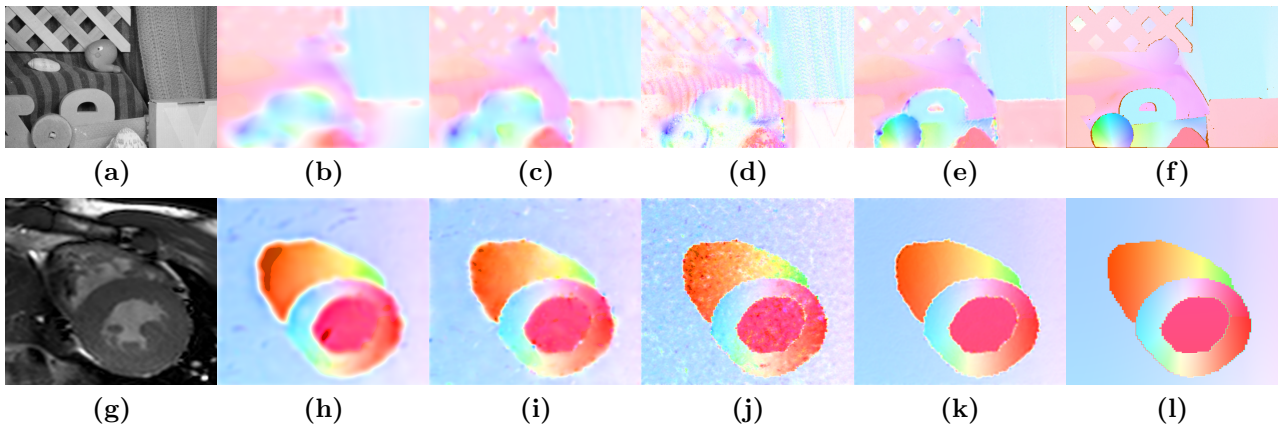


**Figure 6.2** – Visual comparison between the classic **FFDs** and the proposed **SFFD** using the colour scheme from [Baker et al., 2007]. The colour range corresponds to different direction and magnitude of the transformation. (a) and (g) show the rubber whale image from the Middlebury dataset and a frame from the cardiac B experiment, respectively; (f) and (l) display the ground truth transformations with noticeable motion discontinuities; (b-d) and (h-j) show the estimated motion with the classic **FFDs** approach for 512/8mm, 256/4mm, and 64/1mm control point spacing; (e) and (k) exhibit the estimated motion with the proposed **SFFD** approach where  $\lambda_S^N = 0.04$ .

### 6.3.1 Sparse representation of transformation

In this section, we propose estimating the transformation  $\phi$  with a sparse representation of the control points  $\psi$ . We use a multi-level FFD representation [Schnabel et al., 2001],  $\psi = [U^1 \dots U^m \ V^1 \dots V^m \ W^1 \dots W^m]^T$ , as it is well suited for sparse representations. Accordingly, we utilise a multi-level B-splines basis  $B = [B^1 \dots B^m]$ . The transformation  $\phi$  is computed as in eq. (6.1) with the above redefinitions of  $\psi$  and  $B$ . The multi-level FFD is illustrated in Figure 6.1. Our assumption is that a typical FFD can be sparse in its representation as presented in Figure 6.4.

Basis pursuit denoising [Donoho and Huo, 2001] is a mathematical optimisation that balances the trade-off between sparsity and reconstruction fidelity. In the context of image registration, the problem can be formulated as:

$$\arg \min_{\psi} \quad E(\psi) := \|I_t - I_s \circ \phi\|_2^2 + \|\psi\|_1, \quad (6.2)$$

Here the first term corresponds to the sum of squared differences (SSD) between the target image and the transformed source image. The second term enforces the sparsity of the solution  $\psi$  by using the  $L_1$ -norm. The  $L_1$ -norm is used to enforce sparsity because it is convex and has many favourable theoretical results [Donoho and Huo, 2001, Roozgard et al., 2011, Shen and Wu, 2010]. In general, an arbitrary (dis)similarity measure can be utilised in the data term  $E_D(I_t, I_s \circ \phi)$ , including information theoretic measures such as MI or its normalised counterparts NMI [Studholme et al., 1999].

Following these principles, we formulate a novel registration approach, namely the SFFD model, as

$$\arg \min_{\psi} \quad E(\psi) := E_D(I_t, I_s \circ \phi) + \lambda_R \sum_{i \in [0, m]} E_R(\psi^i) + \lambda_S \|\psi\|_1, \quad (6.3)$$

with constants  $\lambda_R, \lambda_S \in \mathbb{R}^+$  weighting the regularisation term and the sparsity term, respectively. Note that the regularisation term imposes smoothness at each level of the multi-level FFD independently, while the sparsity term enforces coupled multi-level sparsity. This

allows us to actively determine the importance of the control points across all levels in a joint manner, not independently as in the classic **FFD** framework. This strategy can be used to estimate deformations fields robustly and to preserve motion discontinuities, as it will be seen in the experimental validation. The **SFFD** model is at the same magnitude of the computational complexity as the classic **FFD** model.

We optimise eq. (6.3) using the interior point method of [Kim et al., 2007] that uses a log barrier function to make the sparsity term differentiable. The parameter  $\lambda_S$  is normalised between the data and the sparsity terms using the finite convergence to zero property. That is, for the  $L_1$ -regularised least squares problem, convergence is achieved for a finite value  $\lambda_{max}$  of  $\lambda_S$ . The value of  $\lambda_{max}$  can be determined using eq. (4) in [Kim et al., 2007]. In our experiments, we use:

$$\lambda_S^N = \lambda_S / \lambda_{max}. \quad (6.4)$$

For completeness, the reader will find the partial derivatives of the similarity measures and the regularisation terms with respect to  $\psi_i$  in the appendix B.

## 6.4 Results

### 6.4.1 Datasets

In this work, we have evaluated the proposed **SFFD** against the classic **FFD** model on four different datasets. The datasets we have used for evaluation include the Middlebury benchmarking dataset (which is a standard dataset widely used in computer vision), 2D cardiac MR images with synthetic smooth and discontinuous motion, and 3D cardiac MR image sequences.

For basic benchmarking we have used six pairs of 2D greyscale natural images from the Middlebury benchmark training dataset [Baker et al., 2007]. The Middlebury benchmark dataset contains deformations with multiple independently moving rigid objects and background. For

this dataset the ground truth deformation between each pair of images is available. The ground truth is derived from the camera position and parameters. There is a relatively large diversity in motion discontinuities present in this dataset. Due to the above reasons, it is used as a primary benchmark to test and develop the [SFFD](#) registration.

In addition, we have tested our approach using 2D and 3D cardiac MR images. For 2D cardiac MR images a synthetically generated transformation has been applied to the images using sinusoidal function as proposed in [[Pizarro et al., 2011](#)]. A single sinusoidal function is used to generate a group of 10 data with smooth motions using different magnitudes and frequencies. This set of data will be referred to as dataset *Cardiac A*. Also, a set of 10 discontinuous motions dataset (*Cardiac B*) is generated where multiple sinusoidal functions are fused into a discontinuous motion using segmentation information which can be seen in [Figure 6.21](#). The registration recovers the synthetic motion between the original image and the transformed image. For the above datasets, the average error between the ground truth deformation and the deformation obtained after registration is measured.

We have also used 13 3D cardiac cine MR images dataset (*Cardiac C*) from normal volunteers to assess the proposed registration framework. The image resolution is  $1.25 \times 1.25 \times 8mm$ . We estimate the accuracy based on the tracking of myocardial boundaries of the left ventricle. Manual expert segmentations of endo- and epicardial surfaces are available at both [ED](#) and [ED](#) phases by a clinician. We then register the [ES](#) phase directly to the [ED](#) phase. We evaluate the surface distance between propagated myocardial surface and manual myocardial surface at [ES](#) phase.

### 6.4.2 Implementation details

During the optimisation of the classic [FFDs](#), we use seven different levels of image resolution. In the coarsest level each voxel is subsampled by a factor of 64 in each dimension. We use B-spline interpolation for the subsampling as evidence suggests that B-spline based interpolation is superior than linear interpolation [[Sun et al., 2010](#), [Modat et al., 2010](#)]. The coefficient for the smoothness penalty is set to 0.001 as in the original approach [[Rueckert et al., 1999](#)] if

**NMI** is used as a similarity measure. If **SSD** is used as a similarity metric the coefficient for the smoothness penalty is set to 1 since **SSD** induces stronger deformations.

One of the most crucial parameters of the classic **FFD** registration is the control point grid spacing. We create a spacing at each image pyramid level by subdividing the **FFD** from the previous level. We have evaluated different initial control point spacings at the coarsest level varying from 512mm to 64mm while the control point spacings at the final level varies from 8mm to 1mm. For the **SFFD**, we use a multi-level **FFD** with the coarsest level having a control point grid spacing of 64mm and finest level having a spacing of 1mm. The number of image pyramid levels and the smoothness penalty  $\lambda_R$  are the same for both methods. Finally, **NMI** is used as similarity measures for the 3D cardiac MR images and **SSD** is used for the 2D cardiac MR images with simulated motion as well as for the Middlebury benchmark. The Middlebury benchmark is an optical flow based benchmark where the assumption of constant intensity generally holds. The assumption holds for the synthetic dataset since no noise is introduced in our case. The constant intensity assumption makes **SSD** a preferable candidate as the similarity measure in these two cases. On the other hand, **NMI** has been proven to be a robust similarity measure especially for clinical MR images with time varying contrast and noise.

### 6.4.3 Effects of the sparsity constraint

In this section we evaluate the effects of the sparsity constraint in the Middlebury dataset. The Middlebury benchmark provides accurate motion ground truth from real images and contains both discontinuous motion and smooth motion. We first apply the classic **FFDs** approach to the data. We use three different levels of resolutions and a smoothness parameter of 1. **SSD** is selected as the similarity measure. It is noticeable in Figure 6.3 that the accuracy is different from image to image. From our observation, the optimal initial grid spacing depends highly on the level of discontinuity of the data. We applied a comparable **SFFD** approach with largest grid spacing of 64mm to the benchmark. The **SFFD** approach shares the same number of image resolutions, smoothness parameter and similarity measure with the classic **FFDs**. In Figure 6.3, the performance of different sparsity constraints is similar across the different images. There

is a significant increase of the accuracy when the sparsity parameter is first introduced and the accuracy remains stable until around  $\lambda_S^N = 0.16$  with a sharp decrease towards the final point of convergence. There is no obvious bias toward different degrees of discontinuity in the dataset.

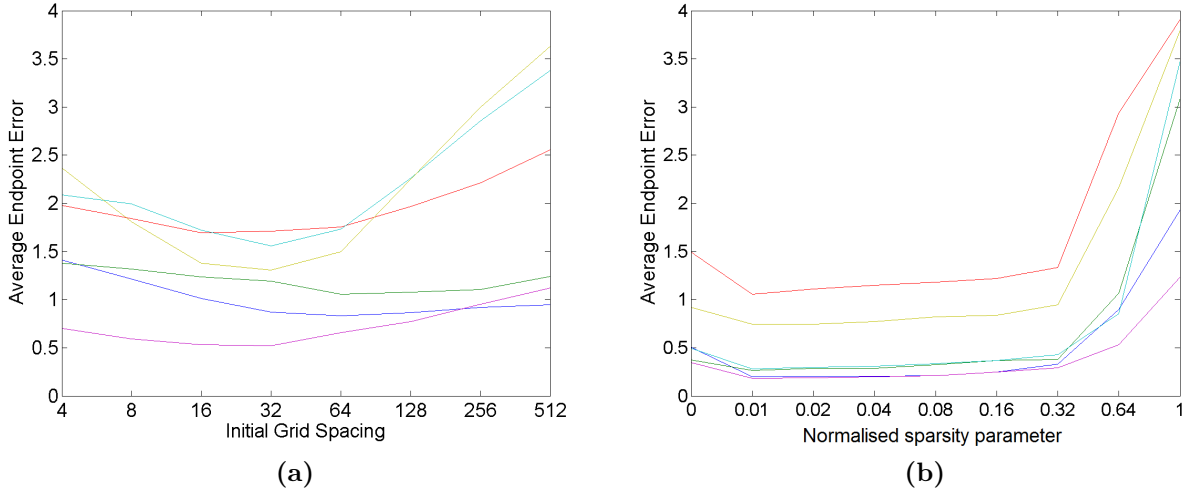


**Figure 6.3** – The accuracy of different parameters. Each line corresponds to a pair of 2D images in the Middlebury benchmark. (a) The influence of different initial grid spacing to the classic FFDs; (b) The influence of different normalised sparsity parameter  $\lambda_S^N$  to the SFFD.

To observe the effect of the sparsity parameter, we plot the  $L_1$ -norm of the SFFD’s parametric basis against the displacement in Figure 6.4. The  $L_1$ -norm of the parametric basis decreases dramatically when the parameter is introduced. It finally reaches zero when the finite convergence condition is met. On the other hand, the  $L_1$ -norm of the displacement is stable without significant decrease until the parameter becomes too large. There is in general a difference of a magnitude between the  $L_1$ -norm of the displacement and the  $L_1$ -norm of the parametric basis when the sparsity parameter is introduced. This shows that the displacement of the FFDs can be represented by a sparse representation in the parametric space if the sparsity constraint is enforced.

In the SFFD framework, one parameter is the coarsest grid spacing in the multi-level FFD representation. Here, we examine the effect of different coarsest grid spacing. The results are presented in Table 6.1. The accuracy increases slightly from 32mm to 64mm. It remains steady from 64mm to 512mm. Overall, the coarsest spacing does not have a huge impact on

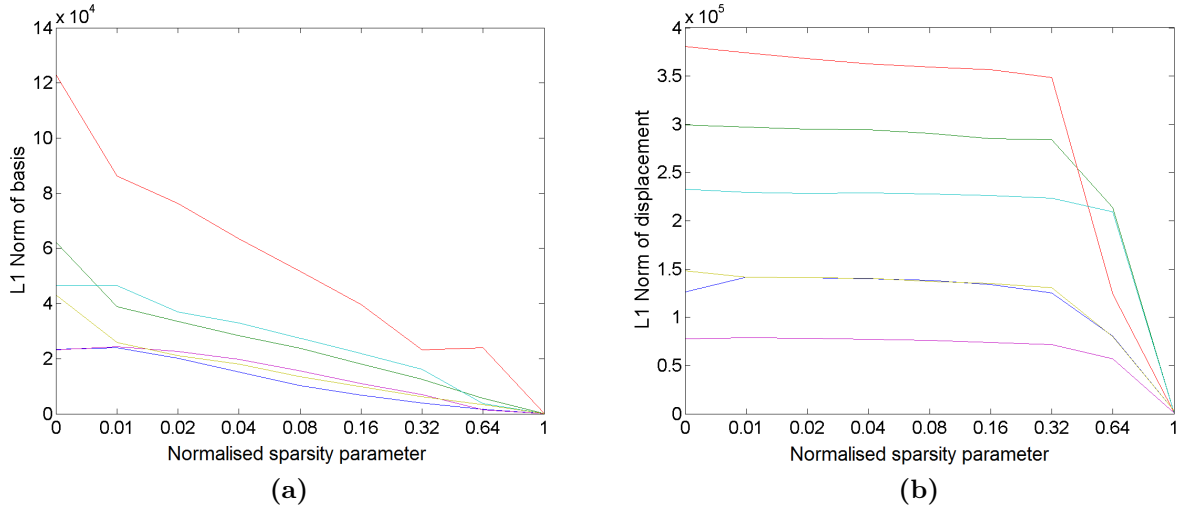


**Figure 6.4** – (a) The  $L_1$ -norm of the parametric basis of the **SFFD** with respect to different normalised sparsity parameter  $\lambda_S^N$ ; (b) The  $L_1$ -norm of the displacement at the finest **FfDs** level of the **SFFD** with respect to different normalised sparsity parameter  $\lambda_S^N$ .

**Table 6.1** – Median and **IQR** of accuracies from the **SFFD** with different coarsest spacing when normalised sparsity parameter  $\lambda_S^N = 0.04$ .

Coarsest spacing	32 mm	64 mm	128 mm	256 mm	512 mm
Accuracy	0.26 (0.46)	0.24 (0.54)	0.25 (0.55)	0.24 (0.54)	0.24 (0.54)

the accuracy. From our experience, it seems beneficial that the control point’s B-spline basis in the coarsest level covers the whole images. This allows to model global transformations. Thus, it is suggested to set the coarsest grid spacing to more than 20% of the image dimension in each direction.

#### 6.4.4 Evaluation

For the classic **FfDs**, different spacing leads to significantly different results as shown in Table 6.2. Moreover, different datasets require different initial spacings to achieve the best performance. It can be seen from the final column in Table 6.2 that the **SFFD** is robust against the choice of  $\lambda_S^N$  compared to the choice of the control point spacing of the **FfDs**. There is little need to adjust  $\lambda_S^N$  across datasets to achieve very good performance for each individual dataset. The result suggests that a  $\lambda_S^N \approx 0.04$  yields consistently good performance.

**Table 6.2** – Median and IQR of accuracies from the classic FFDs with different initial and final spacing and the SFFD with different normalised sparsity parameter  $\lambda_S^N$ . Cardiac A, B and C refer to the 2D cardiac MR image with synthetic smooth motion and discontinuous motion and 3D cardiac MR image sequences respectively. The units of the accuracy metrics are in the bracket. For the results, n/a means that the image is not large enough to contain the initial control point grid spacing, bold font means the best result and \* means statistically significantly different from the best result of the classic FFDs using t-test with p-value 0.05.

Initial/final spacing	64/1 mm	128/2 mm	256/4 mm	512/8 mm
Middlebury (mm)	0.69 (0.58)	0.62 (0.54)	<b>0.61 (0.45)</b>	0.67 (0.66)
Cardiac A (mm)	0.03 (0.04)*	0.02 (0.02)*	0.02 (0.03)	<b>0.01 (0.02)</b>
Cardiac B (mm)	0.07 (0.08)*	<b>0.05 (0.04)</b>	0.05 (0.02)	0.06 (0.05)*
Cardiac C (mm)	<b>1.68 (0.56)</b>	1.86 (0.63)*	1.94 (0.82)*	n/a
$\lambda_S^N$	0.00	0.01	0.04	0.16
Middlebury (mm)	0.68 (0.60)	0.25 (0.56)*	<b>0.24 (0.54)*</b>	0.26 (0.57)*
Cardiac A (mm)	0.03 (.02)	0.01 (0.01)	<b>0.01 (0.01)*</b>	0.01 (0.01)*
Cardiac B (mm)	0.07 (0.03)	0.02 (0.01)*	<b>0.02 (0.01)*</b>	0.02 (0.01)*
Cardiac C (mm)	1.74 (0.64)	1.55 (0.61)	<b>1.54 (0.62)</b>	1.62 (0.64)

The results show that the median using the multi-level FFD representation without sparsity constraint (where  $\lambda_S^N = 0$ ) are 0.68mm, 0.03mm, 0.07mm and 1.74mm for Middlebury and cardiac A, B, C datasets respectively. Thus, all datasets benefit from the sparsity constraint with a consistent increase in registration accuracy. Moreover, the SFFD exhibits a significant improvement against the best results from the classic FFD where discontinuous and highly localised motion patterns are present. The improvement is most significant against ground-truth from the Middlebury dataset and from the 2D cardiac MR image dataset with synthetic discontinuous motion. An increasing ability to capture local and discontinuous motion while maintaining robustness over smooth regions can be also seen in the visual comparison in Figure 6.2.

Finally, in the 3D cardiac MR image sequences, we witness a limited improvement,  $1.54 \pm 0.32$  vs  $1.68 \pm 0.28$ , in the result. Due to the lack of an objective ground truth, we measured the errors only on the LV myocardial surfaces. Apart from that, available accuracy measures in real medial image dataset are often not a good indicator of how well the registration performs [Rohlfing, 2012]. Hence, the result can only partially demonstrate the registration accuracy.

## 6.5 Discussion and conclusions

In this chapter, we have developed a **SFFD** model for registration which addresses some most important short-comings of the original **FFD** registration model. Control points across different **FFD** levels are optimised simultaneously using a sparse representation. Compared to the classic **FFD**, the **SFFD** requires less parameter tuning across different datasets. The user no longer needs to choose an appropriate control point spacing a-priori. Our experiments have shown a consistent improvement compared to the original **FFDs** approach. The most significant improvement can be observed in the Middlebury dataset ( $0.61 \pm 0.22$  vs  $0.24 \pm 0.27$ ) and Cardiac B dataset ( $0.045 \pm 0.016$  vs  $0.021 \pm 0.005$ ) where the deformation field exhibits both smooth and discontinuous motion.

By simply replacing the classic **FFDs** deformation using the proposed **SFFD** deformation model, the registration algorithm may lead to improved results in both cardiac segmentation 4 and motion tracking 5 applications we developed in this thesis. In next chapter, we will show two important clinical applications which fundamental techniques are build on the framework we have developed in the previous chapters.

# Chapter 7

## Clinical applications

### 7.1 Introduction

The work in this chapter has been published in the following papers:

- D. P. O'Regan, W. Shi, B. Ariff, A. J. Baksi, G. Durighel, D. Rueckert, S. A. Cook. (2012). Remodelling after acute myocardial infarction: mapping ventricular dilatation using three dimensional CMR image registration. *Journal of Cardiovascular Magnetic Resonance*, 14(1):41-49.
- SG Duckett, W Shi, X Zhuang, A Shetty, M Ginks, CA Rinaldi, G Carr-White, D Rueckert, RS Razavi. (2012). Cardiac MRI: understanding myocardial motion to predict remodelling pre cardiac resynchronisation therapy. *Journal of Heart* 98:A6-A7.

The previous chapters have focused on developing new methodologies for the segmentation and tracking of the heart in [CMR](#) images. In this chapter we demonstrate the feasibility of applying the developed methods in two different but equally important clinical research applications. The first clinical application aims at selecting patients who will respond positively to [CRT](#). The second clinical application aims at characterising and quantifying longitudinal changes in cardiac morphology and function during cardiac remodelling following myocardial infarction. In

this thesis, we focus more on the feasibility of applying the developed techniques in these clinical contexts rather than focusing on the clinical findings in these studies. We demonstrate that the proposed techniques can meet the specific requirements of these two clinical applications.

## 7.2 Application to cardiac resynchronisation therapy

A significant number of patients that undergo CRT do not derive symptomatic benefit from treatment or remodel <sup>1</sup>. Assessing the synchrony of myocardial motion, such as measuring changes of LV blood pool volume, muscle thickening, deformation and strain, has the potential of improving patient selection for CRT. In this section, we develop a framework for computing and comparing measurements derived from myocardial motion tracking and evaluate their correlation to clinical outcome measures of CRT. Different from the evaluation in Chapter 5, here we focus on the clinical usefulness of the motion tracking instead of the accuracy.

### 7.2.1 Introduction

CRT is a standard treatment for heart failure patients with low EF and conduction delay depicted by left bundle branch block (LBBB) on the surface ECG [Cleland et al., 2005]. However, the number of patients who do not derive clinical benefits still remains at approximately 30% [Cleland et al., 2005].

The TomTec 4D left ventricular (LV) analysis software (TomTec Imaging systems Inc, Munich, Germany) measures global LV mechanical (volume) dyssynchrony and has been shown, in both cardiac cine MR and 3D echocardiography, to provide useful information in predicting whether a patient is likely to respond to CRT or not [Kapetanakis et al., 2005]. This method of assessing global LV dyssynchrony calculates the time taken to reach minimum regional volume for the 16 segments as a percentage of the cardiac cycle. The SDI is then defined as the standard deviation (SD) of these timings with a high SDI denoting more dyssynchrony in the cardiac

---

<sup>1</sup>remodel here refers to decrease in  $ESV > 15\%$  at 6 months.

motion pattern. To allow comparison between patients with different heart rates the **SDI** is expressed as a percentage of the cardiac cycle.

A limitation of using volume change over the cardiac cycle as an indicator of systolic dyssynchrony is that it does not take into account the difference between active and passive motion. Scarred or akinetic myocardial segments can be deformed or stretched by adjacent segments, leading to passive volume changes. It is not clear if or how this phenomenon affects the accuracy of the method, both in determining how truly dyssynchronous a ventricle is and how likely a patient is to respond to **CRT**. Potential ways of taking into account active myocardial motion are to use muscle thickening or strain (radial, circumferential or longitudinal) for computing the **SDI**. However, in a typical clinical **CMR** acquisition, only a small number of **SA** slices are used to assess myocardial motion [Lardo et al., 2005, Han et al., 2010], which does not provide a global understanding of the **LV** motion or dyssynchrony.

In this work, we have developed a method for computing global myocardial muscle thickening, deformation, radial, circumferential and longitudinal strain from cine untagged and tagged **CMR** images. Using this information, we have derived **SDI** for all parameters which are comparable to the **SDI** computed from volume changes. Since thickening, deformation and strain analysis take both active and passive motions into account, we aim to investigate how these techniques can aid clinicians in predicting which patients are likely to respond to **CRT**.

### 7.2.2 Image acquisition

48 patients with severe heart failure fulfilling standard criteria for **CRT** ( $EF \leq 35\%$ , **LV ED** diameter  $\geq 55\text{mm}$  and prolonged QRS  $> 120\text{ms}$ ) were recruited. The patients were scanned using 1.5T **MR**-scanner (Achieva, Philips Healthcare, Best, Netherlands) with a 32-element cardiac coil or a 5-element cardiac coil (large or claustrophobia patients). Cardiac synchronisation was performed with **vector electrocardiography (VECG)**. After localisation and a coil sensitivity reference scan an interactive real-time scan was performed to determine the geometry of the **SA**, four (4CH), three (3CH) and two chamber (2CH). A multiple slice, cine **SSFP** scan was performed in **SA** orientation to assess the ventricular function ( $FA=60$ ,  $TR/TE=2.9/1.5\text{ms}$ ,

resolution 2.2x2.2x10mm, 30 heart phases). The 4CH, 3CH and 2CH views were used to assess LV function for regional wall motion abnormalities. The scan duration of every two cine slice is approximately 12 seconds.

3D tagging was implemented using three sequentially acquired 3D data sets with line tag preparation in each of the three spatial dimensions [Rutz et al., 2008]. A respiratory navigator was used to ensure that the images are spatially aligned. 3D tagged images were acquired of the whole LV using the following parameters: tag separation = 7mm, FOV = 108 x 108 x 108mm, EPI factor = 7, TFE factor = 4. The voxel size for each of the three datasets is 1.00 x 1.00 x 7.71mm, where the direction of low resolution is different for each of the three acquisitions. Depending on the heart rate, cardiac phases were recorded with a temporal resolution of about 30ms with 24 to 30 phases. The scan duration is approximately 60 seconds with 3 breath-holds.

### 7.2.3 Methods

To quantify the SDI for LV volume output, myocardial deformation, strain, and wall thickening, we modify the comprehensive cardiac motion estimation framework presented in Chapter 5 to semi-automatically compute these parameters at each phase across the cardiac cycle. The motion tracking framework consists of the following five steps:

1. Spatial and temporal alignment of the images;
2. Detection of the heart and semi-automatic segmentation of the myocardium from untagged CMR images;
3. Extraction of deformation fields of the heart from both untagged and tagged CMR images;
4. Detection of endo- and epicardial surfaces and computation of volume output, wall thickening;
5. Extraction of deformation fields within the myocardium and computation of myocardial motion, deformation, and strain.

The values of myocardial wall thickening, wall deformation, and strain fields are all mapped onto the coordinate of the ED phase of the SA cine MR image. In this coordinate system the 16 segments of the myocardium LV are defined from the segmentation results. For each subject, we define these 16 segments according to the definition of the AHA [Cerqueira et al., 2002]. The spatial and temporal registration is performed before the segmentation of myocardium to align all images into a common spatial and temporal coordinate system as discussed in Section 4.2.2. At the time that this research was conducted, the automatic segmentation framework in Chapter 4 was not yet completed. Instead, the segmentation was done by a clinician who manually labelled the myocardium of the LV at the ED phase of the cine CMR. Then, we fit a pre-constructed 3D myocardium model, which has the 16 segments defined, onto the manually segmented myocardium using automatic image registration. As a result, we have labelled the myocardium at ED phase for each subject into 16 segments.

After the segmentation step, we extract the deformation fields from both cine untagged and tagged images simultaneously as described in Chapter 5 using the weighted similarity measure. The resulting deformation is used to initialise the registration of the next phase. This process continues until all the phases are registered with the reference image.

Once the cardiac motion pattern has been extracted the segmentation of the endo- and epicardial surfaces of the LV for all phases can then be achieved using the extracted motion: As mentioned before, the segmentation of the ED phase is achieved using manual delineation. After this, we propagate the segmentation from the ED phase to the other phases using the derived motion to achieve automatic segmentation of all frame in the sequence. In this procedure, the ED phase image is selected as the reference image. The segmentation of the reference image is then propagated to all the other phases using the registration results. Finally, having achieved the segmentation of the endo- and epicardial surfaces for all cardiac phases, we compute the volume of the endocardium and the surface distance between the two surfaces for each segment of the LV myocardium.

The myocardial deformation and strain are computed from the deformation field of the myocardium. Having obtained the deformation fields  $\mathbf{d}(\mathbf{x}, i)$  for voxel  $\mathbf{x}$ , from the ED phase

to phase  $i$ , the magnitude of the myocardial motion is computed as follows:  $m(\mathbf{x}) = |\mathbf{d}(\mathbf{x}, i)|$ . To calculate the strain we use the Lagrangian strain tensor [Ogden, 1997] which is defined as  $\mathbf{S} = \mathbf{J}^t \mathbf{J} - \mathbf{I}$  where  $\mathbf{J}$  denotes the Jacobian matrix of the transformation and  $\mathbf{I}$  the identity tensor. The strain tensor describes the strain along any direction. Strain can then be calculated in the longitudinal, radial and circumferential directions defined in the cardiac coordinate system [Elen et al., 2008] using the following definitions: Longitudinal strain  $\mathbf{S}_l = \mathbf{L}^t \cdot \mathbf{S} \cdot \mathbf{L}$ , radial strain  $\mathbf{S}_r = \mathbf{R}^t \cdot \mathbf{S} \cdot \mathbf{R}$  and circumferential strain  $\mathbf{S}_c = \mathbf{C}^t \cdot \mathbf{S} \cdot \mathbf{C}$ .

To assess global LV dyssynchrony we calculate the time taken to reach maximum muscle thickness, peak deformation or strain for each of the 16 segments as a percentage of the cardiac cycle. The SDI is then defined as the SD of these timings with a high SDI denoting more dyssynchrony. To allow comparison between patients with different heart rates the SDI are expressed as a percentage of the cardiac cycle. For segments to be included in SDI computation, the muscle thickening of them should be greater than one millimetre or 10% of the diastolic wall thickness. Figure 7.1 shows the graphs for volume change, thickening, deformation and strain over the cardiac cycle from a patient, which allows us to visually study and interpret the difference of the four methods in LV contraction study.

## 7.2.4 Results

Based on the framework we proposed here, various SDIs are calculated. We found a strong relationship between volume derived SDI and acute response ( $p = 0.008$ ) and remodelling ( $p < 0.001$ ) (Figure 7.2). We found a weaker relationship with remodelling and muscle thickening SDI ( $p = 0.001$ ) (Figure 7.2) and no relationship with a SDI derived from strain indexes (Figure 7.3). More details and further discussions are published in [Duckett et al., 2012].

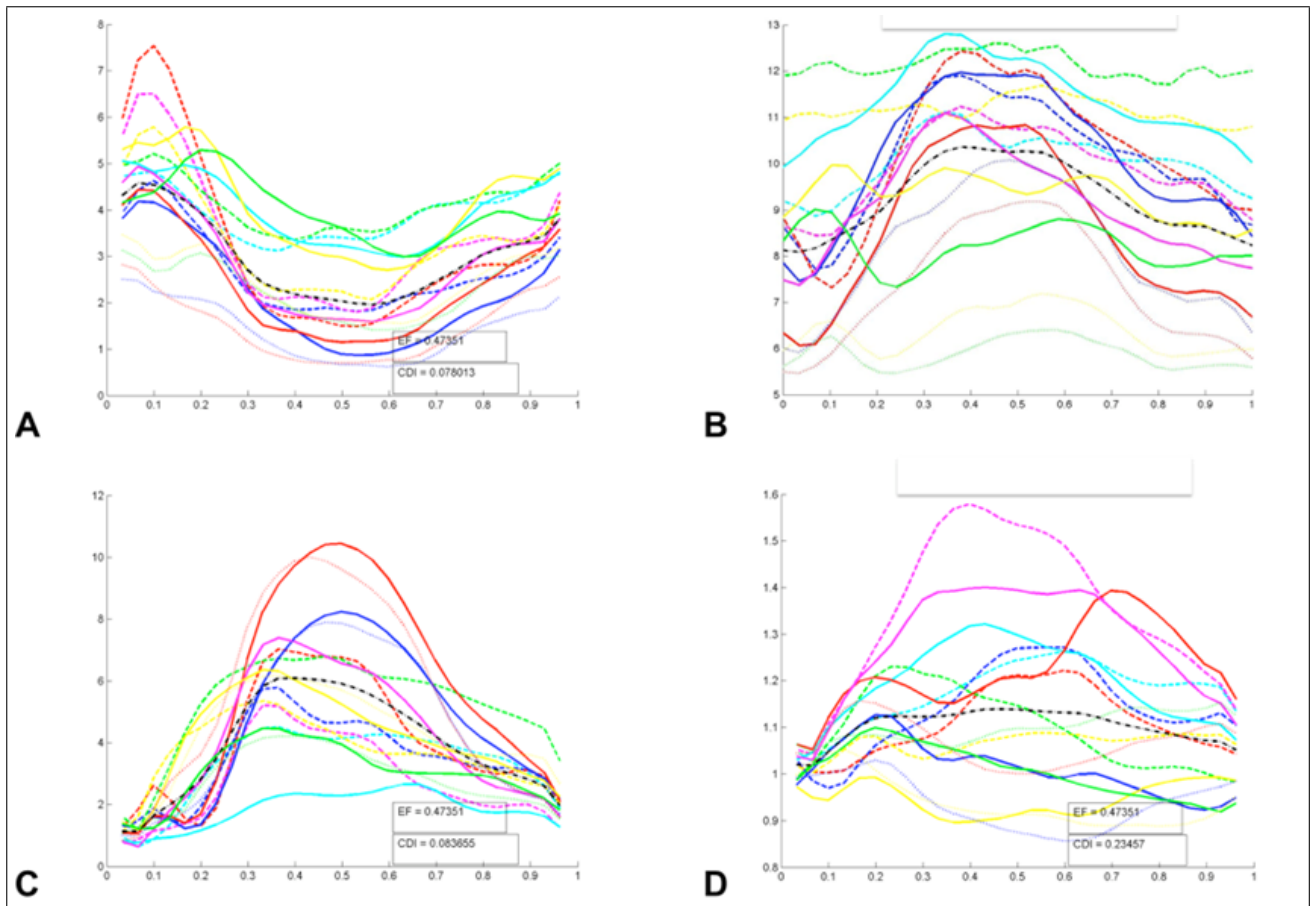


**Figure 7.1** – This figure shows the graphs for **SDI** derived from (A) volume change (in %), (B) **SA** muscle thickening (in %), (C) deformation (in mm) and (D) strain (in %) in a patient with dilated cardiomyopathy. Each curve represents one of the 16 segments over the cardiac cycle.

## 7.3 Application to remodelling after acute myocardial infarction

In this section, we examine the feasibility of using a 3D probabilistic cardiac atlas together with image registration to map the anatomic changes that occur over time in response to acute **STEMI**. For this we modify the proposed segmentation framework developed in Chapter 4 to enable it work with **SSFP** images as well as **LGE** images. Using the **MCEM** estimation developed, we segment not only the myocardium but also the region of the infarct. Finally, we estimate a set of remodelling indices to quantify and characterise the longitudinal changes occurring during remodelling.

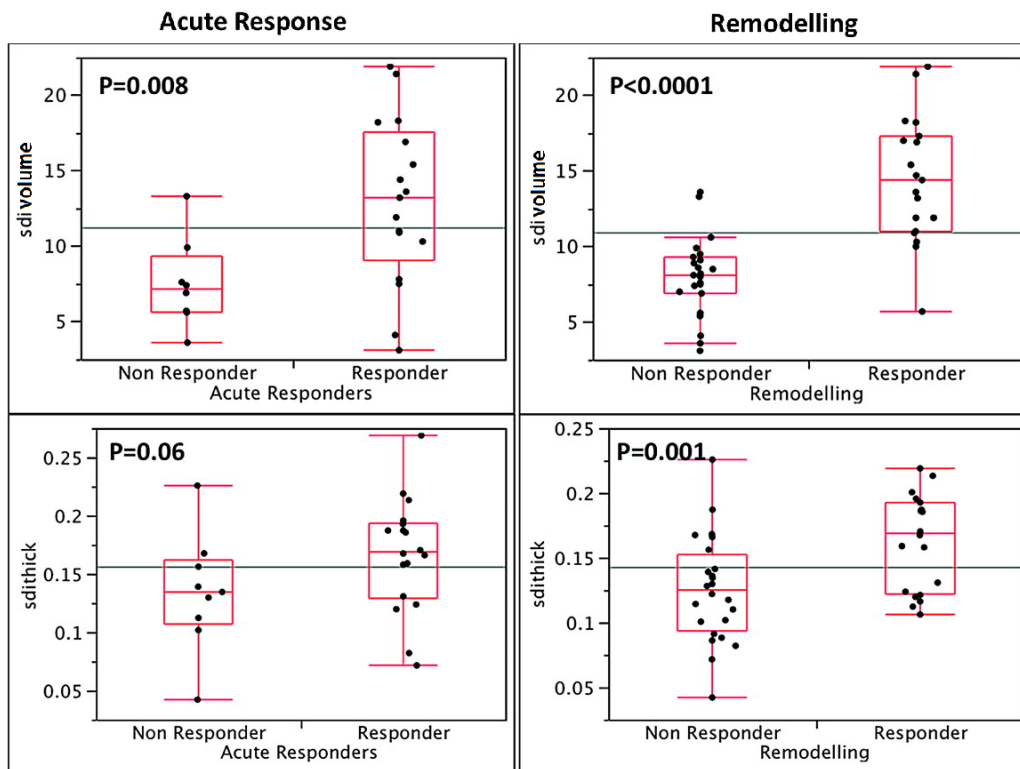


**Figure 7.2** – This figure shows the plots for acute response and remodelling against SDI derived from volume and muscle thickening. [Duckett et al., 2012]

### 7.3.1 Introduction

The heart adaptively responds following myocardial infarction in order to maintain cardiac output. While these effects are beneficial in the short term, they may eventually lead to congestive heart failure [Gaudron et al., 1993] in the longer term. Early remodelling occurs within the first few days and involves slippage and stretching of myocytes within the infarcted zone [Weisman et al., 1988]. Late remodelling also involves changes to the healthy myocardium, resulting in contractile segments becoming elongated [Mitchell et al., 1992]. Determining the evolution of left ventricular remodelling and the relative contribution made by infarcted and remote myocardium to chamber dilatation has importance for evaluating interventions aimed at preventing congestive heart failure.

Atlas-based analysis of cardiac MR images enables delineation and registration of cardiac structures using spatial a-priori information in the form of a probabilistic atlas. Such atlases [Lorenzo-Valdés et al., 2004, Zhuang et al., 2010] are created from the average of a number of manually segmented anatomical images which are transformed into a single reference space.

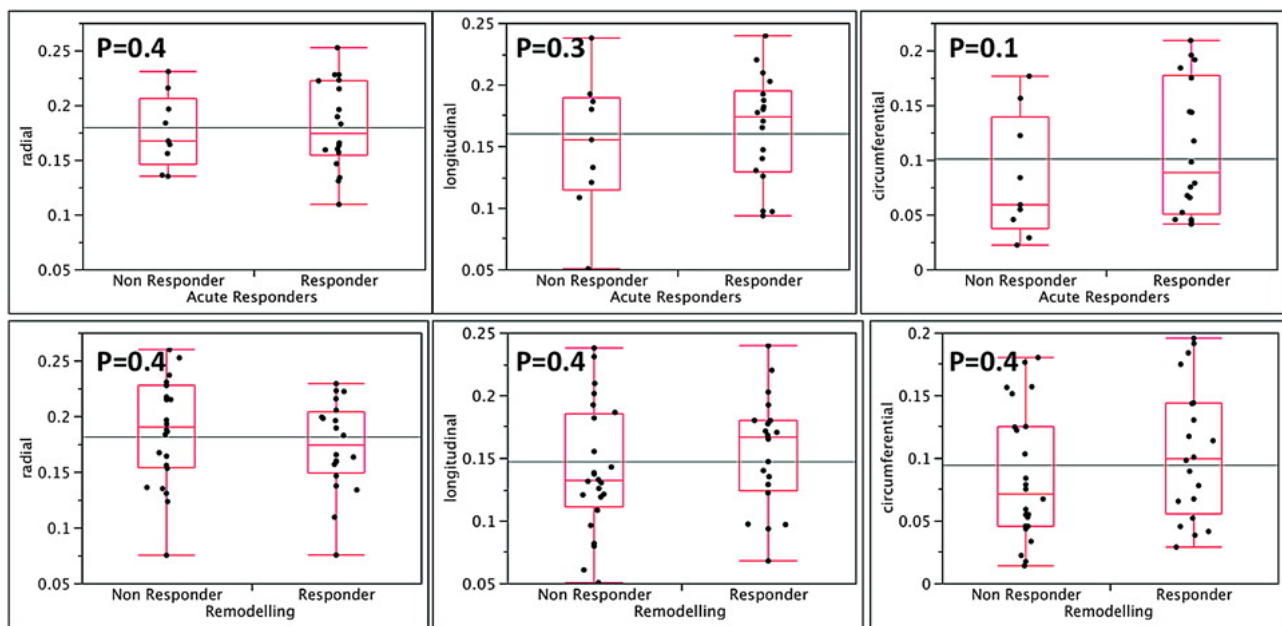


**Figure 7.3** – This figure shows the plots for acute response (top row) and remodelling (bottom row) against SDI derived from different strains. [Duckett et al., 2012]

In this section, we apply atlas-based techniques to align and co-register images of the heart in a prospective cohort study to map the evolution of remodelling over time. This approach can enable consistent and quantitative comparisons to be made between different cardiac MR sequences obtained at various time-points. Regional changes in geometry can be measured by transforming the baseline images onto the segmentation obtained at follow-up. This transformation can be used to reveal how local changes in curvature, thickness and expansion of the left ventricular wall evolve following acute infarction. However, developing these techniques in the heart is challenging as it requires a consistent and accurate approach to co-register and transform the 3D cardiac MR images acquired in a longitudinal study.

### 7.3.2 Image acquisition

In total 46 patients (age range, 33-77 years; mean age 55 years) underwent cardiac MR imaging within 7 days following primary percutaneous coronary intervention for acute STEMI with follow-up at one year. The CMR studies were performed on a 1.5T Philips Achieva system (Best, Netherlands) using 32-channel coil. A multiple slice, cine SSFP scan was performed in SA orientation (image resolution  $2.0 \times 2.2 \times 8\text{mm}$ , 20 heart phases). The scan duration

of every two cine slice is approximately 12 seconds. An intravenous bolus of Gadobutrol 1.0 mmol/ml was administered at a dose of 0.15 mmol/kg. LGE imaging was performed to assess infarct size 10 minutes after contrast injection with a 2D inversion recovery sequence (resolution  $1.6 \times 2.2 \times 8\text{mm}$ ). The scan duration for each slice is approximately 8 seconds. The atlas of healthy volunteers was created from left ventricular SA cine images acquired on a 1.5T Siemens Sonata system [Lorenzo-Valdés et al., 2004].

### 7.3.3 Methods

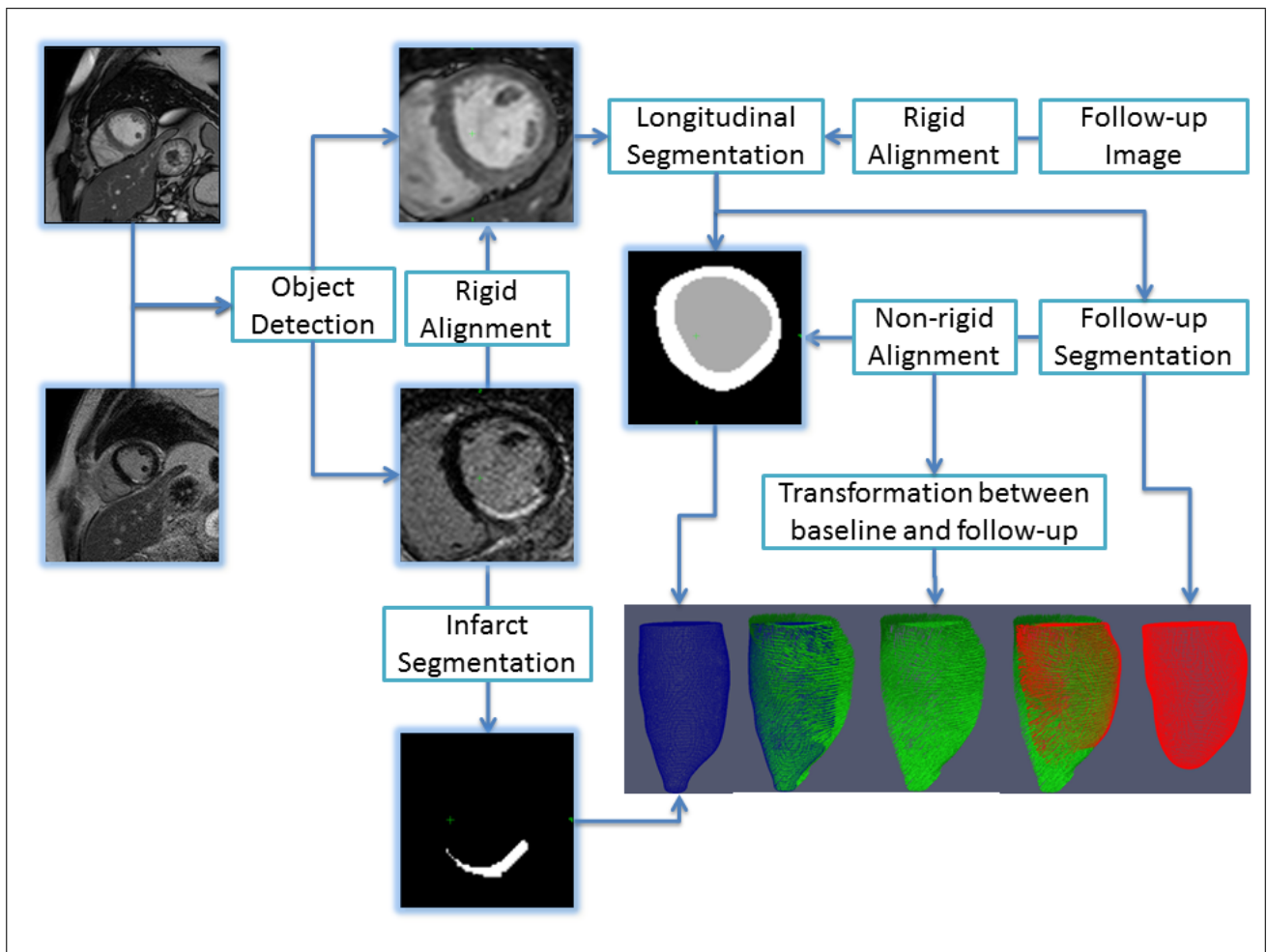


**Figure 7.4** – Flow chart showing the main steps for co-registering and segmenting the cardiac MR images to obtain a 3D transformation between baseline and follow-up images.

The segmentation of cine and LGE images in a longitudinal study poses additional challenges to the segmentation framework we have proposed in Chapter 4. A summary of the steps in the modified analysis process is shown in Figure 7.4. In this application, one of the difficulties arises

from that fact that there is no 3D image available to serve as the reference image during the spatial and temporal alignment stage. In this case, we correct the intra-sequence misalignment by utilising the spatial and temporal information embedded in each of the cine slices. A 2D in-plane translation is used for every cine slice to allow for misregistration between slices as the result of different breath-hold positions. The registration is optimised between 2D+t neighbouring slices to fully utilise the temporal information. The similarity metric used in the registration is defined as a combination of the similarity between the short-axis slices over time. After that, we use the cine image as the reference space and register the LGE image to this reference space using a 3D rigid transformation as well as multiple 2D in-plane translations.

The heart is localised in the SA MR images using the object-detection approach described in Section 4.2.1. The follow-up image is rigidly registered to the baseline image. A probabilistic atlas is registered to both the baseline and follow-up images using affine, local affine and then non-rigid registration independently. Details are described in Section 4.2.3. To obtain a consistent segmentation of the follow-up and baseline images, we propose to use a 4D graph-cuts approach to jointly segment the follow-up and baseline images. This can be achieved using a variation of the segmentation proposed in Chapter 4 in which the multiple image sequences are replaced with the follow-up and baseline images: We modify the term  $S^{inter}$  in Equation 4.14 so that it becomes equal to  $S^{intra}$  in Equation 4.13. We use the MCEM estimation with spatial information from the probabilistic atlas to assign each voxel a probability of background, blood pool or myocardium.

To segment the infarcted myocardium, a further EM segmentation step is then used for the LGE images to define a boundary between enhancing and non-enhancing voxels in order to classify voxels as infarct or remote regions. The infarct percentage is calculated as the volume of enhanced tissue divided by the total volume of myocardial tissue. The transmural extent of infarction is calculated as the proportion of infarcted myocardium in the radial direction of the left ventricular wall.

A 3D mesh reconstruction of the endocardial and epicardial surfaces is created from the baseline segmentation using shape based interpolation [Grevera and Udupa, 2002] and marching cubes

[Lorensen and Cline, 1987]. To enable longitudinal comparisons, a further non-rigid registration between the segmentations from baseline and follow-up images is used to measure the structural changes in the myocardium using SSD. The follow-up mesh is then constructed by propagating the baseline mesh using the transformation obtained from the intensity-based registration. This process enables a one-to-one correspondence of the number and position of mesh vertices during the transformation (Figure 7.4).

The infarct location is used in the rigid registration but not in the non-rigid registration so that any infarct extension will not influence the longitudinal assessment. Points adjacent to the mitral annulus and the left ventricular apex are excluded from the analysis as the calculation of wall thickness is sensitive at these locations. The myocardial wall expansion is defined as the mean change in separation in all directions between each vertex on the mesh and its surrounding neighbours. Wall thickness is calculated along lines joining an epicardial vertex to the nearest endocardial vertex. Regional wall curvature is assessed by calculating the reciprocal of the radius of a sphere aligned to the inner surface of the ventricular mesh in units of  $mm^{-1}$  multiplied by a scaling factor (Appendix C). The curvature value is a measure of the extent to which a region deviates from a flat surface such that a higher value indicates a more spherical geometry and is determined by radial, circumferential and meridional shape. An example of the derived remodelling indices of a patient is illustrated in Figure 7.5.

### 7.3.4 Results

A dot density histogram for each variable derived from the image registration model at baseline and follow-up is illustrated in Figure 7.6. The results suggest the following longitudinal change. Wall expansion within infarcted myocardium was greater than in non-infarcted myocardium. Wall thickness within the infarcted region decreased significantly during the first year and was unchanged in the remote region. Wall curvature increased in both the infarcted region and remote region over the follow-up period. More details and further discussions are published in [Oregon et al., 2012].

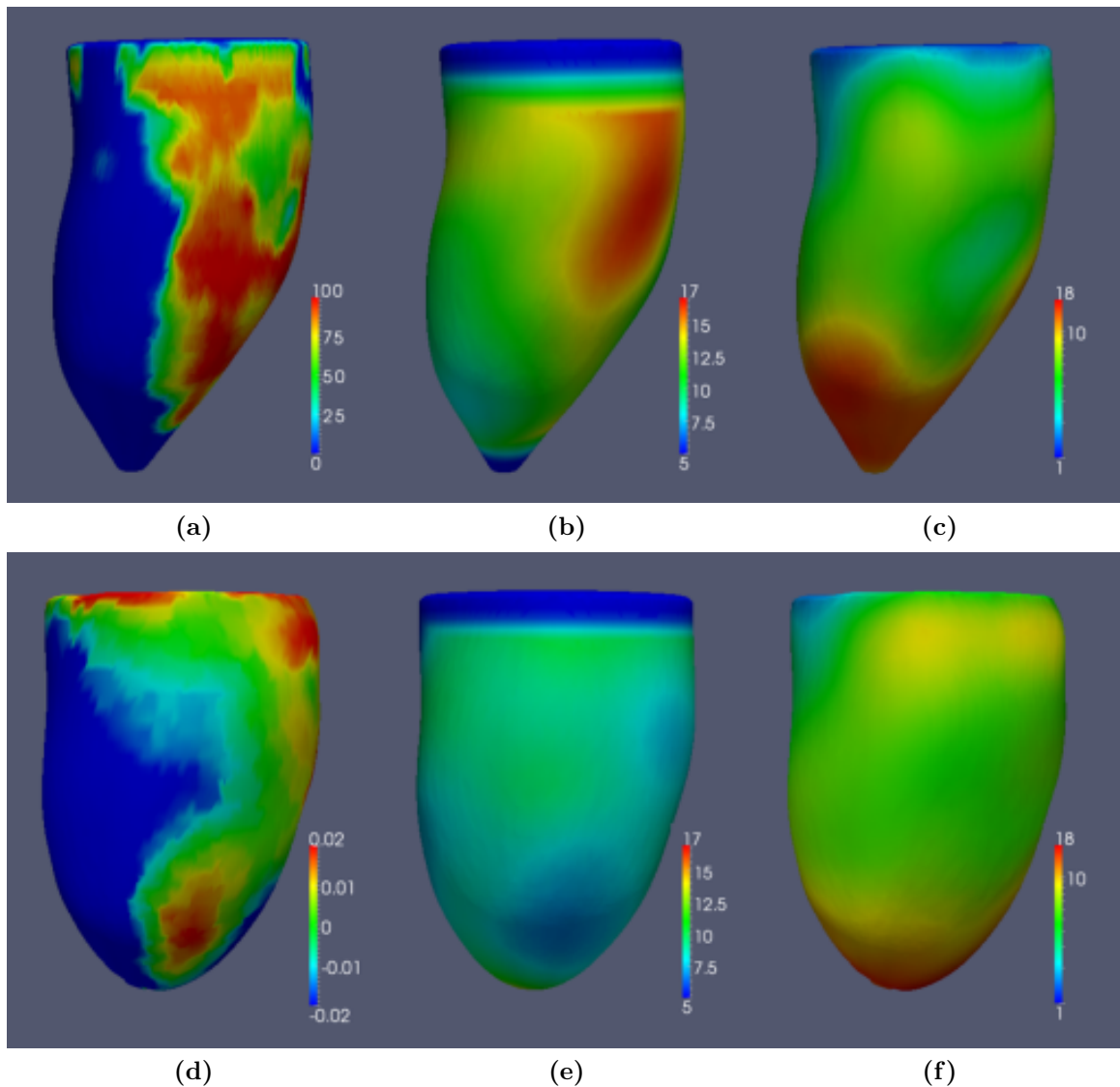


**Figure 7.5** – (a - c). 3D model of the LV in an 51 year old male patient following primary coronary intervention to a left circumflex artery occlusion 3 days previously. The model has been rotated so that lateral wall is nearest the viewpoint and the interventricular septum is furthest away. The model has co-registered LGE and SSFP MR images to a probabilistic atlas. (a) Distribution of enhancing necrosis (transmural percentage of infarcted myocardium). (b) Left ventricular wall thickness (mm). (c) Regional wall curvature ( $1/\text{mm} \times 10^{-4}$ ). (d - f). 3D model of the LV in the same 51 year old male patient demonstrating the changes in morphology at one year following acute STEMI. The same segmentation obtained at baseline has been propagated to the follow-up images. (d) Regional wall expansion ratio (proportional change in adjacent point separation). (e) LV wall thickness (mm). (f) Regional wall curvature ( $1/\text{mm} \times 10^{-4}$ ). [Oregon et al., 2012]

## 7.4 Discussion and conclusions

In this chapter, we have applied our techniques in previous chapters to two clinical applications. We have developed a framework for comparing measures of myocardial motion from cardiac

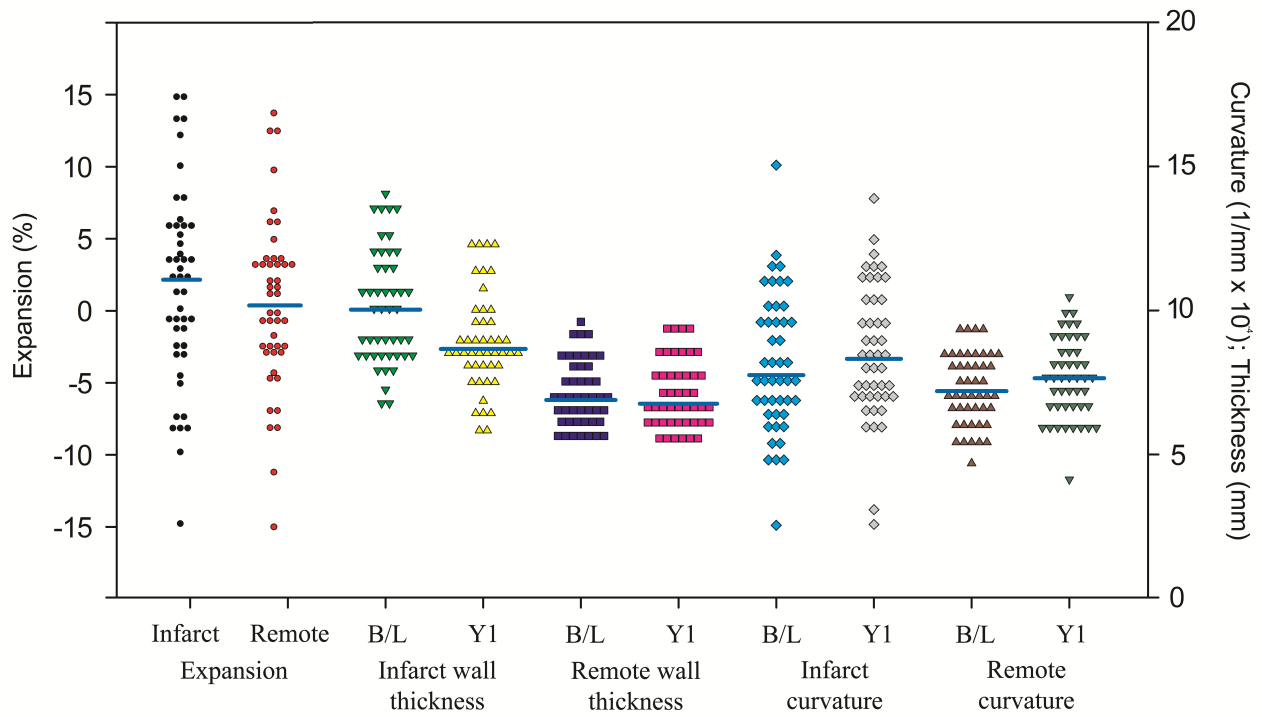


**Figure 7.6** – A Dot density histogram for each variable derived from the image registration model at baseline and follow-up. Each point represents data from an individual patient. [Oregon et al., 2012]

MR imaging and evaluated how these techniques can aid in predicting response to CRT. We also examined the feasibility of using a 3D probabilistic cardiac atlas and image registration to map the anatomic changes that occur over time in response to acute STEMI. In next chapter, we will summarise the works we have presented in this thesis and point out some limitations as well as further research directions.

# Chapter 8

## Conclusion

### 8.1 Summary of current achievements

Providing global and regional cardiac indices from cardiac MRI is one of the fundamental topics of research in medical image analysis. The ability to accurately extract and precisely interpret these indices may enable the development of many novel clinical applications, including early diagnosis, optimisation of treatment and follow-up. Cardiac segmentation, especially *LV* segmentation, provides important morphological information as well as the anatomical basis to calculate global and regional indices such as *EDV*, *LVM* etc. On the other hand, cardiac motion tracking provides important dynamic information during the cardiac cycle to help the estimation of global indices like *EF* as well as regional indices such as *RWM*, *RWN*, *RMSt*.

Different *CMR* image sequences can be acquired in a clinical setting. These different image sequences provide complementary information about the cardiac function. Each imaging sequence has its own advantages and disadvantages: *SA* and *LA* cine *MR* images provide good in-plane resolution in the *SA* and *LA* direction and dynamic information throughout the cardiac cycle. The cardiac anatomy, and in particular the myocardium, is clearly visible in each slices. However, their through-plane resolution is poor. Furthermore, each slice requires a separate breath-hold leading to potential misalignment between slices due to respiratory motion. In terms of cardiac motion, the radial motion of the myocardium can be tracked easily

in untagged cine MR images, since the epi- and endocardial surfaces are clearly visible. On the other hand, the circumferential and longitudinal motion cannot be accurately quantified as there are few features inside the myocardium that can be reliably tracked and there are often not enough long-axis images available. In contrast to this, whole-heart 3D TFE images provide nearly isotropic 3D resolution of the whole heart. However, only one or two phases are typically available, limiting the usefulness of these images to assess cardiac motion. Finally, 3D tagged MR images allow the easy tracking of both longitudinal and circumferential motion. However, in 3D tagged MR images, it is difficult to identify and quantify the cardiac anatomy as the tags obscure the anatomy. Furthermore, the tags degrade progressively throughout the cardiac cycle.

The work in this thesis has been focused on the development of a fully automatic cardiac image analysis framework, using cardiac segmentation and motion tracking techniques from multiple MR sequences simultaneously. CMR images acquired within a single scanning session may have different spatial positions, due to patient movement or different respiratory positions during breath-hold, as well as different temporal resolutions. This misalignment between the different image sequences will cause inconsistencies in the cardiac image analysis framework. Thus, we have developed a spatial and temporal registration approach that registers all the images into a common spatio-temporal reference space.

In addition, we have proposed a combination of state-of-art techniques to segment the LV from multiple MR image sequences. A 3D probabilistic atlas is registered to all untagged image sequences at the same time using a registration algorithm based on LARM and FFDs. The use of LARM [Zhuang et al., 2010] provides an extra degree of robustness towards large anatomical shape variations and pathologies. We estimate the probability of the different anatomical structures using the MCEM estimation. The MCEM algorithm, compared to EM, can estimate the probability of myocardium even in the presence of local varying contrast caused by myocardial infarction. Finally, a multi-image graph cuts approach is developed to refine the segmentation across all images sequences simultaneously. Our experiments have shown that the proposed framework can delineate the LV myocardium accurately in different patient groups. The approach benefits from the additional information provided by the different

image sequences. We have shown that the uncertainty in the probabilistic framework is a valuable source of information in the identification of possible segmentation failures, as well as in distinguishing among different pathologies.

To extract motion information from both untagged and tagged images throughout the cardiac cycle, we have extended a registration algorithm that has been previously used successfully for motion tracking [Chandrashekhara et al., 2004]. In the registration approach, the motion is reconstructed by registering a sequence of images during the cardiac cycle to a reference image at end-diastole. The proposed approach uses stacks of SA and LA untagged MR cine images as well as a sequence of 3D tagged MR images. To allow fully automated motion tracking we use a Haar-feature based object detection algorithm [Viola and Jones, 2002, Pavani et al., 2009, Zheng et al., 2007] to detect a region of interest containing the LV before motion tracking. A spatially-varying, weighted similarity measure is used for the motion tracking using image registration. This similarity measure combines information from untagged and 3D tagged images. The weighting between the different images is spatially varying and depends on the intensity gradient and segmentation of the untagged MR images: at the epicardial and endocardial boundaries, the weighting favours information from the untagged MR images. Inside the myocardium the weighting favours information from the 3D tagged MR images. However, even with the simultaneous use of the tagged and untagged MR images, it is difficult to reconstruct the correct motion of the valve plane. We have explicitly tracked the valve plane using a regional tracker and constrained the estimated motion to be consistent with the motion estimated from the valve plane tracker. This leads to a more accurate estimation of the parameters of cardiac functions such as EF. Finally, we have shown that the comprehensive method outperforms tracking using untagged or tagged images alone, both in terms of accuracy and the extracted regional indices, such as regional strain and volume output.

Image registration is an important component in both cardiac segmentation and motion tracking techniques described above. The classic FFD approach [Rueckert et al., 1999] is one of the most widely used registration methods for medical image registration. One of the main difficulties of the classic FFD approach is the conflict between the robustness of the registration and the ability to model discontinuous and highly localised deformations. This conflict stems from the

fact that the **FFD** approach uses a smooth B-spline basis to model the contribution of each control point to the deformation. To model global and smooth deformations a coarse control point spacing is typically used. To allow for very localised deformations a fine control point spacing is required, making the method less robust. A conventional approach to address this issue uses a coarse-to-fine approach in which the initial coarse control point mesh is successively subdivided.

In this thesis, we have introduced a sparse representation for **FFDs** to estimate the registration transformation. This simple model uses the standard smoothness constraints and only imposes one assumption on the deformation, namely that the basis of the deformation is sparse in the parametric space of the deformation. Based on this assumption, the registration of two images is formulated by using a sparse multi-level **FFD** representation of the control points with coupled multi-level sparsity constraint. The novelty and contributions of this method are the introduction of a sparsity model that avoids the *a priori* selection of an appropriate control point grid spacing. Furthermore, the approach reduces the conflict between global smoothness and local detail of the transformation by optimising over the different **FFD** levels simultaneously with a sparsity constraint. These advantages allow for the robust estimation of deformation fields in the presence of discontinuous motion. The evaluation has demonstrated that the proposed method can consistently capture localised motion with high degrees of accuracy.

The ultimate objective of cardiac image analysis presented above is to provide useful and efficient tools for the diagnosis and treatment of patients with cardiovascular diseases. We have applied the techniques to two clinical applications. We have developed a framework for comparing measures of myocardial motion from cardiac **MR** imaging and evaluated how these techniques can aid in predicting responses to CRT. We also examined the feasibility of using a 3D probabilistic cardiac atlas and image registration to map the anatomic changes that occur over time in response to acute **STEMI**.

## 8.2 Limitations and future work

The thesis has focused on using image registration for cardiac function analysis using multiple MR sequences. The probabilistic, atlas-guided segmentation approach using image registration has three fundamental limitations: Firstly, it is difficult to consider thin regions, which can be critical in separating local substructures, using the intensity-based registration. Examples of such structure is the thin membrane that separates the epicardium and the liver. The membrane is usually displayed as thin regions whose intensity value differs from both the epicardium and the liver. Intensity-based registration techniques may fail to recognise this important anatomical structure due to the small size, meaning it contributes little to the final registration result. Secondly, the segmentation framework is difficult to recover from any registration error during the propagation phase. Finally, the registration approach is computationally expensive compared to other segmentation techniques.

An alternative segmentation approach which has recently attracted significant interest is nonlocal patch-based segmentation [Coupé et al., 2011]. In this approach, the segmentation is achieved by labelling each voxel individually by comparing its surrounding patch with patches in atlases after registration. By using this method, several samples from each atlas can be used during the decision fusion. As an extension of the conventional single atlas segmentation approach, it can be used to address some of the problems mentioned above. Furthermore, due to its nonlocal nature, a coarser registration can be used which reduces the computational cost and increases the registration robustness.

When extracting cardiac motion from multiple MR image sequences, the inter- and intra-sequences misalignment due to respiratory motion is one of the major difficulties. We have developed a spatio-temporal registration scheme to correct such misalignment using either whole-heart 3D image or the 3D tagged MR images. However, if the spatio-temporal registration fails, the different image sequences (e.g. the untagged and tagged MR images) may contain inconsistent motion information. This inconsistency will complicate the cardiac motion estimation and can lead to unrealistic motion estimates in local regions. To address this problem, we could extend the transformation model from 3D to 4D to avoid the need

for temporal alignment [Perperidis et al., 2005, De Craene et al., 2010]. However, this would add significant additional degrees of freedom to the motion estimation challenge. Feature-based registration [Kerwin and Prince, 1998, Kuhl et al., 2004, Sampath and Prince, 2007] may work well for spatial registration if multiple common landmarks can be detected from the different image sequences. However, such a motion tracking approach cannot recover from any accumulation of errors during the tracking. A combination of both approaches may be desirable to ensure both sensitivity and robustness in the motion tracking.

In our approach, we have used an automatic heart localisation algorithm to automatically extract the region of interest and eliminate the need for manual intervention. However, the computational time required for complete analysis is still approximately 3-4 hours. The bottleneck in terms of computational complexity is the image registration process. It is relatively easy to use analytical expressions for the gradients of the registration cost function [Modat et al., 2010] to improve the performance in terms of computational time.

One important characteristic of cardiac motion is that it is continuous in both space and time. In addition, the cardiac motion is typically periodic. [Metz et al., 2011] proposed a spatio-temporal 4D FFD model with periodic behaviour to improve the performance of the registration in the context of cardiac motion analysis. It would be desirable to extend our comprehensive framework to incorporate such a periodic behaviour.

Finally, both the cardiac segmentation and motion tracking framework are based on the concept of image registration. A potential extension of the two segmentation and motion tracking framework would be to replace the classic FFD registration with the proposed SFFD registration developed in Chapter 6. Using the SFFD approach, it avoids *a-priori* selection of deformation parameters like grid spacing to get optimal registration accuracy for different subjects.

# Appendix A

## List of publications

- Wenzhe Shi, Xiahai Zhuang, Luis Pizarro, Wenjia Bai, Haiyan Wang, Kai-Pin Tung, Philip Edwards, Daniel Rueckert. (2012). Registration using sparse free-form deformations. Medical Image Computing and Computer Assisted Intervention (MICCAI), in Press.
- Wenzhe Shi, Xiahai Zhuang, Haiyan Wang, Simon Duckett, Duy V.N. Luong, Catalina Tobon-Gomez, KaiPin Tung, Philip Edwards, Kawal Rhode, Reza Razavi, Sebastien Ourselin, Daniel Rueckert. (2012). A comprehensive cardiac motion estimation framework using both untagged and 3D tagged MR images based on non-rigid registration. IEEE Transactions on Medical Imaging, 31(6):1263-1275.
- Wenzhe Shi, Xiahai Zhuang, Robin Wolz, Duckett Simon, KaiPin Tung, Haiyan Wang, Sebastien Ourselin, Philip Edwards, Reza Razavi, and Daniel Rueckert. (2011). A multi-image graph cut approach for cardiac image segmentation and uncertainty estimation. Statistical Atlases and Computational Models of the Heart: Imaging and Modelling Challenges (STACOM), pages 178-187.
- Wenzhe Shi, Xiahai Zhuang, Haiyan Wang, Duckett Simon, Declan Oregan, Sebastien Ourselin, Eddie Edwards, Daniel Rueckert. (2011). Automatic segmentation from cardiac cine MRI with different pathologies using registration and multiple component

- EM estimation. *Functional Imaging and Modeling of the Heart (FIMH)*, pages 163-170.
- Wenzhe Shi, Maria Murgasova, Eddie Edwards, and Daniel Rueckert. (2010). Simultaneous Reconstruction of 4-D Myocardial Motion from Both Tagged and Untagged MR Images Using Nonrigid Image Registration. *Medical Imaging and Augmented Reality (MIAR)*, pages 98-107.
  - D. P. O'Regan, W. Shi, B. Ariff, A. J. Baksi, G. Durighel, D. Rueckert, S. A. Cook. (2012). Remodelling after acute myocardial infarction: mapping ventricular dilatation using three dimensional CMR image registration. *Journal of Cardiovascular Magnetic Resonance*, 14(1):41.
  - SG Duckett, W Shi, X Zhuang, A Shetty, M Ginks, CA Rinaldi, G Carr-White, D Rueckert, RS Razavi. (2012). Cardiac MRI: understanding myocardial motion to predict remodelling pre cardiac resynchronisation therapy. *Journal of Heart* 98:A6-A7.
  - Kai-Pin Tung, WenZhe Shi, Luis Pizarro Quiroz, HaiYan Wang, Ricardo Guerrero Moreno, Ranil De Silva, Philip Edwards, Daniel Rueckert. (2012). Automatic detection of coronary stent struts in intravascular OCT imaging. *SPIE Medical Imaging*, in Press.
  - Kai-Pin Tung, WenZhe Shi, Ranil de Silva, Eddie Edwards, Daniel Rueckert. (2011). Automated Segmentation of Coronary Vessel Wall in OCT Imaging. *Medical Image Analysis and Understanding (MIUA)*.
  - Kai-Pin Tung, WenZhe Shi, Ranil de Silva, Eddie Edwards, Daniel Rueckert. (2011). Automatic Vessel Wall Detection in Intravascular Coronary OCT. *IEEE International Symposium on Biomedical Imaging: From Nano to Macro (ISBI)*, pages 610-613.
  - Haiyan Wang, Wenzhe Shi, Xiahai Zhuang, Simon Duckett, Kai Pin Tung, Philip Edwards, Reza Razavi, Sebastien Ourselin, and Daniel Rueckert. (2011). Automatic cardiac motion tracking using both untagged and 3D tagged MR images. *Statistical Atlases and Computational Models of the Heart: Imaging and Modelling Challenges (STACOM)*, pages 45-56.

- Jie Shen, Wenzhe Shi and Maja Pantic. (2011). HCI<sup>2</sup> Workbench: A Development Tool for Multimodal Human-Computer Interaction Systems. Facial and Bodily Expressions for Control and Adaptation of Games (ECAG).
- Jiahe Xi , Pablo Lamata, Wenzhe Shi, Steven Niederer, Sander Land, Daniel Rueckert, Duckett Simon, Anoop Shetty, Aldo Rinald, Reza Razavi, Nic Smith. (2011). An automatic data assimilation framework for patient-specific myocardial mechanical parameter estimation. Functional Imaging and Modeling of the Heart (FIMH), pages 392-400.
- Xiahai Zhuang, Wenzhe Shi, S Duckett, Haiyan Wang, Reza Razavi, Daniel Rueckert, Sebastien Ourselin. (2011). A Framework Combining Multi-Sequence MRI for Fully Automated Quantitative Analysis of Cardiac Global And Regional Functions. Functional Imaging and Modeling of the Heart (FIMH), pages 367-374.

# Appendix B

## Derivation of energy gradient

Let  $\mathbf{x} = (x, y, z)$  stand for a world coordinate location and let  $\mathbf{u} = (u, v, w)$  denote a lattice coordinate for a free-form deformation (FFD). The FFD lattice represents the locations of the control point vectors  $\Phi_{l,m,n}$ . The dimensions of the FFD lattice are  $U$ ,  $V$  and  $W$  in the principal directions, we can index the control point vectors so that the subscripts  $l$ ,  $m$  and  $n$  each range from 0 to  $U - 1$ ,  $V - 1$  and  $W - 1$  respectively. The displacement  $\mathbf{h}(\mathbf{x})$  at world location  $\mathbf{x}$  with corresponding lattice coordinates  $\mathbf{u}$  is given by

$$\mathbf{h}(\mathbf{x}) = \sum_{l=0}^{U-1} \sum_{m=0}^{V-1} \sum_{n=0}^{W-1} B_l(u) B_m(v) B_n(w) \Phi_{l,m,n}$$

where  $B_l$ ,  $B_m$  and  $B_n$  are univariate cubic B-Spline kernels centred at  $l$ ,  $m$  and  $n$ . The transformation  $\mathbf{T}$  is obtained by additively applying the deformation:

$$\mathbf{T}(\mathbf{x}) = \mathbf{x} + \mathbf{h}(\mathbf{x})$$

so that the Jacobian of  $\mathbf{T}$  and the Jacobian of  $\mathbf{h} = (\mathbf{h}_x, \mathbf{h}_y, \mathbf{h}_z)$  are related by

$$\frac{\partial \mathbf{T}}{\partial \mathbf{x}} = I + \frac{\partial \mathbf{h}}{\partial \mathbf{x}}$$

where  $I$  is the identity matrix. We will restrict  $J$  to denote the Jacobian of  $\mathbf{T}$  so that, in the world coordinate frame, the Jacobian of the transformation is

$$J = \frac{\partial \mathbf{T}}{\partial \mathbf{x}} = I + \begin{pmatrix} \frac{\partial \mathbf{h}_x}{\partial x} & \frac{\partial \mathbf{h}_x}{\partial y} & \frac{\partial \mathbf{h}_x}{\partial z} \\ \frac{\partial \mathbf{h}_y}{\partial x} & \frac{\partial \mathbf{h}_y}{\partial y} & \frac{\partial \mathbf{h}_y}{\partial z} \\ \frac{\partial \mathbf{h}_z}{\partial x} & \frac{\partial \mathbf{h}_z}{\partial y} & \frac{\partial \mathbf{h}_z}{\partial z} \end{pmatrix} \quad (\text{B.1})$$

We assume that the origin of the world and lattice frames coincide so that the conversion between world and lattice coordinates can be achieved by matrix multiplication. Let  $M$  be the matrix to convert world coordinates to lattice coordinates, i.e.  $\mathbf{u} = M \mathbf{x}$ .

The number of degrees of freedom in the FFD is  $N$  where  $N = 3UVW$ . Let  $\phi = (\phi_0, \phi_1, \dots, \phi_{N-1})^T$  represent the parameter set of the FFD obtained by concatenating all the control point vectors  $\Phi_{l,m,n}$  into a single vector. These can be easily extended to multi-level FFD as described in the main sections.

The energy function to be optimised consists of three parts in a standard formulation [Rueckert et al., 1999]:

$$E = E_D + \lambda_r E_{smooth} + \lambda_v E_{vol}$$

The similarity energy is a spatially integrated function of the difference between images like SSD [Kybic and Unser, 2003]:

$$E_D = \int_{\Omega} D(I_t, I_s, \mathbf{T}, \mathbf{x}) d\mathbf{x}$$

where  $\Omega$  is a fixed region of interest and  $D(I_t, I_s, \mathbf{T}, \mathbf{x}) = (I_t(\mathbf{x}) - I_s(\mathbf{T}(\mathbf{x})))^2$  is the SSD between target image  $I_t$  and source image  $I_s$  after applying transformation  $\mathbf{T}$  at point  $\mathbf{x}$ . We require the gradient of this energy  $E_D$  with respect to the deformation parameters and we assume that  $D(I_t, I_s, \mathbf{T}, \mathbf{x})$ , as a function of the components of  $\phi$  and  $\mathbf{x}$ , satisfies the conditions for

differentiation under the integral sign. This means that we can write

$$\frac{\partial E_D}{\partial \phi} = \int_{\Omega} \frac{\partial D(I_t, I_s, \mathbf{T}, \mathbf{x})}{\partial \phi} d\mathbf{x} \quad (\text{B.2})$$

The differentiate of the integrand  $D(I_t, I_s, \mathbf{T}, \mathbf{x})$  can be easily derived and found in [Kybic and Unser, 2003]

$$\frac{\partial (I_t(\mathbf{x}) - I_s(\mathbf{T}(\mathbf{x})))^2}{\partial \phi_i} = \frac{\partial (I_t(\mathbf{x}) - I_s(\mathbf{T}(\mathbf{x})))^2}{\partial I_t(\mathbf{x})} \frac{\partial I_t(\mathbf{x})}{\partial \mathbf{x}} \frac{\partial \mathbf{x}}{\partial \phi_i}. \quad (\text{B.3})$$

where the first term  $\frac{\partial (I_t(\mathbf{x}) - I_s(\mathbf{T}(\mathbf{x})))^2}{\partial I_t(\mathbf{x})} = 2(I_t(\mathbf{x}) - I_s(\mathbf{T}(\mathbf{x})))$ , the second term equals to the gradient of  $I_t$  at  $\mathbf{x}$  and the third term  $\frac{\partial \mathbf{x}}{\partial \phi_i} = \frac{\partial \mathbf{h}(\mathbf{x})}{\partial \phi_i}$ . For information theory based similarity measures like NMI, readers are suggested to find the gradient in [Modat et al., 2010].

The smooth preservation energy is a spatially integrated function of the bending energy:

$$E_{smooth} = \frac{1}{|\Omega|} \int_{\Omega} \left[ \left( \frac{\partial^2 \mathbf{T}}{\partial x^2} \right)^2 + \left( \frac{\partial^2 \mathbf{T}}{\partial y^2} \right)^2 + \left( \frac{\partial^2 \mathbf{T}}{\partial z^2} \right)^2 + 2 \left( \frac{\partial^2 \mathbf{T}}{\partial xy} \right)^2 + 2 \left( \frac{\partial^2 \mathbf{T}}{\partial xz} \right)^2 + 2 \left( \frac{\partial^2 \mathbf{T}}{\partial yz} \right)^2 \right] d\mathbf{x} \quad (\text{B.4})$$

where  $|\Omega|$  is the size of the region. We require the gradient of this energy with respect to the deformation parameters. Abbreviating Equation B.4 as  $E_{smooth} = \frac{1}{|\Omega|} \int_{\Omega} [A^2 + B^2 + C^2 + 2D^2 + 2E^2 + 2F^2] d\mathbf{x}$ , the derivative of the penalty term with respect to a deformation parameter  $\phi_i$  involves a sum of derivatives each of which can be obtained using the chain rule, e.g.  $\frac{\partial (A^2)}{\partial \phi_i} = 2A \frac{\partial A}{\partial \phi_i}$ . The same chain rule can be applied to each and every component of the Equation B.4.

Finally, the volume preservation energy is a spatially integrated function of the determinant of the Jacobian,  $J$ :

$$E_{vol} = \int_{\Omega} (\log |J|)^2 d\mathbf{x}$$

where  $|\cdot|$  denotes the determinant of  $J$ . We require the gradient of this energy with respect to the deformation parameters and we assume that  $(\log(|J|))^2$ , as a function of the components

of  $\phi$  and  $\mathbf{x}$ , satisfies the conditions for differentiation under the integral sign. This means that we can write

$$\frac{\partial E_{vol}}{\partial \phi} = \int_{\Omega} \frac{\partial \log(|J|)^2}{\partial \phi} d\mathbf{x} \quad (\text{B.5})$$

Differentiating the integrand, we obtain

$$\frac{\partial (\log |J|)^2}{\partial \phi} = \frac{2 \log |J|}{|J|} \frac{\partial |J|}{\partial \phi}. \quad (\text{B.6})$$

$|J|$  and its logarithm are readily calculated so we require an expression for the gradient  $\frac{\partial |J|}{\partial \phi}$ . The  $i^{\text{th}}$  component of the  $\frac{\partial |J|}{\partial \phi}$  is given by

$$\frac{\partial |J|}{\partial \phi_i} = \text{tr} \left( \text{adj}(J) \frac{\partial J}{\partial \phi_i} \right)$$

for  $i = 0 \dots N - 1$ , where  $\text{tr}(\cdot)$  denotes the trace and  $\text{adj}(\cdot)$  denotes the adjugate. We expand  $\frac{\partial J}{\partial \phi_i}$  to give

$$\begin{aligned} \frac{\partial J}{\partial \phi_i} &= \frac{\partial}{\partial \phi_i} \left( \frac{\partial \mathbf{T}}{\partial \mathbf{x}} \right) \\ &= \frac{\partial}{\partial \phi_i} \left( I + \frac{\partial \mathbf{h}}{\partial \mathbf{x}} \right) \\ &= \frac{\partial}{\partial \phi_i} \left( \frac{\partial \mathbf{h}}{\partial \mathbf{x}} \right) \\ &= \frac{\partial}{\partial \phi_i} \left( \frac{\partial \mathbf{h}}{\partial \mathbf{u}} \frac{\partial \mathbf{u}}{\partial \mathbf{x}} \right) \end{aligned} \quad (\text{B.7})$$

We have

$$\frac{\partial \mathbf{u}}{\partial \mathbf{x}} = M,$$

where  $M$  is the constant world to lattice transformation matrix, so, after applying the product rule to Equation B.7, we obtain

$$\frac{\partial}{\partial \phi_i} \left( \frac{\partial \mathbf{h}}{\partial \mathbf{u}} \frac{\partial \mathbf{u}}{\partial \mathbf{x}} \right) = \frac{\partial}{\partial \phi_i} \left( \frac{\partial \mathbf{h}}{\partial \mathbf{u}} \right) M = \frac{\partial^2 \mathbf{h}}{\partial \phi_i \partial \mathbf{u}} M$$

The term  $\frac{\partial \mathbf{h}}{\partial \mathbf{u}}$  is the Jacobian of the deformation in the frame of the FFD lattice. We can re-write

$\frac{\partial \mathbf{h}}{\partial \mathbf{u}}$  as three columns to obtain

$$\frac{\partial}{\partial \phi_i} \left( \frac{\partial \mathbf{h}}{\partial \mathbf{u}} \right) = \begin{bmatrix} \frac{\partial}{\partial \phi_i} \left( \frac{\partial \mathbf{h}}{\partial u} \right) & \frac{\partial}{\partial \phi_i} \left( \frac{\partial \mathbf{h}}{\partial v} \right) & \frac{\partial}{\partial \phi_i} \left( \frac{\partial \mathbf{h}}{\partial w} \right) \end{bmatrix} \quad (\text{B.8})$$

The effect of differentiating with respect to the  $i^{\text{th}}$  parameter  $\phi_i$  depends on whether it corresponds to a displacement in the  $u$ ,  $v$  or  $w$  direction of the lattice. The parameter vector  $\phi$  is obtained by concatenation of the control point vectors  $\Phi_{l,m,n}$  so that the parameters  $\phi_i$  correspond to  $u$ -displacements if  $i = 0 \pmod 3$ ,  $v$ -displacements if  $i = 1 \pmod 3$  and  $w$ -displacements if  $i = 2 \pmod 3$ .

Assume, for example, that parameter  $\phi_i$  corresponds to the first ( $u$ ) component of the specific control point vector  $\Phi_{\lambda,\mu,\nu}$ . Consider the first column of the matrix on the right of Equation B.8:

$$\begin{aligned} \frac{\partial}{\partial \phi_i} \left( \frac{\partial \mathbf{h}}{\partial u} \right) &= \frac{\partial}{\partial \phi_i} \sum_{l,m,n} \frac{dB_l(u)}{du} B_m(v) B_n(w) \Phi_{l,m,n} \\ &= \frac{\partial}{\partial \phi_i} \left[ \frac{dB_\lambda(u)}{du} B_\mu(v) B_\nu(w) \Phi_{\lambda,\mu,\nu} \right] \\ &= \begin{pmatrix} \frac{dB_\lambda(u)}{du} B_\mu(v) B_\nu(w) \\ 0 \\ 0 \end{pmatrix} \end{aligned}$$

The second and third columns can be found in a similar way to give

$$\frac{\partial}{\partial \phi_i} \left( \frac{\partial \mathbf{h}}{\partial \mathbf{u}} \right) = \begin{pmatrix} \frac{dB_\lambda(u)}{du} B_\mu(v) B_\nu(w) & B_\lambda(u) \frac{dB_\mu(v)}{dv} B_\nu(w) & B_\lambda(u) B_\mu(v) \frac{dB_\nu(w)}{dw} \\ 0 & 0 & 0 \\ 0 & 0 & 0 \end{pmatrix}$$

The cases where  $\phi_i$  corresponds to a second ( $v$ ) or third ( $w$ ) component of  $\Phi_{\lambda,\mu,\nu}$  can be found in a similar fashion. The resulting expressions can be substituted back via Equations B.8, B.7 and B.6 to provide the value for the gradient of the volume preservation energy term in Equation B.5.

# Appendix C

## Definition of wall-curvature

For any tetrahedron, there exists a circumsphere such that its vertices lie on the sphere's surface. We may therefore define four vertices on the ventricular model such that the circumscribed sphere approximates to the curvature of the surface in that region. For each cell in the model, we extended three vertices 10mm in length from the cell centre point and anchor them to the mesh surface to form a tetrahedron.

To obtain values of a convenient magnitude we used a scaling factor. The curvature ( $C$ ) was defined as a scaled inverse of the tetrahedron's circumsphere radius ( $r$ ):

$$C = \frac{10000}{r} \tag{C.1}$$

The radius of a given circumsphere of a tetrahedron can be defined as:

$$r = \frac{\sqrt{D_x^2 + D_y^2 + D_z^2 - 4ac}}{2|a|} \tag{C.2}$$

The equation for the circumsphere of the tetrahedron with polygon vertices is  $(x_i, y_i, z_i)$  for  $i = 1, \dots, 4$  is:

$$a \equiv \begin{vmatrix} x_1 & y_1 & z_1 & 1 \\ x_2 & y_2 & z_2 & 1 \\ x_3 & y_3 & z_3 & 1 \\ x_4 & y_4 & z_4 & 1 \end{vmatrix}, \quad c \equiv \begin{vmatrix} x_1^2 + y_1^2 + z_1^2 & x_1 & y_1 & z_1 \\ x_2^2 + y_2^2 + z_2^2 & x_2 & y_2 & z_2 \\ x_3^2 + y_3^2 + z_3^2 & x_3 & y_3 & z_3 \\ x_4^2 + y_4^2 + z_4^2 & x_4 & y_4 & z_4 \end{vmatrix}, \quad (\text{C.3})$$

and

$$D_x \equiv \begin{vmatrix} x_1^2 + y_1^2 + z_1^2 & y_1 & z_1 & 1 \\ x_2^2 + y_2^2 + z_2^2 & y_2 & z_2 & 1 \\ x_3^2 + y_3^2 + z_3^2 & y_3 & z_3 & 1 \\ x_4^2 + y_4^2 + z_4^2 & y_4 & z_4 & 1 \end{vmatrix}, \quad D_y \equiv - \begin{vmatrix} x_1^2 + y_1^2 + z_1^2 & x_1 & z_1 & 1 \\ x_2^2 + y_2^2 + z_2^2 & x_2 & z_2 & 1 \\ x_3^2 + y_3^2 + z_3^2 & x_3 & z_3 & 1 \\ x_4^2 + y_4^2 + z_4^2 & x_4 & z_4 & 1 \end{vmatrix}, \quad D_z \equiv \begin{vmatrix} x_1^2 + y_1^2 + z_1^2 & x_1 & y_1 & 1 \\ x_2^2 + y_2^2 + z_2^2 & x_2 & y_2 & 1 \\ x_3^2 + y_3^2 + z_3^2 & x_3 & y_3 & 1 \\ x_4^2 + y_4^2 + z_4^2 & x_4 & y_4 & 1 \end{vmatrix} \quad (\text{C.4})$$

# Bibliography

- [Aljabar et al., 2009] Aljabar, P., Heckemann, R., Hammers, A., Hajnal, J., and Rueckert, D. (2009). Multi-atlas based segmentation of brain images: Atlas selection and its effect on accuracy. *Neuroimage*, 46(3):726–738.
- [Amini et al., 1998] Amini, A., Chen, Y., Curwen, R., Mani, V., and Sun, J. (1998). Coupled B-snake grids and constrained thin-plate splines for analysis of 2D tissue deformations from tagged MRI. *IEEE Transactions on Medical Imaging*, 17(3):344–356.
- [Amini et al., 2001] Amini, A., Chen, Y., Elayyadi, M., and Radeva, P. (2001). Tag surface reconstruction and tracking of myocardial beads from SPAMM-MRI with parametric B-spline surfaces. *IEEE Transactions on Medical Imaging*, 20(2):94–103.
- [Amini and Prince, 2001] Amini, A. and Prince, J. L. (2001). *Measurement of cardiac deformations from MRI: Physical and mathematical models*, volume 23. Kluwer Academic Pub.
- [Artaechevarria et al., 2008] Artaechevarria, X., Muñoz-Barrutia, A., and Ortiz-de Solórzano, C. (2008). Efficient classifier generation and weighted voting for atlas-based segmentation: Two small steps faster and closer to the combination oracle. *SPIE Medical Imaging*, 6914(3):69141W–1.
- [Artaechevarria et al., 2009] Artaechevarria, X., Muñoz-Barrutia, A., and Ortiz-de Solorzano, C. (2009). Combination strategies in multi-atlas image segmentation: Application to brain MR data. *IEEE Transactions on Medical Imaging*, 28(8):1266–1277.

- [Arts et al., 2010] Arts, T., Prinzen, F., Delhaas, T., Milles, J., Rossi, A., and Clarysse, P. (2010). Mapping displacement and deformation of the heart with local sine-wave modeling. *IEEE Transactions on Medical Imaging*, 29(5):1114–1123.
- [Ashburner and Friston, 2005] Ashburner, J. and Friston, K. J. (2005). Unified segmentation. *NeuroImage*, 26(3):839 – 851.
- [Asman and Landman, 2012] Asman, A. and Landman, B. (2012). Non-local STAPLE: An intensity-driven multi-atlas rater model. *Medical Image Computing and Computer Assisted Intervention (MICCAI)*, pages 426–434.
- [Axel and Dougherty, 1989a] Axel, L. and Dougherty, L. (1989a). Heart wall motion: improved method of spatial modulation of magnetization for MR imaging. *Radiology*, 172(2):349–350.
- [Axel and Dougherty, 1989b] Axel, L. and Dougherty, L. (1989b). MR imaging of motion with spatial modulation of magnetization. *Radiology*, 171(3):841–845.
- [Axel et al., 2005] Axel, L., Montillo, A., and Kim, D. (2005). Tagged Magnetic Resonance imaging of the heart: a survey. *Medical Image Analysis*, 9(4):376–393.
- [Backhaus et al., 2010] Backhaus, M., Britten, R., Do Chung, J., Cowan, B., Fonseca, C., Medrano-Gracia, P., Tao, W., and Young, A. (2010). The cardiac atlas project: development of a framework integrating cardiac images and models. *Statistical Atlases and Computational Models of the Heart. Imaging and Modelling Challenges*, pages 54–64.
- [Baker et al., 2007] Baker, S., Scharstein, D., Lewis, J., Roth, S., Black, M., and Szeliski, R. (2007). A database and evaluation methodology for optical flow. In *International Conference on Computer Vision (ICCV)*, pages 1–8.
- [Bax et al., 2004] Bax, J., Bleeker, G., Marwick, T., Molhoek, S., Boersma, E., Steendijk, P., van der Wall, E., and Schalij, M. (2004). Left ventricular dyssynchrony predicts response and prognosis after cardiac resynchronization therapy. *Journal of the American College of Cardiology*, 44(9):1834–1840.

- [Bistoquet et al., 2008] Bistoquet, A., Oshinski, J., and Škrinjar, O. (2008). Myocardial deformation recovery from cine MRI using a nearly incompressible biventricular model. *Medical Image Analysis*, 12(1):69–85.
- [Bogen et al., 1980] Bogen, D., Rabinowitz, S., Needleman, A., McMahon, T., and Abelmann, W. (1980). An analysis of the mechanical disadvantage of myocardial infarction in the canine left ventricle. *Circulation research*, 47(5):728–741.
- [Boykov and Kolmogorov, 2003] Boykov, Y. and Kolmogorov, V. (2003). Computing Geodesics and Minimal Surfaces via Graph Cuts. In *International Conference on Computer Vision (ICCV)*, volume 2, pages 26–33.
- [Boykov et al., 2001] Boykov, Y., Veksler, O., and Zabih, R. (2001). Fast approximate energy minimization via graph cuts. *IEEE Transactions on Pattern Analysis and Machine Intelligence*, 23(11):1222–1239.
- [Bray, 1999] Bray, J. (1999). *Lecture notes on human physiology*. Wiley-Blackwell.
- [Camara et al., 2009] Camara, O., Oubel, E., Piella, G., Balocco, S., De Craene, M., and Frangi, A. (2009). Multi-sequence Registration of Cine, Tagged and Delay-Enhancement MRI with Shift Correction and Steerable Pyramid-Based Detagging. *International Conference on Functional Imaging and Modeling of the Heart (FIMH)*, pages 330–338.
- [Canny, 1986] Canny, J. (1986). A computational approach to edge detection. *IEEE Transactions on Pattern Analysis and Machine Intelligence*, (6):679–698.
- [Carr, 1958] Carr, H. (1958). Steady-state free precession in nuclear Magnetic Resonance. *Physical Review*, 112(5):1693.
- [Castillo et al., 2003] Castillo, E., Lima, J., and Bluemke, D. (2003). Regional myocardial function: Advances in MR imaging and analysis. *Radiographics*, 23(1):S127–S140.
- [Caudron et al., 2011] Caudron, J., Fares, J., Bauer, F., and Dacher, J. (2011). Evaluation of left ventricular diastolic function with cardiac MR imaging. *Radiographics*, 31(1):239–259.

- [Cerqueira et al., 2002] Cerqueira, M., Weissman, N., Dilsizian, V., Jacobs, A., Kaul, S., Laskey, W., Pennell, D., Rumberger, J., Ryan, T., and Verani, M. (2002). Standardized myocardial segmentation and nomenclature for tomographic imaging of the heart: a statement for healthcare professionals from the Cardiac Imaging Committee of the Council on Clinical Cardiology of the American Heart Association. *Circulation*, 105(4):539.
- [Chandler et al., 2006] Chandler, A., Pinder, R., Netsch, T., Schnabel, J., Hawkes, D., Hill, D., and Razavi, R. (2006). Correction of misaligned slices in multi-slice MR cardiac examinations by using slice-to-volume registration. In *International Symposium on Biomedical Imaging: From Nano to Macro (ISBI)*, pages 474–477.
- [Chandrashekara et al., 2004] Chandrashekara, R., Mohiaddin, R., and Rueckert, D. (2004). Analysis of 3D myocardial motion in tagged MR images using nonrigid image registration. *IEEE Transactions on Medical Imaging*, 23(10):1245–1250.
- [Chen et al., 2010] Chen, T., Wang, X., Chung, S., Metaxas, D., and Axel, L. (2010). Automated 3D motion tracking using gabor filter bank, robust point matching, and deformable models. *IEEE Transactions on Medical Imaging*, 29(1):1–11.
- [Christensen et al., 1996] Christensen, G., Rabbitt, R., and Miller, M. (1996). Deformable templates using large deformation kinematics. *IEEE Transactions on Image Processing*, 5(10):1435–1447.
- [Cigarroa et al., 1993] Cigarroa, C., Brickner, M., Alvarez, L., Wait, M., Grayburn, P., et al. (1993). Dobutamine stress echocardiography identifies hibernating myocardium and predicts recovery of left ventricular function after coronary revascularization. *Circulation*, 88(2):430–436.
- [Cleland et al., 2005] Cleland, J., Daubert, J., Erdmann, E., Freemantle, N., Gras, D., Kappenberger, L., and Tavazzi, L. (2005). The effect of cardiac resynchronization on morbidity and mortality in heart failure. *New England Journal of Medicine*, 352(15):1539–1549.

- [Collignon et al., 1995] Collignon, A., Maes, F., Delaere, D., Vandermeulen, D., Suetens, P., and Marchal, G. (1995). Automated multi-modality image registration based on information theory. In *Information processing in medical imaging (IPMI)*, pages 264–274.
- [Collins et al., 1995] Collins, D., Holmes, C., Peters, T., and Evans, A. (1995). Automatic 3D model-based neuroanatomical segmentation. *Human Brain Mapping*, 3(3):190–208.
- [Cootes et al., 1995] Cootes, T., Taylor, C., Cooper, D., Graham, J., et al. (1995). Active shape models-their training and application. *Computer Vision and Image Understanding*, 61(1):38–59.
- [Coupé et al., 2011] Coupé, P., Manjón, J., Fonov, V., Pruessner, J., Robles, M., and Collins, D. (2011). Patch-based segmentation using expert priors: Application to hippocampus and ventricle segmentation. *Neuroimage*, 54(2):940–954.
- [Cousty et al., 2010] Cousty, J., Najman, L., Couprie, M., Clément-Guinaudeau, S., Goissen, T., and Garot, J. (2010). Segmentation of 4D cardiac MRI: Automated method based on spatio-temporal watershed cuts. *Image and Vision Computing*, 28(8):1229–1243.
- [Dawant et al., 1999] Dawant, B., Hartmann, S., Thirion, J., Maes, F., Vandermeulen, D., and Demaerel, P. (1999). Automatic 3D segmentation of internal structures of the head in MR images using a combination of similarity and free-form transformations. I. methodology and validation on normal subjects. *IEEE Transactions on Medical Imaging*, 18(10):909–916.
- [De Craene et al., 2012] De Craene, M., Piella, G., Camara, O., Duchateau, N., Silva, E., Doltra, A., Dhooge, J., Brugada, J., Sitges, M., and Frangi, A. (2012). Temporal diffeomorphic free-form deformation: Application to motion and strain estimation from 3D echocardiography. *Medical Image Analysis*, 16(2):427 – 450.
- [De Craene et al., 2010] De Craene, M., Piella, G., Duchateau, N., Silva, E., Doltra, A., Gao, H., Dhooge, J., Camara, O., Brugada, J., Sitges, M., et al. (2010). Temporal diffeomorphic free-form deformation for strain quantification in 3D-US images. *Medical Image Computing and Computer Assisted Intervention (MICCAI)*, pages 1–8.

- [Dempster et al., 1977] Dempster, A., Laird, N., and Rubin, D. (1977). Maximum likelihood from incomplete data via the EM algorithm. *Journal of the Royal Statistical Society*, pages 1–38.
- [Deng and Denney Jr, 2005] Deng, X. and Denney Jr, T. (2005). Combined tag tracking and strain reconstruction from tagged cardiac MR images without user-defined myocardial contours. *Journal of Magnetic Resonance Imaging*, 21(1):12–22.
- [Donoho and Huo, 2001] Donoho, D. and Huo, X. (2001). Uncertainty principles and ideal atomic decomposition. *IEEE Transactions on Information Theory*, 47(7):2845–2862.
- [Dougherty et al., 1999] Dougherty, L., Asmuth, J., Blom, A., Axel, L., and Kumar, R. (1999). Validation of an optical flow method for tag displacement estimation. *IEEE Transactions on Medical Imaging*, 18(4):359–363.
- [Duckett et al., 2012] Duckett, S. G., Shi, W., Zhuang, X., Shetty, A., Ginks, M., Rinaldi, C. A., Carr-White, G., Rueckert, D., and Razavi, R. S. (2012). Cardiac MRI: understanding myocardial motion to predict remodelling pre cardiac resynchronisation therapy. *Heart*, 98:A6–A7.
- [Ecabert et al., 2008] Ecabert, O., Peters, J., Schramm, H., Lorenz, C., Von Berg, J., Walker, M., Vembar, M., Olszewski, M., Subramanyan, K., Lavi, G., et al. (2008). Automatic model-based segmentation of the heart in CT images. *IEEE Transactions on Medical Imaging*, 27(9):1189–1201.
- [Edvardsen et al., 2001] Edvardsen, T., Skulstad, H., Aakhus, S., Urheim, S., and Ihlen, H. (2001). Regional myocardial systolic function during acute myocardial ischemia assessed by strain Doppler echocardiography. *Journal of the American College of Cardiology*, 37(3):726–730.
- [Edwards et al., 1998] Edwards, G., Taylor, C., and Cootes, T. (1998). Interpreting face images using active appearance models. In *International Conference on Automatic Face and Gesture Recognition*, pages 300–305.

- [Elen et al., 2008] Elen, A., Choi, H., Loeckx, D., Gao, H., Claus, P., Suetens, P., Maes, F., and D'hooge, J. (2008). Three-dimensional cardiac strain estimation using spatio-temporal elastic registration of ultrasound images: A feasibility study. *IEEE Transactions on Medical Imaging*, 27(11):1580–1591.
- [Fischer et al., 1993] Fischer, S., McKinnon, G., Maier, S., and Boesiger, P. (1993). Improved myocardial tagging contrast. *Magnetic Resonance in Medicine*, 30(2):191–200.
- [Fisher, 1936] Fisher, R. (1936). The use of multiple measurements in taxonomic problems. *Annals of Human Genetics*, 7(2):179–188.
- [Florack et al., 2007] Florack, L., van Assen, H., and Suinesiaputra, A. (2007). Dense multiscale motion extraction from cardiac cine MR tagging using HARP technology. In *International Conference on Computer Vision (ICCV)*, pages 1–8.
- [Foppa et al., 2005] Foppa, M., Duncan, B., and Rohde, L. (2005). Echocardiography-based left ventricular mass estimation. how should we define hypertrophy? *Cardiovascular Ultrasound*, 3(1):17.
- [Frangi et al., 2001] Frangi, A., Niessen, W., and Viergever, M. (2001). Three-dimensional modeling for functional analysis of cardiac images: A review. *IEEE Transactions on Medical Imaging*, 20(1):2–5.
- [Freund and Schapire, 1995] Freund, Y. and Schapire, R. (1995). A decision-theoretic generalization of on-line learning and an application to boosting. In *Computational Learning Theory*, pages 23–37.
- [Fu et al., 2000] Fu, J., Chai, J., and Wong, S. (2000). Wavelet-based enhancement for detection of left ventricular myocardial boundaries in Magnetic Resonance images. *Magnetic Resonance Imaging*, 18(9):1135–1141.
- [Gaudron et al., 1993] Gaudron, P., Eilles, C., Kugler, I., and Ertl, G. (1993). Progressive left ventricular dysfunction and remodeling after myocardial infarction. potential mechanisms and early predictors. *Circulation*, 87(3):755–763.

- [Gering, 2003] Gering, D. (2003). Automatic segmentation of cardiac MRI. *Medical Image Computing and Computer Assisted Intervention (MICCAI)*, pages 524–532.
- [Glocker et al., 2008] Glocker, B., Komodakis, N., Tziritas, G., Navab, N., and Paragios, N. (2008). Dense image registration through MRFs and efficient linear programming. *Medical Image Analysis*, 12(6):731–741.
- [Goldenberg et al., 2001] Goldenberg, R., Kimmel, R., Rivlin, E., and Rudzsky, M. (2001). Fast geodesic active contours. *IEEE Transactions on Image Processing*, 10(10):1467–1475.
- [Goshtasby and Turner, 1995] Goshtasby, A. and Turner, D. (1995). Segmentation of cardiac cine MR images for extraction of right and left ventricular chambers. *IEEE Transactions on Medical Imaging*, 14(1):56–64.
- [Götte et al., 2001] Götte, M., van Rossum, A., Twisk, J., Kuijer, J., Marcus, J., and Visser, C. (2001). Quantification of regional contractile function after infarction: strain analysis superior to wall thickening analysis in discriminating infarct from remote myocardium. *Journal of the American College of Cardiology*, 37(3):808–817.
- [Grevera and Udupa, 2002] Grevera, G. and Udupa, J. (2002). Shape-based interpolation of multidimensional grey-level images. *IEEE Transactions on Medical Imaging*, 15(6):881–892.
- [Haber et al., 2000] Haber, I., Metaxas, D., and Axel, L. (2000). Three-dimensional motion reconstruction and analysis of the right ventricle using tagged MRI. *Medical Image Analysis*, 4(4):335–355.
- [Han et al., 2008] Han, X., Hoogeman, M., Levendag, P., Hibbard, L., Teguh, D., Voet, P., Cowen, A., and Wolf, T. (2008). Atlas-based auto-segmentation of head and neck CT images. *Medical Image Computing and Computer Assisted Intervention (MICCAI)*, pages 434–441.
- [Han et al., 2010] Han, Y., Chan, J., Haber, I., Peters, D., Zimetbaum, P., Manning, W., Yeon, S., et al. (2010). Circumferential myocardial strain in cardiomyopathy with and without left bundle branch block. *Journal of Cardiovasc Magnetic Resonance*, 12(2).

- [Hansen et al., 2008] Hansen, M., Larsen, R., Glocker, B., and Navab, N. (2008). Adaptive parametrization of multivariate B-splines for image registration. In *Computer Vision and Pattern Recognition (CVPR)*, pages 1–8.
- [Heckemann et al., 2006] Heckemann, R., Hajnal, J., Aljabar, P., Rueckert, D., and Hammers, A. (2006). Automatic anatomical brain MRI segmentation combining label propagation and decision fusion. *NeuroImage*, 33(1):115–126.
- [Heller et al., 2002] Heller, G., Cerqueira, M., Weissman, N., Dilsizian, V., Jacobs, A., Kaul, S., Laskey, W., Pennell, D., Rumberger, J., Ryan, T., et al. (2002). Standardized myocardial segmentation and nomenclature for tomographic imaging of the heart. *Journal of Nuclear Cardiology*, 9(2):240–245.
- [Horn and Schunck, 1981] Horn, B. and Schunck, B. (1981). Determining optical flow. *Artificial Intelligence*, 17(1-3):185–203.
- [Hu et al., 2003] Hu, Z., Metaxas, D., and Axel, L. (2003). In vivo strain and stress estimation of the heart left and right ventricles from MRI images. *Medical Image Analysis*, 7(4):435–444.
- [Huang et al., 1999] Huang, J., Abendschein, D., Davila-Roman, V., and Amini, A. (1999). Spatio-temporal tracking of myocardial deformations with a 4D B-spline model from tagged MRI. *IEEE Transactions on Medical Imaging*, 18(10):957–972.
- [Huang et al., 2010] Huang, S., Liu, J., Lee, L., Venkatesh, S., Teo, L., Au, C., and Nowinski, W. (2010). An image-based comprehensive approach for automatic segmentation of left ventricle from cardiac short axis cine MR images. *Journal of Digital Imaging*, pages 1–11.
- [Institute, 2010] Institute, T. H. (2010). <http://www.texasheartinstitute.org/hic/anatomy/coroanat.cfm>.
- [Isgum et al., 2009] Isgum, I., Staring, M., Rutten, A., Prokop, M., Viergever, M., and van Ginneken, B. (2009). Multi-atlas-based segmentation with local decision fusion—Application to cardiac and aortic segmentation in CT scans. *IEEE Transactions on Medical Imaging*, 28(7):1000–1010.

- [Jaochim Nesser et al., 2007] Jaochim Nesser, H., Sugeng, L., Corsi, C., Weinert, L., Niel, J., Ebner, C., Steringer-Mascherbauer, R., Schmidt, F., Schummers, G., Lang, R., et al. (2007). Volumetric analysis of regional left ventricular function with real-time three-dimensional echocardiography: validation by Magnetic Resonance and clinical utility testing. *Heart*, 93(5):572.
- [Jolly, 2006] Jolly, M. (2006). Automatic segmentation of the left ventricle in cardiac MR and CT images. *International Journal of Computer Vision*, 70(2):151–163.
- [Jolly et al., 2009] Jolly, M., Xue, H., Grady, L., and Guehring, J. (2009). Combining registration and minimum surfaces for the segmentation of the left ventricle in cardiac cine MR images. *Medical Image Computing and Computer Assisted Intervention (MICCAI)*, pages 910–918.
- [Kapetanakis et al., 2005] Kapetanakis, S., Kearney, M., Siva, A., Gall, N., Cooklin, M., and Monaghan, M. (2005). Real-time three-dimensional echocardiography. *Circulation*, 112(7):992–1000.
- [Kass, 2002] Kass, D. (2002). Ventricular dyssynchrony and mechanisms of resynchronization therapy. *European Heart Journal Supplements*, 4(suppl D):D23.
- [Kass et al., 1988] Kass, M., Witkin, A., and Terzopoulos, D. (1988). Snakes: Active contour models. *International Journal of Computer Vision*, 1(4):321–331.
- [Katz, 2005] Katz, A. (2005). *Physiology of the Heart*. Lippincott Williams & Wilkins.
- [Kaus et al., 2004] Kaus, M., Berg, J., Weese, J., Niessen, W., and Pekar, V. (2004). Automated segmentation of the left ventricle in cardiac MRI. *Medical Image Analysis*, 8(3):245–254.
- [Kedenburg et al., 2006] Kedenburg, G., Cocosco, C., Kothe, U., Niessen, W., Vonken, E., and Viergever, M. (2006). Automatic cardiac MRI myocardium segmentation using graphcut. In *SPIE Medical Imaging*, volume 6144, page 61440A.

- [Kerwin and Prince, 1998] Kerwin, W. and Prince, J. (1998). Cardiac material markers from tagged MR images. *Medical Image Analysis*, 2(4):339–353.
- [Kim et al., 1996] Kim, R., Chen, E., Lima, J., and Judd, R. (1996). Myocardial gd-dtpa kinetics determine mri contrast enhancement and reflect the extent and severity of myocardial injury after acute reperfused infarction. *Circulation*, 94(12):3318–3326.
- [Kim et al., 2007] Kim, S., Koh, K., Lustig, M., Boyd, S., and Gorinevsky, D. (2007). An interior-point method for large-scale L1-regularized least squares. *IEEE Journal of Selected Topics in Signal Processing*, 1(4):606–617.
- [Klein et al., 2010] Klein, S., Staring, M., Murphy, K., Viergever, M., and Pluim, J. (2010). Elastix: a toolbox for intensity-based medical image registration. *IEEE Transactions on Medical Imaging*, 29(1):196–205.
- [Koay and Basser, 2006] Koay, C. and Basser, P. (2006). Analytically exact correction scheme for signal extraction from noisy magnitude MR signals. *Journal of Magnetic Resonance*, 179(2):317–322.
- [Kramer et al., 1994] Kramer, C., Reichek, N., Ferrari, V., Theobald, T., Dawson, J., and Axel, L. (1994). Regional heterogeneity of function in hypertrophic cardiomyopathy. *Circulation*, 90(1):186.
- [Kuhl et al., 2004] Kuhl, H., Schreckenber, M., Rulands, D., Katoh, M., Schafer, W., Schummers, G., Bucker, A., Hanrath, P., and Franke, A. (2004). High-resolution transthoracic real-time three-dimensional echocardiography: quantitation of cardiac volumes and function using semi-automatic border detection and comparison with cardiac Magnetic Resonance imaging. *Journal of the American College of Cardiology*, 43(11):2083.
- [Kukulski et al., 2003] Kukulski, T., Jamal, F., Herbots, L., D’hooge, J., Bijmens, B., Hatle, L., De Scheerder, I., and Sutherland, G. (2003). Identification of acutely ischemic myocardium using ultrasonic strain measurements: A clinical study in patients undergoing coronary angioplasty. *Journal of the American College of Cardiology*, 41(5):810–819.

- [Kybic, 2009] Kybic, J. (2009). Bootstrap resampling for image registration uncertainty estimation without ground truth. *IEEE Transactions on Image Processing*, 19(1):64–73.
- [Kybic and Unser, 2003] Kybic, J. and Unser, M. (2003). Fast parametric elastic image registration. *IEEE Transactions on Image Processing*, 12(11):1427–1442.
- [Lapp et al., 2004] Lapp, R., Lorenzo-Valdés, M., and Rueckert, D. (2004). 3D/4D cardiac segmentation using active appearance models, non-rigid registration, and the Insight toolkit. *Medical Image Computing and Computer Assisted Intervention (MICCAI)*, pages 419–426.
- [Lardo et al., 2005] Lardo, A., Abraham, T., and Kass, D. (2005). Magnetic resonance imaging assessment of ventricular dyssynchrony: current and emerging concepts. *Journal of the American College of Cardiology*, 46(12):2223.
- [Lauterbur, 1973] Lauterbur, P. (1973). Image formation by induced local interactions: examples employing nuclear Magnetic Resonance. *Nature*, 242(5394):190–191.
- [Ledesma-Carbayo et al., 2005] Ledesma-Carbayo, M., Kybic, J., Desco, M., Santos, A., Suhling, M., Hunziker, P., and Unser, M. (2005). Spatio-temporal nonrigid registration for ultrasound cardiac motion estimation. *IEEE Transactions on Medical Imaging*, 24(9):1113–1126.
- [Lin and Duncan, 2004] Lin, N. and Duncan, J. (2004). Generalized robust point matching using an extended free-form deformation model: application to cardiac images. In *International Symposium on Biomedical Imaging: From Nano to Macro (ISBI)*, pages 320–323.
- [Lin et al., 2006] Lin, X., Cowan, B., and Young, A. (2006). Automated detection of left ventricle in 4D MR images: experience from a large study. *Medical Image Computing and Computer Assisted Intervention (MICCAI)*, pages 728–735.
- [Linguraru et al., 2010] Linguraru, M., Pura, J., Chowdhury, A., and Summers, R. (2010). Multi-organ Segmentation from Multi-phase Abdominal CT via 4D Graphs Using Enhancement, Shape and Location Optimization. *Medical Image Computing and Computer Assisted Intervention (MICCAI)*, pages 89–96.

- [Liu et al., 2006] Liu, N., Crozier, S., Wilson, S., Liu, F., Appleton, B., Trakic, A., Wei, Q., Strugnell, W., Slaughter, R., and Riley, R. (2006). Right ventricle extraction by low level and model-based algorithm. In *International Conference of the Engineering in Medicine and Biology Society*, pages 1607–1610.
- [Liu and Prince, 2010] Liu, X. and Prince, J. (2010). Shortest path refinement for motion estimation from tagged MR images. *IEEE Transactions on Medical Imaging*, 29(8):1560–1572.
- [Lorensen and Cline, 1987] Lorensen, W. and Cline, H. (1987). Marching cubes: A high resolution 3D surface construction algorithm. In *the 14th Annual Conference on Computer Graphics and Interactive Techniques*, pages 163–169.
- [Lorenzo-Valdés et al., 2004] Lorenzo-Valdés, M., Sanchez-Ortiz, G., Elkington, A., Mohiaddin, R., and Rueckert, D. (2004). Segmentation of 4D cardiac MR images using a probabilistic atlas and the EM algorithm. *Medical Image Analysis*, 8(3):255–265.
- [Lorenzo-Valdés et al., 2002] Lorenzo-Valdés, M., Sanchez-Ortiz, G., Mohiaddin, R., and Rueckert, D. (2002). Atlas-based segmentation and tracking of 3D cardiac MR images using non-rigid registration. *Medical Image Computing and Computer Assisted Intervention (MICCAI)*, pages 642–650.
- [Lorenzo-Valdes et al., 2003] Lorenzo-Valdes, M., Sanchez-Ortiz, G., Mohiaddin, R., and Rueckert, D. (2003). Segmentation of 4D cardiac MR images using a probabilistic atlas and the EM algorithm. *Medical Image Computing and Computer Assisted Intervention (MICCAI)*, pages 440–450.
- [Lotjonen et al., 2010] Lotjonen, J., Wolz, R., Koikkalainen, J., Thurfjell, L., Waldemar, G., Soininen, H., Rueckert, D., et al. (2010). Fast and robust multi-atlas segmentation of brain Magnetic Resonance images. *Neuroimage*, 49(3):2352–2365.
- [Lu et al., 2009] Lu, Y., Radau, P., Connelly, K., Dick, A., and Wright, G. (2009). Segmentation of Left Ventricle in Cardiac Cine MRI: An Automatic Image-Driven Method. In

- International Conference on Functional Imaging and Modeling of the Heart (FIMH)*, pages 339–347.
- [Lynch et al., 2006a] Lynch, M., Ghita, O., and Whelan, P. (2006a). Automatic segmentation of the left ventricle cavity and myocardium in MRI data. *Computers in Biology and Medicine*, 36(4):389–407.
- [Lynch et al., 2006b] Lynch, M., Ghita, O., and Whelan, P. (2006b). Left-ventricle myocardium segmentation using a coupled level-set with a priori knowledge. *Computerized Medical Imaging and Graphics*, 30(4):255–262.
- [Makela et al., 2002] Makela, T., Clarysse, P., Sipila, O., Pauna, N., Pham, Q., Katila, T., and Magnin, I. (2002). A review of cardiac image registration methods. *IEEE Transactions on Medical Imaging*, 21(9):1011–1021.
- [Mandapaka et al., 2006] Mandapaka, S., DAgostino, R., and Hundley, W. (2006). Does late gadolinium enhancement predict cardiac events in patients with ischemic cardiomyopathy? *Circulation*, 113(23):2676–2678.
- [Manglik et al., 2004] Manglik, T., Axel, L., Pai, W., Kim, D., Dugal, P., Montillo, A., and Qian, Z. (2004). Use of bandpass Gabor filters for enhancing blood-myocardium contrast and filling-in tags in tagged MR images. *Proc of ISMRM*, 11:1793.
- [Mansi et al., 2009] Mansi, T., Peyrat, J., Sermesant, M., Delingette, H., Blanc, J., Boudjemline, Y., and Ayache, N. (2009). Physically-Constrained Diffeomorphic Demons for the Estimation of 3D Myocardium Strain from Cine-MRI. In *International Conference on Functional Imaging and Modeling of the Heart (FIMH)*, page 210.
- [McCrohon et al., 2003] McCrohon, J., Moon, J., Prasad, S., McKenna, W., Lorenz, C., Coats, A., and Pennell, D. (2003). Differentiation of heart failure related to dilated cardiomyopathy and coronary artery disease using gadolinium-enhanced cardiovascular magnetic resonance. *Circulation*, 108(1):54–59.
- [McInerney and Terzopoulos, 1996] McInerney, T. and Terzopoulos, D. (1996). Deformable models in medical image analysis: A survey. *Medical Image Analysis*, 1(2):91–108.

- [Members et al., 2012] Members, W. G., Roger, V. L., Go, A. S., Lloyd-Jones, D. M., Benjamin, E. J., Berry, J. D., Borden, W. B., Bravata, D. M., Dai, S., Ford, E. S., Fox, C. S., Fullerton, H. J., Gillespie, C., Hailpern, S. M., Heit, J. A., Howard, V. J., Kissela, B. M., Kittner, S. J., Lackland, D. T., Lichtman, J. H., Lisabeth, L. D., Makuc, D. M., Marcus, G. M., Marelli, A., Matchar, D. B., Moy, C. S., Mozaffarian, D., Mussolino, M. E., Nichol, G., Paynter, N. P., Soliman, E. Z., Sorlie, P. D., Sotoodehnia, N., Turan, T. N., Virani, S. S., Wong, N. D., Woo, D., and Turner, M. B. (2012). Heart disease and stroke statistics-2012 update. *Circulation*, 125(1):e2–e220.
- [Mémín and Pérez, 2002] Mémín, E. and Pérez, P. (2002). Hierarchical estimation and segmentation of dense motion fields. *International Journal of Computer Vision*, 46(2):129–155.
- [Metz et al., 2011] Metz, C., Klein, S., Schaap, M., Van Walsum, T., and Niessen, W. (2011). Nonrigid registration of dynamic medical imaging data using nD+t B-splines and a groupwise optimization approach. *Medical Image Analysis*, 15(2):238–249.
- [Mitchell et al., 1992] Mitchell, G., Lamas, G., Vaughan, D., and Pfeffer, M. (1992). Left ventricular remodeling in the year after first anterior myocardial infarction: a quantitative analysis of contractile segment lengths and ventricular shape. *Journal of the American College of Cardiology*, 19(6):1136–1144.
- [Mitchell et al., 2002] Mitchell, S., Bosch, J., Lelieveldt, B., van der Geest, R., Reiber, J., and Sonka, M. (2002). 3D active appearance models: segmentation of cardiac MR and ultrasound images. *IEEE Transactions on Medical Imaging*, 21(9):1167–1178.
- [Mitchell et al., 2001] Mitchell, S., Lelieveldt, B., van der Geest, R., Bosch, H., Reiver, J., and Sonka, M. (2001). Multistage hybrid active appearance model matching: segmentation of left and right ventricles in cardiac MR images. *IEEE Transactions on Medical Imaging*, 20(5):415–423.

- [Mitchell et al., 2000] Mitchell, S., Lelieveldt, B., van der Geest, R., Schaap, J., Reiber, J., and Sonka, M. (2000). Segmentation of cardiac MR images: An active appearance model approach. In *SPIE Medical Imaging*, volume 3979, page 224.
- [Modat et al., 2010] Modat, M., Ridgway, G., Taylor, Z., Lehmann, M., Barnes, J., Hawkes, D., Fox, N., and Ourselin, S. (2010). Fast free-form deformation using graphics processing units. *Computer Methods and Programs in Biomedicine*, 98(3):278–284.
- [Montillo et al., 1996] Montillo, A., Metaxas, D., and Axel, L. (1996). Extracting tissue deformation using gabor filter banks. In *SPIE Medical Imaging*, volume 5369, page 2.
- [Nachtomy et al., 1998] Nachtomy, E., Cooperstein, R., Vaturi, M., Bosak, E., Vered, Z., and Akselrod, S. (1998). Automatic assessment of cardiac function from short-axis MRI: procedure and clinical evaluation. *Magnetic Resonance Imaging*, 16(4):365–376.
- [Ogden, 1997] Ogden, R. (1997). *Non-linear elastic deformations*. Dover Publications.
- [Oregan et al., 2012] Oregan, D., Shi, W., Ariff, B., Baksi, A., Durighel, G., Rueckert, D., and Cook, S. (2012). Remodeling after acute myocardial infarction: mapping ventricular dilatation using three dimensional CMR image registration. *Journal of Cardiovascular Magnetic Resonance*, 14(1):41–49.
- [Osher and Sethian, 1988] Osher, S. and Sethian, J. (1988). Fronts propagating with curvature-dependent speed: Algorithms based on Hamilton-Jacobi formulations. *Journal of Computational Physics*, 79(1):12–49.
- [Osman et al., 1999] Osman, N., Kerwin, W., McVeigh, E., and Prince, J. (1999). Cardiac motion tracking using CINE harmonic phase (HARP) Magnetic Resonance imaging. *Magnetic Resonance in Medicine*, 42(6):1048.
- [Osman et al., 2000] Osman, N., McVeigh, E., and Prince, J. (2000). Imaging heart motion using harmonic phase MRI. *IEEE Transactions on Medical Imaging*, 19(3):186–202.
- [Otsu, 1975] Otsu, N. (1975). A threshold selection method from gray-level histograms. *Automatica*, 11:285–296.

- [Pan et al., 2005] Pan, L., Prince, J., Lima, J., and Osman, N. (2005). Fast tracking of cardiac motion using 3D-HARP. *IEEE Transactions on Biomedical Engineering*, 52(8):1425–1435.
- [Paragios, 2002] Paragios, N. (2002). A variational approach for the segmentation of the left ventricle in cardiac image analysis. *International Journal of Computer Vision*, 50(3):345–362.
- [Park et al., 1996] Park, J., Metaxas, D., and Axel, L. (1996). Analysis of left ventricular wall motion based on volumetric deformable models and MRI-SPAMM. *Medical Image Analysis*, 1(1):53–71.
- [Pavani et al., 2009] Pavani, S., Delgado, D., and Frangi, A. (2009). Haar-like features with optimally weighted rectangles for rapid object detection. *Pattern Recognition*, 43(1):160–172.
- [Pednekar et al., 2006] Pednekar, A., Kurkure, U., Muthupillai, R., Flamm, S., and Kakadiaris, I. (2006). Automated left ventricular segmentation in cardiac MRI. *IEEE Transactions on Biomedical Engineerings*, 53(7):1425–1428.
- [Perperidis et al., 2005] Perperidis, D., Mohiaddin, R., and Rueckert, D. (2005). Spatio-temporal free-form registration of cardiac MR image sequences. *Medical Image Analysis*, 9(5):441–456.
- [Peters et al., 2007] Peters, J., Ecabert, O., Meyer, C., Schramm, H., Kneser, R., Groth, A., and Weese, J. (2007). Automatic whole heart segmentation in static Magnetic Resonance image volumes. *Medical Image Computing and Computer Assisted Intervention (MICCAI)*, pages 402–410.
- [Petitjean and Dacher, 2011] Petitjean, C. and Dacher, J.-N. (2011). A review of segmentation methods in short axis cardiac MR images. *Medical Image Analysis*, 15(2):169–184.
- [Pfeffer and Braunwald, 1990] Pfeffer, M. and Braunwald, E. (1990). Ventricular remodeling after myocardial infarction. experimental observations and clinical implications. *circulation*, 81(4):1161–1172.
- [Pham et al., 2000] Pham, D., Xu, C., and Prince, J. (2000). Current methods in medical image segmentation. *Annual Review of Biomedical Engineering*, 2(1):315–337.

- [Pizarro et al., 2011] Pizarro, L., Delpiano, J., Aljabar, P., Ruiz-del Solar, J., and Rueckert, D. (2011). Towards dense motion estimation in light and electron microscopy. In *International Symposium on Biomedical Imaging: From Nano to Macro (ISBI)*, pages 1939–1942.
- [Pluempitiwiriyaewej et al., 2005] Pluempitiwiriyaewej, C., Moura, J., Wu, Y., and Ho, C. (2005). STACS: New active contour scheme for cardiac MR image segmentation. *IEEE Transactions on Medical Imaging*, 24(5):593–603.
- [Prince and McVeigh, 1992] Prince, J. and McVeigh, E. (1992). Motion estimation from tagged MR image sequences. *IEEE Transactions on Medical Imaging*, 11(2):238–249.
- [Qian et al., 2007] Qian, T., Huang, R., Metaxas, D., and Axel, L. (2007). A novel tag removal technique for tagged cardiac MRI and its applications. In *International Symposium on Biomedical Imaging: From Nano to Macro (ISBI)*, pages 364–367.
- [Qian et al., 2006] Qian, Z., Metaxas, D., and Axel, L. (2006). Extraction and tracking of MRI tagging sheets using a 3D Gabor filter bank. In *International Conference of the IEEE Engineering in Medicine and Biology Society*, pages 711–714.
- [Qian et al., 2008] Qian, Z., Metaxas, D., and Axel, L. (2008). Non-tracking-based 2D strain estimation in tagged MRI. In *International Symposium on Biomedical Imaging: From Nano to Macro (ISBI)*, pages 528–531.
- [Rangarajan et al., 1997] Rangarajan, A., Chui, H., Mjolsness, E., Pappu, S., Davachi, L., Goldman-Rakic, P., and Duncan, J. (1997). A robust point-matching algorithm for autoradiograph alignment. *Medical Image Analysis*, 1(4):379–398.
- [Remme et al., 2005] Remme, E., Augenstein, K., Young, A., and Hunter, P. (2005). Parameter distribution models for estimation of population based left ventricular deformation using sparse fiducial markers. *IEEE Transactions on Medical Imaging*, 24(3):381–388.
- [Risholm et al., 2010] Risholm, P., Pieper, S., Samset, E., and Wells, W. (2010). Summarizing and visualizing uncertainty in non-rigid registration. *Medical Image Computing and Computer Assisted Intervention (MICCAI)*, pages 554–561.

- [Rohlfing, 2012] Rohlfing, T. (2012). Image similarity and tissue overlaps as surrogates for image registration accuracy: Widely used but unreliable. *IEEE Transactions on Medical Imaging*, 31(2):153–163.
- [Rohlfing et al., 2004] Rohlfing, T., Brandt, R., Menzel, R., and Maurer, C. (2004). Evaluation of atlas selection strategies for atlas-based image segmentation with application to confocal microscopy images of bee brains. *NeuroImage*, 21(4):1428–1442.
- [Rohlfing and Maurer, 2001] Rohlfing, T. and Maurer, C. (2001). Intensity-based non-rigid registration using adaptive multilevel free-form deformation with an incompressibility constraint. In *Medical Image Computing and Computer Assisted Intervention (MICCAI)*, pages 111–119.
- [Rohlfing et al., 2003] Rohlfing, T., Maurer Jr, C., Bluemke, D., and Jacobs, M. (2003). Volume-preserving nonrigid registration of MR breast images using free-form deformation with an incompressibility constraint. *IEEE Transactions on Medical Imaging*, 22(6):730–741.
- [Roozgard et al., 2011] Roozgard, A., Barzigar, N., Cheng, S., and Verma, P. (2011). Dense image registration using sparse coding and belief propagation. In *International Conference on Signal Processing and Communication Systems*, pages 1–5.
- [Roth and Black, 2005] Roth, S. and Black, M. (2005). On the spatial statistics of optical flow. In *International Conference on Computer Vision (ICCV)*, volume 1, pages 42–49.
- [Rouchdy et al., 2007] Rouchdy, Y., Pousin, J., Schaerer, J., and Clarysse, P. (2007). A nonlinear elastic deformable template for soft structure segmentation: application to the heart segmentation in MRI. *Inverse Problems*, 23:1017.
- [Rougon et al., 2005] Rougon, N., Petitjean, C., Prketeux, F., Cluzel, P., and Grenier, P. (2005). A non-rigid registration approach for quantifying myocardial contraction in tagged MRI using generalized information measures. *Medical Image Analysis*, 9(4):353–375.
- [Rubin and Reisner, 2009] Rubin, E. and Reisner, H. (2009). *Essentials of Rubin’s pathology*. Lippincott Williams & Wilkins.

- [Rueckert et al., 2006] Rueckert, D., Aljabar, P., Heckemann, R., Hajnal, J., and Hammers, A. (2006). Diffeomorphic registration using B-splines. *Medical Image Computing and Computer Assisted Intervention (MICCAI)*, pages 702–709.
- [Rueckert et al., 2003] Rueckert, D., Frangi, A., and Schnabel, J. (2003). Automatic construction of 3D statistical deformation models of the brain using nonrigid registration. *IEEE Transactions on Medical Imaging*, 22(8):1014–1025.
- [Rueckert et al., 1999] Rueckert, D., Sonoda, L., Hayes, C., Hill, D., Leach, M., and Hawkes, D. (1999). Nonrigid registration using free-form deformations: application to breast MR images. *IEEE Transactions on Medical Imaging*, 18(8):712–721.
- [Rutz et al., 2008] Rutz, A., Ryf, S., Plein, S., Boesiger, P., and Kozerke, S. (2008). Accelerated whole-heart 3D CSPAMM for myocardial motion quantification. *Magnetic Resonance in Medicine*, 59(4):755–763.
- [Ryf et al., 2002] Ryf, S., Spiegel, M., Gerber, M., and Boesiger, P. (2002). Myocardial tagging with 3D-CSPAMM. *Journal of Magnetic Resonance Imaging*, 16(3):320–325.
- [Saeed et al., 1989] Saeed, M., Wagner, S., Wendland, M. F., Derugin, N., Finkbeiner, W. E., and Higgins, C. B. (1989). Occlusive and reperfused myocardial infarcts: differentiation with mn-dpdp-enhanced MR imaging. *Radiology*, 172(1):59–64.
- [Sampath and Prince, 2007] Sampath, S. and Prince, J. (2007). Automatic 3D tracking of cardiac material markers using slice-following and harmonic-phase MRI. *Magnetic Resonance Imaging*, 25(2):197–208.
- [Schaerer et al., 2010] Schaerer, J., Casta, C., Pousin, J., and Clarysse, P. (2010). A dynamic elastic model for segmentation and tracking of the heart in MR image sequences. *Medical Image Analysis*, 14(6):738 – 749.
- [Schnabel et al., 2001] Schnabel, J., Rueckert, D., Quist, M., Blackall, J., Castellano-Smith, A., Hartkens, T., Penney, G., Hall, W., Liu, H., Truwit, C., et al. (2001). A generic framework for non-rigid registration based on non-uniform multi-level free-form deformations. In *Medical Image Computing and Computer Assisted Intervention (MICCAI)*, pages 573–581.

- [Senegas et al., 2004] Senegas, J., Cocosco, C., and Netsch, T. (2004). Model-based segmentation of cardiac MRI cine sequences: a bayesian formulation. In *SPIE Medical Imaging*, volume 5370, page 432.
- [Sethian, 1996] Sethian, J. (1996). A fast marching level set method for monotonically advancing fronts. *Proceedings of the National Academy of Sciences*, 93(4):1591.
- [Shechter et al., 2004] Shechter, G., Ozturk, C., Resar, J., and McVeigh, E. (2004). Respiratory motion of the heart from free breathing coronary angiograms. *IEEE Transactions on Medical Imaging*, 23(8):1046–1056.
- [Shen and Wu, 2010] Shen, X. and Wu, Y. (2010). Sparsity model for robust optical flow estimation at motion discontinuities. In *Computer Vision and Pattern Recognition (CVPR)*, pages 2456–2463.
- [Shi et al., 2011] Shi, W., Zhuang, X., Wang, H., Duckett, S., O’regan, D., Edwards, P., Ourselin, S., and Rueckert, D. (2011). Automatic segmentation of different pathologies from cardiac cine MRI using registration and multiple component EM estimation. In *International Conference on Functional Imaging and Modeling of the Heart (FIMH)*, pages 163–170.
- [Studholme et al., 1999] Studholme, C., Hill, D., Hawkes, D., et al. (1999). An overlap invariant entropy measure of 3D medical image alignment. *Pattern recognition*, 32(1):71–86.
- [Su Huang, 2009] Su Huang, Jimin Liu, e. (2009). Segmentation of the Left Ventricle from Cine MR Images Using a Comprehensive Approach. In *International Conference on Functional Imaging and Modeling of the Heart (FIMH)*, pages 355–363. Springer-Verlag.
- [Suinesiaputra et al., 2012] Suinesiaputra, A., Cowan, B., Finn, J., Fonseca, C., Kadish, A., Lee, D., Medrano-Gracia, P., Warfield, S., Tao, W., and Young, A. (2012). Left ventricular segmentation challenge from cardiac MRI: A collation study. In *Statistical Atlases and Computational Models of the Heart. Imaging and Modelling Challenges*, volume 7085, pages 88–97.
- [Sun et al., 2010] Sun, D., Roth, S., and Black, M. (2010). Secrets of optical flow estimation and their principles. In *Computer Vision and Pattern Recognition (CVPR)*, pages 2432–2439.

- [Sundar et al., 2009] Sundar, H., Litt, H., and Shen, D. (2009). Estimating myocardial motion by 4D image warping. *Pattern Recognition*, 42(11):2514–2526.
- [Sutton and Sharpe, 2000] Sutton, M. and Sharpe, N. (2000). Left ventricular remodeling after myocardial infarction: pathophysiology and therapy. *Circulation*, 101(25):2981–2988.
- [Thirion, 1998] Thirion, J. (1998). Image matching as a diffusion process: an analogy with maxwell’s demons. *Medical Image Analysis*, 2(3):243–260.
- [Tobon-Gomez et al., 2012] Tobon-Gomez, C., De Craene, M., Dahl, A., Kapetanakis, S., Carr-White, G., Lutz, A., Rasche, V., Etyngier, P., Kozerke, S., Schaeffter, T., et al. (2012). A multimodal database for the 1 st cardiac motion analysis challenge. *Statistical Atlases and Computational Models of the Heart. Imaging and Modelling Challenges*, pages 33–44.
- [Torres and Moayedi, 2007] Torres, M. and Moayedi, S. (2007). Evaluation of the acutely dyspneic elderly patient. *Clinics in Geriatric Medicine*, 23(2):307–325.
- [Tustison et al., 2003] Tustison, N., Davila-Roman, V., and Amini, A. (2003). Myocardial kinematics from tagged MRI based on a 4D B-spline model. *IEEE Transactions on Biomedical Engineering*, 50(8):1038–1040.
- [Uribe et al., 2007] Uribe, S., Muthurangu, V., Boubertakh, R., Schaeffter, T., Razavi, R., Hill, D., and Hansen, M. (2007). Whole-heart cine MRI using real-time respiratory self-gating. *Magnetic Resonance in Medicine*, 57(3):606–613.
- [Uzumcu et al., 2006] Uzumcu, M., van der Geest, R., Swingen, C., Reiber, J., and Lelieveldt, B. (2006). Time continuous tracking and segmentation of cardiovascular Magnetic Resonance images using multidimensional dynamic programming. *Investigative Radiology*, 41(1):52.
- [Vercauteren et al., 2008] Vercauteren, T., Pennec, X., Perchant, A., and Ayache, N. (2008). Symmetric log-domain diffeomorphic registration: A demons-based approach. *Medical Image Computing and Computer Assisted Intervention (MICCAI)*, pages 754–761.

- [Veress et al., 2005] Veress, A., Gullberg, G., and Weiss, J. (2005). Measurement of strain in the left ventricle during diastole with cine-MRI and deformable image registration. *Journal of Biomechanical Engineering*, 127:1195.
- [Viola and Jones, 2002] Viola, P. and Jones, M. (2002). Robust real-time object detection. *International Journal of Computer Vision*, 57(2):137–154.
- [Viola and Wells III, 1997] Viola, P. and Wells III, W. (1997). Alignment by maximization of mutual information. *International Journal of Computer Vision*, 24(2):137–154.
- [Wang and Amini, 2011] Wang, H. and Amini, A. (2011). Cardiac motion and deformation recovery from MRI: A review. *IEEE Transactions on Medical Imaging*, 31(2):487–503.
- [Wang et al., 2008] Wang, X., Chen, T., Zhang, S., Metaxas, D., and Axel, L. (2008). Lv motion and strain computation from tMRI based on meshless deformable models. *Medical Image Computing and Computer Assisted Intervention (MICCAI)*, pages 636–644.
- [Wang et al., 2001] Wang, Y., Chen, Y., and Amini, A. (2001). Fast lv motion estimation using subspace approximation techniques. *IEEE Transactions on Medical Imaging*, 20(6):499–513.
- [Warfield et al., 2004] Warfield, S., Zou, K., and Wells, W. (2004). Simultaneous truth and performance level estimation (staple): an algorithm for the validation of image segmentation. *IEEE Transactions on Medical Imaging*, 23(7):903–921.
- [Weickert et al., 1998] Weickert, J., Romeny, B., and Viergever, M. (1998). Efficient and reliable schemes for nonlinear diffusion filtering. *IEEE Transactions on Image Processing*, 7(3):398–410.
- [Weisenfeld and Warfield, 2011] Weisenfeld, N. and Warfield, S. (2011). Learning likelihoods for labeling (L3): a general multi-classifier segmentation algorithm. *Medical Image Computing and Computer Assisted Intervention (MICCAI)*, pages 322–329.
- [Weisman et al., 1988] Weisman, H., Bush, D., Mannisi, J., Weisfeldt, M., and Healy, B. (1988). Cellular mechanisms of myocardial infarct expansion. *Circulation*, 78(1):186.

- [Wijnhout et al., 2009] Wijnhout, J., Hendriksen, D., Van Assen, H., and Van der Geest, R. (2009). LV Challenge LKEB Contribution: Fully Automated Myocardial Contour Detection. *Midas Journal*, page 683.
- [Wolz et al., 2010] Wolz, R., Heckemann, R., Aljabar, P., Hajnal, J., Hammers, A., Lötjönen, J., and Rueckert, D. (2010). Measurement of hippocampal atrophy using 4d graph-cut segmentation: Application to adni. *NeuroImage*, 52(1):109–118.
- [Xu and Prince, 1997] Xu, C. and Prince, J. (1997). Gradient vector flow: A new external force for snakes. In *Computer Vision and Pattern Recognition (CVPR)*, pages 66–71.
- [Yan et al., 2007] Yan, P., Sinusas, A., and Duncan, J. (2007). Boundary element method-based regularization for recovering of lv deformation. *Medical Image Analysis*, 11(6):540–554.
- [Young, 1999] Young, A. (1999). Model tags: direct three-dimensional tracking of heart wall motion from tagged Magnetic Resonance images. *Medical Image Analysis*, 3(4):361–372.
- [Young and Axel, 1992] Young, A. and Axel, L. (1992). Three-dimensional motion and deformation of the heart wall: estimation with spatial modulation of magnetization—a model-based approach. *Radiology*, 185(1):241–247.
- [Yu et al., 2005] Yu, C., Bleeker, G., Fung, J., Schalij, M., Zhang, Q., van der Wall, E., Chan, Y., Kong, S., and Bax, J. (2005). Left ventricular reverse remodeling but not clinical improvement predicts long-term survival after cardiac resynchronization therapy. *Circulation*, 112(11):1580–1586.
- [Zerhouni et al., 1988] Zerhouni, E., Parish, D., Rogers, W., Yang, A., and Shapiro, E. (1988). Human heart: tagging with MR imaging—a method for noninvasive assessment of myocardial motion. *Radiology*, 169(1):59–63.
- [Zhang et al., 2001] Zhang, Y., Brady, M., and Smith, S. (2001). Segmentation of brain MR images through a hidden Markov random field model and the expectation-maximization algorithm. *IEEE Transactions on Medical Imaging*, 20(1):45–57.

- [Zheng et al., 2007] Zheng, Y., Barbu, A., Georgescu, B., Scheuering, M., and Comaniciu, D. (2007). Fast automatic heart chamber segmentation from 3D CT data using marginal space learning and steerable features. In *International Conference on Computer Vision (ICCV)*, pages 1–8.
- [Zhuang et al., 2008] Zhuang, X., Rhode, K., Arridge, S., Razavi, R., Hill, D., Hawkes, D., and Ourselin, S. (2008). An atlas-based segmentation propagation framework using locally affine registration—application to automatic whole heart segmentation. *Medical Image Computing and Computer Assisted Intervention (MICCAI)*, pages 425–433.
- [Zhuang et al., 2010] Zhuang, X., Rhode, K., Razavi, R., Hawkes, D., and Ourselin, S. (2010). A registration-based propagation framework for automatic whole heart segmentation of cardiac MRI. *IEEE Transactions on Medical Imaging*, 29(9):1612–1625.
- [Zhuang et al., 2011] Zhuang, X., Shi, W., Duckett, S., Wang, H., Razavi, R., Hawkes, D., Rueckert, D., and Ourselin, S. (2011). A framework combining multi-sequence MRI for fully automated quantitative analysis of cardiac global and regional functions. In *International Conference on Functional Imaging and Modeling of the Heart (FIMH)*, volume 6666, pages 367–374.